



University of  
**Nottingham**

UK | CHINA | MALAYSIA

**Modelling store operated calcium  
entry: Creating a three dimensional  
spatio-temporal model to predict  
local calcium signals.**

Emma McIvor, MSc

Thesis submitted to The University of Nottingham  
for the degree of Doctor of Philosophy

# Abstract

Calcium ( $\text{Ca}^{2+}$ ) is a signalling messenger that is crucial to cellular function, controlling a diverse range of processes such as apoptosis, cell proliferation and muscle contraction. Store operated  $\text{Ca}^{2+}$  entry (SOCE) is a specific pathway coupling depletion of the  $\text{Ca}^{2+}$  stores within the endoplasmic reticulum (ER) to  $\text{Ca}^{2+}$  influx through Orai channels on the plasma membrane. SOCE occurs in small sub-cellular regions called 'ER-PM junctions' which are typically less than 300nm in diameter. The small size of these domains prevent direct measurement of the  $\text{Ca}^{2+}$  signals as current  $\text{Ca}^{2+}$  imaging techniques cannot resolve the local signals within ER-PM junctions. The  $\text{Ca}^{2+}$  signals associated with SOCE control many downstream cellular processes, such as gene expression and immune responses. There is substantial evidence demonstrating that the placement of the  $\text{Ca}^{2+}$  signalling machinery, including Orai channels and SERCA pumps, is vital to the generation of spatially distinct  $\text{Ca}^{2+}$  signals which then enhance the selectivity of the  $\text{Ca}^{2+}$  signal. However, experimental techniques cannot investigate the local  $\text{Ca}^{2+}$  dynamics occurring on a spatial scale of micrometres so mathematical modelling techniques can be used to close this gap in understanding how the local  $\text{Ca}^{2+}$  dynamics affect the experimentally observed global  $\text{Ca}^{2+}$  dynamics.

In this thesis, we construct a three dimensional spatio-temporal model of  $\text{Ca}^{2+}$  dynamics and investigate the relationship between the placement of core components of the  $\text{Ca}^{2+}$  signalling machinery, e.g. Orai channels and SERCA pumps, and the spatial  $\text{Ca}^{2+}$  profiles generated as well as the rates of ER refilling observed. The model includes a spatially extended ER-PM junction to examine the spatial signature of the  $\text{Ca}^{2+}$  profiles generated and a spatially extended sub-PM ER to examine the impact of Orai channel and SERCA pump placement on ER refilling dynamics. The model is the first to include spatially extended versions of both the ER-PM junction and sub-PM ER. In this thesis, we first focus on the construction of the spatio-temporal model and the solu-

tion techniques used to solve the model. We implement a semi-analytical solution using Green's functions to calculate the analytical solution of the spatial component of the diffusion equation and use numerical time stepping methods in MATLAB to evolve the spatial  $\text{Ca}^{2+}$  profile over time. We compare the predictions of the model to expected biological outcomes and then use the model to investigate how the placement of Orai channels, and in particular how clustering of Orai channels, creates spatially distinct  $\text{Ca}^{2+}$  profiles. We then examine whether the spatial  $\text{Ca}^{2+}$  profile affects ER refilling and what factors control ER refilling.

We find that Orai channel clustering creates spatially distinct  $\text{Ca}^{2+}$  profiles within the ER-PM junction but does not enhance ER refilling. ER refilling is more strongly controlled by the proximity of SERCA pumps to Orai channels. In fact, the placement of SERCA2b pumps weakly affects ER refilling but the major regulator of ER refilling is the placement of SERCA2a pumps within the ER-PM junction. However, ER refilling continues, albeit at reduced rates, regardless of Orai channel and SERCA pump placement which suggests that other factors, such as the geometry of the ER-PM junction, could be important regulators of ER refilling.

This work is relevant to experimental biologists and mathematicians within the  $\text{Ca}^{2+}$  signalling community as the  $\text{Ca}^{2+}$  signals generated within the ER-PM junction are crucial for advancing the understanding of how  $\text{Ca}^{2+}$  signals regulate cellular function. The local  $\text{Ca}^{2+}$  dynamics are important regulators of whole cell  $\text{Ca}^{2+}$  dynamics and so mathematical methods allowing rigorous investigation of the mechanisms controlling local  $\text{Ca}^{2+}$  signalling will be invaluable to furthering our understanding of how SOCE regulates cell function.

# Acknowledgements

I would like to express my sincerest thanks to my supervisor, Rüdiger Thul, for providing me with invaluable support and guidance throughout my PhD. I am also very grateful to my co-supervisor, Steven Coombes, for all his help and advice.

I would like to thank Dave Parkin for all his support with my computing needs.

Finally, I would like to thank my family and friends for their support and encouragement.

# Contents

<b>1</b>	<b>Introduction</b>	<b>1</b>
1.1	Motivation . . . . .	1
1.2	Biological literature review . . . . .	2
1.3	Mathematical literature review . . . . .	14
<b>2</b>	<b>Constructing a mathematical model of SOCE</b>	<b>18</b>
2.1	Mathematical model . . . . .	18
2.1.1	Geometry . . . . .	23
2.1.2	Model assumptions . . . . .	26
2.1.3	PDE model . . . . .	27
2.2	Discussion and conclusion . . . . .	34
<b>3</b>	<b>Solution and Implementation of the Model</b>	<b>38</b>
3.1	Solution techniques . . . . .	38
3.1.1	Barton's solution method . . . . .	38
3.2	Green's functions . . . . .	44
3.2.1	ER-PM junction . . . . .	45
3.2.2	Sub-PM ER . . . . .	50
3.3	Failure of Barton's method . . . . .	57
3.4	Felder's method . . . . .	62
3.4.1	ER-PM junction . . . . .	63
3.4.2	Sub-PM ER . . . . .	75
3.5	Numerical challenges . . . . .	82

3.6	Discussion . . . . .	86
<b>4</b>	<b>The relationship between the spatio-temporal discretisation and the <math>\text{Ca}^{2+}</math> profile generated</b>	<b>89</b>
4.1	How does the spatial discretisation affect the $\text{Ca}^{2+}$ profile generated? . . . . .	89
4.2	How does the time step, $dt$ , affect the $\text{Ca}^{2+}$ dynamics? . . . . .	102
4.3	Discussion . . . . .	104
<b>5</b>	<b>The effect of Orai channel and SERCA pump placement on ER refilling</b>	<b>108</b>
5.1	Clustering: microdomains . . . . .	109
5.2	Clustering: refilling . . . . .	112
5.3	Orai-SERCA distance: refilling . . . . .	116
5.4	O-S distance:SERCA2b:refilling . . . . .	118
5.5	Interactions between Orai channels and SERCA pumps cause highly heterogeneous $\text{Ca}^{2+}$ profiles in the ER-PM junction . . .	121
5.6	Discussion and Conclusion . . . . .	124
<b>6</b>	<b>Conclusions</b>	<b>128</b>
<b>A</b>	<b>Green's functions</b>	<b>134</b>
A.1	Bulk Cytoplasm . . . . .	134
A.2	Bulk ER . . . . .	137
<b>B</b>	<b>Separation of variables in the ER-PM junction</b>	<b>141</b>
B.1	$V_{j,1}$ . . . . .	141
B.2	$V_{j,2}$ . . . . .	142
B.3	$V_{j,3}$ . . . . .	142
<b>C</b>	<b>Separation of variables in the sub-PM ER</b>	<b>144</b>
C.1	$V_{s,1}$ . . . . .	144
C.2	$V_{s,2}$ . . . . .	145



# Chapter 1

## Introduction

### 1.1 Motivation

Calcium ( $\text{Ca}^{2+}$ ) is frequently referred to as a promiscuous intracellular messenger because it is involved in many cellular functions, such as apoptosis, gene expression and cell proliferation [21,67]. A recent addition to the calcium field is the store operated calcium entry (SOCE) pathway. It was discovered in the mid-1970s and is the only pathway coupling the depletion of endoplasmic reticulum (ER)  $\text{Ca}^{2+}$  stores to  $\text{Ca}^{2+}$  influx through store operated  $\text{Ca}^{2+}$  (SOC) channels [61,65,65]. In the mid-2000s the key regulators of SOCE were discovered [26] and it was well known that SOCE was crucial to a plethora of cellular functions, such as gene expression [72], and abnormal SOCE was linked to immunodeficiency diseases, such as severe combined immune deficiency (SCID) [26]. SOCE occurs in small subcellular regions called ER-PM junctions, typically less than 300nm in diameter, and the most prominent SOC channel is the Orai channel, which has a much smaller single channel current than other  $\text{Ca}^{2+}$  channels, e.g. the L-type voltage channel [55].

SOCE creates highly heterogeneous local  $\text{Ca}^{2+}$  signals and the local  $\text{Ca}^{2+}$  signals have been observed to control whole cell cellular functions; therefore, SOCE is an important regulator of cellular function. The placement of the  $\text{Ca}^{2+}$  signalling machinery provides a mechanism for generating spatially distinct  $\text{Ca}^{2+}$  signals and allows greater control over the shape and amplitude of the  $\text{Ca}^{2+}$  signal. In turn, this creates highly versatile  $\text{Ca}^{2+}$  signals which could be used to selectively activate downstream signalling processes.

Experimental techniques allow precise measurement of macroscopic  $\text{Ca}^{2+}$  sig-

nals, for instance whole cell  $\text{Ca}^{2+}$  oscillations and levels of gene expression. However, the small size of the ER-PM junctions precludes direct measurement of the local  $\text{Ca}^{2+}$  concentrations with current  $\text{Ca}^{2+}$  imaging techniques. These local  $\text{Ca}^{2+}$  signals are important as they control whole cell  $\text{Ca}^{2+}$  signals. Mathematical models can close this gap in understanding how local  $\text{Ca}^{2+}$  signals affect global  $\text{Ca}^{2+}$  processes by simulating the local  $\text{Ca}^{2+}$  signals generated within ER-PM junctions. Using spatio-temporal modelling we can predict the shape and amplitude of the spatial  $\text{Ca}^{2+}$  signal and thus compare how different arrangements of the  $\text{Ca}^{2+}$  signalling machinery affect the spatial  $\text{Ca}^{2+}$  profile generated. Mathematical modelling provides a way of investigating the relationship between the placement of Orai channels and the  $\text{Ca}^{2+}$  signals generated to further understand how SOCE regulates cellular signalling and can selectively activate downstream signalling processes. ER refilling is a fundamental aspect of SOCE and we can use mathematical models to elucidate how ER refilling depends on the  $\text{Ca}^{2+}$  signals generated, for instance the impact of Orai channel and SERCA pump location on the rate of ER refilling. Mathematical modelling can be used to investigate the local signalling behaviours and thus bridge the gap in understanding between microscopic and macroscopic  $\text{Ca}^{2+}$  signals to enhance current insights into local  $\text{Ca}^{2+}$  signals such as SOCE.

## 1.2 Biological literature review

Calcium ions are ubiquitous intracellular messengers and increases in the cytoplasmic  $\text{Ca}^{2+}$  concentration result in  $\text{Ca}^{2+}$  signals which are propagated throughout the cell [3]. These  $\text{Ca}^{2+}$  signals mediate cellular functions, ranging from muscle contraction, which requires a very rapid response, to apoptosis, which requires a much slower response [21].  $\text{Ca}^{2+}$  signals are typically generated by discharges of  $\text{Ca}^{2+}$  from intracellular stores such as the endoplasmic reticulum (ER), and entry of extracellular  $\text{Ca}^{2+}$  through plasma membrane (PM)  $\text{Ca}^{2+}$  channels. The mechanisms controlling such elevations in the cytoplasmic  $\text{Ca}^{2+}$  concentration are key to understanding how  $\text{Ca}^{2+}$  signals are generated [3,21].

The  $\text{Ca}^{2+}$  concentration in the cytoplasm is kept relatively low, around 100nM, compared to the  $\text{Ca}^{2+}$  concentrations in the extracellular fluid, approximately 1mM, and ER lumen, approximately 400 $\mu$ M, which are much higher [3,9,41], as illustrated in Figure 1.1. When a signalling pathway results in the opening

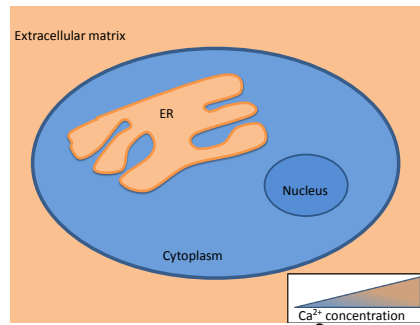


**Figure 1.1:** Illustration of the relative  $\text{Ca}^{2+}$  concentrations in cells.

of  $\text{Ca}^{2+}$  channels in the PM or ER membrane there is a rapid rush of  $\text{Ca}^{2+}$  into the cytoplasm which increases the cytoplasmic  $\text{Ca}^{2+}$  concentration near the open  $\text{Ca}^{2+}$  channels, creating local  $\text{Ca}^{2+}$  signals [3].

Store operated  $\text{Ca}^{2+}$  entry is the influx of  $\text{Ca}^{2+}$  into the cytoplasm through store operated  $\text{Ca}^{2+}$  PM channels in response to the depletion of intracellular  $\text{Ca}^{2+}$  stores of the ER. This method of generating  $\text{Ca}^{2+}$  influx is important to the physiology of eukaryotic cells as abnormal SOCE has been linked to diseases [56], such as immunodeficiency [26], congenital myopathy [25] and inhibition of motor control in Purkinje neurons [31,32].

There are many types of SOC channels and we will focus on the  $\text{Ca}^{2+}$  release activated  $\text{Ca}^{2+}$  (CRAC) channel of the PM, one of the principal  $\text{Ca}^{2+}$  influx pathways. The discovery of biphasic  $\text{Ca}^{2+}$  oscillations in the 1970s prompted further investigation into the mechanisms behind this oscillatory behaviour [61]. Putney [61] found that biphasic oscillations were composed of an initial transient spike in the cytoplasmic  $\text{Ca}^{2+}$  concentration followed by sustained elevation of the cytoplasmic  $\text{Ca}^{2+}$  concentration. The sustained phase depended on the presence of external  $\text{Ca}^{2+}$  suggesting that this phase was triggered by an influx of  $\text{Ca}^{2+}$  [42,61]. In 1981, Putney [65] proposed that activation of receptors caused depletion of  $\text{Ca}^{2+}$  from a cellular pool consequently causing the opening of PM  $\text{Ca}^{2+}$  channels and influx of  $\text{Ca}^{2+}$ .

The process connecting the release of  $\text{Ca}^{2+}$  from the ER pool and the influx of  $\text{Ca}^{2+}$  across the PM remained elusive but it was thought that  $\text{Ca}^{2+}$  influx could be a direct consequence of inositol trisphosphate ( $\text{IP}_3$ ) activation. Putney [62] proposed the capacitative calcium entry (CCE) model in which depletion of the  $\text{Ca}^{2+}$  store causes a pathway to open facilitating  $\text{Ca}^{2+}$  movement between the extracellular space and intracellular pool. This hypothetical pathway allows  $\text{Ca}^{2+}$  to enter the cytoplasm but ER  $\text{Ca}^{2+}$  pumps accumulate the  $\text{Ca}^{2+}$  so

rapidly that there is no sustained elevation of the bulk cytoplasmic  $\text{Ca}^{2+}$  concentration at this stage. The CCE model allows  $\text{Ca}^{2+}$  release and  $\text{Ca}^{2+}$  entry to be controlled by the  $\text{IP}_3$  receptors ( $\text{IP}_3\text{Rs}$ ) and the bulk cytoplasmic  $\text{Ca}^{2+}$  concentration is not affected until  $\text{Ca}^{2+}$  was released from internal stores by  $\text{IP}_3$  [62,64].

Zweifach *et al.* [88] observed that the  $\text{Ca}^{2+}$  current across the PM developed before the increase in cytoplasmic  $\text{Ca}^{2+}$  concentration, which meant  $\text{Ca}^{2+}$  influx through PM channels began before  $\text{Ca}^{2+}$  released from the ER by  $\text{IP}_3$  diffused into the cytoplasm. Therefore, the increase in cytoplasmic  $\text{Ca}^{2+}$  concentration due to  $\text{IP}_3\text{R}$  activation cannot be responsible for  $\text{Ca}^{2+}$  influx into the cell [88]. Further to this, Dolmetsch *et al.* [20] showed that calcium oscillations were generated independently of  $\text{IP}_3$ , almost entirely depended on the  $\text{Ca}^{2+}$  influx across the PM, and that activation of this influx required at least partial depletion of intracellular  $\text{Ca}^{2+}$  stores. This demonstration that the  $\text{Ca}^{2+}$  influx occurred independently of receptor activation showed that the  $\text{Ca}^{2+}$  entry causing the sustained phase of the biphasic  $\text{Ca}^{2+}$  oscillation was not a direct consequence of  $\text{IP}_3\text{R}$  activation [64] and the oscillations were linked to the amount of  $\text{Ca}^{2+}$  in the intracellular stores [20,61,65,88].

In the early 1990s, an area of contention within the field was whether  $\text{Ca}^{2+}$  entered the cytoplasm directly through PM channels, in accordance with Putney's CCE theory, or entered the intracellular  $\text{Ca}^{2+}$  store directly through a pathway connecting the extracellular fluid and the intracellular  $\text{Ca}^{2+}$  store, as proposed by Casteels and Droogmans [10]. To differentiate between these two concepts, cells were exposed to Thapsigargin (TG). Thapsigargin is a tumour promoter that inhibits sarco/endoplasmic reticulum  $\text{Ca}^{2+}$  ATPase (SERCA) pumps and application of TG elevates cytoplasmic  $\text{Ca}^{2+}$  concentrations by mobilising  $\text{Ca}^{2+}$  release from the ER. The application of TG to a resting cell with full  $\text{Ca}^{2+}$  stores activated  $\text{Ca}^{2+}$  influx to the same extent as PLC activation but did not increase  $\text{IP}_3$  formation. This showed that TG does not open ER channels [76] so  $\text{Ca}^{2+}$  must move directly into the cytoplasm via PM channels.

Hoth and Penner [35] discovered an electrical current, which they termed a CRAC current ( $I_{\text{CRAC}}$ ), corresponding to the  $\text{Ca}^{2+}$  influx across the PM through CRAC channels. This further reinforced Putney's hypothesis that  $\text{Ca}^{2+}$  entered the cytoplasm directly through PM channels. The depletion of the intracellular calcium stores activated the  $\text{Ca}^{2+}$  current,  $I_{\text{CRAC}}$ , which was the first store operated current to be characterised [35]. CRAC currents are inwardly recti-

fyng with a high selectivity for  $\text{Ca}^{2+}$ , a low single channel conductance and a very small current magnitude [35,63]. These unique properties are used to differentiate CRAC currents from other SOC currents. Hoth and Penner [35] observed that the delay before activation of  $I_{\text{CRAC}}$  was not consistent with  $\text{IP}_3$  induced  $\text{Ca}^{2+}$  release, providing further evidence that  $\text{IP}_3$  does not gate the  $I_{\text{CRAC}}$  current directly.

The extremely small conductance of CRAC channels, 10 – 24 fS, precludes direct recording of single channel currents. The single channel current magnitude has been estimated to be in the range of 1 – 4 fA using whole cell patch clamps and noise analysis techniques [23,27,39,55,88]. This unitary  $\text{Ca}^{2+}$  current corresponds to a flux rate of 3,000 – 12,000  $\text{Ca}^{2+}$  ions per second which is 100 fold smaller than other known  $\text{Ca}^{2+}$  channel flux rates such as the L type voltage channel which has a flux rate of 1,890,000 ions per second [28,39].

The next major breakthrough came with the discovery of key regulators of the SOCE process; the stromal interacting molecules STIM1 and STIM2 [44,85]. STIM1 and STIM2 were identified from large siRNA screens and knockdown of STIM1 and STIM2 suppressed the sustained  $\text{Ca}^{2+}$  influx phase of the biphasic calcium oscillations without affecting the peak amplitude of the transient phase [44]. Both STIM proteins have a single EF-hand  $\text{Ca}^{2+}$  binding domain which resides in the lumen of the ER. STIM2 proteins are only found in the ER and are responsible for controlling the basal levels of cytoplasmic and ER  $\text{Ca}^{2+}$  concentrations [78]. Experiments showed that STIM1 knockdown in HeLa cells inhibited SOCE demonstrating that STIM1 proteins are essential mediators of the SOCE pathway [26,44]. Similarly, overexpression of STIM1 significantly increased the  $\text{Ca}^{2+}$  influx through the SOC channel, reinforcing STIM1's role in regulating SOCE [44].

The spatial localisation of STIM1 was investigated to see if there was a connection between the location of STIM1 and activation of CRAC channels during SOCE. This led to the discovery that STIM1 were diffusely distributed throughout the ER of cells with full calcium stores, illustrated in Figure 1.2(a), but upon store depletion they translocated to the cell periphery, where they clustered together in puncta [44,81,85], as shown in Figure 1.2(b). Liou *et al.* [44] observed that the STIM1 redistribution occurred in the absence of extracellular  $\text{Ca}^{2+}$  which suggested that the STIM1 redistribution was a cause of  $\text{Ca}^{2+}$  influx and not a consequence.

It was proposed that STIM1 may function as  $\text{Ca}^{2+}$  sensors, using their EF-hand

domain to monitor calcium store levels [44,85]. Liou *et al.* [44] mutated the EF-hand domain of STIM1 to prevent binding of  $\text{Ca}^{2+}$  which resulted in STIM1 relocating and forming puncta on the cell periphery even if the  $\text{Ca}^{2+}$  stores were full. Liou *et al.* [44] observed an influx of  $\text{Ca}^{2+}$  with the mutated STIM1 even when the  $\text{Ca}^{2+}$  stores were full suggesting that the opening of the CRAC channels depends on the location of STIM1.

In cells with full  $\text{Ca}^{2+}$  stores STIM1 bind  $\text{Ca}^{2+}$  to their EF-hands and diffuse freely along the ER membrane with diffusion coefficients in the range  $0 - 0.4\mu\text{m}^2\text{s}^{-1}$  [44, 82, 85]. Store depletion causes  $\text{Ca}^{2+}$  to dissociate from the EF-hand of STIM1. This results in conformational changes in STIM1 structure that expose the C terminal polybasic domain and CRAC activation domain (CAD) [43, 57, 73]. Within 5 seconds of these conformational changes STIM1 oligomerises to form STIM1 multimers [43] which continue to diffuse throughout the ER membrane. STIM1 oligomers diffuse much more slowly with a mean diffusion coefficient of approximately  $0.05\mu\text{m}^2/\text{s}$  [43]. Luik *et al.* [45] demonstrated that oligomerization of STIM1, independent of  $\text{Ca}^{2+}$  store concentrations, was sufficient to drive SOCE demonstrating that oligomerization is required for  $\text{Ca}^{2+}$  influx through CRAC channels to occur.

The localisation of STIM1 after store depletion is important for understanding the signalling pathway responsible for activating the CRAC channels. Liou *et al.* [44] proposed that STIM1 localised in sections of the ER membrane in close proximity to the PM whereas Zhang *et al.* [85] proposed that STIM1 translocated from the ER to the PM and activated the CRAC channels from the PM. Wu *et al.* [81] demonstrated that STIM1 originating in the ER did not insert into the PM. STIM1 puncta were visualised using electron microscopy and STIM1 puncta formed at junctional ER sites which were approximately 10 – 25nm from the PM [81]. STIM1 oligomers diffuse slowly along the PM and the polybasic domain of STIM1 bind to polyphosphoinositides (e.g.  $\text{PIP}_2$ ) present in the PM causing clustering of STIM1 at these junctional ER puncta sites [12, 43, 45, 73]. The translocation of STIM1 oligomers, formed in response to store depletion, to the junctional ER sites takes approximately 40s and STIM1 can travel around  $2\mu\text{m}$  in this time. The ER-PM junctions where STIM1 cluster must be within  $2\mu\text{m}$  of STIM1 to ensure that STIM1 localise to the sites of  $\text{Ca}^{2+}$  influx in time to activate SOCE [43, 45].

Liou and Zhang [44, 85] hypothesised that STIM1 redistribution causes SOCE and activates  $I_{\text{CRAC}}$ . Wu *et al.* [81] tested this hypothesis and observed that

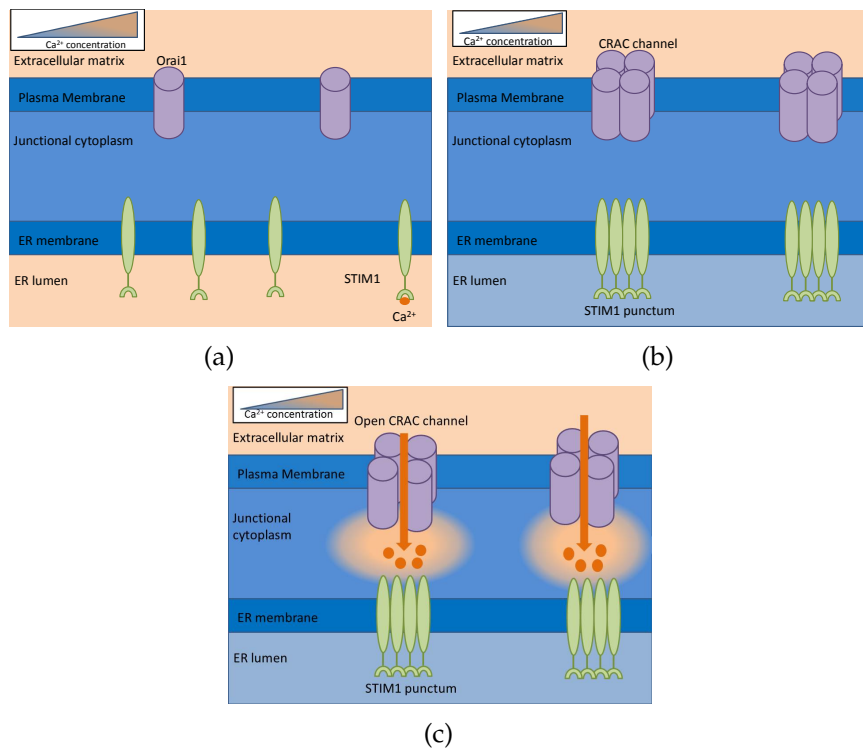


**Figure 1.2:** Illustration of the signalling mechanism behind SOCE proposed by [46]. (a) Distribution of STIM1 and Orai1 when the intracellular  $\text{Ca}^{2+}$  stores are full. (b) Distribution of STIM1 and Orai1 when the intracellular  $\text{Ca}^{2+}$  stores have been depleted. (c)  $\text{Ca}^{2+}$  influx through the open CRAC channels.

STIM1 accumulation in the ER precedes CRAC channel activation and development of the CRAC current, showing that STIM1 redistribution has a causal role in the activation of  $I_{\text{CRAC}}$ . STIM1 acts as a  $\text{Ca}^{2+}$  sensor and the depletion of intracellular stores causes the dissociation of  $\text{Ca}^{2+}$  from STIM1, resulting in the translocation of STIM1 to puncta at junctional ER sites [44, 81, 85]. Therefore this translocation is an essential early component of the signalling pathway activating CRAC channels,  $I_{\text{CRAC}}$  and SOCE.

The CRAC pathway requires additional components other than STIM1 so the search for the remaining components of the CRAC channel continued. RNAi screens resulted in the discovery of *olf186-F*, known as dOrai, a *Drosophila* protein with three human homologues; Orai1, Orai2 and Orai3. Knockdown of dOrai completely inhibited SOCE induced by TG, showing that dOrai is another regulator of CRAC channel activation [26, 84].

Zhang *et al.* [84] demonstrated that overexpression of *Drosophila* STIM or Orai increases the magnitude of  $I_{\text{CRAC}}$  and overexpressing both proteins together resulted in a significant increase in the size of the CRAC current. They hypothesised that dOrai constitutes part of the CRAC channel and STIM acts as a messenger for activation of the channel [84]. Further to this, Feske [26] showed that SOCE only occurred after store depletion, even if the extracellular  $\text{Ca}^{2+}$  concentration was much larger than the cytoplasmic  $\text{Ca}^{2+}$  concentration. Therefore, Orai1 is a key component of the CRAC activation pathway and the CRAC channel is closed and impermeable to  $\text{Ca}^{2+}$  when the CRAC pathway has not been activated.

To understand the activation of CRAC channels and the functions of STIM1 and Orai1 as regulators of the CRAC pathway the spatial relationship between STIM1, Orai1 and CRAC channels was investigated. In resting cells with full intracellular  $\text{Ca}^{2+}$  stores, STIM1 and Orai1 proteins are distributed diffusely in the ER and PM, respectively, as shown in Figure 1.2(a). Upon store depletion STIM1 oligomerize, diffuse slowly along the ER membrane and bind to  $\text{PIP}_2$  causing STIM1 to cluster in puncta at junctional ER sites. Orai1 proteins diffuse along the PM with diffusion coefficients in the range of  $0 - 0.4 \mu\text{m}^2/\text{s}$ , but the diffusion is slightly restricted (subdiffusive) in the PM of resting cells [82]. STIM1's CAD binds to passing Orai1 causing STIM1 and Orai1 to co-localise on the opposing membranes [46, 83] creating clusters of CRAC channels within the junction [57, 87], as shown in Figure 1.2(b). Park *et al.* [57] showed that the binding of STIM1's CAD to Orai1 activates the CRAC channels and allows

$\text{Ca}^{2+}$  influx into the cell to refill the depleted  $\text{Ca}^{2+}$  stores. Xu *et al.* [83] observed that when STIM1 proteins were not expressed, store depletion did not result in redistribution and clustering of Orai1 proteins on the PM. This demonstrates that Orai1 recruitment to sites opposite the STIM1 puncta requires prior aggregation of STIM1 and close proximity of the ER and PM to allow direct binding of STIM1's CAD and Orai1 [83].

Using single particle tracking (SPT), Wu *et al.* [82] were able to show that STIM1 and Orai1 movement was restricted to puncta within the ER-PM junction and that the diffusion coefficients of STIM1 and Orai1 displayed very similar distributions consistent with the formation of a STIM1-Orai1 complex. They also showed that approximately 25% of the STIM1 and Orai1 populations were immobile after store depletion and proposed that the binding of STIM1 to  $\text{PIP}_2$  on the PM or STIM1-Orai1 complex formation was sufficient to trap STIM1 within the ER-PM junction. This trapping caused STIM1 and Orai1 to accumulate at ER-PM junctions as the result of a diffusion trap rather than the result of very slow diffusion of the STIM1-Orai1 complex alone [82].

By imaging  $\text{Ca}^{2+}$  influx sites, Luik *et al.* [46] found that each site represents a cluster of open CRAC channels and that all sites of  $\text{Ca}^{2+}$  influx were tightly associated with STIM1 puncta, suggesting that CRAC channels are only activated in extremely close proximity to the STIM1 puncta [46]. Since STIM1 and Orai1 are both necessary for CRAC channel activation this co-localisation and close apposition of STIM1 and Orai1 could provide a mechanism for local activation of the CRAC channels and subsequent SOCE. The steps involved in the activation of the CRAC channel leading to SOCE are shown in Figure 1.2.

By mutating the Orai1 protein the  $\text{Ca}^{2+}$  selectivity of the CRAC channel was reduced and SOCE was impeded, showing that Orai1 proteins function as the highly  $\text{Ca}^{2+}$  selective pore-forming subunit of the CRAC channel [59, 80]. This discovery was fundamental to the understanding of the molecular nature of the CRAC channel since STIM1 and Orai1 are the major regulators of the CRAC channel. We will now refer to the CRAC channel as the Orai channel.

Through RNAi screens the SERCA pump was shown to be another mediator of the SOCE process, with knockdown of SERCA pumps suppressing  $I_{\text{CRAC}}$  [84]. SERCA pumps are essential for filling/refilling of  $\text{Ca}^{2+}$  stores and this reduction in  $I_{\text{CRAC}}$  could be due to deactivation of the Orai channel as the cytoplasmic  $\text{Ca}^{2+}$  concentration at the mouth of the channel will be high if SERCA pumps are inhibited [37, 54, 84]. It was then discovered that SERCA

pumps co-localised with STIM1 in puncta in the ER-PM junctions after ER store depletion [5,18,48,49,68]. Manjarres *et al.* [48,49] observed that SERCA2b pumps co-localised with STIM1 in the ER-PM junction after store depletion and estimated that the SERCA pumps would sit tens of nanometres from the Orai channels. Sampieri *et al.* [68] observed that SERCA2a pumps also co-localised with Orai channels in the ER-PM junction. This led to the conclusion that SERCA pumps are the third component regulating SOCE and the only component to ensure ER refilling occurs. Furthermore, a scaffolding protein, partner of STIM1 (POST), has been shown to promote binding of STIM1 to SERCA and PM  $\text{Ca}^{2+}$ -ATPase (PMCA) pumps after store depletion [38], so PMCA pumps must also localise to the SOCE sites. This close apposition of the SERCA pumps to the microdomain of high  $\text{Ca}^{2+}$  concentration around the Orai channel allows fast refilling of the  $\text{Ca}^{2+}$  store in the ER. POST facilitates binding of STIM1 to PMCA and this binding was shown to inhibit PMCA activity, decreasing  $\text{Ca}^{2+}$  efflux from the cell and increasing the  $\text{Ca}^{2+}$  available for ER refilling and local  $\text{Ca}^{2+}$  signalling [38,71]. PMCA and SERCA pumps act as removal mechanisms which are highly active after SOCE and control the amount of  $\text{Ca}^{2+}$  available for signalling [71]. If the  $\text{Ca}^{2+}$  concentration at the mouth of the Orai channel is too high then the Orai channel deactivates by  $\text{Ca}^{2+}$  dependent inactivation (CDI) stopping the  $\text{Ca}^{2+}$  influx [51,71].

The three key components regulating SOCE (STIM1, Orai1 and SERCA pumps) are all contained within the ER-PM junctions. ER-PM junctions have very small dimensions with typical diameters less than 300nm and heights of 10 – 25nm, according to estimates in the literature. Therefore, the three components of SOCE reside in close proximity through the co-localisation of each component to the ER-PM junction. The  $\text{Ca}^{2+}$  signalling machinery present in each ER-PM junction is shown in Figure 1.3. We see that the components involved in SOCE (Orai1, STIM1, POST, SERCA and PMCA pumps) are dispersed throughout the cell at rest but upon store depletion they co-localise to the ER-PM junction. This causes STIM1 to bind Orai1 thus opening the Orai channel and allowing  $\text{Ca}^{2+}$  influx, increasing the local  $\text{Ca}^{2+}$  concentration which then activates the SERCA pumps to refill the ER.

Despite knowing that all three components co-localise, the numbers of Orai channels and SERCA pumps contained within each ER-PM junction has not been directly measured. It is especially difficult to measure Orai channels using electrophysiological methods because of their small single channel current of 2.1fA [35, 88] leading to a whole cell current of approximately 5 – 10pA

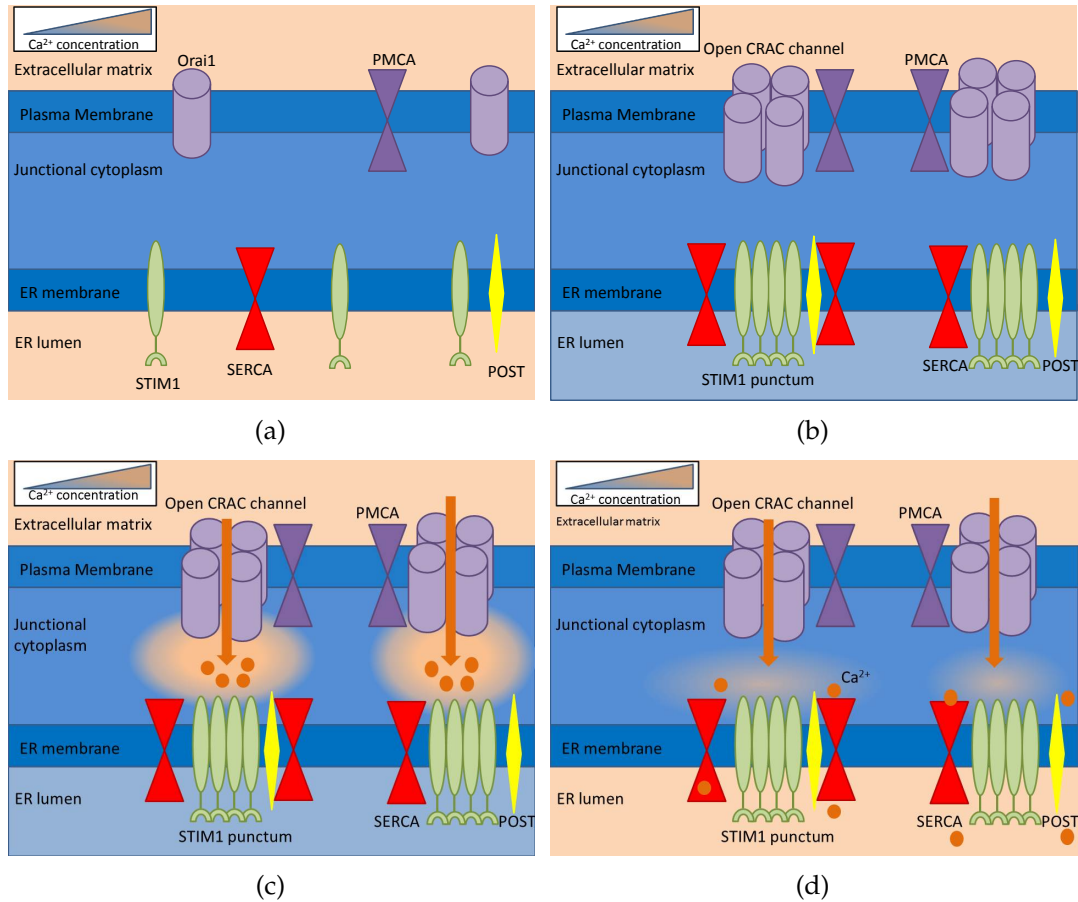


**Figure 1.3:** Illustration of the recent description of the signalling mechanism behind SOCE [71], including the  $Ca^{2+}$  pumps and POST protein which were shown to be regulators of the SOCE pathway [38]. (a) Distribution of STIM1, Orai1, SERCA, PMCA and POST when the intracellular  $Ca^{2+}$  stores are full. (b) Distribution of STIM1, Orai1, SERCA, PMCA and POST when the intracellular  $Ca^{2+}$  stores have been depleted. (c)  $Ca^{2+}$  influx through the open CRAC channels. (d) Refilling of the ER  $Ca^{2+}$  stores by SERCA pumps.

[11, 60]. There are many estimates of the number of Orai channels in the literature, ranging from 1700 Orai channels per cell [33] to 10000 channels per cell [60, 88]. Different cell types express different numbers of Orai channels leading to discrepancies in the estimates of Orai channel numbers. One method of increasing the Orai channel single channel current is to overexpress the numbers of STIM1 and Orai1 present in the cell thus amplifying the current. However, overexpression studies lead to overestimates of the number of Orai channels expressed in the cell. For instance, Ji *et al.* [36] estimated there to be 400,000 Orai channels in a HEK239 cell with each ER-PM junction containing approximately 1300 channels. This estimate was influenced by the overexpression of STIM1 which results in more Orai channels opening, an increase in the junction size and a higher estimate of the number of Orai channels expressed per cell with physiological levels of STIM1 and Orai1 [67]. So although overexpression studies create better conditions for electrophysiological experimental techniques they do not provide representative estimates of the number of endogenously expressed Orai channels per ER-PM junction or per cell. Other methods of quantifying the number of Orai channels per ER-PM junction, e.g. analysis of electron micrographs, estimate there to be 4 – 5 endogenously expressed Orai channels per ER-PM junction [33, 67].

Although the number of Orai channels in the ER-PM junction has been estimated there is still very little information about the location of the Orai channels (or SERCA pumps) within the ER-PM junction as current  $\text{Ca}^{2+}$  imaging techniques cannot resolve regions as small as ER-PM junctions. However, it has been observed experimentally that co-localisation of Orai channels to ER-PM junctions strengthens NFAT activation and spatio-temporal modelling demonstrated that the inter-channel distance controlled the amplitude and spread of the  $\text{Ca}^{2+}$  signal [67]. This lead Samanta *et al.* [67] to hypothesise that clustering of Orai channels will control the magnitude and shape of the  $\text{Ca}^{2+}$  profile and therefore enhance activation of downstream signalling processes such as c-fos stimulation and gene expression. This highlights the importance of Orai channel location for controlling downstream signalling processes and also the need for mathematical modelling to further understand how local dynamics influence global processes.

Recent investigations into the single channel dynamics observed two distinct Orai channel open states: "flickers" during which the Orai channel is open for 100 – 200ms and longer "pulses" during which the Orai channel is open for 1 – 3 seconds [23]. Further to this, Dynes *et al.* [23] did not observe stochastic

channel opening and hypothesised that upon binding of STIM1 to Orai1 the Orai channel is held in an open state and remains open until STIM1 unbinds.

The diffusion of  $\text{Ca}^{2+}$  through an open Orai channel results in elevation of the local  $\text{Ca}^{2+}$  concentration, creating a microdomain of high  $\text{Ca}^{2+}$  around the channel mouth. The microdomain decreases in amplitude as the distance from the channel increases due to cytoplasmic  $\text{Ca}^{2+}$  buffering and diffusion [53,55]. Such  $\text{Ca}^{2+}$  microdomains are depicted by the orange puffs in Figures 1.3(c) and 1.3(d). This gradient occurs over a very small volume so the local  $\text{Ca}^{2+}$  concentration can be very high in this microdomain in comparison to the bulk cytoplasmic  $\text{Ca}^{2+}$  concentration [6,55]. This local elevation of  $\text{Ca}^{2+}$  is important for cell signalling as it has been proposed that local  $\text{Ca}^{2+}$  influxes drive cellular functions such as gene expression. Furthermore, clustering of Orai channels causes the microdomains to overlap and create complex local  $\text{Ca}^{2+}$  signals within the ER-PM junction [33,55]. This reinforces the proposal that the location of Orai channels controls cell signalling because the channel microdomains will overlap to different extents depending on the inter-channel distance, therefore creating vastly different spatial  $\text{Ca}^{2+}$  profiles. In fact, the clustering of Orai channels could act as a potential mechanism for enhancing the selectivity of the  $\text{Ca}^{2+}$  signal and distinctly activate specific downstream cellular processes by controlling the amplitude and shape of the  $\text{Ca}^{2+}$  profile [17,46,67,72]. Therefore,  $\text{Ca}^{2+}$  microdomains in the ER-PM junction are important for cell signalling as they provide specificity to local  $\text{Ca}^{2+}$  signals [16,17,58]. They allow direct activation of effectors residing within the microdomain and enhance the ability to govern downstream cellular functions [34,55,67].

In summary, SOCE is a compartmentalised process and all the key components of the Orai activation pathway (STIM1, Orai1, SERCA, PMCA) are localised in each Orai channel microdomain, as illustrated in Figure 1.3(b). The elevated  $\text{Ca}^{2+}$  concentration of the microdomains of the cell provide specificity to cellular signals and functions [40]. In resting cells SOCE is initiated by depletion of the intracellular  $\text{Ca}^{2+}$  store in the ER. This causes  $\text{Ca}^{2+}$  to dissociate from STIM1 which then oligomerise, diffuse along the ER membrane and cluster in puncta at junctional ER sites through  $\text{PIP}_2$  binding, as shown in Figure 1.3(a). Orai1 channels diffuse along the PM and co-localise with STIM1 on the ER membrane when STIM1's CAD binds to Orai1. STIM1 recruits the adaptor protein POST to facilitate binding of STIM1 to SERCA and PMCA pumps, which have relocated to the immediate vicinity of the Orai channel in response

to POST, depicted in Figure 1.3(b). The close apposition of STIM1 and Orai1 causes the Orai channel to open and  $\text{Ca}^{2+}$  diffuses down the steep gradient from the extracellular fluid into the cytoplasm, shown in Figure 1.3(c). This sudden influx of  $\text{Ca}^{2+}$  induces an electrical current across the PM, known as  $I_{\text{CRAC}}$ , and the establishment of a local  $\text{Ca}^{2+}$  microdomain around the channel with very high cytoplasmic  $\text{Ca}^{2+}$  concentrations. STIM1 and POST inhibit the PMCA pump allowing more  $\text{Ca}^{2+}$  to remain in the microdomain for efficient refilling of the  $\text{Ca}^{2+}$  store by SERCA pumps, shown in Figure 1.3(d). When the ER  $\text{Ca}^{2+}$  stores are full the EF-hand of STIM1 binds  $\text{Ca}^{2+}$  and undergoes conformational changes to unbind STIM1's CAD from Orai1 allowing STIM1 and Orai1 to diffuse along the ER membrane and PM, respectively. The SOCE components return to their original distributions. SOCE is a method of increasing the local  $\text{Ca}^{2+}$  concentration of the ER-PM junction to allow fast refilling of the ER  $\text{Ca}^{2+}$  stores. The single channel current of Orai channels is very small and the number of Orai channels per ER-PM junction is small, approximately 5 channels. Despite the small population of Orai channels and the small single channel current they are able to provide sufficient  $\text{Ca}^{2+}$  influx to refill the  $\text{Ca}^{2+}$  store [27]. SOCE microdomains are signalling hubs and the local  $\text{Ca}^{2+}$  signals generated during SOCE are crucial for cell function, regulating processes such as gene expression. To fully appreciate the signalling potential of SOCE microdomains, it would be desirable to determine the range of  $\text{Ca}^{2+}$  concentrations in ER-PM junctions. However, this is difficult to measure experimentally because of the small dimensions of the ER-PM junctions [55], which are typically less than 300nm in diameter and 10 – 20nm in height [33,44,79,81].

### 1.3 Mathematical literature review

The field of  $\text{Ca}^{2+}$  signalling contains a diverse collection of both experimental and modelling techniques to understand  $\text{Ca}^{2+}$  signalling and the mechanisms controlling the creation of  $\text{Ca}^{2+}$  signals. Mathematical models are used to investigate  $\text{Ca}^{2+}$  signalling because the processes underlying the generation of  $\text{Ca}^{2+}$  signals are non-linear and thus cannot be readily described by intuitive and qualitative reasoning [21].

The field of  $\text{Ca}^{2+}$  signalling has many areas which benefit from the application of mathematical modelling and detailed reviews of the mathematical models used in  $\text{Ca}^{2+}$  signalling can be found in e.g. [21,22]. Dupont *et al.* [21] cre-

ated a mathematical model of the mGlu5 G-protein receptor signalling pathway and using an ordinary differential equation framework they accounted for the changing concentrations of  $\text{Ca}^{2+}$ , diacylglycerol (DAG) and protein kinase C (PKC) to understand the relationship between the components involved in the signalling pathway leading to the generation of  $\text{Ca}^{2+}$  oscillations. This model described whole cell  $\text{Ca}^{2+}$  oscillations to highlight aspects of the pathway that play an important role in the generation of  $\text{Ca}^{2+}$  oscillations, such as PKC. The model averaged the concentrations in the cytoplasm to describe  $\text{Ca}^{2+}$  dynamics at the whole cell level. However, mathematical models can also take account of the spatial aspect of  $\text{Ca}^{2+}$  dynamics and describe local  $\text{Ca}^{2+}$  signalling processes in which the spatial aspect of the signal is important. Examples of spatially extended  $\text{Ca}^{2+}$  dynamics include  $\text{Ca}^{2+}$  waves and  $\text{Ca}^{2+}$  microdomains.  $\text{Ca}^{2+}$  waves occur in response to  $\text{Ca}^{2+}$  release from internal stores; the wave of increased  $\text{Ca}^{2+}$  concentration can be propagated throughout the cell in a continuous manner, for example the fertilization wave in *Xenopus* mature oocytes, but the wave can also travel with burst-like behaviour, for example in immature *Xenopus* oocytes and cardiac myocytes [14]. Dawson *et al.* developed a mathematical model to provide insight into the factors controlling whether a wave is propagated continuously or in a saltatory manner [14]. High resolution three-dimensional spatio-temporal modelling was used by Thul *et al.* [77] to assess the effect of each factor controlling the propagation of saltatory  $\text{Ca}^{2+}$  waves in atrial myocytes and the model predicted that the cell boundary acts as a wave guide for the  $\text{Ca}^{2+}$  signal.  $\text{Ca}^{2+}$  microdomains are regions of locally high  $\text{Ca}^{2+}$  concentration formed around e.g.  $\text{Ca}^{2+}$  channels after  $\text{Ca}^{2+}$  influx and the local  $\text{Ca}^{2+}$  concentrations cannot be measured experimentally due to the small size of the microdomains. Griffith *et al.* [29] developed a three dimensional reaction-diffusion model to describe the spatio-temporal  $\text{Ca}^{2+}$  dynamics within a dendritic spine and used finite element methods to solve the model and bridge the spatial scales between the dendritic spine and signalling microdomains. The model demonstrated that  $\text{Ca}^{2+}$  signal location plays an important role for synaptic plasticity within the spine. These models investigate  $\text{Ca}^{2+}$  dynamics within one compartment but mathematical models can couple multiple compartments together to allow investigation of how  $\text{Ca}^{2+}$  signals are propagated between compartments and compare the signals created within each compartment. Sneyd *et al.* [70] developed a mathematical model to investigate how membrane fluxes between the cytoplasm and ER control the total cell load and how this controls the cells

ability to generate  $\text{Ca}^{2+}$  oscillations. The model includes two compartments, the cytoplasm and ER, and considers the averaged  $\text{Ca}^{2+}$  concentration in each compartment, using an ODE framework. By analysing the model they predicted that blocking membrane fluxes can eliminate  $\text{Ca}^{2+}$  oscillations and that the timing of the block controlled the extent to which the oscillations were reduced.

Since SOCE is a relatively recent addition to the field of  $\text{Ca}^{2+}$  signalling as mentioned above, there are relatively few mathematical models of SOCE [22]. However, research into SOCE is at the forefront of  $\text{Ca}^{2+}$  signalling and experimental techniques are limited as they cannot measure the  $\text{Ca}^{2+}$  concentrations within the small regions in which SOCE induced  $\text{Ca}^{2+}$  dynamics occur. Therefore mathematical models can further current understanding of SOCE.

The first model, presented by Ong *et al.* [54], examines the relationship between the cytoplasmic  $\text{Ca}^{2+}$  dynamics and the  $\text{Ca}^{2+}$  concentrations of the sub-PM ER and bulk ER. They describe the interplay between the  $\text{Ca}^{2+}$  dynamics of the ER-PM junction and both ER compartments for controlling SOCE activation. This model used an ODE framework which averaged the  $\text{Ca}^{2+}$  concentrations in the compartments based on the model in [70] discussed earlier. The model demonstrated that the sub-PM ER was depleted to a greater extent than the bulk ER during SOCE. This model was developed before the discovery that Orai1 was the pore forming subunit of Orai (CRAC) channels. In a similar vein, Croisier *et al.* [13] investigated averaged  $\text{Ca}^{2+}$  concentrations to shed light on how SOCE controls agonist induced  $\text{Ca}^{2+}$  oscillations in airway smooth muscle cells in the presence and absence of SERCA pump blockers.

There is significant evidence demonstrating that local  $\text{Ca}^{2+}$  signals are important for regulating downstream signalling processes and therefore the factors controlling the shape of the spatial  $\text{Ca}^{2+}$  profile, such as the placement of  $\text{Ca}^{2+}$  signalling machinery, are also key regulators of downstream signalling processes. Samanta *et al.* [67] investigated the importance of Orai channel placement on NFAT activation experimentally and found that clustering of Orai channels within ER-PM junctions strengthened c-fos activation and NFAT activation. However, they could not ascertain how the placement of the Orai channels changes the local  $\text{Ca}^{2+}$  profile. They developed a three dimensional spatio-temporal mathematical model to investigate the impact of Orai channel placement on the shape of the generated  $\text{Ca}^{2+}$  signal [67]. Using their mathematical model they demonstrate that clustering of Orai channels leads to dis-

tinct  $\text{Ca}^{2+}$  signatures and in particular that clustering controls the amplitude of the  $\text{Ca}^{2+}$  signal. They propose that clustering of Orai channels increases the amplitude and spread of the  $\text{Ca}^{2+}$  signal thus enhancing NFAT activation [67]. Samanta *et al.* [67] prescribed no flux boundary conditions on all the boundaries of the domain and included an internal source term to describe  $\text{Ca}^{2+}$  influx through Orai channels. Furthermore, the model only focused on the  $\text{Ca}^{2+}$  concentrations generated within the ER-PM junction in response to  $\text{Ca}^{2+}$  influx through Orai channels and did not include SERCA pumps or an ER compartment to investigate the effect on ER refilling.

# Chapter 2

## Constructing a mathematical model of SOCE

As discussed in Chapter 1, SOCE occurs in all eukaryotic cells and is a selective activator of many diverse cellular signalling processes [1, 17, 55, 58, 66, 74]. The key question we will address is: how does the spatial organisation of signalling components involved in SOCE regulate ER refilling dynamics and control the generation of distinct  $\text{Ca}^{2+}$  signals leading to selective activation of downstream processes, such as gene expression or endothelial cell proliferation?

By creating a 3D spatio-temporal mathematical model of SOCE we can investigate how the placement of channels and pumps involved in SOCE and  $\text{Ca}^{2+}$  signalling shapes spatial  $\text{Ca}^{2+}$  signals and affects refilling of the ER  $\text{Ca}^{2+}$  stores. We can use the model to cluster channels and provide insight into how the  $\text{Ca}^{2+}$  signals generated within the ER-PM junction and surrounding area depend on channel position. We may then determine the key factors controlling ER refilling and  $\text{Ca}^{2+}$  signalling during SOCE and highlight optimal positioning of channels, pumps and effectors for selective activation of cellular processes.

### 2.1 Mathematical model

SOCE is a complex process and is the only pathway to couple ER  $\text{Ca}^{2+}$  store depletion to  $\text{Ca}^{2+}$  influx across the PM to refill the  $\text{Ca}^{2+}$  stores of the ER. While SOCE is involved in a plethora of cellular signalling processes,  $\text{Ca}^{2+}$  influx

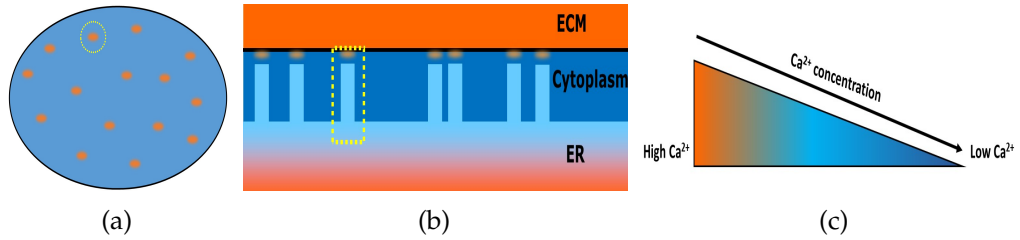


**Figure 2.1:** (a) Illustration of the  $\text{Ca}^{2+}$  influx sites which occur during SOCE. (b) Illustration of the structure of the ER during SOCE. The areas in orange represent high  $\text{Ca}^{2+}$  concentrations and the areas in dark blue represent the lower  $\text{Ca}^{2+}$  concentrations in the cell. (c) A colour scale representing the relative  $\text{Ca}^{2+}$  concentrations.

through Orai channels to refill the depleted ER  $\text{Ca}^{2+}$  stores and generate  $\text{Ca}^{2+}$  signals is a fundamental component of SOCE common to all cell types. We construct a 3D spatio-temporal model capable of simulating  $\text{Ca}^{2+}$  influx via Orai channels and the subsequent ER refilling and creation of associated  $\text{Ca}^{2+}$  signals in the ER-PM junction, thereby capturing the key features of SOCE. The model is novel as it is the first to provide a spatio-temporal description of both the ER-PM junction and sub-PM ER domains and couple the spatially extended domains with SERCA pumps. We implement a mathematical framework with a high spatial resolution to enable simultaneous investigation of the refilling properties of SOCE and the key features controlling the spatial signature of  $\text{Ca}^{2+}$  signals.

There are hundreds of ER-PM junctions per cell [33,67] and  $\text{Ca}^{2+}$  influx at the ER-PM junctions is illustrated by the orange puffs in Figure 2.1(a). The orange puffs represent regions of high  $\text{Ca}^{2+}$  concentration formed during  $\text{Ca}^{2+}$  influx. The dashed yellow line in Figure 2.1(a) encircling the sites of  $\text{Ca}^{2+}$  influx represents the maximal distance STIM1 can be from the ER-PM junction and still diffuse into the junction to take part in the SOCE process [43]. Therefore, there exists a natural ‘unit’, surrounded by the dashed yellow lines in Figures 2.1(a) and 2.1(b), which includes a single ER-PM junction and a portion of the surrounding cytoplasm which can be defined in accordance with experimentally observed length scales [43]. There is then the potential to create a network of these units of  $\text{Ca}^{2+}$  influx to provide insights into the global  $\text{Ca}^{2+}$  dynamics as a result of SOCE at multiple influx sites. This is something we will consider in future work.

The narrow gap between the PM and ER membrane, a distinguishing feature of ER-PM junctions, is created when a region of the ER is extended towards

the PM. This extension is illustrated in Figure 2.1(b) and we refer to this ER extension as the 'sub-PM ER'. The colours depict the range of  $\text{Ca}^{2+}$  concentrations in accordance with the colour scale of Figure 2.1(c). We also include a portion of the surrounding ER within one unit of  $\text{Ca}^{2+}$  influx to enable future investigation into the global ER refilling experienced by a cell with a network of  $\text{Ca}^{2+}$  influx units refilling distinct subregions of the ER.

SOCE is a highly compartmentalised process; the key components of SOCE we include in this model, Orai channels (purple) and SERCA pumps (green), co-localise to the ER-PM junction as shown in Figure 2.2, an illustration of the process we will model in more detail. Orai channels on the PM, formed upon STIM1 and Orai binding and represented by purple ovals, allow  $\text{Ca}^{2+}$  influx upon  $\text{Ca}^{2+}$  store depletion. SERCA pumps on the ER membrane ensure ER refilling is achieved and are represented by the green ovals. The orange arrows represent  $\text{Ca}^{2+}$  influx and the orange puffs represent  $\text{Ca}^{2+}$  microdomains formed around the channels/pumps.

The open Orai channels allow  $\text{Ca}^{2+}$  influx across the PM and this creates local  $\text{Ca}^{2+}$  microdomains around the channel mouths within the junction as shown by the orange puffs in Figure 2.2(a). As  $\text{Ca}^{2+}$  diffuses in the ER-PM junction this raises the  $\text{Ca}^{2+}$  concentration near the SERCA pumps,  $\text{Ca}^{2+}$  is then transported from the ER-PM junction into the sub-PM ER via SERCA pumps on the ER membrane, as illustrated in Figure 2.2(b).

Whilst the ER  $\text{Ca}^{2+}$  store is sufficiently depleted, Orai channels remain open. This allows  $\text{Ca}^{2+}$  influx to continue, which in turn preserves the  $\text{Ca}^{2+}$  microdomains within the ER-PM junction.  $\text{Ca}^{2+}$  cannot diffuse across the ER membrane creating a  $\text{Ca}^{2+}$  gradient in the sub-PM ER and driving  $\text{Ca}^{2+}$  diffusion towards the bulk ER, facilitating the ER refilling process, as shown in Figure 2.2(c).

There is no physical barrier between the ER-PM junction and the bulk cytoplasm so it is possible for  $\text{Ca}^{2+}$  to diffuse out of the ER-PM junction if it is not captured by SERCA pumps. When the  $\text{Ca}^{2+}$  in the sub-PM ER is sufficiently high, STIM1 will bind to  $\text{Ca}^{2+}$ , disassemble the Orai channel and move out of the ER-PM junction. In our model we are not concerned with STIM1 or Orai as separate entities, only their bound form as Orai channels. Once the channel disassembles it stops  $\text{Ca}^{2+}$  influx and is absent from the model. The microdomains of  $\text{Ca}^{2+}$ , preserved by the constant  $\text{Ca}^{2+}$  influx, dissipate throughout the ER-PM junction and the SERCA pumps continue to transport  $\text{Ca}^{2+}$

from the ER-PM junction into the sub-PM ER. In the sub-PM ER the  $\text{Ca}^{2+}$  gradient still exists so  $\text{Ca}^{2+}$  will continue diffusing until the  $\text{Ca}^{2+}$  concentration has equilibrated and the ER is refilled, shown in Figure 2.2(d).

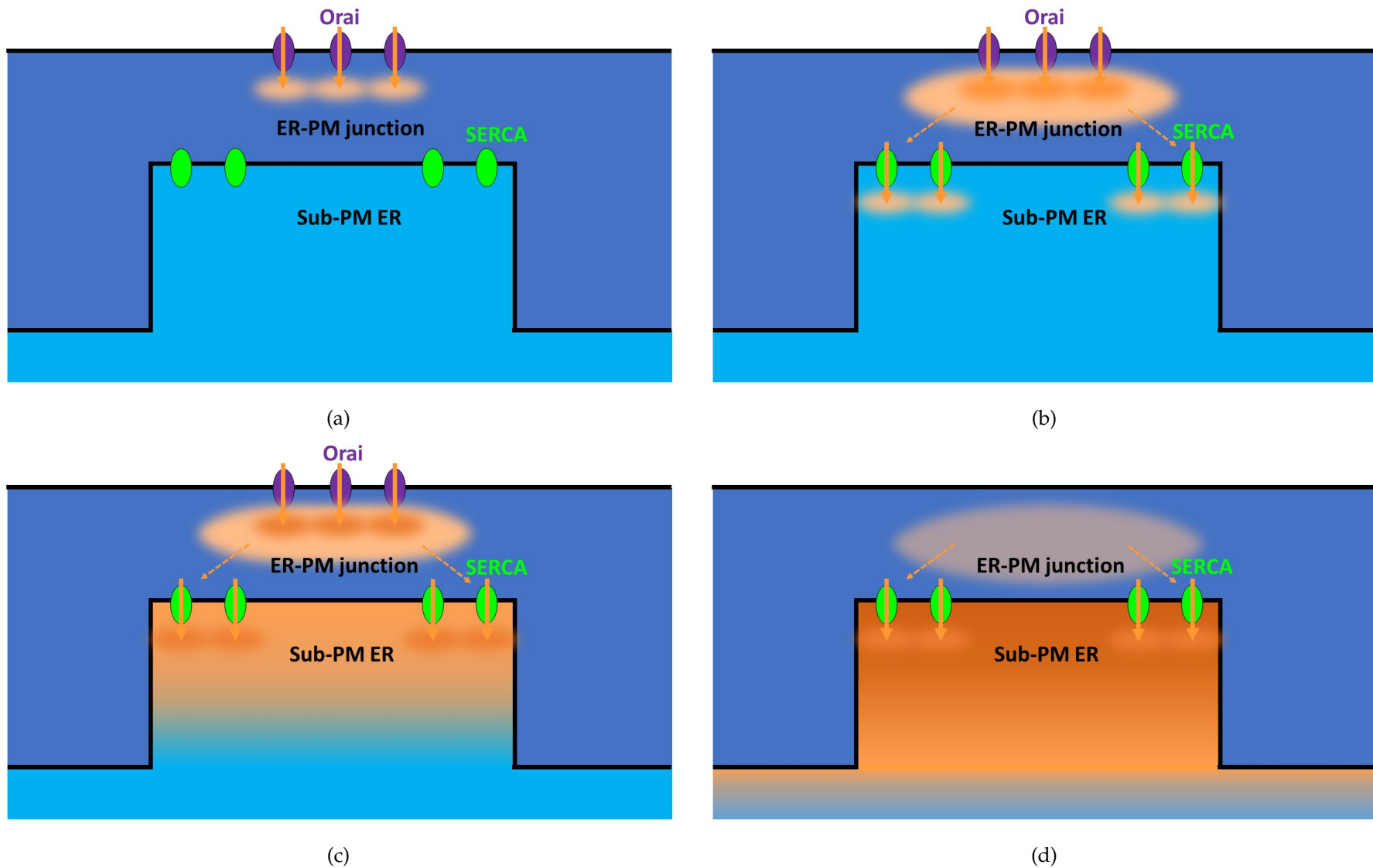


**Figure 2.2:** Illustration of SOCE. (a) Ca<sup>2+</sup> influx through Orai channels. (b) Activation of SERCA pumps. (c) Refilling of sub-PM ER. (d) Refilling of ER and dissociation of Orai channels.

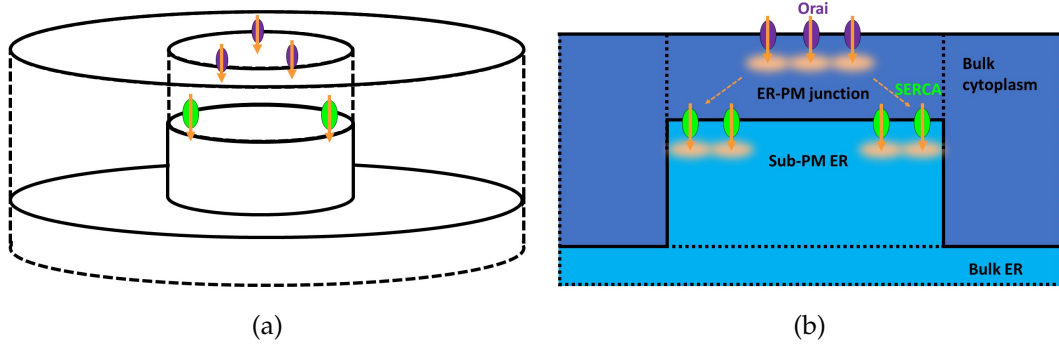


**Figure 2.3:** (a) 3D representation of the four domain mathematical model (b) 2D representation of the four domain mathematical model.

### 2.1.1 Geometry

We will model a single ER-PM junction and the adjacent sub-PM ER to provide insight into the  $\text{Ca}^{2+}$  concentration profiles generated in these regions to further understand the local  $\text{Ca}^{2+}$  dynamics.

We also include a small portion of the cytoplasm surrounding the ER-PM junction and sub-PM ER, which we refer to as the ‘bulk cytoplasm’. The bulk cytoplasm domain will extend far enough into the cytoplasm so that any STIM1 present in the bulk cytoplasm will be able to diffuse into the ER-PM junction for SOCE. We also include a ‘bulk ER’ compartment to model the refilling of the internal ER  $\text{Ca}^{2+}$  stores. The full domain of the model is the area enclosed by the yellow dashed lines in Figures 2.1(a) and 2.1(b).

The inclusion of the bulk cytoplasm will allow investigation into the global  $\text{Ca}^{2+}$  dynamics to examine the extent to which the local  $\text{Ca}^{2+}$  dynamics impact global  $\text{Ca}^{2+}$  signalling. Inclusion of the bulk ER will allow the model to capture the long term ER refilling behaviour and investigate the factors regulating ER refilling.

We construct a 3D spatio-temporal model as shown in Figure 2.3(a) with a 2D projection shown in Figure 2.3(b). The solid black lines represent the physical boundaries, the PM and ER membrane, present in our model. Biologically, the ER-PM junction is continuous with the bulk cytoplasm and the sub-PM ER is continuous with the bulk ER. To create our mathematical model we need to separate these domains and introduce boundaries, represented by the dashed black lines. These boundaries are not physically present in the system so they will not impede  $\text{Ca}^{2+}$  diffusion between the domains.

The ER-PM junction is a region of the cytoplasm that is characterised by the

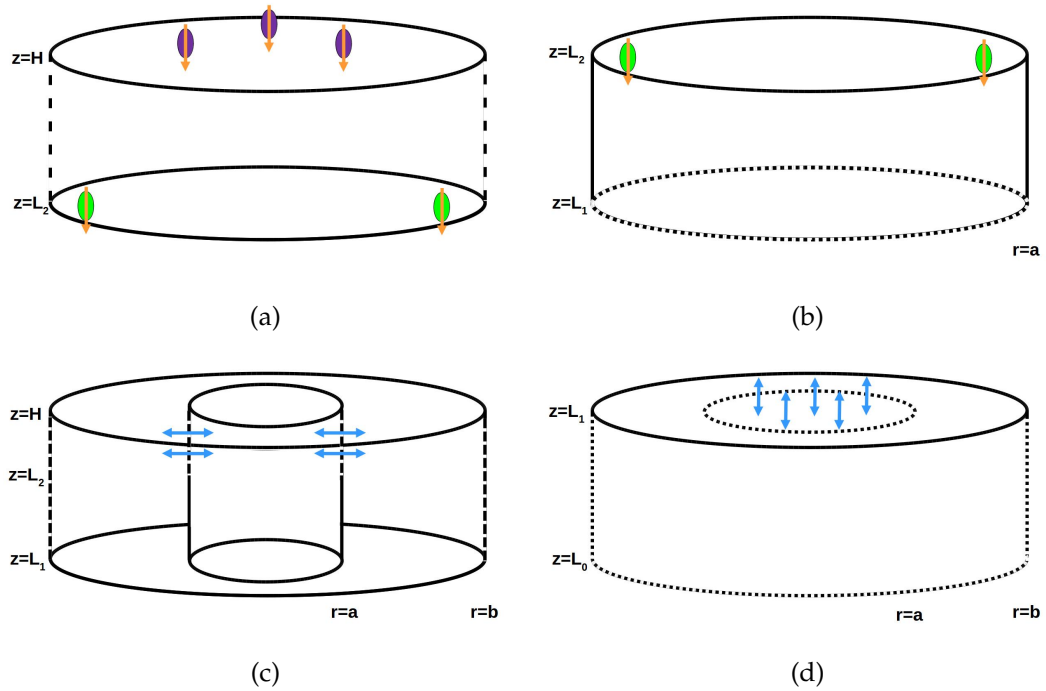


**Figure 2.4:** 3D representation of the (a) ER-PM junction (b) sub-PM ER (c) bulk cytoplasm (d) bulk ER. The  $\text{Ca}^{2+}$  flux due to free  $\text{Ca}^{2+}$  diffusion between local and global domains is denoted by the light blue arrows.

narrow gap between the PM and ER membrane in this region. We model this region as a cylinder, illustrated in Figure 2.4(a). The PM, represented by the upper face of the cylinder at height  $z = H$ , and the ER membrane, represented by the lower face of the cylinder at height  $z = L_2$ , are two physical boundaries of this domain, as shown by the solid black lines. The ER-PM junction is continuous with the bulk cytoplasm so there is no physical boundary between these two domains. We therefore impose a non-physical boundary at the edge of the ER-PM junction, represented by the dashed lines at  $r = a$  in Figure 2.4(a). This boundary does not impede  $\text{Ca}^{2+}$  diffusion between the ER-PM junction and the bulk cytoplasm. The top face of the cylinder, the PM, only allows  $\text{Ca}^{2+}$  movement across the membrane through Orai channels (purple). The bottom face of the cylinder represents the ER membrane which allows  $\text{Ca}^{2+}$  flux only through SERCA pumps (green).

The sub-PM ER domain is an extension of the ER which helps form the ER-PM junction. We model this as a cylinder of the same radius as the ER-PM junction, shown in Figure 2.4(b). The sub-PM ER is bounded by the ER membrane, separating it from the ER-PM junction and bulk cytoplasm. This is illustrated by the solid black lines along the mantle and upper face of the cylinder. The

sub-PM ER is an extension of the bulk ER so there is no physical boundary between these domains. We impose a non-physical boundary between the sub-PM ER and bulk ER, represented by the dashed lines in Figure 2.4(b).  $\text{Ca}^{2+}$  diffusion between the domains is not obstructed by this boundary.

The upper face and mantle of the cylinder in Figure 2.4(b) represent the ER membrane. The only  $\text{Ca}^{2+}$  movements across the ER membrane occur through the SERCA pumps (light green), which are localised to the upper face of the cylinder.  $\text{Ca}^{2+}$  is transported from the ER-PM junction into the sub-PM ER via SERCA pumps on the ER membrane but no other  $\text{Ca}^{2+}$  fluxes across the ER membrane are included.

The bulk cytoplasmic domain is illustrated in Figure 2.4(c) and we model this domain as an annulus as the bulk cytoplasm surrounds both the ER-PM junction and sub-PM ER. The relative positions of these domains are depicted in Figure 2.3(a). The upper face of the annulus represents the PM, represented by solid black lines. We do not include any channels or pumps outside of the ER-PM junction so there is no flux across the PM in this region. The upper fraction of the inner mantle boundary represents the section of bulk cytoplasm adjacent to the ER-PM junction.  $\text{Ca}^{2+}$  diffuses freely between the bulk cytoplasm and ER-PM junction and this is represented by the dashed line along this section of the inner mantle of the annulus. The ER membrane is a physical boundary and is represented by the solid black lines along the bottom face of the annulus and the inner mantle. We have neglected channels and pumps not associated to the SOCE process and only included the SERCA pumps involved in SOCE. These pumps are localised to the ER membrane of the ER-PM junction. The outer mantle has dashed lines to represent the lack of physical boundary which allows  $\text{Ca}^{2+}$  to diffuse freely across this boundary into the cytoplasm of the cell away from any  $\text{Ca}^{2+}$  influx sites.

The bulk ER domain is only bounded by the ER membrane and sits beneath the bulk cytoplasm and sub-PM ER domains, shown in Figure 2.3(a). We model this domain as a cylinder with the same radius as the outer radius of the bulk cytoplasm cylinder, illustrated in Figure 2.4(d). The upper face of the cylinder represents the ER membrane, denoted by the solid black line.  $\text{Ca}^{2+}$  can diffuse freely between the sub-PM ER and bulk ER across the section of the bulk ER beneath the sub-PM ER, illustrated by the dashed black lines in Figure 2.4(d). We do not include SERCA pumps on the ER membrane outside the ER-PM junction as they are not involved in the SOCE process. The width of the bulk

ER is chosen to coincide with the width of the bulk cytoplasm so that the  $\text{Ca}^{2+}$  concentration at the mantle of the bulk ER cylinder and bottom face of the bulk ER cylinder are not affected by the SOCE induced  $\text{Ca}^{2+}$  dynamics in the sub-PM ER. Again, these are mathematically imposed boundaries, represented by the black dashed lines.

Together, these compartments form the full domain of the SOCE model, shown in Figure 2.3.

## 2.1.2 Model assumptions

In resting cells STIM1 and Orai diffuse freely along the ER membrane and PM, respectively [82]. The SERCA pumps are situated on the ER membrane but little is known about their positions and movements along the membranes [5, 48, 49]. The translocation of STIM1 and Orai to the ER-PM junctions is an important feature of SOCE but does not mediate ER refilling or  $\text{Ca}^{2+}$  signalling [44]. The model developed in this chapter is primarily concerned with the local actions induced through SOCE so we will not consider translocation of STIM1 or Orai in the model at this time.

Dynes *et al.* [23] hypothesised that STIM1 binding to Orai holds the Orai channel in an open state and they did not observe stochastic single Orai channel opening while recording single channel dynamics. Therefore, we assume that once the Orai channel is open it remains open until the ER is sufficiently refilled and STIM1 unbinds. We also neglect  $\text{Ca}^{2+}$  dependent inactivation at this time but this process will be included in future work. The open Orai channels allow a constant  $\text{Ca}^{2+}$  influx with an experimentally observed unitary current of 2.1fA [35, 88]. Although STIM1 and Orai diffuse freely along the ER membrane and PM, upon binding to form open Orai channels the observed diffusion coefficient of the Orai channels is severely decreased [82]. To simplify our model, we assume this diffusion coefficient is negligible and that the Orai channels and SERCA pumps are stationary on the membranes [23, 27, 41, 55, 82].

At rest, the SERCA pumps continue to pump  $\text{Ca}^{2+}$  into the ER so there is a constant influx of  $\text{Ca}^{2+}$ . To balance this the ER membrane allows a constant 'leak' out of the ER to ensure the homeostatic  $\text{Ca}^{2+}$  content of the ER  $\text{Ca}^{2+}$  stores. We are primarily concerned with ER refilling which will dominate the  $\text{Ca}^{2+}$  dynamics as the magnitude of the  $\text{Ca}^{2+}$  leak is much smaller than the  $\text{Ca}^{2+}$  influx through the SERCA pumps. Therefore, the  $\text{Ca}^{2+}$  leak will not

contribute greatly to the  $\text{Ca}^{2+}$  dynamics so we do not include this leak across the ER membrane in the model at this time.

We assume that once  $\text{Ca}^{2+}$  enters the ER-PM junction or sub-PM ER  $\text{Ca}^{2+}$  movement within each domain is governed purely by diffusion, with membrane fluxes through either Orai channels or SERCA pumps transporting  $\text{Ca}^{2+}$  into or out of the domains. It is well known that the cytoplasm contains  $\text{Ca}^{2+}$  buffers which decrease the rate of  $\text{Ca}^{2+}$  diffusion throughout the cytoplasm. We can incorporate this slower  $\text{Ca}^{2+}$  movement through a reduced diffusion coefficient. We have set the  $\text{Ca}^{2+}$  diffusion coefficient of the bulk cytoplasm to be the buffered  $\text{Ca}^{2+}$  diffusion coefficient,  $D_C = 30\mu\text{m}^2\text{s}^{-1}$  [4]. The ER-PM junction is small and hard to measure experimentally so very little is known about the presence and impact of  $\text{Ca}^{2+}$  buffers in this domain [55]. It is thought that the  $\text{Ca}^{2+}$  microdomains created around the channels rapidly overwhelm buffers within the ER-PM junction allowing  $\text{Ca}^{2+}$  to diffuse freely in this region [55,58]. We follow the work of Samanta *et al.* [67] and Hogan [33] and neglect the effect of  $\text{Ca}^{2+}$  buffers in this model and use the free  $\text{Ca}^{2+}$  diffusion coefficient in the ER-PM junction,  $D_J = 220\mu\text{m}^2\text{s}^{-1}$  [4]. The diffusion coefficient of  $\text{Ca}^{2+}$  in the ER lumen has not been definitively measured. However, crowding within the ER lumen is thought to slow  $\text{Ca}^{2+}$  diffusion [15,52]. Dayel *et al.* [15] found diffusion within the ER lumen to be 3 – 6 times slower than the bulk cytoplasmic diffusion coefficient and estimated the diffusion coefficient of  $\text{Ca}^{2+}$  in the ER lumen to be  $5 - 10\mu\text{m}^2\text{s}^{-1}$ . Swietach *et al.* [75] measured the  $\text{Ca}^{2+}$  diffusion coefficient of the SR lumen as  $8 - 9\mu\text{m}^2\text{s}^{-1}$  so in our model we use a diffusion coefficient,  $D_{\text{ER}} = 10\text{m}^2\text{s}^{-1}$ , in the sub-PM ER and bulk ER. We assume the  $\text{Ca}^{2+}$  diffusion is uniform in each compartment.

We also assume the  $\text{Ca}^{2+}$  concentrations at the boundary of the full model domain, denoted by the yellow dashed lines in Figure 2.1 are far enough from the  $\text{Ca}^{2+}$  influx sites to be unaffected by the  $\text{Ca}^{2+}$  dynamics of the ER-PM junction and sub-PM ER.

### 2.1.3 PDE model

The small size of the ER-PM junction prevents imaging of the  $\text{Ca}^{2+}$  concentrations in the junction. It has been demonstrated that the  $\text{Ca}^{2+}$  dynamics, and in particular the spatial  $\text{Ca}^{2+}$  profiles, in the ER-PM junction mediate many signalling processes, such as immunodeficiencies, motor control and gene ex-

pression [26, 32, 67]. Therefore, insights into the  $\text{Ca}^{2+}$  dynamics will improve understanding of the regulatory nature of SOCE and the  $\text{Ca}^{2+}$  signals generated.

While there are few mathematical models of SOCE in the literature [22], the importance of understanding the factors mediating SOCE have been recognised in the literature with the spatial organisation of the SOCE signalling machinery receiving particular interest, and this is achievable through mathematical modelling [33]. Previous models have explored the relationship between ER depletion and SOCE activity [54] and the relationship between inter-channel Orai distances and the spatial  $\text{Ca}^{2+}$  signals generated to further understand how clustering Orai channels stimulates gene expression [67].

We model the  $\text{Ca}^{2+}$  dynamics of each domain separately and couple the domains by the  $\text{Ca}^{2+}$  fluxes across the boundaries. We use a PDE framework to capture the spatial  $\text{Ca}^{2+}$  dynamics in each domain instead of an ODE framework which would average out the  $\text{Ca}^{2+}$  concentration in each domain. The  $\text{Ca}^{2+}$  dynamics of each domain depend on the influx or efflux of  $\text{Ca}^{2+}$ , which we incorporate into the boundary conditions, and the rate of  $\text{Ca}^{2+}$  diffusion within the domain, which we incorporate through the diffusion coefficient. We assume that the  $\text{Ca}^{2+}$  movement within each domain is governed purely by diffusion with membrane fluxes, through either Orai channels or SERCA pumps, transporting  $\text{Ca}^{2+}$  across membranes to allow  $\text{Ca}^{2+}$  transport between the cytoplasmic and ER domains.

The  $\text{Ca}^{2+}$  influx per unit area due to the Orai channels,  $J_{\text{Orai}}$ , is calculated using the magnitude of the single channel Orai current,  $I_{\text{Orai}}$ . We use Faraday's law of electrolysis and calculate the amount of  $\text{Ca}^{2+}$  entering the system per unit area,  $F_{\text{Orai}}$ ,

$$F_{\text{Orai}} = \frac{I_{\text{Orai}}}{FzA_O},$$

where  $F$  is Faraday's constant,  $z$  is the valency of  $\text{Ca}^{2+}$  and  $A_O$  is the estimated area of the Orai channel [56].

The SERCA pumps transport  $\text{Ca}^{2+}$  from the ER-PM junction into the sub-PM ER where  $C_J$  and  $C_S$  are the  $\text{Ca}^{2+}$  concentrations of the ER-PM junction and sub-PM ER, respectively. If the ER-PM junction has a very high  $\text{Ca}^{2+}$  concentration then the SERCA pumps will take up more  $\text{Ca}^{2+}$  and transport it across faster. If the  $\text{Ca}^{2+}$  concentration of the sub-PM ER is very high then the rate of  $\text{Ca}^{2+}$  transport through the SERCA pumps will slow down so less  $\text{Ca}^{2+}$  is

transported into the sub-PM ER. The SERCA pump transport system depends on the  $\text{Ca}^{2+}$  concentrations on either side of the membrane so we use a bidirectional SERCA pump model to account for the  $\text{Ca}^{2+}$  concentrations on both sides of the membrane. The  $\text{Ca}^{2+}$  flux per unit area per SERCA pump is given by [69],

$$F_{\text{SERCA}} = \frac{Q}{A_S} \frac{V_{\max,F} (C_J/K_F)^H - V_{\max,R} (C_S/K_R)^H}{1 + (C_J/K_F)^H + (C_S/K_R)^H},$$

where  $V_{\max,F}$  and  $V_{\max,R}$  are the forward and reverse maximal pump rate,  $Q$  is a temperature coefficient,  $A_S$  is the area of the SERCA pump,  $H$  is the Hill coefficient, and  $K_F$  and  $K_R$  are the forward and reverse binding coefficients.

The bidirectional sensing attributed to the SERCA pumps is an important feature of our model and cannot be ignored or simplified to a unidirectional model because we want the model to capture the refilling dynamics of the system, including the reduced SERCA transport as the ER  $\text{Ca}^{2+}$  store is refilled. Other bidirectional SERCA pump models, such as the model proposed by Sneyd *et al.* [70] or those discussed in [22], could also be used to model the SERCA pump flux.

The last type of  $\text{Ca}^{2+}$  movements occur at the non-physical boundaries we have imposed in our model, denoted by the dashed black lines in Figures 2.3 and 2.4. At these boundaries we want to ensure that the local  $\text{Ca}^{2+}$  concentration is continuous with that of the global  $\text{Ca}^{2+}$  concentration as there are no physical barriers so we should have no impedance to the  $\text{Ca}^{2+}$  diffusion. We impose the continuity of concentration and continuity of flux boundary conditions to ensure  $\text{Ca}^{2+}$  is able to diffuse freely between the domains.

We have two possible boundary conditions; prescribing the value of the  $\text{Ca}^{2+}$  concentration on the boundary (continuity of concentration) or prescribing the  $\text{Ca}^{2+}$  gradient on the boundary (continuity of flux). We will prescribe one condition on each side of the boundary. In this way we can use the information we have from the neighbouring domain to inform our prescribed boundary conditions. The choice of boundary condition is considered in detail and justified in the following chapter; for now we impose the continuity of concentration boundary condition at the local boundaries and the continuity of flux at the global boundaries.

The model constructed in this chapter includes both cytoplasmic and ER domains to enable investigation into the refilling properties of SOCE. We use a PDE framework to explore the relationship between the spatial organisation

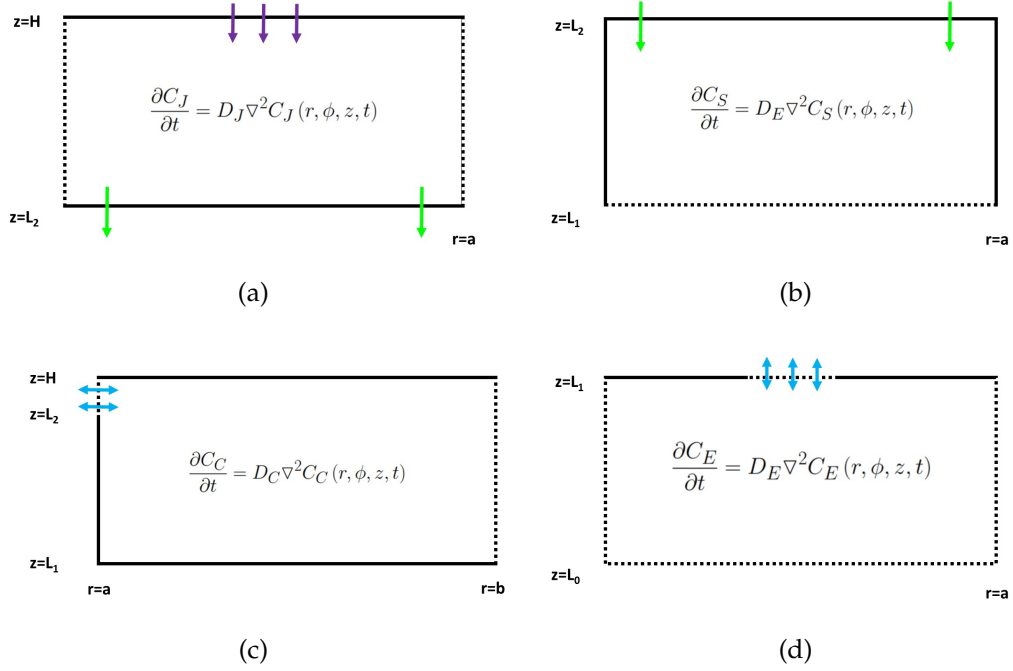


**Figure 2.5:** 2D representation of the (a) ER-PM junction (b) sub-PM ER (c) bulk cytoplasm (d) bulk ER. Orai channel and SERCA pump fluxes are denoted by purple and green arrows, respectively. The  $\text{Ca}^{2+}$  flux due to free  $\text{Ca}^{2+}$  diffusion between local and global domains is denoted by the light blue arrows.

of SOCE components (Orai channels and SERCA pumps) and the spatial signature of the  $\text{Ca}^{2+}$  signals generated. The model is novel as it incorporates the impact of spatial organisation into the  $\text{Ca}^{2+}$  signalling dynamics and ER refilling process.

We now look at each domain separately and create a spatio-temporal mathematical model of  $\text{Ca}^{2+}$  diffusion in each domain. The combination of all four domains gives the full model of SOCE.

### ER-PM junction

The main components of SOCE, Orai channels and SERCA pumps, reside in the ER-PM junction. The  $\text{Ca}^{2+}$  fluxes occurring in the ER-PM junction are depicted in Figure 2.5(a) and the Orai channel and SERCA pump fluxes are represented by the purple and green arrows, respectively. The  $\text{Ca}^{2+}$  channels and pumps occupy small regions of the membrane so we model the  $\text{Ca}^{2+}$  movement across the membrane as a boundary flux at a single point on the membrane. The solid black lines in Figure 2.5(a) represent a zero flux boundary as

the PM and ER membrane only allow  $\text{Ca}^{2+}$  flux through specific points (channels or pumps) on the boundary. To ensure the  $\text{Ca}^{2+}$  moves freely between the ER-PM junction and bulk cytoplasm we impose the continuity of concentration on the ER-PM junction and continuity of flux on the bulk cytoplasm.

The  $\text{Ca}^{2+}$  concentration in the ER-PM junction,  $C_J = C_J(r, \phi, z, t)$ , is governed by the diffusion equation,

$$\frac{\partial C_J}{\partial t} = D_J \nabla^2 C_J, \quad (2.1)$$

where  $r \in (0\text{nm}, 75\text{nm}]$ ,  $\phi \in [0, 2\pi)$ ,  $z \in [2485\text{nm}, 2500\text{nm}]$  and  $t \geq 0$ . The diffusion equation satisfies the following initial and boundary conditions:

$$\begin{aligned} C_J(r, \phi, z, 0) &= 0.1\mu\text{M}, & D_J \frac{\partial C_J}{\partial z} \Big|_{z=H} &= J_{\text{Orai}}, \\ C_J(a, \phi, z, t) &= C_C(a, \phi, z, t), & D_J \frac{\partial C_J}{\partial z} \Big|_{z=L_2} &= J_{\text{SERCA}}. \end{aligned} \quad (2.2)$$

Here,  $C_C = C_C(r, \phi, z, t)$  denotes the  $\text{Ca}^{2+}$  concentration in the bulk cytoplasm. The flux per unit area per channel or pump across a membrane is defined as

$$J_x = \begin{cases} F_x, & (r, \phi) = (r_x, \phi_x), \\ 0, & \text{otherwise,} \end{cases}$$

where  $x \in \{\text{Orai}, \text{SERCA}\}$  and  $(r_x, \phi_x)$  denote the position of the Orai channel or SERCA pump on the membrane.

### Sub-PM ER

In the sub-PM ER domain we have similar  $\text{Ca}^{2+}$  movement as in the ER-PM junction;  $\text{Ca}^{2+}$  is transported into the sub-PM ER through SERCA pumps which we model as a  $\text{Ca}^{2+}$  flux through a single point in the membrane. The membrane fluxes are illustrated by the green arrows in Figure 2.5(b). To ensure the  $\text{Ca}^{2+}$  moves freely between the sub-PM ER and bulk ER we impose the continuity of concentration on the sub-PM ER and continuity of flux on the bulk ER.

The  $\text{Ca}^{2+}$  concentration in the sub-PM ER,  $C_S = C_S(r, \phi, z, t)$ , is governed by the diffusion equation

$$\frac{\partial C_S}{\partial t} = D_E \nabla^2 C_S, \quad (2.3)$$

where  $r \in (0\text{nm}, 75\text{nm}]$ ,  $\phi \in [0, 2\pi)$ ,  $z \in [2000\text{nm}, 2485\text{nm}]$  and  $t \geq 0$ . The

diffusion equation satisfies the following initial and boundary conditions:

$$\begin{aligned} C_S(r, \phi, z, 0) &= 150\mu\text{M}, & D_E \frac{\partial C_S}{\partial z} \Big|_{z=L_2} &= J_{\text{SERCA}}, \\ C_S(r, \phi, L_1, t) &= C_E(r, \phi, L_1, t), & D_E \frac{\partial C_S}{\partial r} \Big|_{r=a} &= 0. \end{aligned} \quad (2.4)$$

Here,  $C_E = C_E(r, \phi, z, t)$  denotes the  $\text{Ca}^{2+}$  concentration in the bulk ER. The flux per unit area per SERCA pump is defined as

$$J_{\text{SERCA}} = \begin{cases} F_{\text{SERCA}}, & (r, \phi) = (r_{\text{SERCA}}, \phi_{\text{SERCA}}), \\ 0, & \text{otherwise.} \end{cases}$$

where  $(r_{\text{SERCA}}, \phi_{\text{SERCA}})$  denotes the position of the SERCA pump on the ER membrane. We deplete the  $\text{Ca}^{2+}$  store in the sub-PM ER from a resting concentration of  $[\text{Ca}^{2+}]_{\text{ER}} \approx 400\mu\text{M}$  [41] to  $150\mu\text{M}$  to take account of the greater depletion observed in the sub-PM ER by Ong *et al.* [54] and to ensure significant  $\text{I}_{\text{CRAC}}$  activation, for which a dissociation constant of  $K_{1/2} = 169\mu\text{M}$  has been reported [45].

### Bulk Cytoplasm

We assume the flux across the outer boundary,  $r = b$  in Figure 2.5(c), is negligible as it is far from the SOCE induced  $\text{Ca}^{2+}$  dynamics and so we prescribe the  $\text{Ca}^{2+}$  concentration at the outer mantle boundary to be the same as the baseline  $\text{Ca}^{2+}$  concentration of the rest of the cytoplasm.

In the ER-PM junction we imposed continuity of  $\text{Ca}^{2+}$  concentration on the junctional side of the boundary,  $r = a$ . We impose continuity of flux on the bulk cytoplasmic side of the boundary so that the  $\text{Ca}^{2+}$  gradient across the boundary is consistent and the  $\text{Ca}^{2+}$  flux into the bulk cytoplasm is equal to the  $\text{Ca}^{2+}$  flux out of the ER-PM junction. The light blue arrows across the dashed black lines in Figure 2.5(c) represent the continuity of flux boundary condition. Imposing both continuity conditions ensures that there are no obstructions to  $\text{Ca}^{2+}$  movement between these domains across this boundary.

The  $\text{Ca}^{2+}$  concentration in the bulk cytoplasm,  $C_C = C_C(r, \phi, z, t)$ , is governed by the diffusion equation

$$\frac{\partial C_C}{\partial t} = D_C \nabla^2 C_C,$$

where  $r \in (75\text{nm}, 1000\text{nm}]$ ,  $\phi \in [0, 2\pi)$ ,  $z \in [2000\text{nm}, 2500\text{nm}]$  and  $t \geq 0$ . The diffusion equation satisfies the following initial and boundary conditions:

$$\begin{aligned} C_C(r, \phi, z, 0) &= 0.1\mu\text{M}, & D_C \frac{\partial C_C}{\partial z} \Big|_{z=H} &= 0, \\ C_C(b, \phi, z, t) &= 0.1\mu\text{M}, & D_C \frac{\partial C_C}{\partial z} \Big|_{z=L_1} &= 0, \\ D_C \frac{\partial C_C}{\partial r} \Big|_{r=a} &= \begin{cases} D_C \frac{\partial C_I}{\partial z} \Big|_{r=a}, & z \in (L_2, H], \\ 0, & z \in [L_1, L_2). \end{cases} \end{aligned}$$

### Bulk ER

The bulk ER only receives  $\text{Ca}^{2+}$  influx across the interface between the bulk ER and sub-PM ER, denoted by the black dashed line on the top face of Figure 2.5(d). The  $\text{Ca}^{2+}$  influx refills the bulk ER and the light blue arrows represent the continuity of flux boundary condition. The solid black lines either side of the dashed lines represent the zero flux boundary condition of the ER membrane. The other boundaries of the bulk ER are continuous with the remainder of the ER but we assume that those boundaries are far enough from the sites of  $\text{Ca}^{2+}$  influx that they do not feel the effects of the  $\text{Ca}^{2+}$  dynamics. Then we can fix the  $\text{Ca}^{2+}$  concentration at the boundaries to be the baseline  $\text{Ca}^{2+}$  concentration of the ER.

The  $\text{Ca}^{2+}$  concentration in the bulk ER,  $C_E = C_E(r, \phi, z, t)$ , is governed by the diffusion equation

$$\frac{\partial C_E}{\partial t} = D_E \nabla^2 C_E,$$

where  $r \in (0\text{nm}, 1000\text{nm}]$ ,  $\phi \in [0, 2\pi)$ ,  $z \in [1000\text{nm}, 2000\text{nm}]$  and  $t \geq 0$ . The diffusion equation satisfies following initial and boundary conditions:

$$\begin{aligned} C_E(r, \phi, z, 0) &= 150\mu\text{M}, & D_E \frac{\partial C_E}{\partial z} \Big|_{z=L_1} &= \begin{cases} D_E \frac{\partial C_S}{\partial z} \Big|_{z=L_1}, & r \in (0, a], \\ 0, & \text{otherwise.} \end{cases} \\ C_E(b, \phi, z, t) &= 150\mu\text{M}, & C_E(r, \phi, L_0, t) &= 150\mu\text{M}. \end{aligned}$$

### Four domain model

The four domain model is summarised in Figure 2.6. The solid black lines represent physical boundaries which only allow  $\text{Ca}^{2+}$  fluxes across at specific

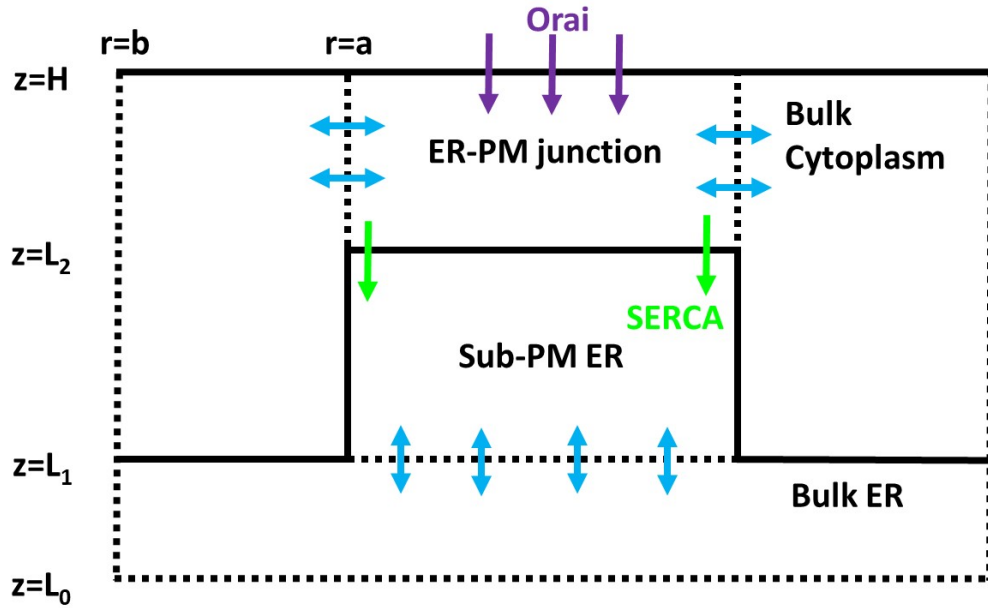


**Figure 2.6:** Schematic diagram summarising the mathematical model of SOCE including domain dimensions and boundary fluxes. The Orai channels, SERCA pumps and free  $\text{Ca}^{2+}$  diffusion flux are denoted by the purple, light green and blue arrows, respectively.

points denoted by the coloured arrows. The dashed black lines represent the non-physical boundaries which must obey the continuity of flux and concentration boundary conditions, denoted by the blue arrows, to ensure  $\text{Ca}^{2+}$  diffusion is not affected by the inclusion of the boundary. The diffusion equation in each domain governs the  $\text{Ca}^{2+}$  dynamics according to the boundary conditions imposed on each domain.

## 2.2 Discussion and conclusion

In this chapter we developed a 3D spatio-temporal model describing the  $\text{Ca}^{2+}$  concentrations within the cytoplasm and ER surrounding the site of  $\text{Ca}^{2+}$  influx. We included four domains to allow investigation of the local  $\text{Ca}^{2+}$  dynamics occurring within the ER-PM junction and sub-PM ER and the global dynamics of the bulk cytoplasm and bulk ER. We chose physiologically realistic geometries and showed how to incorporate  $\text{Ca}^{2+}$  transport through either membrane fluxes or through continuity boundary conditions.

SOCE is very complex and the current model focuses only on ER refilling and the generation of  $\text{Ca}^{2+}$  signals. These processes are fundamental to SOCE and occur in all cell types so the current model can be used as a foundation upon

which we can expand and develop more biologically realistic models. Future development of the model could incorporate cell specificity through inclusion of cell specific kinetic parameters and particular cell signalling components. This would enable exploration of the relationship between SOCE and the different signalling molecules present in the ER-PM junction which are involved in specific SOCE induced downstream cellular functions. We could introduce additional  $\text{Ca}^{2+}$  signalling components, for instance PMCA pumps, mitochondria and  $\text{IP}_3$  receptors to introduce further complexity to the system. The model could then be tailored towards specific cell types to investigate the impact of SOCE on particular cell signalling pathways, for instance, the intricate relationship between abnormal SOCE and immunodeficiencies in T cells [26].

Addition of mobile and immobile buffers in the ER-PM junction is another potential extension to the current model. This would provide a more realistic insight to the biological dynamics and allow investigation of  $\text{Ca}^{2+}$  buffers in these sub-cellular regions, which is experimentally difficult due to the small size of the ER-PM junctions.

We have focused solely on  $\text{Ca}^{2+}$  movement in this model but the model has the potential to simulate the full SOCE cycle by including the movement of STIM1, the  $\text{Ca}^{2+}$  sensor which triggers SOCE. Depletion of ER  $\text{Ca}^{2+}$  stores causes  $\text{Ca}^{2+}$  to unbind from STIM1, STIM1 then translocates to the ER-PM junction where it binds to Orai and initiates  $\text{Ca}^{2+}$  influx. We could include the ability of STIM1 to sense the  $\text{Ca}^{2+}$  store content and ensure that STIM1 translocation towards the ER-PM junction is activated when the surrounding  $\text{Ca}^{2+}$  falls below a certain threshold. This would introduce the delay observed between store depletion and  $\text{Ca}^{2+}$  influx [44, 81] and develop a more biologically realistic model. In a similar manner, we could also include the closing of the Orai channels when the surrounding  $\text{Ca}^{2+}$  concentration is sufficiently high and STIM1 binds to  $\text{Ca}^{2+}$ , disassembling the Orai channel and stopping  $\text{Ca}^{2+}$  influx. Again, this provides a realistic description of the termination of SOCE and could be used as a method of examining the time frames required for ER refilling in specific situations to further compare the factors governing SOCE. In the model we assumed the Orai channels are stationary in the ER-PM junction as they diffuse very slowly [82]. We could incorporate non-stationary channels and pumps in our model to examine the impact of channel and pump movement on the spatial  $\text{Ca}^{2+}$  signals produced.

SOCE is initiated in response to depletion of the ER  $\text{Ca}^{2+}$  store and we have

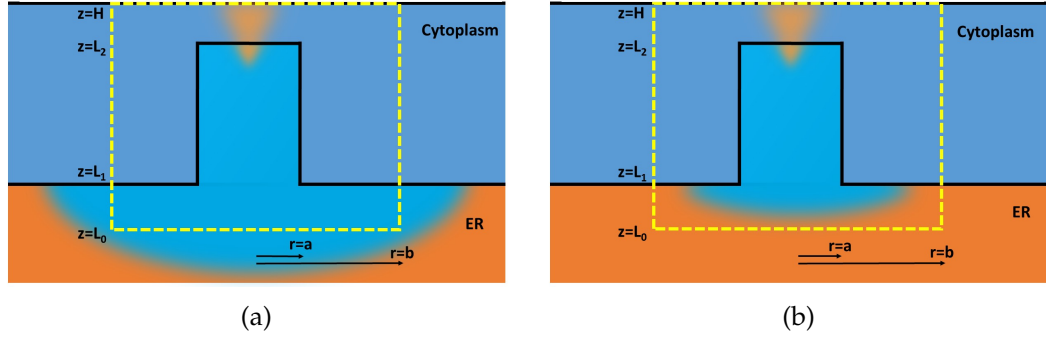


**Figure 2.7:** (a) Illustration of a globally depleted ER: the bulk ER is depleted to the same extent as the sub-PM ER. (b) Illustration of a locally depleted ER: the sub-PM ER is fully depleted but the bulk ER is only depleted near the sub-PM ER region.

modelled this  $\text{Ca}^{2+}$  store depletion by setting the  $\text{Ca}^{2+}$  concentration of the sub-PM ER to be  $150\mu\text{M}$ . We can model local and global  $\text{Ca}^{2+}$  store depletion by varying the  $\text{Ca}^{2+}$  concentrations within the bulk ER. For instance, a globally depleted bulk ER is illustrated in Figure 2.7(a). The entire bulk ER has been depleted to the same level as the sub-PM ER. The area in blue represents the depleted region,  $C_E = 150\mu\text{M}$ , and the area in orange represents the full  $\text{Ca}^{2+}$  store,  $C_E = 400\mu\text{M}$ . This depletion extends beyond the bulk ER domain to ensure that the  $\text{Ca}^{2+}$  concentration is continuous across the boundary denoted by the yellow dashed line. A locally depleted ER is illustrated in Figure 2.7(b). The bulk ER domain has only been partially depleted demonstrated by the smaller region of blue within the bulk ER domain. Local depletion could occur through transport of  $\text{Ca}^{2+}$  at specific sites, e.g.  $\text{IP}_3$  receptors nearby to the ER-PM junction which do not deplete internal ER  $\text{Ca}^{2+}$  stores. Local depletion may be more physiologically accurate but the model is able to examine the  $\text{Ca}^{2+}$  dynamics occurring as a result of both forms of store depletion.

The model is composed of a local model of  $\text{Ca}^{2+}$  dynamics, consisting of the ER-PM junction and sub-PM ER, and a global model of  $\text{Ca}^{2+}$  dynamics, consisting of all four domains. The majority of SOCE occurs in the ER-PM junction and the early ER refilling mainly affects the sub-PM ER so we can reduce the full system to the local model when we are concerned with the local  $\text{Ca}^{2+}$  dynamics and early ER refilling. Further to this, if we are only interested in how the inter-channel Orai distances affect the  $\text{Ca}^{2+}$  dynamics, as Samanta *et al.* were [67], then we can consider the ER-PM junction only. Many signalling effector molecules are assumed to sit within the ER-PM junction leading to activation of a range of signalling pathways and cellular functions. The  $\text{Ca}^{2+}$

dynamics solely attributed to ER-PM junction interactions may be sufficient for investigation into the relationship between the spatial  $\text{Ca}^{2+}$  patterns and signalling molecule placement. This allows us to reduce the complexity of the model and consider the particular domains we are interested in according to what aspect of SOCE we are investigating. We will focus on the local model in the following chapters as we are primarily concerned with the local  $\text{Ca}^{2+}$  signalling and refilling dynamics. It would be interesting to examine the impact the local  $\text{Ca}^{2+}$  dynamics have on  $\text{Ca}^{2+}$  signalling in the bulk cytoplasm and the ER refilling process; however, we will first analyse the local factors influencing  $\text{Ca}^{2+}$  signalling and ER refilling. Then we can investigate the relationship between local and global  $\text{Ca}^{2+}$  dynamics to further determine the key components governing SOCE.

In conclusion, we have constructed a 3D spatio-temporal model of  $\text{Ca}^{2+}$  signalling and ER refilling in this chapter. We have included both local and global components to allow investigation into both the local and global  $\text{Ca}^{2+}$  dynamics and explore how the local dynamics impact global  $\text{Ca}^{2+}$  signals. SOCE is very complex so we have included the most important facets of SOCE in our model, ER refilling and the spatial signature of  $\text{Ca}^{2+}$  signals. The model enables visualisation of the  $\text{Ca}^{2+}$  signals generated in the ER-PM junction and sub-PM ER, which is not achievable with current  $\text{Ca}^{2+}$  imaging techniques. The incorporation of a refilling pathway with spatial organisation is novel and can provide a mechanism to investigate current thoughts about spatial organisation of  $\text{Ca}^{2+}$  signalling components within the junctions and even that the dimensions of the junctions themselves are capable of regulating ER refilling and  $\text{Ca}^{2+}$  signalling.

# Chapter 3

## Solution and Implementation of the Model

### 3.1 Solution techniques

In Chapter 2, we created a spatio-temporal model of coupled PDEs to describe the movement of  $\text{Ca}^{2+}$  in the cytoplasm and ER during SOCE. The model accounts for  $\text{Ca}^{2+}$  influx and efflux from Orai channels and SERCA pumps and the diffusion of  $\text{Ca}^{2+}$  within the domains to describe the  $\text{Ca}^{2+}$  concentrations throughout SOCE. We will employ a semi-analytical technique involving Green's functions to solve our PDE system.

As mentioned in Chapter 2, we will focus on the two domain model coupling the  $\text{Ca}^{2+}$  concentrations in the ER-PM junction,  $C_J = C_J(r, \phi, z, t)$ , and the sub-PM ER,  $C_S = C_S(r, \phi, z, t)$ . The  $\text{Ca}^{2+}$  concentrations,  $C_J$  and  $C_S$ , of each domain obey the diffusion equation,

$$\frac{\partial C_x}{\partial t} = D_x \nabla^2 C_x, \quad (3.1)$$

where  $x$  defines the domain,  $x \in \{J, S\}$ , and  $D_x$  is the diffusion coefficient in that domain. The  $\text{Ca}^{2+}$  concentrations obey the initial conditions and boundary conditions detailed in Chapter 2.

#### 3.1.1 Barton's solution method

The solution,  $C(r, \phi, z, t)$ , to a system of PDEs in absence of internal source terms on a stationary domain of volume  $V$  and boundary  $S$  using the method

discussed in [8], which we will refer to as ‘Barton’s method’, is given by,

$$C_x = \int_V G_x(\mathbf{r}, \mathbf{r}', T, t_0) C_{x,0} d\mathbf{V}' + D_x \int_{t_0}^T dt' \int_S [G_x(\mathbf{r}, \mathbf{r}', T, t_0) \partial'_n C_{x,t} - (\partial'_n G(\mathbf{r}, \mathbf{r}', T, t_0)) C_{x,t}] d\mathbf{S}', \quad (3.2)$$

where  $t_0$  denotes the initial time,  $G_x(\mathbf{r}, \mathbf{r}', T, t_0)$  is the Green’s function of the system propagating the solution between  $t = t_0$  and  $t = T$ ,  $C_{x,0}$  is the initial condition of the system,  $\partial'_n C_{x,t}$  is a prescribed flux boundary condition and  $C_{x,t}$  is a prescribed Dirichlet boundary condition across the boundary.

The first integral propagates the effect of the initial condition of the  $\text{Ca}^{2+}$  concentration. The second integral propagates the effect of the inhomogeneous boundary conditions,  $\partial'_n C_S$  when Von Neumann boundary conditions are used and  $C_S$  when Dirichlet boundary conditions are used. Together the integrals describe the change in the concentration profile from  $t = 0$  to  $t$  and take account of the diffusion of  $\text{Ca}^{2+}$  and the influx/efflux across the boundary.

If we discretise time, according to  $t = (t_0, t_1, \dots, t_{n-1}, t_n = T)$ , then we can split the integral of equation (3.2) as follows,

$$C_x = \int_V G_x(\mathbf{r}, \mathbf{r}', T, t_0) C_{x,0} d\mathbf{V}' + D_x \int_{t_0}^{t_1} dt' \int_S [G_x(\mathbf{r}, \mathbf{r}', t_1, t_0) \partial'_n C_{x,t} - (\partial'_n G(\mathbf{r}, \mathbf{r}', t_1, t_0)) C_{x,t}] d\mathbf{S}' + D_x \int_{t_1}^{t_2} dt' \int_S [G_x(\mathbf{r}, \mathbf{r}', t_2, t_1) \partial'_n C_{x,t} - (\partial'_n G(\mathbf{r}, \mathbf{r}', t_2, t_1)) C_{x,t}] d\mathbf{S}' + \dots + D_x \int_{t_{n-1}}^T dt' \int_S [G_x(\mathbf{r}, \mathbf{r}', T, t_{n-1}) \partial'_n C_{x,t} - (\partial'_n G(\mathbf{r}, \mathbf{r}', T, t_{n-1})) C_{x,t}] d\mathbf{S}'. \quad (3.3)$$

The solution at time  $T$ ,  $C_x$ , is the sum of the boundary condition solutions between each time point in  $t$ . We use a temporal mesh with uniform spacing,  $dt$ , and time translationally invariant Green’s functions [8] so the Green’s function is the same throughout the sum, allowing equation (3.3) to be written as

$$C_x = \int_V G_x(\mathbf{r}, \mathbf{r}', T, t_0) C_{x,0} d\mathbf{V}' + D_x \int_0^{dt} dt' \int_S [G_x(\mathbf{r}, \mathbf{r}', t') \partial'_n C_{x,0} - (\partial'_n G_x(\mathbf{r}, \mathbf{r}', t')) C_{x,0}] d\mathbf{S}' + D_x \int_0^{dt} dt' \int_S [G_x(\mathbf{r}, \mathbf{r}', t') \partial'_n C_{x,1} - (\partial'_n G_x(\mathbf{r}, \mathbf{r}', t')) C_{x,1}] d\mathbf{S}' + \dots + D_x \int_0^{dt} dt' \int_S [G_x(\mathbf{r}, \mathbf{r}', t') \partial'_n C_{x,n-1} - (\partial'_n G_x(\mathbf{r}, \mathbf{r}', t')) C_{x,n-1}] d\mathbf{S}'. \quad (3.4)$$

The first integral propagates the effect of the inhomogeneous initial condition throughout the system over the time interval  $T$  and the remaining integrals propagate the effect of the inhomogeneous boundary condition at time  $t_i$ , where  $\partial'_n C_{x,i}$  is the inhomogeneous boundary condition at time  $t_i$ . However, instead of propagating the initial condition over one large time interval,  $T$ , we can propagate the initial condition over a small interval,  $dt$ , to get the  $\text{Ca}^{2+}$  concentration at time  $t_1$ ,  $C_{x,1}$ , and then propagate this  $\text{Ca}^{2+}$  concentration over another small interval to get the  $\text{Ca}^{2+}$  concentration at time  $t_2$ ,  $C_{x,2}$ . By propagating the previously computed  $\text{Ca}^{2+}$  concentration,  $C_{x,i-1}$ , over a small time interval,  $dt$ , we will eventually propagate the original initial condition over the full time interval. The solution after the  $i^{\text{th}}$  time step can then be written as

$$C_{x,i} = \int_V G_x(\mathbf{r}, \mathbf{r}', dt) C_{x,i-1} + D_x \int_0^{dt} dt' \int_S [G_x(\mathbf{r}, \mathbf{r}', t') \partial'_n C_{x,i-1} - (\partial'_n G_x(\mathbf{r}, \mathbf{r}', t')) C_{x,i-1}] d\mathbf{S}', \quad (3.5)$$

where  $C_{x,i-1}$  is the previously calculated solution and if  $i = 1$  then we use the prescribed initial condition,  $C_{x,0}$ .

We can approximate the  $\text{Ca}^{2+}$  concentration at time  $T$ ,  $C_x$ , using a discretised time variable,  $t$ , with a time step of  $dt$  by time stepping the solution as follows:

1. Calculate the solution after one time step,  $C_{x,1}$ , according to equation (3.5) using the prescribed initial condition  $C_{x,0}$ .
2. For  $i = 2$  to  $i = n$  calculate the  $i^{\text{th}}$  solution, given by equation (3.5).
3. Stop when  $i = n$ , as we have calculated the solution from  $t = t_0$  to  $t = T$ ,  $C_x$ .

Iterating the solution in this way, we capture the evolution of the  $\text{Ca}^{2+}$  concentrations within the system and determine the  $\text{Ca}^{2+}$  concentration at specific time points. We illustrate the iterative time stepping scheme using the following PDE to represent diffusion of  $\text{Ca}^{2+}$ ,  $C = C(x, t)$ , on a 1D line of length  $L$  over a time interval  $T$ ,

$$\frac{\partial C}{\partial t} = \frac{\partial^2 C}{\partial x^2}. \quad (3.6)$$

The initial condition is depicted graphically in Figure 3.1(a) and has no flux boundary conditions at  $x = 0$  and  $x = L$ . We use a spatial mesh size,  $dx = 0.1$ , and a time step,  $dt = 0.01$ , to compare the final  $\text{Ca}^{2+}$  profiles calculated when using one large time interval, equation (3.2), and the iterative time step

method. The iterative time step method, represented by the dashed red line in Figure 3.1(b), results in the same  $\text{Ca}^{2+}$  profile at  $t = 1\text{s}$  as the analytical solution (calculated using equation (3.2)), represented by the solid blue line. This demonstrates that the final  $\text{Ca}^{2+}$  concentration profile is well approximated by the iterative time stepping scheme. We compare the  $\text{Ca}^{2+}$  concentration profiles at different times in Figure 3.1(c) with the solid blue representing the exact  $\text{Ca}^{2+}$  concentration at each time point, calculated using equation (3.2), and the dashed red lines representing the iterative time stepping scheme. The exact  $\text{Ca}^{2+}$  profiles are well approximated at each time point using the iterative scheme. Figure 3.1(d) shows the  $\text{Ca}^{2+}$  peak at  $x = 5\text{nm}$  throughout the simulation and clearly demonstrates that the iterative time stepping approach provides a good approximation to the temporal evolution of the  $\text{Ca}^{2+}$  profile throughout the simulation.

We have discretised space, time and also truncated the number of modes ( $M$ ) in our Green's function when calculating the analytical and iterative solutions shown in Figure 3.1. Discretising these variables introduces error into our solution e.g. we approximate the volume integral using the trapezium rule over the discretised spatial variables and smaller discretisations will provide better approximations than larger discretisations. Therefore, it is important to check how the solution is affected by such discretisations and ensure that the discretisations chosen are sensible and do not introduce large errors into the system. We first look at how changing our spatial discretisation,  $dx$ , affects the iterative solution. In Figure 3.2(a) we reproduce Figure 3.1(b) but now include the  $\text{Ca}^{2+}$  concentration calculated with increasing  $dx$  by the dotted lines. We see that as  $dx$  gets larger the solution is less accurate (reaching values of  $C = 40\mu\text{M}$ ). This is more clearly illustrated in Figure 3.2(b) where we plot the final  $\text{Ca}^{2+}$  concentration at  $x = 5\text{nm}$  and see that as the spatial discretisation increases (up to  $dx = 0.3\text{nm}$ ) the  $\text{Ca}^{2+}$  solution becomes less accurate. The final  $\text{Ca}^{2+}$  solution has converged to approximately  $0.3\mu\text{M}$  by  $dx = 0.2\text{nm}$  so our discretisation of  $dx = 0.1\text{nm}$  is sufficiently small to ensure the solution is a good approximation. We performed similar comparisons to examine the effect of changing the temporal discretisation and number of modes included in the Green's function in Figure 3.2(c) and 3.2(d). We again plot the final  $\text{Ca}^{2+}$  concentration at  $x = 5\text{nm}$  as a function of the temporal discretisation ( $dt$ ) and number of modes ( $M$ ). In these cases we find that the calculated  $\text{Ca}^{2+}$  concentration does not depend on  $dt$  or  $M$ . This is because we have not included any sources or boundary fluxes that vary with time. This is examined in more detail in section

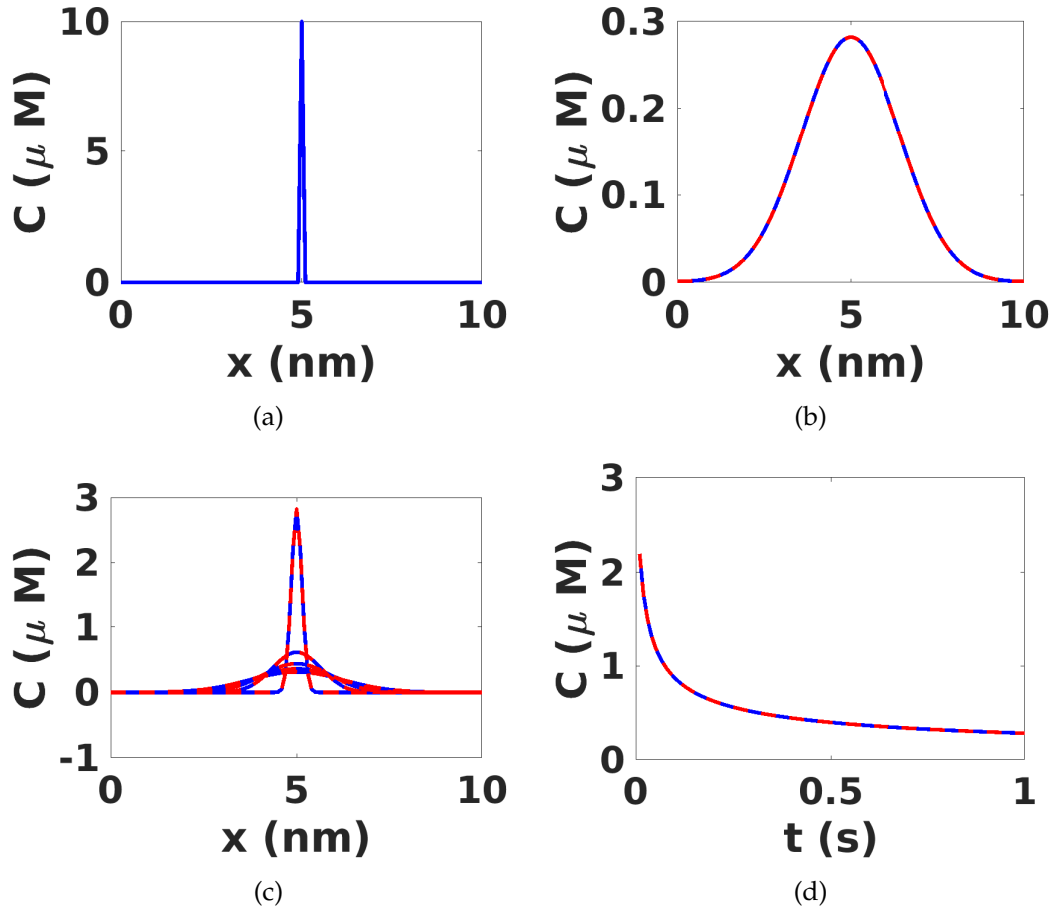


**Figure 3.1:** (a) Initial condition. (b)-(d) Simulations of the  $\text{Ca}^{2+}$  concentration on the line at different points in time. The solid blue line represents the exact solution calculated using equation (3.2) and the red dashed line is the  $\text{Ca}^{2+}$  solution calculated using the iterative time stepping method in equation (3.5). (b)  $\text{Ca}^{2+}$  concentration after time interval,  $T$ . (c)  $\text{Ca}^{2+}$  concentration at increasing points in time leading to lower peaks of  $\text{Ca}^{2+}$ . (d) Temporal evolution of the  $\text{Ca}^{2+}$  concentration at  $x = 5\text{nm}$ . Parameters:  $T = 1\text{s}$ ,  $L = 10\text{nm}$ ,  $dx = 0.1$ ,  $dt = 0.01$ ,  $M = 100$ .

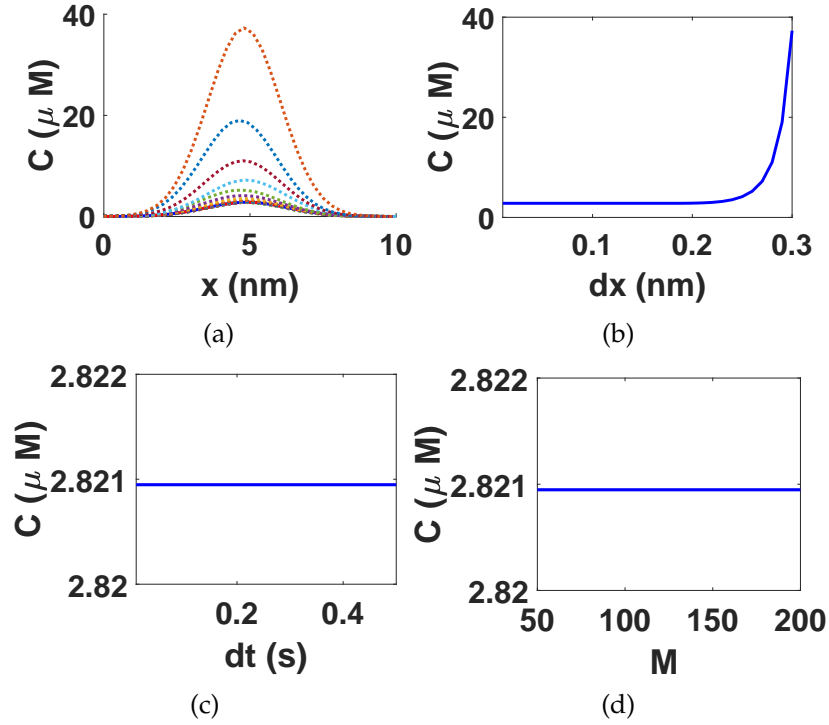


**Figure 3.2:** Numerical investigation of how discretisation affects accuracy of final  $\text{Ca}^{2+}$  solution. (a) solid blue line represents analytical  $\text{Ca}^{2+}$  solution, dashed red line represents iterative final  $\text{Ca}^{2+}$  solution with  $dx = 0.1\text{nm}$  and dotted lines represent iterative final solutions with  $dx$  ranging from  $0.01\text{nm}$  to  $0.3\text{nm}$ . (b) final  $\text{Ca}^{2+}$  solution at  $x = 5\text{nm}$  calculated using iterative time stepping method plotted for the range of  $dx$ . (c) final  $\text{Ca}^{2+}$  solution at  $x = 5\text{nm}$  calculated using iterative time stepping method plotted for the range of  $dt$ . (d) final  $\text{Ca}^{2+}$  solution at  $x = 5\text{nm}$  calculated using iterative time stepping method plotted for the range of  $M$ . Parameters:  $T = 1\text{s}$ ,  $L = 10\text{nm}$ .

4.2 when we investigate how changing  $dt$  affects the  $\text{Ca}^{2+}$  dynamics in both the ER-PM junction and sub-PM ER which have constant fluxes (Orai channel) and  $\text{Ca}^{2+}$  and time dependent fluxes (SERCA pump), respectively.

The size of the temporal mesh is important so we will use a time step,  $dt = 10^{-6}\text{s}$ , in our simulations of the local  $\text{Ca}^{2+}$  dynamics to provide a good approximation to the temporal evolution of the  $\text{Ca}^{2+}$  concentration. The impact of the time step on the extent of  $\text{Ca}^{2+}$  diffusion is discussed later in this chapter, in section 3.2.1. We will discretise the model spatially so we can simulate the model in MATLAB. We have chosen uniform meshes in the  $r$ ,  $\phi$  and  $z$  directions with mesh sizes  $\Delta r$ ,  $\Delta\phi$  and  $\Delta z$  respectively.

Using an iterative scheme with a uniform temporal mesh to approximate the  $\text{Ca}^{2+}$  evolution in time ensures the Green's functions are always of the form

$G_x(\mathbf{r}, dt)$ . Therefore, we can pre-compute the Green's function on each domain. Computation of the Green's function takes approximately 5 hours so by pre-computing the Green's function at the start of the simulation we will reduce the simulation time by approximately 5 hours per time step. Thus reducing the run time of the simulation as we will not need to compute the Green's function at each time step.

## 3.2 Green's functions

Green's functions describe the effect of diffusion on the  $\text{Ca}^{2+}$  profile within the domain. To solve the SOCE PDE model, given in Chapter 2, we must first calculate the Green's function of each domain. We focus on the two local domains: the ER-PM junction (J) and sub-PM ER (S) which are defined on cylinders.

Green's functions obey the original PDE and inhomogeneous initial condition but satisfy the homogeneous versions of the boundary conditions [8]. The homogeneous boundary conditions allow us to use the separation of variables technique to calculate the solution which propagates the effect of diffusion on the initial condition and from this we can derive the Green's function for the domain. The separation of variables technique separates the solution into a combination of functions of the four variables,  $\rho(r)$ ,  $\theta(\phi)$ ,  $h(z)$  and  $T(t)$ . Since the ER-PM junction and sub-PM ER domains are both defined as cylinders then the separation of variables technique will lead to the same system of equations for the  $\text{Ca}^{2+}$  concentration on the ER-PM junction and sub-PM ER. The solutions of these equations will depend on the homogeneous versions of the boundary conditions, leading to different solutions, and resulting in two distinct solutions for  $C_J(r, \phi, z, t)$  and  $C_S(r, \phi, z, t)$ .

The PDE model with  $C_x = C_x(r, \phi, z, t)$  and homogeneous boundary conditions on a general cylindrical domain is given by,

$$\frac{\partial C_x}{\partial t} = D_x \nabla^2 C_x, \quad (3.7)$$

where  $x \in \{J, S\}$  denotes the domain and  $D_x$  the diffusion coefficient of that domain.

To apply the separation of variables technique we decompose the general solution for a cylindrical domain with homogeneous boundary conditions as fol-

lows,

$$C_x(r, \phi, z, t) = T(t)\rho(r)\theta(\phi)h(z). \quad (3.8)$$

The functions  $\rho$ ,  $\theta$ ,  $h$  and  $T$  denote the dependence of the  $\text{Ca}^{2+}$  concentration,  $C_x$ , on the  $r$ ,  $\phi$ ,  $z$  and  $t$  variables, respectively. We can write the general initial condition on a cylindrical domain as

$$C_x(r, \phi, z, 0) = T(0)\tilde{\rho}(r)\tilde{\theta}(\phi)\tilde{h}(z), \quad (3.9)$$

where the variables  $\tilde{\rho}$ ,  $\tilde{\theta}$  and  $\tilde{h}$  denote the dependence of the initial condition on the  $r$ ,  $\phi$  and  $z$  variables, respectively.

We substitute equation (3.8) into the general diffusion equation (3.7) and apply the separation of variables technique to separate the system into the following equations for a cylindrical domain:

$$T' + D_J (\mu^2 + \eta^2) T = 0, \quad (3.10)$$

$$h'' + \mu^2 h = 0, \quad (3.11)$$

$$\theta'' + \gamma^2 \theta = 0, \quad (3.12)$$

$$r^2 \rho'' + r \rho' + \rho(r^2 \eta^2 - \gamma^2) = 0. \quad (3.13)$$

where  $\mu$ ,  $\eta$  and  $\gamma$  are defined using the homogeneous versions of the boundary conditions of each domain. Equation (3.13) is Bessel's equation.

We now look at the specific solutions on the ER-PM junction and sub-PM ER.

### 3.2.1 ER-PM junction

The inhomogeneous initial condition and homogeneous boundary conditions of the ER-PM junction are given by,

$$\begin{aligned} C_{J,0} = 0.1\mu\text{M}, & \quad D_J \frac{\partial C_J}{\partial z} \Big|_{z=H} = 0, \\ C_J \Big|_{r=a} = 0, & \quad D_J \frac{\partial C_J}{\partial z} \Big|_{z=L_2} = 0, \end{aligned} \quad (3.14)$$

with periodic boundary conditions in  $\phi$  and  $D_J$  is the diffusion coefficient in the ER-PM junction. Applying the inhomogeneous initial condition and homogeneous boundary conditions to the separable equations (3.10) - (3.13) we

obtain the following solutions,

$$T(t) = T(0)e^{-D_J(\mu_m^2 + \eta^2)t}, \quad (3.15)$$

$$h(z) = \frac{1}{H - L_2} \int_{L_2}^H \tilde{h}(z') dz' \left[ 1 + 2 \sum_{m=1}^M \cos(\mu_m(z' - L_2)) \cos(\mu_m(z - L_2)) \right], \quad (3.16)$$

$$\theta(\phi) = \frac{1}{2\pi} \int_0^{2\pi} \tilde{\theta}(\phi') d\phi' \left[ 1 + 2 \sum_{n=1}^N \cos(n(\phi - \phi')) \right], \quad (3.17)$$

$$\rho(r) = \frac{2}{a^2} \int_0^a \tilde{\rho}(r') r' dr' \sum_{j=1}^J \frac{J_n(\alpha_{n,j} r' / a) J_n(\alpha_{n,j} r / a)}{J_{n+1}^2(\alpha_{n,j})}, \quad (3.18)$$

where  $\mu = \mu_m = m\pi / (H - L_2)$  for  $m = 1, 2, \dots, M$ ,  $\gamma = n$  for  $n = 0, 1, 2, \dots, N$ ,  $\eta = \alpha_{n,j} / a$  and  $\alpha_{n,k}$  satisfies  $J_n(\alpha_{n,j}) = 0$  for  $j = 1, 2, \dots, J$  where  $J_n(x)$  are Bessel's functions of order  $n$ .

We substitute each solution into equation (3.8) and substitute in equation (3.9) to return the initial condition,  $C_{J,0}$ , and reach the following solution for  $C_J$ ,

$$C_J = \int_V dV' G_J(r, r', \phi, \phi', z, z', t) C_{J,0}, \quad (3.19)$$

where  $G_J$  is the Green's function in the ER-PM junction. Equation (3.19) describes the diffusion of the initial  $\text{Ca}^{2+}$  profile,  $C_{J,0}$ , in the ER-PM junction. By setting the initial condition to a 3D polar delta function,

$$C_{J,0} = \frac{\delta(r - r') \delta(\phi - \phi') \delta(z - z')}{r'}, \quad (3.20)$$

we recover the Green's function from equation (3.19). The Green's function in the ER-PM junction is given by

$$\begin{aligned} G_J(r, r', \phi, \phi', z, z', dt) = & \\ & \frac{1}{\pi a^2 (H - L_2)} \left[ 1 + 2 \sum_{m=1}^M \cos(\mu_m(z' - L_2)) \cos(\mu_m(z - L_2)) \exp(-D_J \mu_m^2 t) \right] \\ & \times \sum_{j=1}^J \left[ \frac{J_0(\alpha_{0,j} r' / a) J_0(\alpha_{0,j} r / a)}{J_1(\alpha_{0,j})^2} \exp\left(-D_J \left(\frac{\alpha_{0,j}}{a}\right)^2 dt\right) \right. \\ & \left. + 2 \sum_{n=1}^N \frac{J_n(\alpha_{n,j} r' / a) J_n(\alpha_{n,j} r / a)}{J_{n+1}(\alpha_{n,j})^2} \cos(n(\phi - \phi')) \exp\left(-D_J \left(\frac{\alpha_{n,j}}{a}\right)^2 dt\right) \right]. \end{aligned} \quad (3.21)$$

The Green's function is the only function in equation (3.19) that incorporates the diffusion coefficient and time step. The Green's function controls the extent of  $\text{Ca}^{2+}$  diffusion on the system and by changing the size of the time step,  $dt$ , or the diffusion coefficient,  $D_j$ , we will influence the extent of  $\text{Ca}^{2+}$  diffusion observed during one time step in the ER-PM junction. We have chosen  $D_j = 220\mu\text{m}^2\text{s}^{-1}$  in accordance with the values used in the literature, as discussed in Chapter 2. The length of the time step is crucial to modelling  $\text{Ca}^{2+}$  release and  $\text{Ca}^{2+}$  uptake through  $\text{Ca}^{2+}$  pumps as the pump rate will vary in real time with the changing  $\text{Ca}^{2+}$  concentration. By approximating the changing  $\text{Ca}^{2+}$  concentration over time as a discrete series of  $\text{Ca}^{2+}$  concentrations we will approximate the  $\text{Ca}^{2+}$  flux through the SERCA pump as a constant  $\text{Ca}^{2+}$  flux over one time step so that we can approximate the overall  $\text{Ca}^{2+}$  flux as a series of constant  $\text{Ca}^{2+}$  fluxes. To be able to approximate the  $\text{Ca}^{2+}$  flux through the pump as a constant flux we must have a small enough time step that the  $\text{Ca}^{2+}$  profile near the SERCA pump does not change considerably during one time step. If we choose a time step that is too large we could neglect vital changes to the pump strength resulting in over or under-estimates of the  $\text{Ca}^{2+}$  influx. The time step is also important for controlling the shape and intensity of the elevated  $\text{Ca}^{2+}$  profile in the microdomain surrounding the Orai channel and if we choose a small time step then the microdomain will have a large  $\text{Ca}^{2+}$  elevation that is tightly concentrated around the channel but if the time step is much larger then the microdomain would have a lower  $\text{Ca}^{2+}$  elevation and a larger microdomain because the  $\text{Ca}^{2+}$  will have diffused much further in this larger time step.

The shape of the Green's function with various time steps is illustrated in Figure 3.3. We can see that using a large time step,  $dt = 10^{-5}\text{s}$ , allows the  $\text{Ca}^{2+}$  concentration to diffuse throughout the whole domain and even interact with the boundary. Thus, the  $\text{Ca}^{2+}$  peak is no longer evident and in fact, there is little structure in the polar plane, as seen in Figure 3.3(a). The Green's function is also symmetric in  $z$ , as shown by the lack of structure around the channel in the  $z$  direction in Figure 3.3(b). This means that in one time step,  $dt = 10^{-5}\text{s}$ , the  $\text{Ca}^{2+}$  concentration within the junction equilibrates and the local elevations due to the  $\text{Ca}^{2+}$  influx through a channel are no longer apparent.

In Figures 3.3(c) and 3.3(d) we have decreased the time step to  $dt = 10^{-6}\text{s}$  and we can see that the polar Green's function retains its peak in the polar plane so the  $\text{Ca}^{2+}$  profile within the ER-PM junction retains the structure of the microdomain after diffusion over one time step. In the  $z$  direction the  $\text{Ca}^{2+}$

profile is again symmetric in  $z$  but the height of the junction is three times smaller than the radius of the junction so we would need a much smaller time step to maintain a  $\text{Ca}^{2+}$  peak in the  $z$  direction after diffusion in one time step,  $dt = 10^{-6}\text{s}$ .

In Figures 3.3(e) and 3.3(f) we have decreased the time step to  $dt = 10^{-8}\text{s}$  and we can see that the Green's function has a very concentrated peak in the polar plane and also has a strong peak in the  $z$  direction as the  $\text{Ca}^{2+}$  is not able to diffuse as far during such a small time step so the microdomain structure is preserved.

If we consider how the time step changes the shape of the Green's function then we realise that by using a larger time step, such as  $dt = 10^{-5}\text{s}$  we will smooth out the  $\text{Ca}^{2+}$  concentration profile and any  $\text{Ca}^{2+}$  microdomains forming around the channel and pump mouths will equilibrate as  $\text{Ca}^{2+}$  diffuses within the junction. The local high  $\text{Ca}^{2+}$  concentrations will no longer affect the pump rates and we will need to wait for global rises in  $\text{Ca}^{2+}$  rather than local changes to affect the  $\text{Ca}^{2+}$  pumping and refilling. The smallest time step,  $dt = 10^{-8}\text{s}$ , has very concentrated peaks so the  $\text{Ca}^{2+}$  profile will not diffuse much over one time step. The  $\text{Ca}^{2+}$  microdomain will remain very tightly concentrated around the channel mouth and take longer to diffuse enough to cause an increase in concentration near the SERCA pumps. However, this would be computationally intensive as we would need to run longer simulations. The middle time step,  $dt = 10^{-6}\text{s}$ , has a fairly concentrated  $\text{Ca}^{2+}$  peak in the polar directions but the  $\text{Ca}^{2+}$  profile has little structure in the  $z$  direction. This time step allows the SERCA pumps to feel the increase in local  $\text{Ca}^{2+}$  concentrations around the pumps from the  $\text{Ca}^{2+}$  influx through Orai channels without completely diffusing throughout the entire domain. If we use the smallest time step,  $dt = 10^{-8}\text{s}$ , to simulate a total time of  $T = 10^{-4}\text{s}$ , we need to run  $10^4$  time steps per simulation. However, if we use a time step of  $dt = 10^{-6}\text{s}$  we only need to run 100 time steps per simulation. Therefore, we will use a time step of  $dt = 10^{-6}\text{s}$  in our simulations as we run fewer time steps per simulation and reduce the total run time of the simulation compared to smaller time steps.

We can check our Green's function behaves correctly by testing that when  $t = 0$  the Green's function is a composition of delta functions,

$$G_J(r, r', \phi, \phi', z, z', 0) = \frac{\delta(r - r')\delta(\phi - \phi')\delta(z - z')}{r'}$$

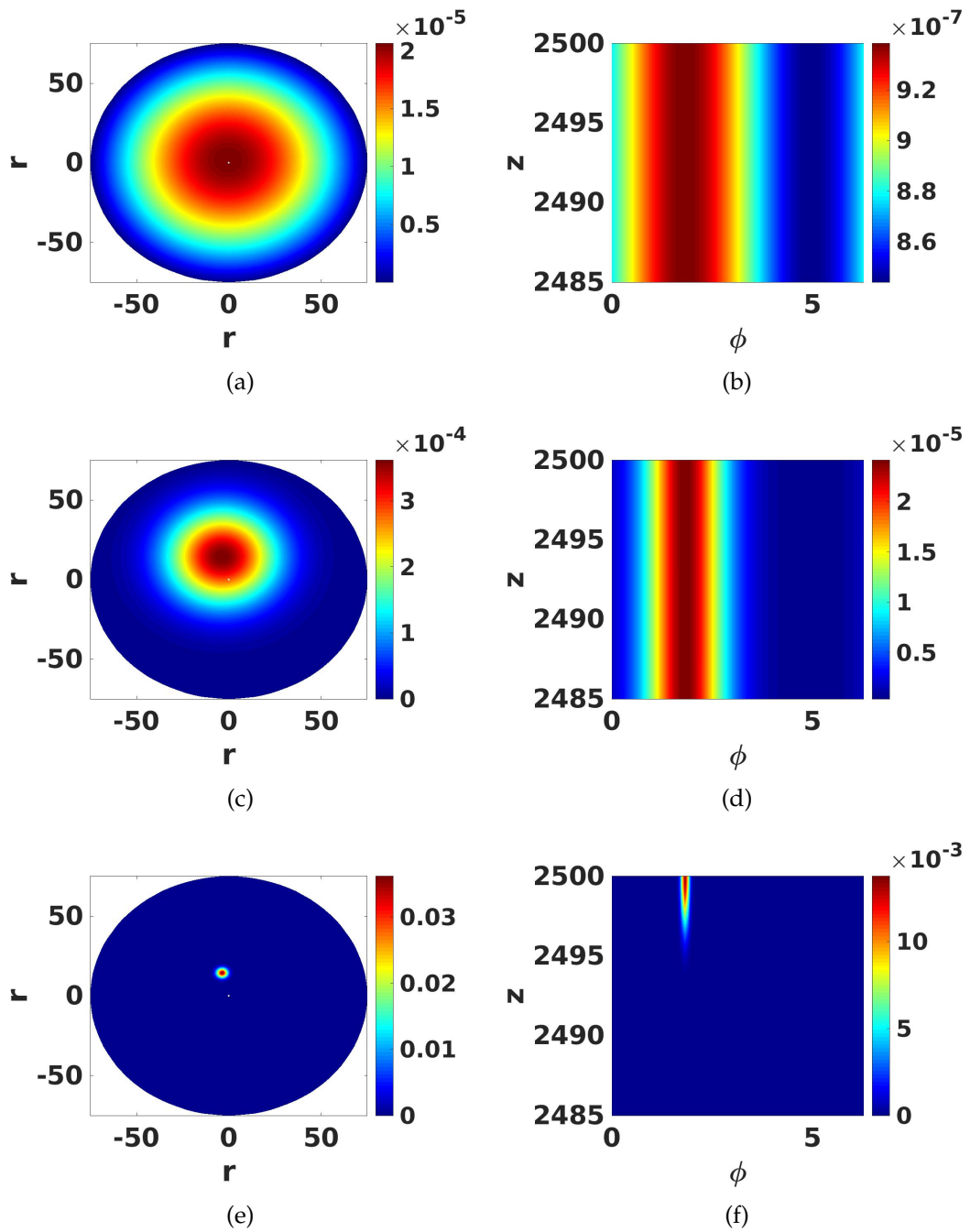


**Figure 3.3:** Green's functions in the ER-PM junction with different time steps. (a) and (b) have a time step  $dt = 10^{-5}$ s and the  $\text{Ca}^{2+}$  profile in the ER-PM junction is very flat. (c) and (d) have a time step  $dt = 10^{-6}$ s and the peak is flattened but still visible in the polar direction, the  $\text{Ca}^{2+}$  concentration in the  $z$  direction is almost homogeneously distributed. (e) and (f) have a time step  $dt = 10^{-8}$ s and the peak in the  $z$  and polar directions is very clear. The parameters used are  $J = 150$ ,  $M = 100$ ,  $N = 50$

Here, we use the convolution property of delta functions,

$$\int f(x)\delta(x-a) = f(a). \quad (3.22)$$

We know the Green's function is comprised of three delta functions when  $t = 0$  and can be decomposed into solutions in each direction so we can then use the convolution property of delta functions, equation (3.22), to check that the representation is a Green's function. The representations of the delta function in each direction are shown in Figures 3.4(a), 3.4(c) and 3.4(e), however we have small oscillations about zero away from the peak. The Green's function can be convolved in each direction according to equation (3.22) using a Gaussian expression, shown in blue in Figures 3.4(b), 3.4(d) and 3.4(f), with the convolution shown in dashed red lines. As we see, the convolution exactly matches the original function showing that the convolution property of delta functions (3.22) is satisfied. Therefore, equation (3.21) does indeed represent a Green's function for small  $dt$ .

By increasing the number of terms in the sums (increasing  $J, N$  and  $M$ ) in Figures 3.5(a), 3.5(c) and 3.5(e) we see that the peak increases but has also smoothed the oscillations. In fact, the oscillations remain the same but the peak has increased and on this scale the oscillations are not visible on the new graphs. In Figures 3.5(b), 3.5(d) and 3.5(f), we see that the Green's function with more terms in the sum no longer behaves like a delta function as the red dashed line is approximately 10 times larger than the solid blue line. We will use  $J = 150, N = 50$  and  $M = 100$  in the Green's function sums but remain aware when analysing our results that there may be small oscillations the  $\text{Ca}^{2+}$  concentration which are attributed to the oscillations in the delta functions.

### 3.2.2 Sub-PM ER

The inhomogeneous initial condition and homogeneous boundary conditions of the sub-PM ER are given by,

$$\begin{aligned} C_{S,0} = 150\mu\text{M}, & \quad D_S \frac{\partial C_S}{\partial z} \Big|_{z=L_2} = 0, \\ C_S \Big|_{z=L_1} = 0, & \quad D_S \frac{\partial C_S}{\partial r} \Big|_{r=a} = 0, \end{aligned} \quad (3.23)$$

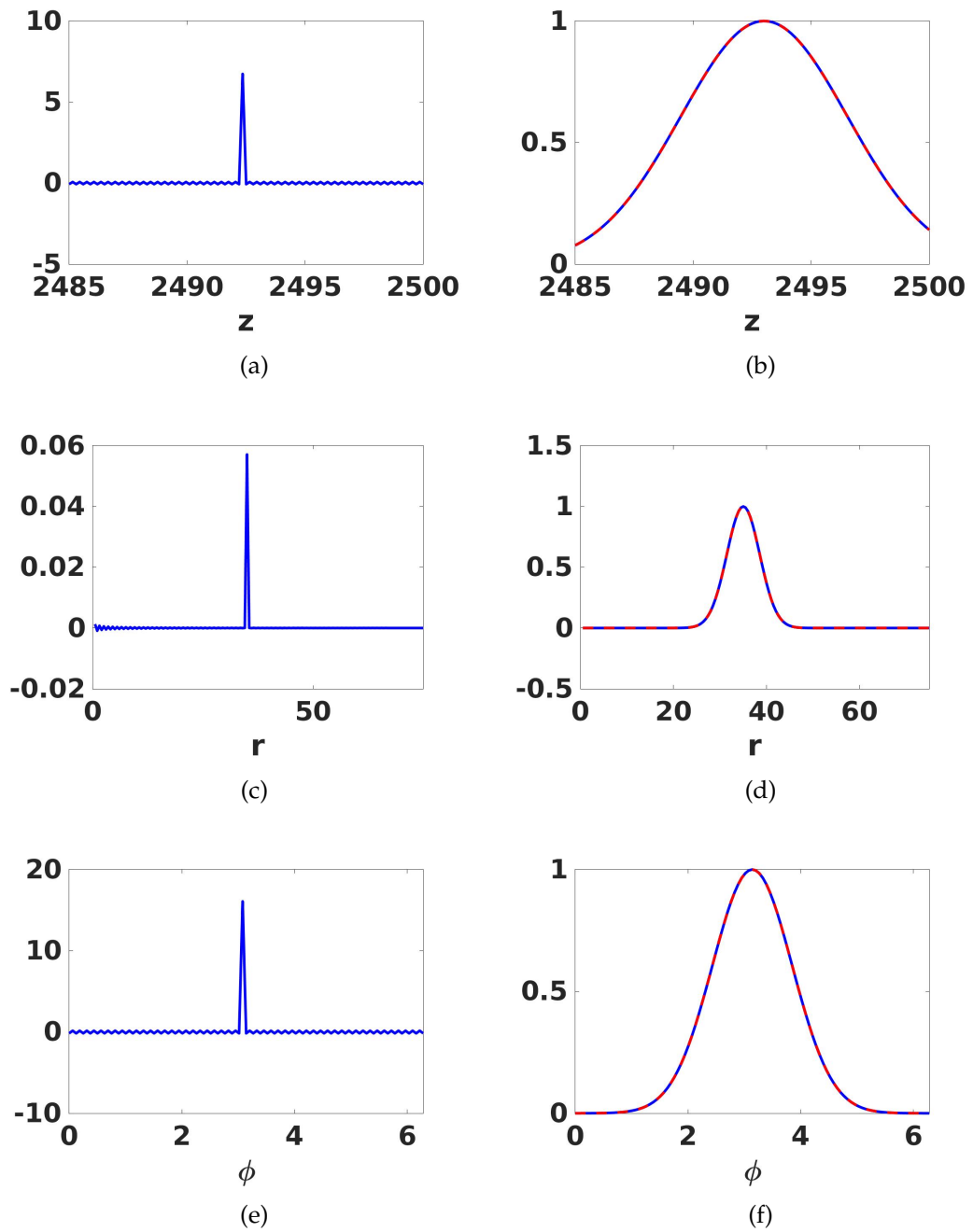


**Figure 3.4:** Checks that the Green's function in the ER-PM junction acts like a delta function when  $dt = 0$ . (a, c, e) show the shape of the  $z, r, \phi$  components of the Green's function. (b, d, f) show that the Green's functions components convolve like delta functions where the solid blue line is the original function and the red dashed line is the convolution. The parameters used are  $M = 100, J = 150$  and  $N = 50$

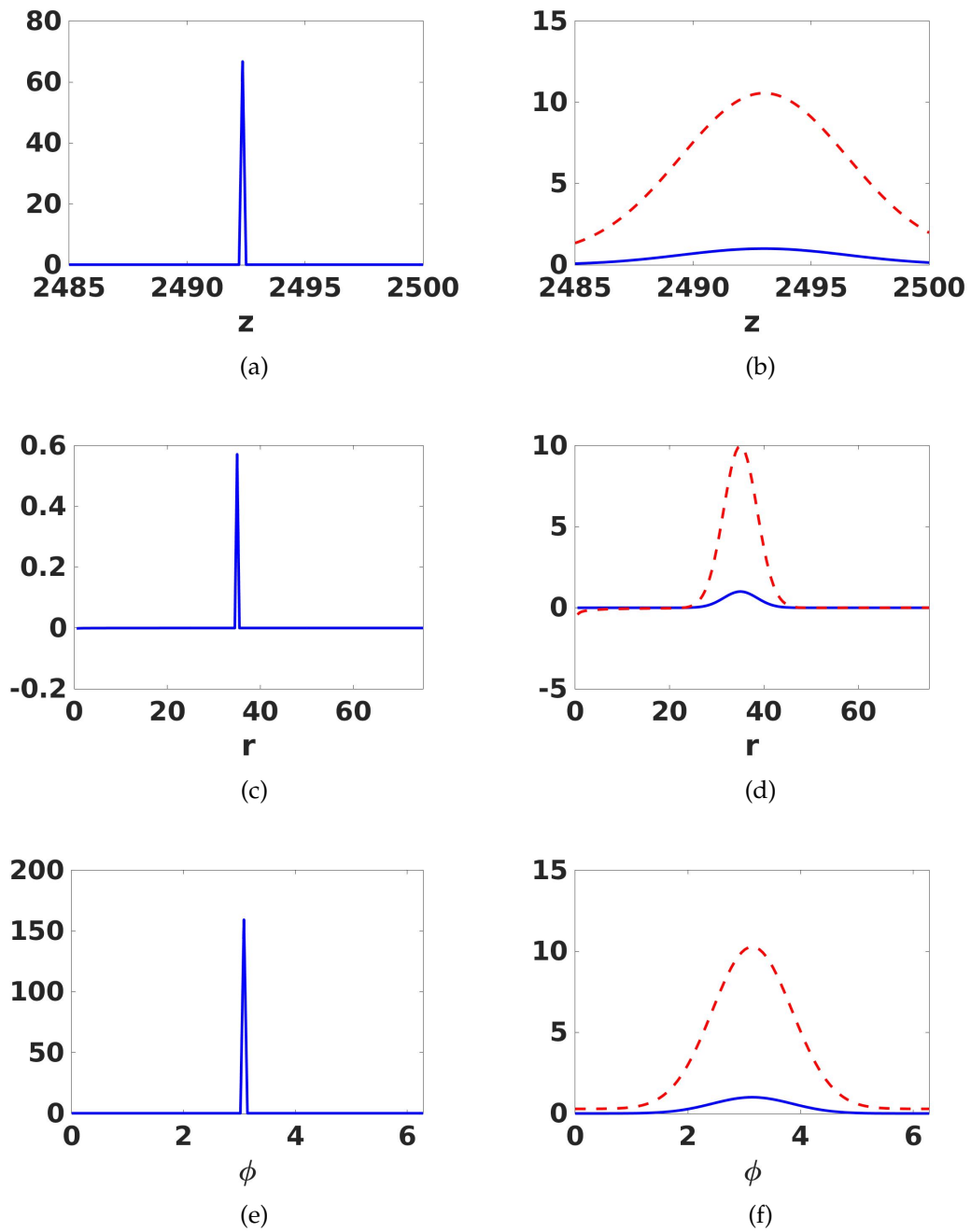


**Figure 3.5:** Check to see how the Green's function shape and properties change by increasing the number of terms in the sum. (a,c,e) show the shape of the  $z, r, \phi$  components of the Green's function and (b,d,f) show that the Green's functions components do not convolve correctly when we have more terms in the sum. The parameters used are  $M = 1000$ ,  $J = 1500$  and  $N = 500$ .

with periodic boundary conditions in  $\phi$  and  $D_S$  is the diffusion coefficient in the sub-PM ER. We apply the inhomogeneous initial condition and homogeneous boundary conditions separable variable equations (3.10) - (3.13) to get the following solutions on the sub-PM ER,

$$T(t) = T(0)e^{-D_S(\mu^2+\eta^2)t}, \quad (3.24)$$

$$h(z) = \frac{2}{L_2 - L_1} \int_{L_1}^{L_2} \tilde{h}(z') dz' \sum_{m=1}^M \cos(\mu_m(L_2 - z')) \cos(\mu_m(L_2 - z)), \quad (3.25)$$

$$\theta(\phi) = \frac{1}{2\pi} \int_0^{2\pi} \tilde{\theta}(\phi') d\phi' \left[ 1 + 2 \sum_{n=1}^N \cos(n(\phi - \phi')) \right], \quad (3.26)$$

$$\rho(r) = \frac{2}{a^2} \int_0^a \tilde{\rho}(r') r' dr' \sum_{j=1}^J \frac{J_n(\beta_{n,j} r'/a) J_n(\beta_{n,j} r/a)}{J_n^2(\beta_{n,j}) (1 - (n/\beta_{n,j})^2)}. \quad (3.27)$$

where  $\mu_m = (2m - 1)\pi/(2(L_2 - L_1))$  for  $m = 1, 2, \dots, M$ ,  $\gamma = n$  for  $n = 0, 1, \dots, N$ ,  $\eta = \beta_{n,j}/a$  and  $\beta_{n,j}$  satisfies  $J'_n(\beta_{n,j}) = 0$  for  $j = 1, 2, \dots, J$ .

By comparing equations (3.15) and (3.17) with (3.24) and (3.26) we see that the solutions in  $t$  and  $\phi$  are of the same format in the ER-PM junction and sub-PM ER. The parameters will be different because they are on different domains but the conditions were the same: one inhomogeneous initial condition and periodic boundary conditions in  $\phi$ . However, the equations governing the solution in the  $z$  direction are different in the ER-PM junction, equation (3.16), and the sub-PM ER, equation (3.25), because the domains have different boundary conditions in this direction. The ER-PM junction has two no flux boundary conditions, to account for the PM and ER membrane, whereas the sub-PM ER has one no flux boundary condition, to account for the ER membrane, but the second boundary condition is a Dirichlet boundary condition to ensure the continuity of concentration between the sub-PM ER and bulk ER, as discussed in Chapter 2. Similarly, the equations governing the solution in the  $r$  direction are different in the ER-PM junction, equation (3.18), and the sub-PM ER, equation (3.27). The ER-PM junction has a Dirichlet boundary condition on the radial boundary to ensure the continuity of concentration so  $\text{Ca}^{2+}$  can diffuse freely between the ER-PM junction and bulk cytoplasm whereas the sub-PM ER has a no flux boundary condition along the mantle of the cylinder to account for the ER membrane.

We substitute each solution into equation (3.8) and substitute in equation (3.9)

to return the initial condition  $C_{S,0}$  to reach the following solution for  $C_S$ ,

$$C_S = \int_V dV' C_{S,0} G_S (r, r', \phi, \phi', z, z', t), \quad (3.28)$$

where  $G_S$  is the Green's function of the sub-PM ER. Equation (3.28) describes the diffusion of the original  $\text{Ca}^{2+}$  profile,  $C_S(r, \phi, z, 0)$ , up to time  $t$ , in the sub-PM ER. By setting the initial condition to a 3D polar delta function,

$$C_{S,0} = \frac{\delta(r - r')\delta(\phi - \phi')\delta(z - z')}{r'}, \quad (3.29)$$

we obtain the Green's function from equation (3.28). The Green's function in the sub-PM ER is given by

$$\begin{aligned} G_S (r, r', \phi, \phi', z, z', dt) = & \\ & \frac{2}{\pi a^2 (L_2 - L_1)} \left[ \sum_{m=1}^M \cos(\mu_m (L_2 - z')) \cos(\mu_m (L_2 - z)) e^{-D_S \mu_m^2 dt} \right] \\ & \times \sum_{k=1}^K \left[ \frac{J_0(\beta_{0,k} r' / a) J_0(\beta_{0,k} r / a)}{J_0(\beta_{0,k})^2} e^{-D_S (\beta_{0,k} / a)^2 dt} \right. \\ & \left. + 2 \sum_{n=1}^N \frac{J_n(\beta_{n,k} r' / a) J_n(\beta_{n,k} r / a)}{J_n(\beta_{n,k})^2 \left(1 - \frac{n^2}{\beta_{n,k}^2}\right)} \cos(n(\phi - \phi')) e^{-D_S (\beta_{n,k} / a)^2 dt} \right]. \end{aligned} \quad (3.30)$$

The Green's function on the sub-PM ER domain is illustrated in Figure 3.6 and we can see that with a time step of  $dt = 1 \times 10^{-6}$ s the  $\text{Ca}^{2+}$  concentration peak is very concentrated in the  $z$  direction and polar plane. The sub-PM ER is much larger than the ER-PM junction in the  $z$  direction so the  $\text{Ca}^{2+}$  can diffuse much further before encountering a barrier that would impede  $\text{Ca}^{2+}$  diffusion. This causes the  $\text{Ca}^{2+}$  to peak more strongly in the  $z$  direction of the sub-PM ER because it has not diffused far enough to be affected by nearby boundaries within one time step. As discussed in Chapter 2, the diffusion coefficient of the sub-PM ER is smaller than the diffusion coefficient of the ER-PM junction ensuring that  $\text{Ca}^{2+}$  diffuses much more slowly in the sub-PM ER than the ER-PM junction. This also contributes to the generation of more tightly concentrated  $\text{Ca}^{2+}$  peaks in the sub-PM ER than the ER-PM junction.

We do not examine the Green's functions with larger or smaller time steps because  $dt = 1 \times 10^{-6}$ s is already the largest time step we can use in the ER-PM junction and we will use the same time step throughout all our domains

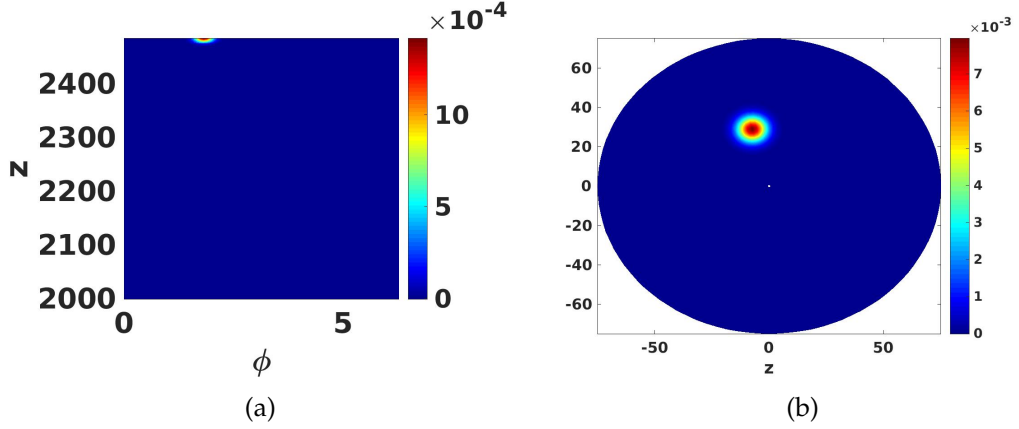


**Figure 3.6:** Simulation showing the shape of the Green's function in (a) the  $z$  direction and (b) polar direction in the sub-PM ER. The parameters used are  $J = 150$ ,  $M = 100$ ,  $N = 50$

in the simulations. As we can see from Figure 3.6, the peak of the Green's function is already very concentrated so a smaller time step will result in an even tighter peak which will take a long time to diffuse in the larger domains.

We can check that our representation given in equation (3.30) actually is a Green's function by checking the behaviour when  $dt = 0$ . We know the Green's function is composed of three delta functions when  $dt = 0$  so we check that the representation of the Green's function in each direction satisfies the convolution property of delta functions, equation (3.22). We see in Figures 3.7(a), 3.7(c) and 3.7(e) that the representations look similar to delta functions and peak only at the specified location. We still have the oscillations about zero in the  $r$  and  $\phi$  directions, however, the oscillations are small in comparison to the peak. We can see in Figures 3.7(b), 3.7(d) and 3.7(f) that the representations convolve with a Gaussian correctly, as shown by the matching of the dashed red lines with the solid blue lines.

The representation in equation (3.30) obeys the same properties as delta functions so we have confirmed our representation is indeed a Green's function for the sub-PM ER domain. We will use  $J = 150$ ,  $M = 100$  and  $N = 50$  in our sums to ensure that equation (3.30) represents a Green's function.

Although we are focusing on the local  $\text{Ca}^{2+}$  dynamics of SOCE the Green's functions of the bulk cytoplasm and bulk ER with the corresponding delta function checks are given in Appendix A.

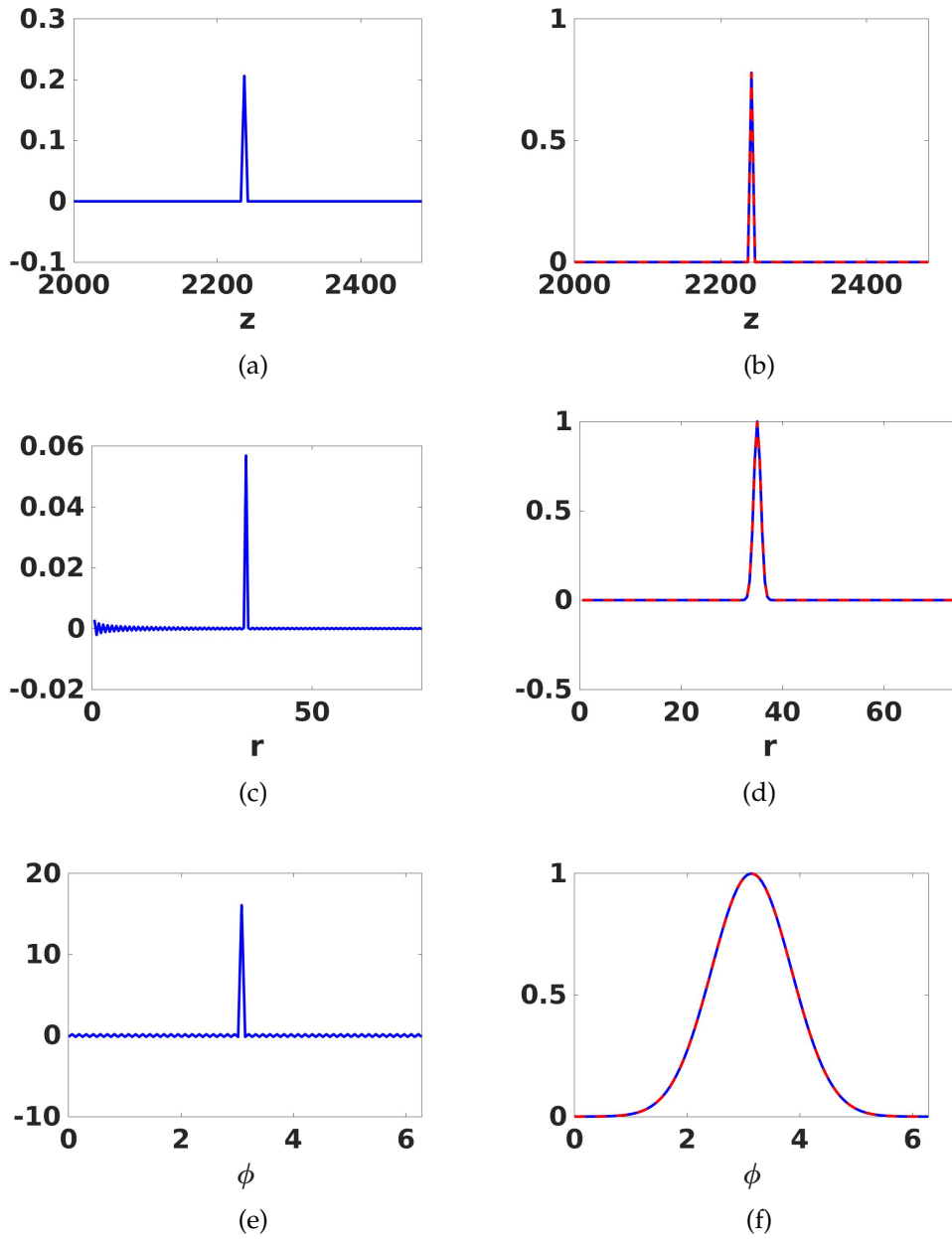


**Figure 3.7:** Checks that the Green's function in the sub-PM ER acts like a delta function when  $dt = 0$ . (a, c, e) show the shape of the  $z, r, \phi$  components of the Green's function and (b, d, f) show that the Green's functions components convolve correctly.

### 3.3 Failure of Barton's method

The solution,  $C(r, \phi, z, t)$ , to a system of PDEs in absence of internal source terms on a stationary domain of volume  $V$  and boundary  $S$  is given by equation (3.2). As discussed earlier, we are using a small time step,  $dt = 10^{-6}$ s, and assuming that the  $\text{Ca}^{2+}$  concentration within the domain will not change considerably during one time step, so we can approximate the  $\text{Ca}^{2+}$  flux through a SERCA pump as a constant flux over one time step. We then time step the solution using the iterative scheme discussed in section 3.1. The boundary conditions are approximated as a constant flux through the Orai channel or SERCA pump and calculated at each new time point using the new initial concentration. The new initial condition includes the  $\text{Ca}^{2+}$  influx from the previous boundary condition so the first integral describes how the concentration changes due to diffusion and then the second integral describes the  $\text{Ca}^{2+}$  fluxes across the boundaries. The new boundary conditions have 'felt' the change in  $\text{Ca}^{2+}$  concentration due to  $\text{Ca}^{2+}$  diffusion and  $\text{Ca}^{2+}$  influx/efflux through channels and pumps on the membranes in the previous time step. We iterate the solution by updating the initial condition and boundary fluxes at each new time point and calculate the concentration profile incrementally so that the  $\text{Ca}^{2+}$  concentration calculated at each time point is a good approximation to the evolution of the  $\text{Ca}^{2+}$  profile during SOCE.

Using Barton's formula [8] the solution to the PDE on the sub-PM ER over a time interval,  $T$ , is given by,

$$\begin{aligned} C_S = & D_E \int_0^T dt' \int_0^{2\pi} \int_0^a r' dr' d\phi' G(r, r', \phi, \phi', z, L_2, t') J_{\text{SERCA}}(r', \phi') \\ & - D_E \int_0^T dt' \int_0^{2\pi} \int_0^a r' dr' d\phi' \partial_n' G(r, r', \phi, \phi', z, L_1, t') C_E(r', \phi', L_1, t') \\ & + \int_V dV' G(r, r', \phi, \phi', z, z', t) C_S(r', \phi', z', 0). \end{aligned} \quad (3.31)$$

Barton highlights the ability of this method to solve all PDEs but also acknowledges that the method is not always the fastest approach and discusses the pitfalls associated with this method. For instance, in example 9.4.2 [8, p. 214], the method appears to fail when Dirichlet boundary conditions are used and Barton describes techniques to overcome the issue. This is such an instance where Barton's method, although capable of solving the PDE, is not the most efficient method. We encounter similar problems with our system as the solution determined using Barton's method does not satisfy the boundary conditions we

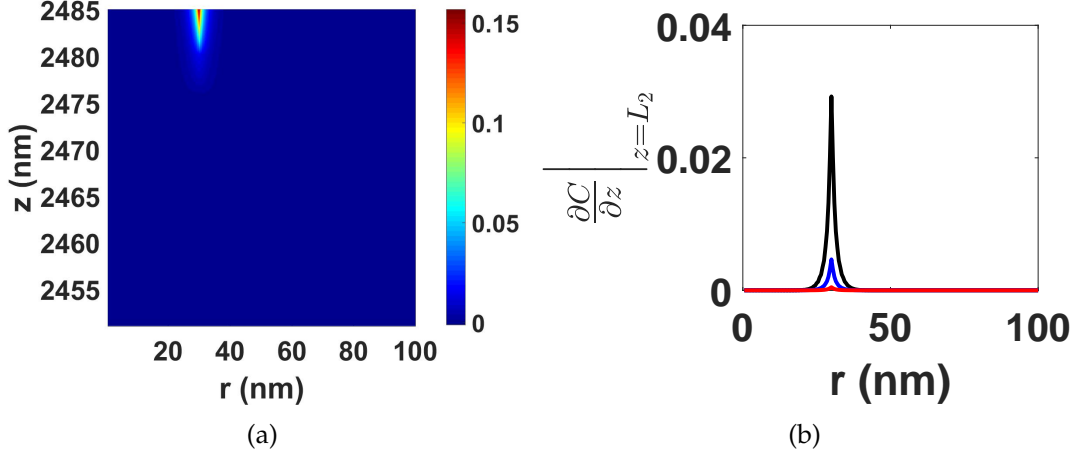


**Figure 3.8:** (a)  $\text{Ca}^{2+}$  concentration in the sub-PM ER beneath the SERCA pump at  $(r_{\text{SERCA}}, \phi_{\text{SERCA}})$ . (b) Gradient at  $z = L_2$  where the black, blue and red lines represent  $\Delta z = 4.85\text{nm}$ ,  $\Delta z = 0.485\text{nm}$  and  $\Delta z = 0.0485\text{nm}$ , respectively, near to  $z = L_2$ .

impose on the system so the solution appears to fail.

To illustrate this, we now consider the sub-PM ER domain with  $\text{Ca}^{2+}$  concentration  $C_S$  because this domain has prescribed one inhomogeneous flux boundary condition on the ER membrane at  $z = L_2$  and one inhomogeneous Dirichlet boundary condition at  $z = L_1$ . Suppose we have a constant initial condition  $C_S(r, \phi, z, 0) = 150\mu\text{M}$  with a unit boundary flux,  $J_{\text{SERCA}}$ , through a SERCA pump at position  $(\hat{r}, \hat{\phi})$  on the ER membrane and a constant Dirichlet boundary condition,  $C_C(r', \phi', L_1, t') = \tilde{C} = 150\mu\text{M}$ , at  $z = L_1$ . The  $\text{Ca}^{2+}$  concentration in the sub-PM ER must obey the boundary conditions given in system (2.4) so if we look at the gradient of  $C_S$  at  $z = L_2$ , the ER membrane, we should recover the unit flux through the SERCA pump across the ER membrane and the  $\text{Ca}^{2+}$  concentration along  $z = L_1$ ,  $\tilde{C}$ , should be  $150\mu\text{M}$ .

We test if the solution,  $C_S$ , satisfies the boundary conditions analytically by differentiating  $C_S$ , given by equation (3.31), with respect to  $z$  to check the gradient along the ER membrane,  $z = L_1$ , and by looking at the  $\text{Ca}^{2+}$  concentration at  $z = L_1$ .

Differentiating the  $\text{Ca}^{2+}$  concentration,  $C_S$ , with respect to  $z$  gives,

$$\begin{aligned} \frac{\partial C_S}{\partial z} &= \frac{\partial}{\partial z} D_E \int_0^t dt' \int_{S_{L_2}} dS' G(r, r', \phi, \phi', z, L_2, t') J_{\text{SERCA}} \\ &\quad - \frac{\partial}{\partial z} D_E \int_0^t dt' \int_{S_{L_1}} dS' \left( \frac{\partial}{\partial z'} G(r, r', \phi, \phi', z, z', t') \right) \Big|_{z'=L_1} C_c(r', \phi', L_1, t') \\ &\quad + \frac{\partial}{\partial z} \int_V dV' G(r, r', \phi, \phi', z, z', t) C_S(r', \phi', z', 0), \end{aligned} \quad (3.32)$$

where  $S_{L_2}$  and  $S_{L_1}$  denote the upper and lower faces of the cylinder, respectively.

We are integrating over the surfaces  $S_{L_2}$  and  $S_{L_1}$  and the volume  $V$  which are all constant, with respect to the primed variables,  $r', \phi'$  and  $z'$ , so we can rewrite equation (3.32) as [2]

$$\begin{aligned} \frac{\partial C_S}{\partial z} &= D_E \int_0^t dt' \int_{S_{L_2}} dS' \left( \frac{\partial}{\partial z} G(r, r', \phi, \phi', z, L_2, t') \right) J_{\text{SERCA}} \\ &\quad - D_E \int_0^t dt' \int_{S_{L_1}} dS' \left( \frac{\partial^2}{\partial z' \partial z} G(r, r', \phi, \phi', z, z', t') \right) \Big|_{z'=L_1} C_c(r', \phi', L_1, t') \\ &\quad + \int_V dV' \left( \frac{\partial}{\partial z} G(r, r', \phi, \phi', z, z', t) \right) C_S(r', \phi', z', 0). \end{aligned} \quad (3.33)$$

Here  $\partial G / \partial z$  and  $\partial^2 G / \partial z' \partial z$  are given by

$$\begin{aligned} \frac{\partial G}{\partial z} &= \frac{2}{\pi a^2 (L_2 - L_1)} \left[ \sum_{m=1}^M \mu_m \cos(\mu_m (L_2 - z')) \sin(\mu_m (L_2 - z)) e^{-D_S \mu_m^2 t} \right] \\ &\quad \times \sum_{k=1}^K \left( \frac{J_0(\beta_{0,k} r' / a) J_0(\beta_{0,k} r / a)}{J_0(\beta_{0,k})^2} e^{-D_S \left( \frac{\beta_{0,k}}{a} \right)^2 t} \right. \\ &\quad \left. + 2 \sum_{n=1}^N \frac{J_n(\beta_{n,k} r' / a) J_n(\beta_{n,k} r / a)}{J_n(\beta_{n,k})^2 \left( 1 - \frac{n^2}{\beta_{n,k}^2} \right)} \cos(n(\phi - \phi')) e^{-D_S \left( \frac{\beta_{n,k}}{a} \right)^2 t} \right), \end{aligned} \quad (3.34)$$

and

$$\begin{aligned}
\frac{\partial^2 G}{\partial z' \partial z} = & \frac{2}{\pi a^2 (L_2 - L_1)} \left[ \sum_{m=1}^M \mu_m \sin(\mu_m (L_2 - z')) \sin(\mu_m (L_2 - z)) e^{-D_S \mu_m^2 t} \right] \\
& \times \sum_{k=1}^K \left( \frac{J_0(\beta_{0,k} r' / a) J_0(\beta_{0,k} r / a)}{J_0(\beta_{0,k})^2} e^{-D_S \left(\frac{\beta_{0,k}}{a}\right)^2 t} \right. \\
& \left. + 2 \sum_{n=1}^N \frac{J_n(\beta_{n,k} r' / a) J_n(\beta_{n,k} r / a)}{J_n(\beta_{n,k})^2 \left(1 - \frac{n^2}{\beta_{n,k}^2}\right)} \cos(n(\phi - \phi')) e^{-D_S \left(\frac{\beta_{n,k}}{a}\right)^2 t} \right).
\end{aligned} \tag{3.35}$$

The integrals in equation 3.33 only depend on  $z$  through

$$\sin(\mu_m (L_2 - z))$$

in  $\partial G / \partial z$  and  $\partial^2 G / \partial z' \partial z$ . We evaluate these expressions and substitute  $z = L_2$  into equations (3.34) and (3.35) and we find that each term in the series is zero and thus,

$$\left. \frac{\partial G}{\partial z} \right|_{z=L_2} = 0, \quad \text{and} \quad \left. \frac{\partial^2 G}{\partial z' \partial z} \right|_{z=L_2} = 0. \tag{3.36}$$

The first integral is equal to zero on the surface  $z = L_2$ , and not equal to the  $\text{Ca}^{2+}$  influx across the boundary as prescribed by our boundary conditions. The second and third integrals are also equal to zero at  $z = L_2$ . Therefore,

$$\left. \frac{\partial C_S}{\partial z} \right|_{z=L_2} = 0, \tag{3.37}$$

demonstrating that the calcium concentration,  $C_S$ , does not satisfy the prescribed boundary condition at  $z = L_2$ . We plot the first integral of equation (3.31) in Figure 3.8(a) and observe a plume of elevated  $\text{Ca}^{2+}$  beneath the SERCA pump. However, when we check the gradient numerically in Figure 3.8(b) we observe that the gradient decreases to zero as the mesh size,  $\Delta z$ , is refined near  $L_2$ .

Similarly, we can check whether the  $\text{Ca}^{2+}$  concentration satisfies the boundary

condition at  $z = L_1$ . Substituting  $z = L_1$  into equation (3.31) results in

$$\begin{aligned}
C_S(r, \phi, L_1, t) = & \\
D_E \int_0^t dt' \int_0^{2\pi} \int_0^a r' dr' d\phi' G(r, r', \phi, \phi', L_1, L_2, t') J_{\text{SERCA}}(r', \phi') & \\
- D_E \int_0^t dt' \int_0^{2\pi} \int_0^a r' dr' d\phi' \left( \frac{\partial}{\partial z'} G(r, r', \phi, \phi', L_1, L_1, t') \right) C_c(r', \phi', L_1, t') & \\
+ \int_V dV' G(r, r', \phi, \phi', L_1, z', t) C_S(r', \phi', z', 0), & 
\end{aligned} \tag{3.38}$$

and we see from equations (3.30) and (3.34) that the Green's function and the partial derivative of the Green's function with respect to  $z$  only depend on  $z$  through

$$\cos(\mu_m(L_2 - z)).$$

When  $z = L_1$  then we know that

$$\cos(\mu_m(L_2 - L_1)) = 0, \tag{3.39}$$

and so

$$C_S(r, \phi, L_1, t) = 0$$

demonstrating that the  $\text{Ca}^{2+}$  concentration at  $z = L_1$  does not satisfy the prescribed Dirichlet boundary condition,  $C_S(r, \phi, L_1, t) = C_E(r, \phi, L_1, t)$

We have shown that the  $\text{Ca}^{2+}$  concentration,  $C_S$ , calculated using Barton's method does not appear to satisfy either boundary condition despite the  $\text{Ca}^{2+}$  plumes generated within the domain. However, this is very similar to example 9.4.2 in [8] as every term in the series vanished on the boundary thus appearing to fail to satisfy the prescribed boundary conditions. Barton shows that this occurs because sums of the form,

$$\sum_{n=1}^{\infty} \frac{\sin(n\theta)}{n},$$

are not uniformly convergent. Barton discusses methods which can overcome such problems where the solution appears not to satisfy the boundary conditions. However, the techniques involve making the solution more complicated and introducing additional approximations which we would like to avoid. We decided that Barton's method is not easily applicable to this PDE system and so ultimately we did not use this technique.

### 3.4 Felder's method

The standard analytical solution technique for PDEs, Barton's method, is not usefully applicable to our systems so we apply the method for solving PDEs discussed in [24], which we refer to as 'Felder's method'. This approach involves splitting the full solution,  $C(r, \phi, z, t)$ , into two solutions, a time independent solution,  $V(r, \phi, z)$ , solving the steady state PDE subject to the inhomogeneous boundary conditions and a time dependent solution,  $U(r, \phi, z, t)$ , solving the original PDE subject to homogeneous versions of the boundary conditions.

We have already calculated the solutions to the original PDE problems with homogeneous boundary conditions in the ER-PM junction and sub-PM ER when calculating the Green's function in each domain. These solutions are given by equations (3.19) and (3.28), respectively. The time independent solution obeys the steady state diffusion equation and two or three inhomogeneous boundary conditions, depending on the domain. We can apply the separation of variables technique provided we have only one inhomogeneous boundary condition. The time independent solution is then further split into separate solutions which solve the steady state PDE with only one inhomogeneous boundary condition. We sum these individual solutions to get the full solution to the steady state PDE with inhomogeneous boundary conditions. The time dependent solution and time independent solution are then added together to provide the full solution of the original PDE with inhomogeneous initial condition and boundary conditions.

The separation of variables technique is very similar to the method followed in sections 3.2.1 and 3.2.2. We solve for the time-independent solutions in this section so we first write the concentration as a function of each variable, e.g.  $C(r, \phi, z) = \rho(r)\theta(\phi)h(z)$ , and then derive a set of equations dependent on each variable. When calculating the Green's functions we imposed homogeneous versions of the boundary conditions and used the inhomogeneous initial condition to find the exact solution of each function,  $\rho(r)$ ,  $\theta(\phi)$  and  $h(z)$ ; now we will use the single inhomogeneous boundary condition to define each function and the overall solution.

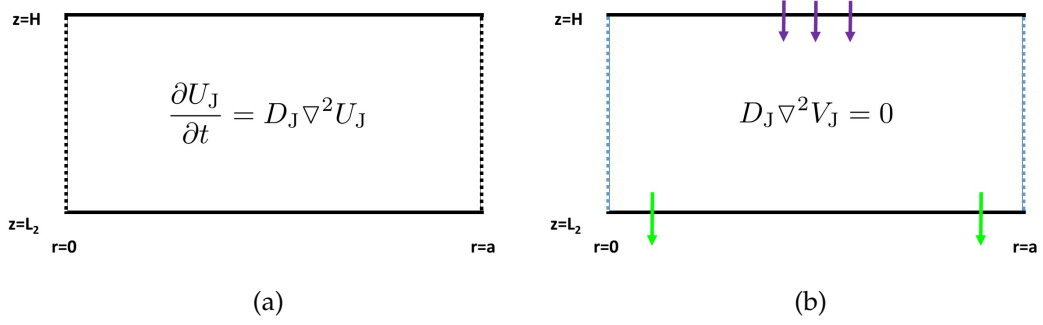


**Figure 3.9:** Illustration of the ER-PM junction boundary conditions satisfied by (a)  $U_J(r, \phi, z, t)$  and (b)  $V_J(r, \phi, z)$ , respectively. The solid black lines denote homogeneous von Neumann boundary conditions and the dashed black lines denote homogeneous Dirichlet boundary conditions. The purple and green arrows represent  $\text{Ca}^{2+}$  flux across the boundary through Orai channels and SERCA pumps, respectively. The dashed blue line represents the inhomogeneous Dirichlet boundary condition which matches the  $\text{Ca}^{2+}$  concentration on the boundary with the  $\text{Ca}^{2+}$  concentration in the bulk cytoplasm.

### 3.4.1 ER-PM junction

The  $\text{Ca}^{2+}$  concentration in the ER-PM junction,  $C_J$ , obeys the diffusion equation and boundary condition given in the previous chapter. We will solve the PDE system using Felder's method and split the solution into the solution of the diffusion equation with homogeneous boundary conditions,  $U_J = U_J(r, \phi, z, t)$ , as illustrated in Figure 3.9(a), and the steady state solution,  $V_J = V_J(r, \phi, z)$ , as illustrated in Figure 3.9(b), which satisfies the inhomogeneous boundary conditions.

We let

$$C_J = U_J + V_J, \quad (3.40)$$

and substitute into the original PDE to decompose the problem into two sub-problems. We now have the solution to the homogeneous problem governed by the diffusion equation,

$$\frac{\partial U_J}{\partial t} = D_J \nabla^2 U_J$$

with initial condition

$$U_{J,0} = C_{J,0} - V_J \quad (3.41)$$

and homogeneous von Neumann boundary conditions on the membranes,  $z = H$  and  $z = L_2$ , and homogeneous Dirichlet boundary condition on the mantle of the cylinder,  $r = a$ , which represents the non-physical boundary between

the ER-PM junction and bulk cytoplasm.

The steady state solution to the problem with the original boundary conditions satisfies the diffusion equation,

$$D_J \nabla^2 V_J = 0,$$

with the inhomogeneous boundary conditions,

$$\begin{aligned} D_J \frac{\partial V_J}{\partial z} \Big|_{z=H} &= J_{\text{Orai}}, \\ D_J \frac{\partial V_J}{\partial z} \Big|_{z=L_2} &= J_{\text{SERCA}}, \\ V_J \Big|_{r=a} &= C_C \Big|_{r=a}. \end{aligned}$$

We solved the homogeneous problem, equation (3.40), in section 3.2.1 when calculating the Green's function. Therefore, the solution to the homogeneous problem on the ER-PM junction is given by

$$U_J = \int_V dV' G_J(r, r', \phi, \phi', z, z', t) U_{J,0}, \quad (3.42)$$

where  $G_J$  is the Green's function in the ER-PM junction, given by equation (3.21).

To solve the steady state solution with inhomogeneous boundary conditions we split the problem into three sub problems, with only one inhomogeneous boundary condition each, allowing us to apply the separation of variables technique.

Each solution,  $V_{J,y}$ , for  $y \in \{1, 2, 3\}$  solves the steady state diffusion equation,

$$D_J \nabla^2 V_{J,y} = 0, \quad (3.43)$$

for each sub problem with boundary conditions as illustrated in Figures 3.10(a) - 3.10(c), respectively.

The first solution,  $V_{J,1}$ , solves the steady state diffusion equation (3.43) with the boundary conditions as illustrated in Figure 3.10(a). The only non-zero flux is through the Orai channels on the PM,  $z = H$ , denoted by the purple arrows. We impose a zero flux across the entire ER membrane,  $z = L_2$ , denoted by the solid black line along the ER membrane. The  $\text{Ca}^{2+}$  concentration at the edge

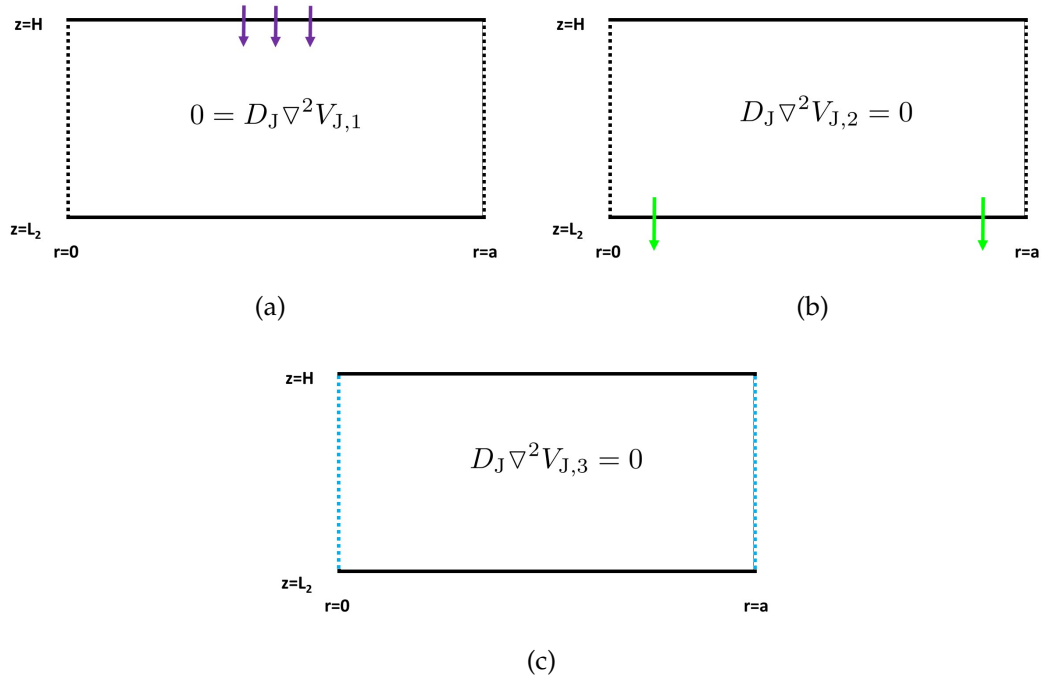


**Figure 3.10:** Illustration of the ER-PM junction boundary conditions satisfied by the steady state solutions (a)  $V_{J,1}(r, \phi, z)$ , (b)  $V_{J,2}(r, \phi, z)$  and (c)  $V_{J,3}(r, \phi, z)$ , respectively. The solid black lines denote homogeneous von Neumann boundary conditions and the dashed black lines denote homogeneous Dirichlet boundary conditions. The purple and green arrows represent  $\text{Ca}^{2+}$  flux across the boundary through Orai channels and SERCA pumps, respectively. The dashed blue line represents the inhomogeneous Dirichlet boundary condition which matches the  $\text{Ca}^{2+}$  concentration on the boundary with the  $\text{Ca}^{2+}$  concentration in the bulk cytoplasm.

of the ER-PM junction,  $r = a$ , is held at zero, denoted by the dashed black line along the mantle.

We let

$$V_{J,1} = \rho(r)\theta(\phi)h(z), \quad (3.44)$$

and apply the separation of variables technique by substituting equation (3.44) into the diffusion equation (3.43) to get the separated equations (B.1) - (B.3) in section B.1 of the Appendix. We can write the inhomogeneous boundary condition as

$$\left. \frac{\partial V_{J,1}}{\partial z} \right|_{z=H} = \bar{\rho}(r)\bar{\theta}(\phi)h'(H), \quad (3.45)$$

where  $\bar{\rho}$  and  $\bar{\theta}$  now represent the dependence of the inhomogeneous boundary condition on the  $r$  and  $\phi$  variables, respectively. We use the inhomogeneous boundary condition to solve the separated equations leading to the solutions given by equations (B.4) - (B.6) in section B.1 of the Appendix. We substitute the solutions of  $\rho(r)$ ,  $\theta(\phi)$  and  $h(z)$  into equation (3.44) to get the following solution for  $V_{J,1}$ ,

$$\begin{aligned} V_{J,1} = & \int_0^{2\pi} \int_0^a J_{\text{Orai}} r' dr' d\theta' \\ & \times \frac{1}{\pi a^2} \sum_{j=1}^J \left[ \frac{J_0(\alpha_{0,j} r'/a) J_0(\alpha_{0,j} r/a)}{J_1^2(\alpha_{0,j})} \frac{a}{\alpha_{0,j}} \frac{e^{-(H-z)\alpha_{0,j}/a} + e^{-(H+z-2L_2)\alpha_{0,j}/a}}{1 - e^{-2(H-L_2)\alpha_{0,j}/a}} \right. \\ & + 2 \sum_{n=1}^N \left( \frac{J_n(\alpha_{n,j} r'/a) J_n(\alpha_{n,j} r/a) \cos(n(\phi - \phi'))}{J_{n+1}^2(\alpha_{n,j})} \right. \\ & \left. \left. \frac{a}{\alpha_{n,j}} \frac{e^{-(H-z)\alpha_{n,j}/a} + e^{-(H+z-2L_2)\alpha_{n,j}/a}}{1 - e^{-2(H-L_2)\alpha_{n,j}/a}} \right) \right], \end{aligned} \quad (3.46)$$

which is illustrated in Figures 3.11(a) and 3.11(b). The  $\text{Ca}^{2+}$  concentration peaks at the  $z = H$  plane in Figure 3.11(a) and the plumes decrease further from the channel. A consequence of the small height of the ER-PM junction is that the  $\text{Ca}^{2+}$  concentration opposite the Orai channel on the ER membrane is already elevated after one time step, as shown in Figure 3.11(a). The small distance between the PM and ER membrane could enhance the  $\text{Ca}^{2+}$  diffusion to the SERCA pumps on the ER membrane, resulting in faster refilling of the sub-PM ER. In Figure 3.11(b), the  $\text{Ca}^{2+}$  concentration peaks at the Orai channel and forms a microdomain of high  $\text{Ca}^{2+}$  concentration around the channel. The  $\text{Ca}^{2+}$  concentration decreases near the boundary at the mantle of the cylinder

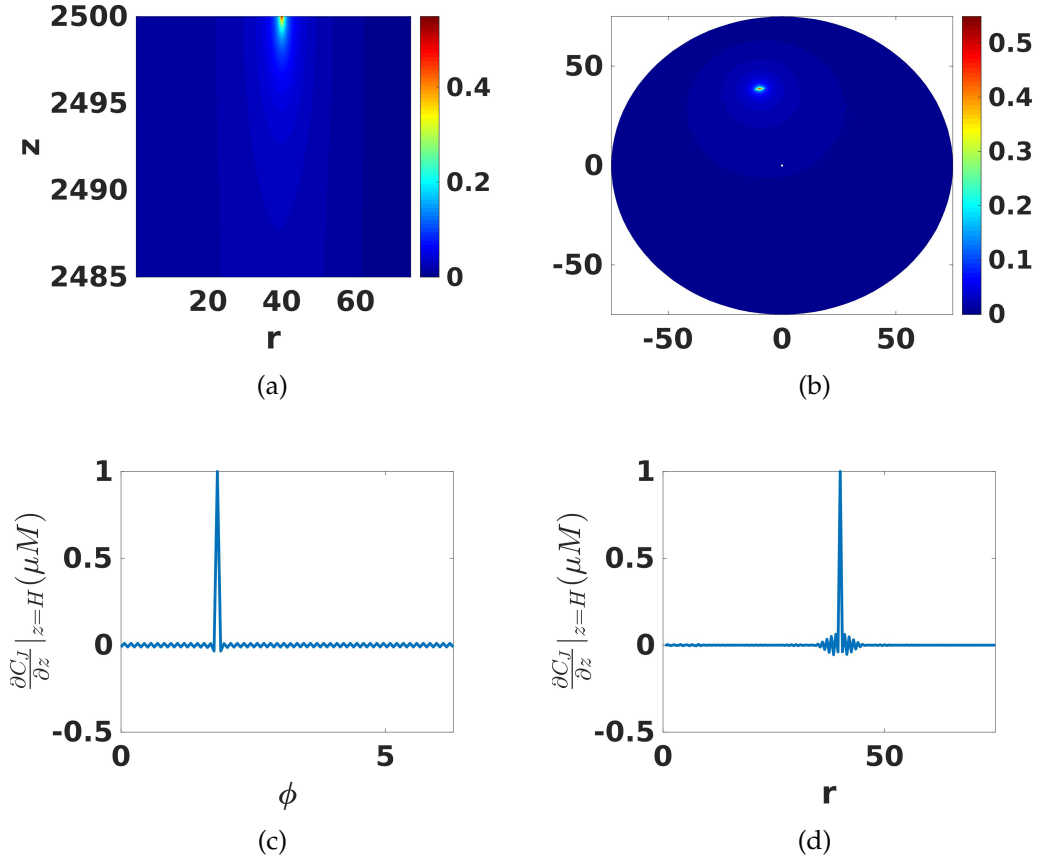


**Figure 3.11:** Simulation showing the solution to  $V_{J,1}$  in the (a)  $z$  and (b) polar directions. (c, d) show the gradient at the Orai channel in the  $\phi$  and  $r$  directions, respectively. Parameters:  $J=150$  and  $N=50$ .

which obeys a zero Dirichlet boundary condition thus breaking the symmetry of the governing equations.

We can check that the solution satisfies the boundary condition by differentiating with respect to  $z$  to get,

$$\begin{aligned}
\frac{\partial V_{J,1}}{\partial z} &= \int_0^{2\pi} \int_0^a J_{\text{Orai}} r' dr' d\theta' \\
&\times \frac{1}{\pi a^2} \sum_{j=1}^J \left[ \frac{J_0(\alpha_{0,j} r'/a) J_0(\alpha_{0,j} r/a) e^{-(H-z)\alpha_{0,j}/a} - e^{-(H+z-2L_2)\alpha_{0,j}/a}}{J_1^2(\alpha_{0,j})} \frac{1}{1 - e^{-2(H-L_2)\alpha_{0,j}/a}} \right. \\
&+ 2 \sum_{n=1}^N \left( \frac{J_n(\alpha_{n,j} r'/a) J_n(\alpha_{n,j} r/a) \cos(n(\phi - \phi'))}{J_{n+1}^2(\alpha_{n,j})} \right. \\
&\left. \left. \times \frac{e^{-(H-z)\alpha_{n,j}/a} - e^{-(H+z-2L_2)\alpha_{n,j}/a}}{1 - e^{-2(H-L_2)\alpha_{n,j}/a}} \right) \right].
\end{aligned}$$

We set  $z = H$  to check the gradient on the PM,

$$\begin{aligned} \frac{\partial V_{J,1}}{\partial z} \Big|_{z=H} &= \int_0^{2\pi} \int_0^a J_{\text{Orai}} r' dr' d\theta' \\ &\times \frac{1}{\pi a^2} \sum_{j=1}^J \left[ \frac{J_0(\alpha_{0,j} r'/a) J_0(\alpha_{0,j} r/a)}{J_1^2(\alpha_{0,j})} \right. \\ &\left. + 2 \sum_{n=1}^N \left( \frac{J_n(\alpha_{n,j} r'/a) J_n(\alpha_{n,j} r/a) \cos(n(\phi - \phi'))}{J_{n+1}^2(\alpha_{n,j})} \right) \right], \end{aligned}$$

and since,

$$\begin{aligned} \frac{\delta(r - r') \delta(\phi - \phi')}{r} &= \\ \frac{1}{\pi a^2} \sum_{j=1}^J &\left[ \frac{J_0(\alpha_{0,j} r'/a) J_0(\alpha_{0,j} r/a)}{J_1^2(\alpha_{0,j})} \right. \\ &\left. + 2 \sum_{n=1}^N \left( \frac{J_n(\alpha_{n,j} r'/a) J_n(\alpha_{n,j} r/a) \cos(n(\phi - \phi'))}{J_{n+1}^2(\alpha_{n,j})} \right) \right] \end{aligned} \quad (3.47)$$

the gradient becomes

$$\begin{aligned} \frac{\partial V_{J,1}}{\partial z} \Big|_{z=H} &= \int_0^{2\pi} \int_0^a J_{\text{Orai}} r' dr' d\theta' \frac{\delta(r - r') \delta(\phi - \phi')}{r'}, \\ &= J_{\text{Orai}}. \end{aligned}$$

We let  $J_{\text{Orai}}$  be the unit flux through an Orai channel and plot the gradient at the Orai channel in the  $r$  and  $\phi$  directions to see if the analytical gradient and numerical gradient agree. We can see in Figures 3.11(c) and 3.11(d) that the numerical gradient at the channel is 1 and zero otherwise, which agrees with the analytical gradient. We also see that there are small oscillations in the gradient near the channel, that are a result of numerically integrating over delta functions.

The second solution,  $V_{J,2}$ , solves the steady state diffusion equation given by (3.43) with the boundary conditions as illustrated in Figure 3.10(b). The only non-zero flux occurs across the SERCA pumps on the ER membrane,  $z = L_2$ , denoted by the green arrows. We impose a zero flux across the PM,  $z = H$ , denoted by the solid black line and fix the  $\text{Ca}^{2+}$  concentration at zero on the mantle of the ER-PM junction,  $r = a$ , as denoted by the dashed black line.

We let

$$V_{J,2} = \rho(r)\theta(\phi)h(z), \quad (3.48)$$

and apply the separation of variables technique by substituting equation (3.48) into the diffusion equation (3.43) to get the separated equations (B.7) - (B.9) in section B.2 of the Appendix. We can write the inhomogeneous boundary condition as

$$\left. \frac{\partial V_{J,2}}{\partial z} \right|_{z=L_2} = \bar{\rho}(r)\bar{\theta}(\phi)h'(L_2). \quad (3.49)$$

We use the inhomogeneous boundary condition to calculate the solutions of the separated equations, given by (B.10) - (B.12) in section B.2 of the Appendix. We substitute the solutions of  $\rho(r)$ ,  $\theta(\phi)$  and  $h(z)$  into equation (3.48) to get the following solution for  $V_{J,2}$ ,

$$\begin{aligned} V_{J,2} = & \int_0^{2\pi} \int_0^a J_{\text{SERCA}} r' dr' d\theta' \\ & \times \frac{1}{\pi a^2} \sum_{j=1}^J \left[ \frac{J_0(\alpha_{0,j} r'/a) J_0(\alpha_{0,j} r/a)}{J_1^2(\alpha_{0,j})} \frac{a}{\alpha_{0,j}} \frac{e^{-(2H-z-L_2)\alpha_{0,j}/a} + e^{-(z-L_2)\alpha_{0,j}/a}}{e^{-2(H-L_2)\alpha_{0,j}/a} - 1} \right. \\ & + 2 \sum_{n=1}^N \left( \frac{J_n(\alpha_{n,j} r'/a) J_n(\alpha_{n,j} r/a) \cos(n(\phi - \phi'))}{J_{n+1}^2(\alpha_{n,j})} \right. \\ & \left. \left. \frac{a}{\alpha_{n,j}} \frac{e^{-(2H-z-L_2)\alpha_{0,j}/a} + e^{-(z-L_2)\alpha_{0,j}/a}}{e^{-2(H-L_2)\alpha_{0,j}/a} - 1} \right) \right]. \end{aligned}$$

The solution,  $V_{J,2}$ , and gradient at the SERCA pumps, where  $J_{\text{SERCA}}$  is the unit flux through a SERCA pump, are illustrated in Figure 3.12. The solution is zero everywhere except at the SERCA pump, which is negative, because the SERCA pump removes  $\text{Ca}^{2+}$  from the ER-PM junction and transports it into the sub-PM ER. The steady state solution,  $V_{J,2}$ , is added on to the homogeneous solution,  $U_j$ , and other steady state solutions,  $V_{J,1}$  and  $V_{J,3}$ , so, although this solution is negative the overall solution is positive. We see in Figure 3.12(a) that there are a series of  $\text{Ca}^{2+}$  plumes, decreasing in strength further away from the SERCA pump so the SERCA pump is strongest near the ER membrane. In Figure 3.12(b) the  $\text{Ca}^{2+}$  plumes are very strong around the SERCA pump. The  $\text{Ca}^{2+}$  concentration is held at zero on the mantle of the cylinder, by the homogeneous Dirichlet boundary condition, and the  $\text{Ca}^{2+}$  profile ‘feels’ this boundary leading to the asymmetric shape of the  $\text{Ca}^{2+}$  plume. The  $\text{Ca}^{2+}$  microdomain created in response to the SERCA pump is spatially restricted as shown by the very concentrated peaks near the pump which drop off very quickly as we move away from the pump.

We can check that the solution satisfies the boundary condition by differenti-

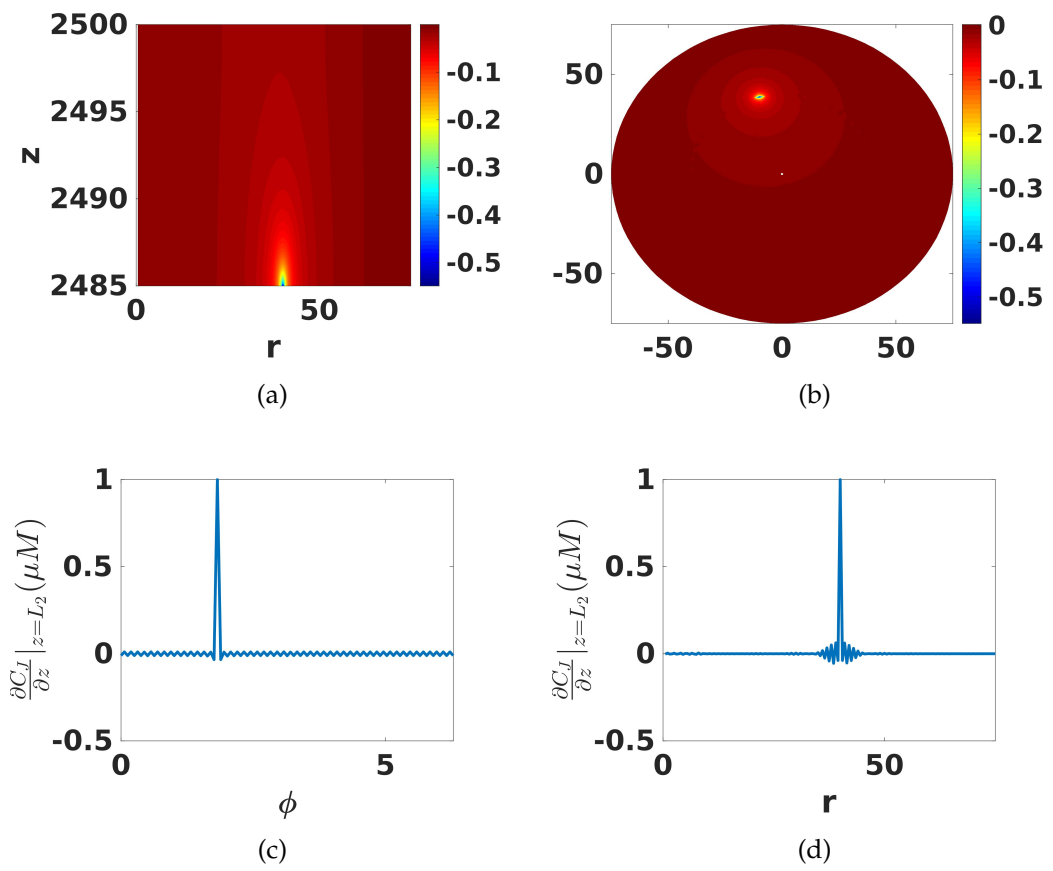


**Figure 3.12:** Simulation showing the solution to  $V_{J,2}$  in the (a)  $z$  and (b) polar directions. (c, d) show the gradient at the SERCA pump in the  $\phi$  and  $r$  directions, respectively. Parameters:  $J=150$  and  $N=50$ .

ating with respect to  $z$  to get

$$\begin{aligned} \frac{\partial V_{J,2}}{\partial z} &= \int_0^{2\pi} \int_0^a J_{\text{SERCA}} r' dr' d\theta' \\ &\times \frac{1}{\pi a^2} \sum_{j=1}^J \left[ \frac{J_0(\alpha_{0,j} r'/a) J_0(\alpha_{0,j} r/a) e^{-(H-z)\alpha_{0,j}/a} - e^{-(H+z-2L_2)\alpha_{0,j}/a}}{J_1^2(\alpha_{0,j})} \right. \\ &+ 2 \sum_{n=1}^N \left( \frac{J_n(\alpha_{n,j} r'/a) J_n(\alpha_{n,j} r/a) \cos(n(\phi - \phi'))}{J_{n+1}^2(\alpha_{n,j})} \right. \\ &\left. \left. \times \frac{e^{-(H-z)\alpha_{n,j}/a} - e^{-(H+z-2L_2)\alpha_{n,j}/a}}{1 - e^{-2(H-L_2)\alpha_{n,j}/a}} \right) \right], \end{aligned}$$

and setting  $z = L_2$  to check the gradient on the ER membrane we have

$$\begin{aligned} \left. \frac{\partial V_{J,2}}{\partial z} \right|_{z=L_2} &= \int_0^{2\pi} \int_0^a J_{\text{SERCA}} r' dr' d\theta' \\ &\times \frac{1}{\pi a^2} \sum_{j=1}^J \left[ \frac{J_0(\alpha_{0,j} r'/a) J_0(\alpha_{0,j} r/a)}{J_1^2(\alpha_{0,j})} \right. \\ &+ 2 \sum_{n=1}^N \left. \frac{J_n(\alpha_{n,j} r'/a) J_n(\alpha_{n,j} r/a) \cos(n(\phi - \phi'))}{J_{n+1}^2(\alpha_{n,j})} \right] \\ &= \int_0^{2\pi} \int_0^a J_{\text{SERCA}} r' dr' d\theta' \frac{\delta(r - r') \delta(\phi - \phi')}{r'} \\ &= J_{\text{SERCA}}. \end{aligned}$$

The numerical gradients, plotted in Figures 3.12(c) and 3.12(d), show that the gradient is 1 at the SERCA pump, as expected from the analytical calculation of the gradient. Again, there are small oscillations which occur because we are numerically integrating over delta functions.

The third solution,  $V_{J,3}$ , solves the steady state diffusion equation given by equation (3.43) with the boundary conditions as illustrated in Figure 3.10(c). We impose continuity of concentration, denoted by the blue dashed lines, at the mantle of the cylinder,  $r = a$ , to ensure that the  $\text{Ca}^{2+}$  concentration is not impeded when diffusing between the ER-PM junction and bulk cytoplasm. We impose zero flux across both the PM and ER membrane.

We let

$$V_{J,3} = \rho(r), \theta(\phi) h(z), \quad (3.50)$$

and apply the separation of variables technique by substituting equation (3.50) into the diffusion equation (3.43) to get the separated equations (B.13) - (B.15)

in section B.3 of the Appendix. We can write the inhomogeneous boundary condition as

$$V_{J,3}(a, \phi, z) = \rho(a)\bar{\theta}(\phi)\bar{h}, \quad (3.51)$$

where  $\bar{\theta}$  and  $\bar{h}$  represent the dependence of the inhomogeneous boundary condition on  $\phi$  and  $z$ . We use the inhomogeneous boundary condition to solve the individual separable equations leading to the solutions (B.16) - (B.18) in section B.3 of the Appendix. We substitute the solutions of  $\rho(r)$ ,  $\theta(\phi)$  and  $h(z)$  into equation (3.50) to get the following solution for  $V_{J,3}$ ,

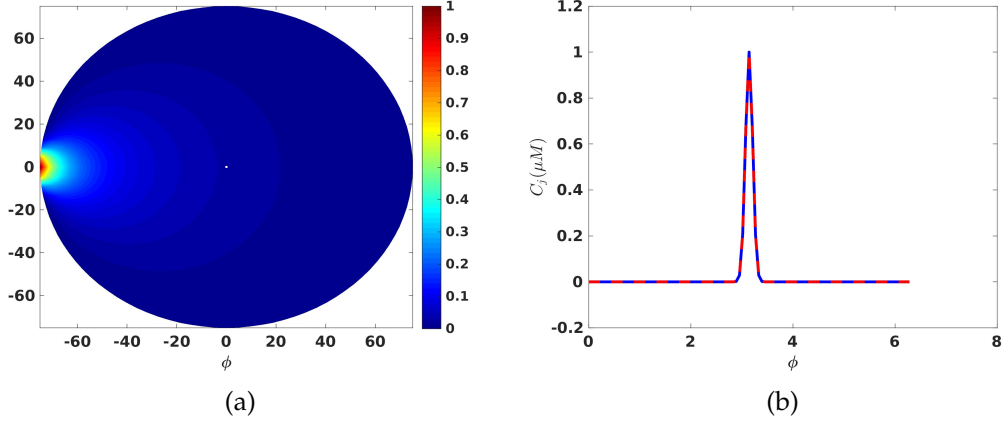
$$\begin{aligned} V_{J,3} = & \frac{1}{2\pi(H-L_2)} \int_0^{2\pi} \int_{L_2}^H d\phi' dz' C_c(a, \phi', z', t) \left[ 1 + 2 \sum_{n=1}^N \cos(n(\phi - \phi')) \left(\frac{r}{a}\right)^n \right. \\ & + 2 \sum_{m=1}^M \cos(\mu_m(z' - L_2)) \cos(\mu_m(z - L_2)) \\ & \left. \times \left( \frac{I_0(\mu_m r)}{I_0(\mu_m a)} + 2 \sum_{n=1}^N \frac{I_n(\mu_m r) \cos(n(\phi - \phi'))}{I_n(\mu_m a)} \right) \right]. \end{aligned}$$

Figure 3.13(a) is an illustration of the solution,  $V_{J,3}$ , at  $z = H$  and shows how the  $\text{Ca}^{2+}$  concentration spreads out along the  $r$  and  $\phi$  directions. We have imposed the boundary condition across the mantle,  $r = a$ , to be a  $\text{Ca}^{2+}$  peak at  $z = H$ , shown by the blue line in Figure 3.13(b), and we can see that the  $\text{Ca}^{2+}$  concentration decreases further from the mantle and the  $\text{Ca}^{2+}$  source at the mantle.

We can check the solution satisfies the boundary condition by substituting  $r = a$  into the full solution

$$\begin{aligned} V_{J,3}(r, \phi, z) = & \frac{1}{2\pi(H-L_2)} \int_0^{2\pi} \int_{L_2}^H d\phi' dz' C_c(a, \phi', z', t) \left[ 1 + 2 \sum_{n=1}^N \cos(n(\phi - \phi')) \right. \\ & \left. + 2 \sum_{m=1}^M \cos(\mu_m(z' - L_2)) \cos(\mu_m(z - L_2)) \left( 1 + 2 \sum_{n=1}^N \cos(n(\phi - \phi')) \right) \right], \\ = & \frac{1}{(H-L_2)} \int_0^{2\pi} \int_{L_2}^H d\phi' dz' C_c(a, \phi', z', t) \\ & \times \delta(\phi - \phi') \left[ 1 + 2 \sum_{m=1}^M \cos(\mu_m(z' - L_2)) \cos(\mu_m(z - L_2)) \right], \\ = & \int_0^{2\pi} \int_{L_2}^H d\phi' dz' C_c(a, \phi', z', t) \delta(\phi - \phi') \delta(z - z'), \\ = & C_c(a, \phi, z, t). \end{aligned}$$

In Figure 3.13(b) the blue line is the prescribed  $\text{Ca}^{2+}$  concentration at the man-



**Figure 3.13:** (s) Simulation of the solution,  $V_{J,3}$  in the polar direction. (b) The  $\text{Ca}^{2+}$  concentration at  $r = a$  (red dashed line) agrees with the prescribed Dirichlet boundary condition (solid blue line). Parameters:  $N=50$  and  $M=100$ .

tle of the cylinder at  $z = H$  and the red dashed line is the solution,  $V_{J,3}$ , at  $z = H$  when  $r = a$  which shows that the solution satisfies the boundary condition.

The mantle of the cylinder represents the interface between the ER-PM junction and the bulk cytoplasm so we ensure  $\text{Ca}^{2+}$  is able to diffuse freely across this boundary by prescribing the continuity of concentration and flux across the boundary. In the full four domain model, we solve the continuity of flux and continuity of concentration boundary conditions simultaneously. However, when solving the two domain model we only apply one boundary condition on this interface and, in this case, we have chosen to impose the continuity of concentration across the mantle of the cylinder and assumed that the calcium concentration is fixed at the baseline  $\text{Ca}^{2+}$  concentration,  $[\text{Ca}^{2+}]_i = 0.1\mu\text{M}$ . There is no biological reason for imposing our boundary conditions this way and switching the boundary conditions is also a valid option. However, the choice of boundary condition is subtle, but very important, and we will see that in our system we are limited to the original choice of boundary condition,  $C_j = C_C$  along the mantle of the cylinder. We examine the consequences of using the other arrangement of continuity boundary conditions by imposing a continuity of flux across the mantle of the cylinder,  $r = a$ , and considering the solution equivalent to  $V_{J,1}$ . We have a non-zero flux across the PM, zero flux across the ER membrane and zero flux along the mantle of the cylinder, instead of a zero Dirichlet boundary condition. Separation of variables will lead to equations (B.1) - (B.3) where  $\eta = \beta_{n,j}/a$  and  $\beta_{n,k}$  satisfies  $J'_n(\beta_{n,j}) = 0$  for  $j = 1, 2, \dots, J$ . Previously,  $\eta_{n,j} > 0$  for all  $n, j$  but now we have

a fully insulated system which admits a zero eigenvalue [8],  $\eta_{0,1} = 0$ , and so we have two solutions for equation (B.1). When  $\eta_{n,j} > 0$  we have the same solution as equation (B.4) but when  $\eta_{n,j} = 0$  we need to solve

$$h'' = 0,$$

subject to  $h'(H) = J_{\text{Orai}}$  and  $h'(L_2) = 0$ . The general solution is,

$$h(z) = A + Bz,$$

and the gradient will be given by,

$$h'(z) = B.$$

We cannot solve this equation since substituting in our boundary conditions would result in  $B = J_{\text{Orai}}$  and  $B = 0$  but we assume  $J_{\text{Orai}} \neq 0$ . So using flux boundary conditions at  $r = a$  leads to an insoluble equation and therefore we must choose the arrangement of continuity of flux and continuity of concentration boundary conditions carefully. Furthermore, Felder's method requires a steady state solution and if we have a sub-problem with an insulated domain and a constant flux through one point on the boundary then we will never reach a steady state. Therefore, having flux boundary conditions everywhere in the ER-PM will never admit a steady state solution in this particular situation so we must be careful to choose our boundary conditions so that the domain has a steady state solution.

To solve the diffusion equation in the ER-PM junction we combine the solution of the homogeneous problem and the steady state solution as follows,

$$\begin{aligned} C_J &= U_J + V_J \\ &= \int_V dV' G_J(r, r', \phi, \phi', z, z', t) U_{J,0} + V_J \\ &= \int_V dV' G_J(r, r', \phi, \phi', z, z', t) (C_{J,0} - V_J) + V_J, \end{aligned} \quad (3.52)$$

where  $V_J = V_{J,1} + V_{J,2} + V_{J,3}$  and  $U_{J,0}$  is given by equation (3.41). Then  $C_J$  is the solution to the full system which satisfies the original diffusion equation, initial condition and boundary conditions.

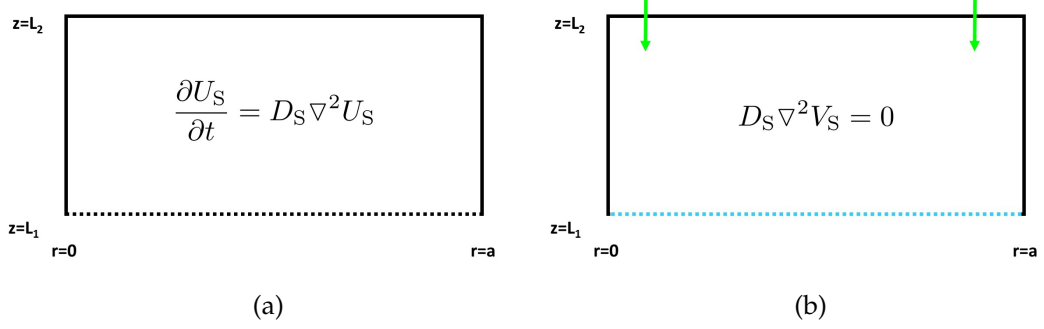


**Figure 3.14:** Illustration of the sub-PM ER boundary conditions satisfied by (a)  $U_S(r, \phi, z, t)$  and (b)  $V_S(r, \phi, z)$ , respectively. The solid black lines denote homogeneous von Neumann boundary conditions and the dashed black lines denote homogeneous Dirichlet boundary conditions. The green arrows represent  $\text{Ca}^{2+}$  flux across the boundary SERCA pumps. The dashed blue line represents the inhomogeneous Dirichlet boundary condition.

### 3.4.2 Sub-PM ER

We use the same approach as we did in the ER-PM junction and split the solution,  $C_S$ , into two sub solutions,  $U_S = U_S(r, \phi, z, t)$  which satisfies the original diffusion equation with homogeneous versions of the boundary conditions, illustrated in Figure 3.14(a), and  $V_S = V_S(r, \phi, z)$  which satisfies the steady state diffusion equation with the original boundary conditions, illustrated in Figure 3.14(b).

We let

$$C_S = U_S + V_S,$$

and substitute this into the original diffusion equation and decompose the problem into two sub problems. We have already calculated the solution to the original diffusion equation with homogeneous boundary conditions when we found our Green's functions so we have the solution to the diffusion equation,

$$\frac{\partial U_S}{\partial t} = D_S \nabla^2 U_S, \quad (3.53)$$

with initial condition

$$U(r, \phi, z, 0) = C(r, \phi, z, 0) - V_S, \quad (3.54)$$

which obeys homogeneous von Neumann boundary conditions on the ER membrane,  $z = L_2$  and  $r = a$ , and homogeneous Dirichlet boundary condition on  $z = L_1$ , which represents the non-physical boundary between the sub-PM

ER and bulk ER.

The steady state solution,  $V_S$ , satisfies the diffusion equation,

$$D_S \nabla^2 V_S = 0, \quad (3.55)$$

subject to the boundary conditions,

$$\begin{aligned} D_S \frac{\partial V_S}{\partial z} \Big|_{z=L_2} &= J_{\text{SERCA}}, \\ D_S \frac{\partial V_S}{\partial r} \Big|_{r=a} &= 0, \\ V_S(r, \phi, L_1, t) &= C_e(r, \phi, L_1, t), \end{aligned}$$

where  $J_{\text{SERCA}}$  denotes the  $\text{Ca}^{2+}$  influx through a SERCA pump at position  $(r_{\text{SERCA}}, \phi_{\text{SERCA}})$  on the ER membrane. We impose the continuity of concentration at the interface between the sub-PM ER and bulk ER,  $z = L_1$ , by setting the  $\text{Ca}^{2+}$  concentration at the bottom of the cylinder,  $V_S(r, \phi, L_1, t)$ , to be equal to the  $\text{Ca}^{2+}$  concentration at the top of the bulk ER,  $C_e(r, \phi, L_1, t)$ . We have already solved the homogeneous problem, equation (3.53), in section 3.2.2 where we calculated the Green's function as we found the solution of the original PDE with homogeneous versions of the boundary conditions. Therefore, the solution to the homogeneous problem on the sub-PM ER is given by

$$U_S = \int_V dV' G_S(r, r', \phi, \phi', z, z', t) U_{S,0}, \quad (3.56)$$

where  $G_S$  is the Green's function in the ER-PM junction, given by equation (3.30).

There are two inhomogeneous boundary conditions so we split the solution,  $V_S$ , into two sub problems which solve the steady state version of the PDE with only one inhomogeneous boundary condition, allowing us to apply the separation of variables technique.

Each solution,  $V_{S,y}$ , for  $y \in \{1, 2\}$  solves the steady state diffusion equation,

$$D_S \nabla^2 V_{S,y} = 0, \quad (3.57)$$

for each sub problem with boundary conditions as illustrated in Figure 3.15.

First we consider the steady state solution to the diffusion equation given in equation (3.57) with the boundary conditions as illustrated in Figure 3.15(a).

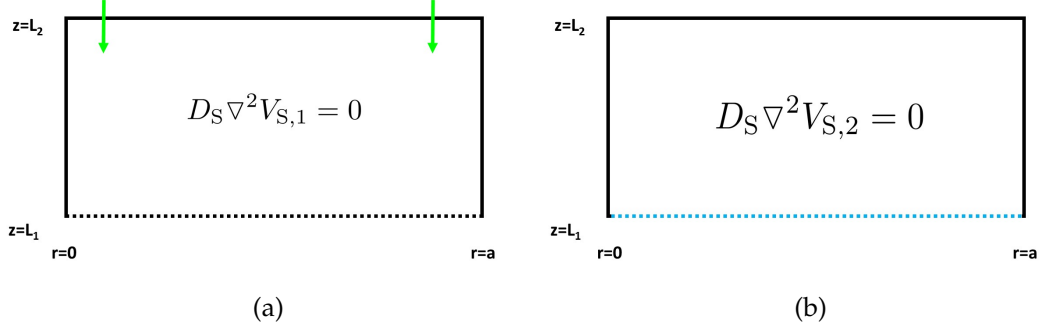


**Figure 3.15:** Illustration of the sub-PM ER boundary conditions satisfied by the steady state solutions (a)  $V_{S,1}(r, \phi, z)$  and (b)  $V_{S,2}(r, \phi, z)$ . The solid black lines denote homogeneous von Neumann boundary conditions and the dashed black lines denote homogeneous Dirichlet boundary conditions. The green arrows represent  $\text{Ca}^{2+}$  flux across the boundary through SERCA pumps. The dashed blue line represents the inhomogeneous Dirichlet boundary condition which matches the  $\text{Ca}^{2+}$  concentration on the boundary with the  $\text{Ca}^{2+}$  concentration in the bulk ER.

The only non-zero flux occurs through SERCA pumps on the ER membrane, denoted by green arrows, and the rest of the ER membrane is zero flux as shown by the solid black lines. We impose continuity of concentration boundary conditions at  $z = L_1$  so we fix the  $\text{Ca}^{2+}$  concentration to zero here, shown by the dashed black lines. We let

$$V_{S,1} = \rho(r)\theta(\phi)h(z), \quad (3.58)$$

and apply the separation of variables technique by substituting equation (3.58) into the diffusion equation (3.57) to get the separated equations (C.1) - (C.3) in section C.1 of the Appendix. We can write the inhomogeneous boundary condition as

$$\left. \frac{\partial V_{S,1}}{\partial z} \right|_{z=L_2} = \bar{\rho}(r)\bar{\theta}(\phi)h'(L_2), \quad (3.59)$$

where  $\bar{\rho}$  and  $\bar{\theta}$  now represent the dependence of the inhomogeneous boundary condition on the  $r$  and  $\phi$  variables, respectively. We use the inhomogeneous boundary condition to solve the separated equations leading to the solutions (C.4) - (C.6) in section C.1 of the Appendix. We substitute the solutions of  $\rho(r)$ ,

$\theta(\phi)$  and  $h(z)$  into equation (3.58) to get the following solution for  $V_{S,1}$ ,

$$\begin{aligned}
V_{S,1} = & \frac{1}{\pi a^2} \int_0^{2\pi} \int_0^a r' d' d\phi' J_{\text{SERCA}} [z - L_1 \\
& + \sum_{j=2}^J \frac{J_0(\beta_{0,j} r'/a) J_0(\beta_{0,j} r/a)}{J_0^2(\beta_{0,j})} \frac{a}{\beta_{0,j}} \frac{e^{\beta_{0,j}(z-L_2)/a} - e^{-\beta_{0,j}(z+L_2-2L_1)/a}}{1 + e^{-2\beta_{0,j}(L_2-L_1)/a}} \\
& + 2 \sum_{j=1}^J \sum_{n=1}^N \frac{J_n(\beta_{n,j} r'/a) J_n(\beta_{n,j} r/a) \cos(n(\phi - \phi'))}{J_n^2(\beta_{n,j}) (1 - (n/\beta_{n,j})^2)} \frac{a}{\beta_{n,j}} \\
& \times \frac{e^{\beta_{n,j}(z-L_2)/a} - e^{-\beta_{n,j}(z+L_2-2L_1)/a}}{1 + e^{-2\beta_{n,j}(L_2-L_1)/a}} \Big].
\end{aligned}$$

In Figure 3.16(a) the  $\text{Ca}^{2+}$  plumes around the SERCA pump in the sub-PM ER appear more concentrated in the  $z$  direction than in the ER-PM junction. This is because the height of the sub-PM ER is approximately 32 times larger than the height of the ER-PM junction, so although the  $\text{Ca}^{2+}$  plumes extend to similar distances this is difficult to see because of the different length scales. In the sub-PM ER we have imposed no flux boundary conditions around the mantle of the cylinder so that  $\text{Ca}^{2+}$  entering the domain from the SERCA pump can only filter down towards the bulk ER. The  $\text{Ca}^{2+}$  profile is higher near the ER membrane as a result of the  $\text{Ca}^{2+}$  influx through SERCA pumps leading to a  $\text{Ca}^{2+}$  gradient to ensure  $\text{Ca}^{2+}$  diffuses down towards the bulk ER, as seen in Figure 3.16(b). The no flux boundary condition on the mantle of the cylinder also affect the shape of the  $\text{Ca}^{2+}$  microdomain, as shown in Figure 3.16(c). The elevated  $\text{Ca}^{2+}$  at the edge of the microdomain will reach the mantle of the cylinder ( $r = a$ ), encounter the ER membrane, which obeys the no flux boundary condition, and reflect back into the cylinder. This increases the  $\text{Ca}^{2+}$  concentration near the boundary and interferes with the symmetric spread of  $\text{Ca}^{2+}$  from the SERCA pump.

We can check that this solution satisfies the inhomogeneous boundary condi-

tion,

$$\begin{aligned}
\left. \frac{\partial V_{S,1}}{\partial z} \right|_{z=L_2} &= \frac{1}{\pi a^2} \int_0^{2\pi} \int_0^a r' d' d\phi' J_{\text{SERCA}} \left[ 1 + \sum_{j=2}^J \frac{J_0(\beta_{0,j} r'/a) J_0(\beta_{0,j} r/a)}{J_0^2(\beta_{0,j})} \right. \\
&\quad \left. + 2 \sum_{j=1}^J \sum_{n=1}^N \frac{J_n(\beta_{n,j} r'/a) J_n(\beta_{n,j} r/a) \cos(n(\phi - \phi'))}{J_n^2(\beta_{n,j}) (1 - (n/\beta_{n,j})^2)} \right] \\
&= \frac{1}{\pi a^2} \int_0^{2\pi} \int_0^a r' d' d\phi' J_{\text{SERCA}} \left[ \frac{\delta(r - r')}{r'} + 2 \sum_{n=1}^N \frac{\delta(r - r')}{r'} \cos(n(\phi - \phi')) \right] \\
&= \frac{1}{\pi a^2} \int_0^{2\pi} \int_0^a r' d' d\phi' J_{\text{SERCA}} \frac{\delta(r - r') \delta(\phi - \phi')}{r'} \\
&= J_{\text{SERCA}}.
\end{aligned}$$

Again, if  $J_{\text{SERCA}}$  is a unit flux through a SERCA pump and we numerically calculate the gradient at the SERCA pump on the ER membrane, we have the gradients given in Figures 3.16(d) and 3.16(e). The numerical gradients show that the gradient is 1 at the SERCA pump and approximately zero elsewhere, as expected. The oscillations are a result of numerically integrating delta functions.

Had we included the continuity of flux boundary condition at  $z = L_1$  then we would have had an insoluble equation for  $h(z)$ , as discussed above, so the choice of boundary condition for continuity of flux and concentration is not arbitrary.

The second solution,  $V_{S,2}$ , solves the steady state diffusion equation (3.57) according to the boundary conditions given in Figure 3.15(b). We impose the continuity of concentration boundary condition at  $z = L_1$ , between the sub-PM ER and bulk ER, as denoted by the dashed blue lines. The solid black lines along the ER membrane denote the zero flux boundary conditions applied here.

We let

$$V_{S,2} = \rho(r)\theta(\phi)h(z), \quad (3.60)$$

and apply the separation of variables technique by substituting equation (3.60) into the diffusion equation (3.57) to get the separated equations (C.7) - (C.9) in section C.2 of the Appendix. We can write the inhomogeneous boundary condition as

$$V_{S,2}(r, \phi, L_1) = \bar{\rho}(r)\bar{\theta}(\phi)h(L_1), \quad (3.61)$$

where  $\bar{\rho}$  and  $\bar{\theta}$  represent the dependence of the inhomogeneous boundary con-

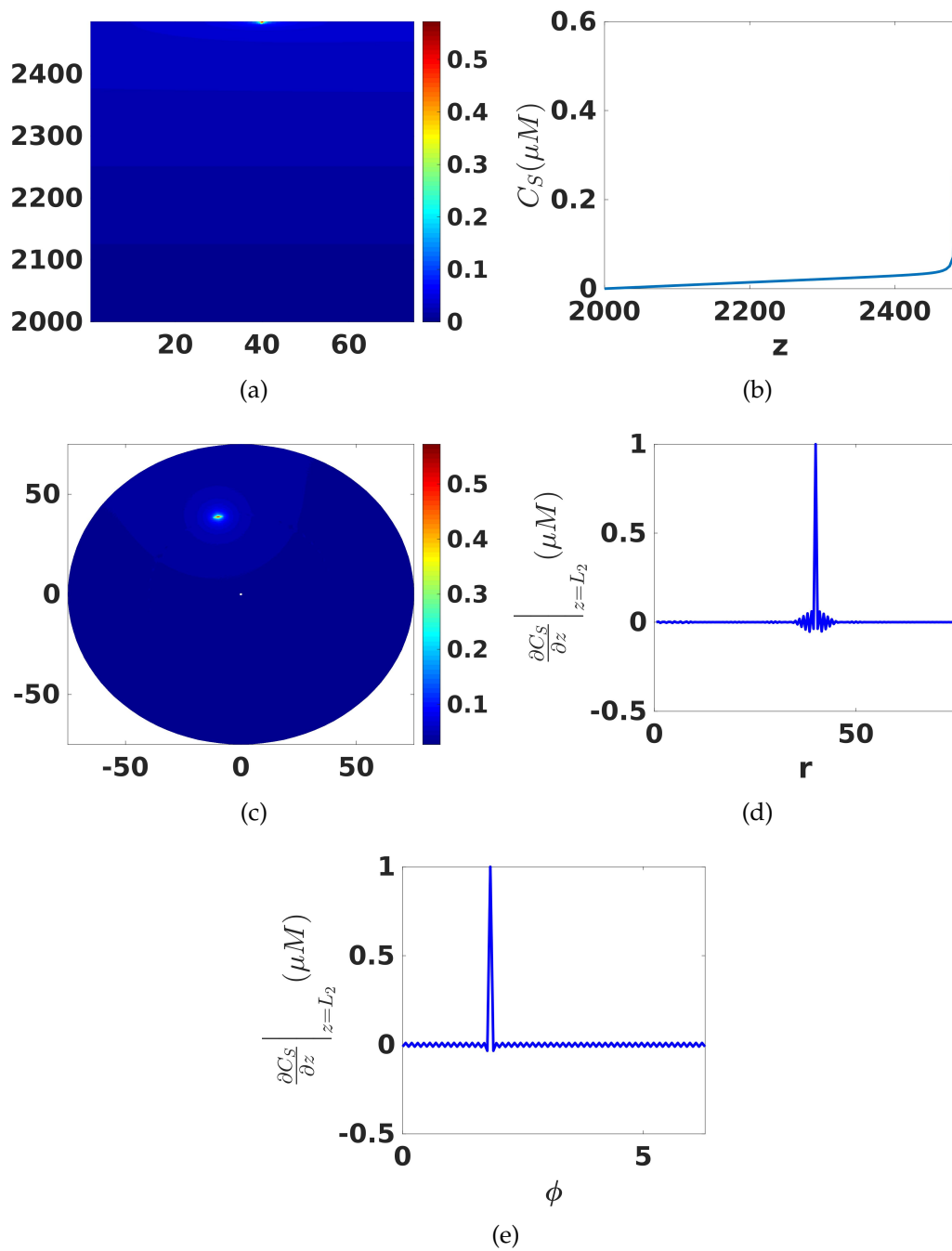


**Figure 3.16:** Simulation showing the solution,  $V_{S,1}$  in the (a)  $z$  direction, (b)  $z$  direction directly beneath the SERCA pump and (c) polar direction. (d, e) show the gradient at the SERCA pumps in the  $r$  and  $\phi$  directions. Parameters:  $J=150$  and  $N=50$ .

dition on  $r$  and  $\phi$ , respectively. We use the inhomogeneous boundary condition to solve the separated equations resulting in the solutions (C.10) - (C.12) in section C.2 of the Appendix. We substitute the solutions of  $\rho(r)$ ,  $\theta(\phi)$  and  $h(z)$  into equation (3.60) to get the following solution for  $V_{S,2}$ ,

$$\begin{aligned}
V_{S,2} = & \frac{1}{\pi a^2} \int_0^{2\pi} \int_0^a r' d' d\phi' C_e(r, \phi, L_1, t) [1 \\
& + \sum_{j=2}^J \frac{J_0(\beta_{0,j} r'/a) J_0(\beta_{0,j} r/a)}{J_0^2(\beta_{0,j})} \frac{e^{\beta_{0,j}(z+L_1-2L_2)/a} + e^{-\beta_{0,j}(z-L_1)/a}}{1 + e^{-2\beta_{0,j}(L_2-L_1)/a}} \\
& + 2 \sum_{j=1}^J \sum_{n=1}^N \frac{J_n(\beta_{n,j} r'/a) J_n(\beta_{n,j} r/a) \cos(n(\phi - \phi'))}{J_n^2(\beta_{n,j}) (1 - (n/\beta_{n,j})^2)} \\
& \left. \frac{e^{\beta_{n,j}(z+L_1-2L_2)/a} + e^{-\beta_{n,j}(z-L_1)/a}}{1 + e^{-2\beta_{n,j}(L_2-L_1)/a}} \right].
\end{aligned}$$

The distance between the top of the ER membrane,  $z = L_2$ , and the gap between the sub-PM ER and bulk ER,  $z = L_1$ , is quite large so we assume that the  $\text{Ca}^{2+}$  concentration at the bottom of the sub-PM ER cylinder has equilibrated and is constant across the whole face,  $C_e \Big|_{z=L_1} = \tilde{C}_e$ . This means that we assume the structured  $\text{Ca}^{2+}$  profile has diffused into a homogeneous distribution near the bulk ER. Then, because we are integrating over a constant function,

$$\int_0^{2\pi} \cos(n(\phi - \phi')) = 0,$$

and by the orthogonality of Bessel functions [7],

$$\int_0^a \sum_{j=2}^J J_0(\beta_{0,j} r'/a) J_0(\beta_{0,j} r/a) r' dr' = 0,$$

so the solution is reduced to,

$$V_{S,2}(r, \phi, z) = \tilde{C}_e,$$

which clearly satisfies the boundary conditions.

To solve the diffusion equation in the sub-PM ER we combine the solution of

the homogeneous problem and the steady state solution as follows,

$$\begin{aligned}
C_S &= U_S + V_S \\
&= \int_V dV' G_S(r, r', \phi, \phi', z, z', t) U_{S,0} + V_S \\
&= \int_V dV' G_S(r, r', \phi, \phi', z, z', t) (C_{S,0} - V_S) + V_S,
\end{aligned} \tag{3.62}$$

where  $V_S(r, \phi, z) = V_{S,1}(r, \phi, z) + V_{S,2}(r, \phi, z)$  and  $U_{S,0} = C_{S,0} - V_S$ . Then  $C_S(r, \phi, z, t)$  is the solution to the original diffusion equation and boundary conditions.

### 3.5 Numerical challenges

To simulate SOCE and diffusion within each domain we solve the diffusion equations semi-analytically and implement the solution in MATLAB. When simulating diffusion in the sub-PM ER we noticed that there were depletions around the centre of the cylinder even though there were no sinks present in the system.

To understand what caused these errors we considered the sub-PM ER with homogeneous versions of the boundary conditions, illustrated in Figure 3.14(a), and a flat initial  $\text{Ca}^{2+}$  profile,  $C_{S,0} = 1\mu\text{M}$ . We evaluated equation (3.62) and expected the flat  $\text{Ca}^{2+}$  profile to remain unchanged by the integral as there are no  $\text{Ca}^{2+}$  sources or sinks in the cylinder and the boundary conditions are homogeneous which prevents  $\text{Ca}^{2+}$  influx/efflux. However, the integral still generated areas of depleted  $\text{Ca}^{2+}$  in the centre of the cylinder, as seen in Figure 3.17. To understand what causes the dips even when we have a flat initial condition we considered each aspect of the volume integral in equation (3.62) separately. We discovered that the integral over the radial terms,

$$\sum_{j=1}^{\infty} \int_0^a \frac{2J_n(\beta_{n,j}r/a) J_n(\beta_{n,j}r'/a) e^{-\beta_{n,j}^2 t}}{a^2 (1 - (n/\beta_{n,j})^2) J_n^2(\beta_{n,j})} C_{S,0} r' dr', \tag{3.63}$$

was not integrating to  $C_{S,0}$  as we expected. Bessel functions are orthogonal in  $n$  and obey the following orthogonality condition [7]

$$\int_0^a \frac{2J_n(\beta_{n,j}r/a) J_n(\beta_{n,k}r/a)}{a^2 (1 - (n/\beta_{n,j})^2) J_n^2(\beta_{n,k})} r dr = \delta_{j,k}. \tag{3.64}$$

When  $n = 0$  we have a zero eigenvalue,  $\beta_{0,1} = 0$ , and if we set  $k = 1$  the

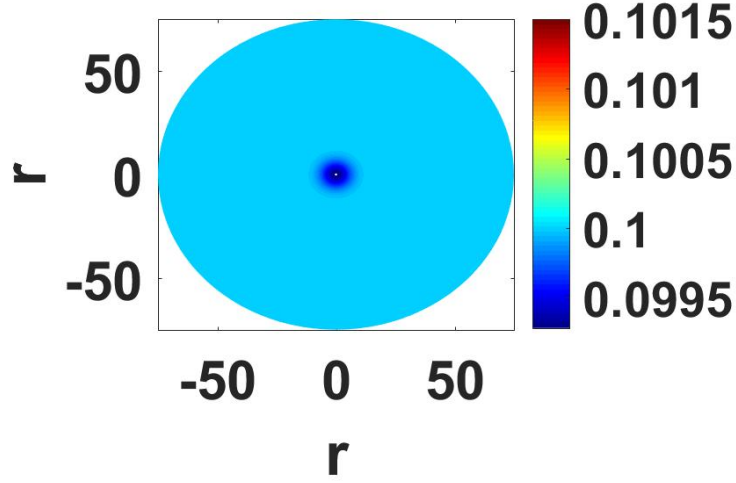


**Figure 3.17:** Diffused  $\text{Ca}^{2+}$  concentration in the sub-PM ER after one time step with a constant initial condition,  $C_{S,0} = 0.1\mu\text{M}$ .

orthogonality condition becomes

$$\int_0^a \frac{2J_0(\beta_{0,j}r/a)}{a^2} r dr = \delta_{j,1}. \quad (3.65)$$

Therefore,

$$\int_0^a J_0(\beta_{0,j}r/a) r dr = 0 \quad \text{when } j \neq 1, \quad (3.66)$$

is a special case of the orthogonality relation.

We evaluated equation (3.66) numerically and found that MATLAB was unable to evaluate the expression correctly<sup>1</sup>. In Figure 3.18 we compare the analytical and numerical evaluations of equation (3.63). The blue solid line represents the analytical solution and the red dashed line represents the numerical evaluation. The numerical error near  $r = 0$  occurs when evaluating equation (3.63) with  $C_{S,0} = 1$  and  $n = 0$  as MATLAB does not evaluate the orthogonality condition, equation (3.66), correctly. However, MATLAB is able to evaluate equation (3.63) correctly when  $C_{S,0}$  is a non-constant function of  $r$ . We therefore split all the concentrations in our integrals into a constant concentration,  $\bar{C}$ , and a non-constant concentration,  $\Delta C$ , so the overall concentration can be written as

$$C_{S,0} = \bar{C} + \Delta C, \quad (3.67)$$

<sup>1</sup>We contacted Mathworks to inquire about this feature and they acknowledged the problem with the software but were unable to fix the bug.

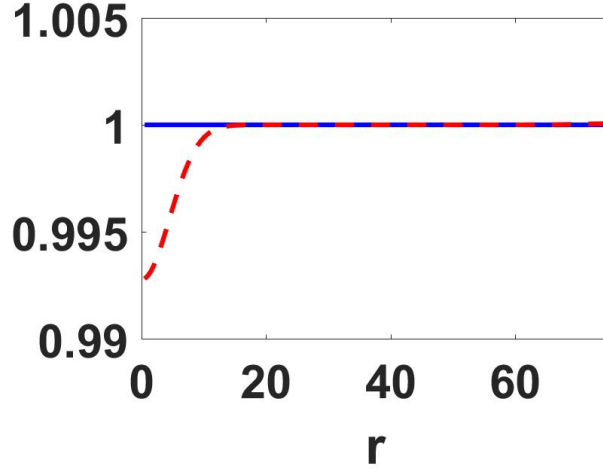


**Figure 3.18:** Analytical and numerical evaluations of equation (3.63) in solid blue and dashed red lines, respectively.  $C_{S,0} = 1\mu\text{M}$ .

with  $\Delta C$  having minimal support. We can substitute equation (3.67) into equation (3.62) to get

$$C_S = \int_V dV' G_S(r, r', \phi, \phi', z, z', t) (C_{S,0} - V_S) + V_S, \quad (3.68)$$

$$= \int_V dV' G_S(r, r', \phi, \phi', z, z', t) (\bar{C} + \Delta C - V_S) + V_S,$$

$$= \bar{C} + \int_V dV' G_S(r, r', \phi, \phi', z, z', t) (\Delta C - V_S) + V_S, \quad (3.69)$$

which we can now evaluate numerically. This procedure is illustrated in Figure 3.19. Figures 3.19(a) and 3.19(c) depict  $C$  and  $\Delta C$ , respectively, where  $\Delta C$  has minimal support when  $\bar{C} = 0.1\mu\text{M}$ . Figures 3.19(b) and 3.19(d) show the  $\text{Ca}^{2+}$  profiles calculated according to equations (3.68) and (3.69). The constant concentrations present in the initial condition of Figure 3.19(a) lead to the depleted  $\text{Ca}^{2+}$  in the dark blue regions of Figure 3.19(b). However, when using the splitting technique and evaluating equation (3.69) where we have evaluated the constant  $\text{Ca}^{2+}$  concentration analytically we calculate the  $\text{Ca}^{2+}$  concentration profile of Figure 3.19(d) which shows the  $\text{Ca}^{2+}$  peak diffusing radially as expected with no regions of depleted  $\text{Ca}^{2+}$  concentration.

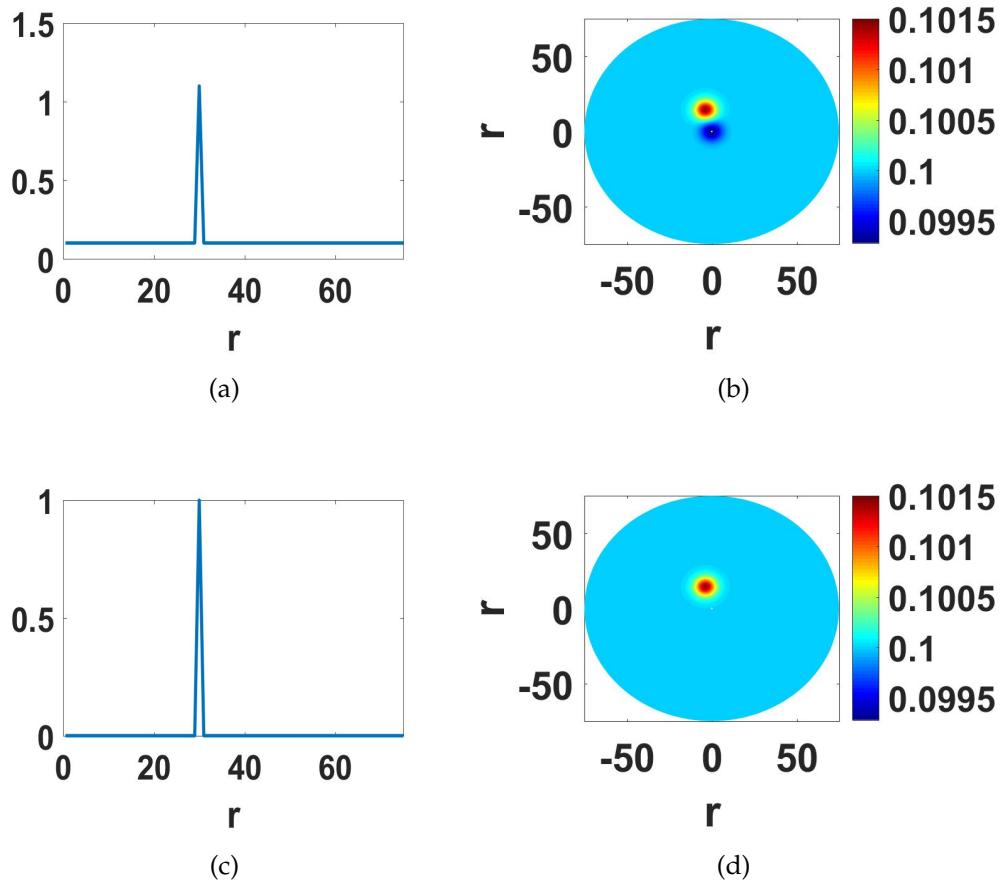


**Figure 3.19:** (a) Point source initial condition with a constant base  $\text{Ca}^{2+}$  concentration of  $0.1\mu\text{M}$  and a peak at  $r = 30\text{nm}$  of  $1\mu\text{M}$ . (b)  $\text{Ca}^{2+}$  concentration after evaluation of equation (3.68) in MATLAB with point source initial condition given in (a). (c) Using equation (3.67) we split the point source in (a) into a constant concentration  $\bar{C} = 0.1\mu\text{M}$  and the non-constant concentration  $\Delta C$  shown in (c). (d)  $\text{Ca}^{2+}$  concentration after evaluation of equation (3.69) in MATLAB with point source initial condition given in (a) and  $\bar{C} = 0.1\mu\text{M}$  removed to give  $\Delta C$  in (c).

### 3.6 Discussion

In Chapter 2 we created a spatio-temporal mathematical model describing the  $\text{Ca}^{2+}$  dynamics in a region of the cell during SOCE. The model is comprised of a system of diffusion equations and boundary conditions, summarised in Figure 2.6. We decided to use an analytical approach to solve the  $\text{Ca}^{2+}$  concentration within the domains and to approximate the evolution of the  $\text{Ca}^{2+}$  concentration in the domains over time. To approximate the temporal evolution of the  $\text{Ca}^{2+}$  concentration we time step the solution and calculate the  $\text{Ca}^{2+}$  concentration at the  $i^{\text{th}}$  time step,  $C_{x,i}$ , by propagating the diffusion of the  $\text{Ca}^{2+}$  concentration of the previous time step,  $C_{x,i-1}$ , including the effect of the boundary conditions during each iteration. We assume the time step,  $dt$ , is sufficiently small that the discretised temporal solution is a good approximation to the continuous  $\text{Ca}^{2+}$  evolution of the system.

Barton's method [8] is a standard analytical technique for solving PDEs with inhomogeneous boundary conditions analytically. We solved our PDE model according to Barton's method but discovered that, despite observing  $\text{Ca}^{2+}$  plumes around the  $\text{Ca}^{2+}$  influx site, the numerical solution did not satisfy the boundary conditions. This was supported by the analytical calculation of the gradient which is also zero. Barton highlights an example in [8] where the solution appears to violate the boundary condition because the series is not uniformly convergent and mentions that this method may not always be the most efficient method to calculate the solution.

We applied Felder's solution method [24] which involves splitting the overall solution into two sub-solutions, one that solved the PDE with homogeneous boundary conditions and another that solved the steady state PDE equation with inhomogeneous boundary conditions. This method produced solutions which satisfied the boundary conditions analytically and numerically, as shown in section 3.4.

We discretise the spatial profile of the model so we can apply numerical integration techniques to simulate the model. One advantage of solving the model analytically is that we can pre-compute key components of the solution to reduce the amount of calculations required per time step during the simulation, thus reducing the computational intensity of the model. We pre-compute the Green's functions and the channel and pump boundary solutions since we know the shape of the flux profile. We can compute the solution for

a unit flux and then multiply this solution by the magnitude of the constant  $\text{Ca}^{2+}$  flux at each time step.

We wanted to create a good approximation to the evolution of the temporal  $\text{Ca}^{2+}$  profile so we considered three different time step sizes in section 3.2.1. The ER-PM junction contains the  $\text{Ca}^{2+}$  channels and SERCA pumps involved in SOCE so the most complex  $\text{Ca}^{2+}$  dynamics will occur in this domain. Furthermore, the ER-PM junction has the largest  $\text{Ca}^{2+}$  diffusion coefficient, as discussed in Chapter 2, so the  $\text{Ca}^{2+}$  will diffuse much farther during one time step in this domain than the other domains. We examined the effect of the different time steps in the ER-PM junction because this domain requires the finest time step. If the time step is small enough to capture the evolution of the  $\text{Ca}^{2+}$  concentration in the ER-PM junction then it will provide a good approximation to the  $\text{Ca}^{2+}$  dynamics occurring in the larger domains.

Looking at the different time steps,  $dt$ , in Figure 3.3 we notice that the time step is crucial to the solution profile because it controls the extent of  $\text{Ca}^{2+}$  diffusion within the domain. Although a very small time step, such as  $dt = 10^{-8}\text{s}$ , results in little diffusion and could be a very good approximation to the changing  $\text{Ca}^{2+}$  profile it will also considerably increase the computational intensity of the model simulations. We needed to find a balance between the size of the time step and the computational intensity and run time of the simulations. For instance, using  $dt = 10^{-8}\text{s}$  instead of  $dt = 10^{-6}\text{s}$  results in 100 times more calculations and during each time step we must numerically evaluate the analytical solution. Therefore, increasing the number of time steps will increase the overall number of calculations required to simulate the model. We will use a time step of  $dt = 10^{-6}\text{s}$  but the effect of time step size on the simulations will be something to consider in the future.

We used a uniform mesh size in the  $r$ ,  $\phi$ , and  $z$  directions. However, the uniform  $r$  and  $\phi$  meshes cause a non-uniform grid system on the cylinder, as seen by the different sized grid elements in Figure 3.20. Currently, the mesh is very fine near the centre of the cylinder and coarser towards the edges of the cylinder. This is not ideal as the area of each surface element is different and we have assumed that the  $\text{Ca}^{2+}$  flux through the Orai channels and pumps occurs through one surface element. But if the surface elements do not have the same area then we are assuming the channels and pumps are different sizes at different points on the face. We will investigate the effect of mesh uniformity on the simulations in the next chapter and in the future we will investigate the

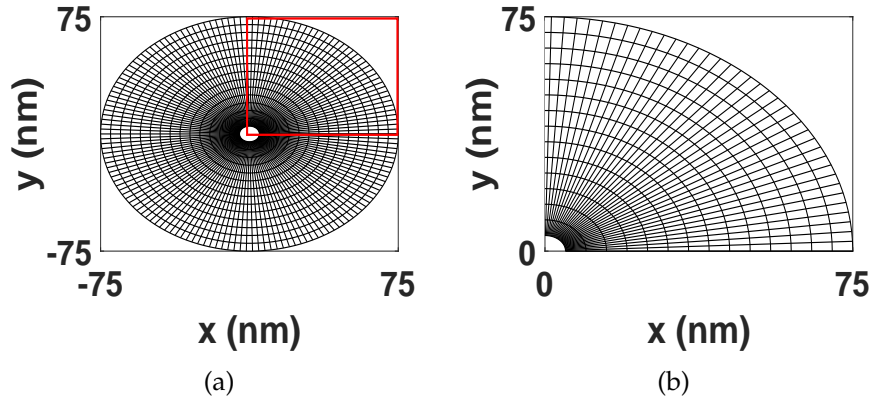


**Figure 3.20:** (a) Illustration of the grid structure after discretisation of the domain. (b) Zoom in on the upper quadrant enclosed within the red rectangle in (a). Parameter values:  $\Delta r = 5\text{nm}$ ,  $\Delta\theta = 0.0419$ ,  $\Delta z = 0.15\text{nm}$ .

impact of using a uniform surface element mesh instead of using uniform  $r$  and  $\phi$  meshes.

The PDE problem discussed in the previous chapter could also be solved numerically and in finite element methods the mesh is finer near the sites of  $\text{Ca}^{2+}$  flux, to ensure the simulation captures the rapid changes in  $\text{Ca}^{2+}$  concentration. In our current set-up the mesh at the centre of the cylinder is much finer than the rest of the cylinder. However, very few pumps or channels are present so close to the centre and by making the polar grid uniform we will spread the computational power more efficiently and possibly reduce the simulation time. It would be interesting to compare the solution techniques to assess the advantages and disadvantages of each method in this case.

In the future we could check if it is possible to use different time steps in each domain and perhaps increase the size of the time step in the larger domains (bulk cytoplasm and bulk ER). We would need to check how much  $\text{Ca}^{2+}$  diffuses into each domain from the smaller connected domain and whether increasing the time step would significantly impact the  $\text{Ca}^{2+}$  diffusion between the ER-PM junction and bulk cytoplasm and between the sub-PM ER and bulk ER. If we can use different time steps then we could further speed up the simulations.

# Chapter 4

## The relationship between the spatio-temporal discretisation and the $\text{Ca}^{2+}$ profile generated

In Chapter 3 we used analytical techniques to solve the 3D spatio-temporal model of SOCE proposed in Chapter 2 and numerically implemented the solution in MATLAB to check that the solution satisfied the prescribed boundary conditions. In this chapter we will examine the effect of the spatio-temporal discretisation on  $\text{Ca}^{2+}$  profiles to ensure that we have a suitable spatial discretisation and time step for investigating the  $\text{Ca}^{2+}$  dynamics of SOCE.

### 4.1 How does the spatial discretisation affect the $\text{Ca}^{2+}$ profile generated?

We simulated the  $\text{Ca}^{2+}$  profile generated by one Orai channel placed on the PM at  $r = 30\text{nm}$  and  $\phi = 1.8221$  in the ER-PM junction. The  $\text{Ca}^{2+}$  profile at the PM in the polar plane is shown in Figure 4.1(a) and we see a microdomain of elevated  $\text{Ca}^{2+}$  around the Orai channel, as expected. However, in Figure 4.1(b) we take a slice through the Orai channel in the azimuthal direction and observe oscillations in the  $\text{Ca}^{2+}$  concentration. Although the magnitude of these oscillations is small in comparison to the  $\text{Ca}^{2+}$  peak the oscillations still introduce artificial structure into the  $\text{Ca}^{2+}$  profile.

There are estimated to be five Orai channels per ER-PM junction [33, 67] so we simulated the  $\text{Ca}^{2+}$  profile generated by five Orai channels in Figure 4.2.

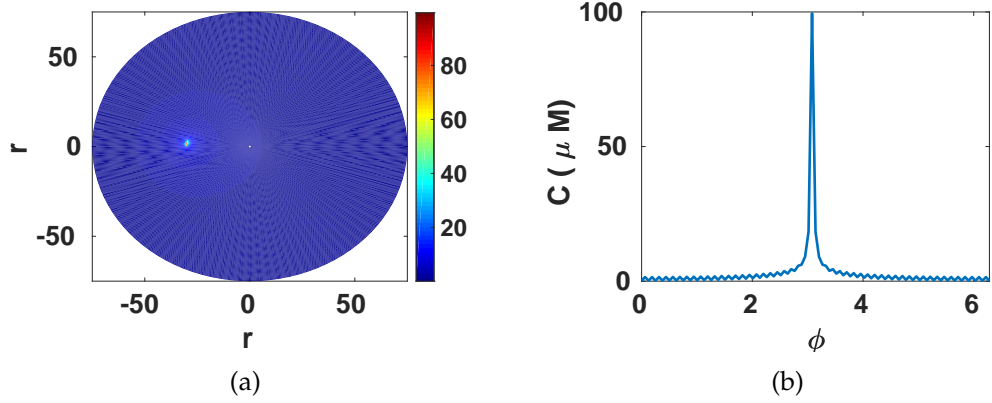


**Figure 4.1:**  $\text{Ca}^{2+}$  profiles generated in the ER-PM junction with one Orai channel present. (a)  $\text{Ca}^{2+}$  profile at the PM. (b) Slice in the azimuthal direction through the Orai channel in (a) to examine the  $\text{Ca}^{2+}$  profile in  $\phi$  direction. Parameters:  $\Delta\phi = 0.0628$  radians,  $\Delta r = 0.5\text{nm}$ ,  $\Delta z = 0.15\text{nm}$ ,  $N = 50$ ,  $J = 150$ ,  $M = 100$ ,  $r_{\text{Orai}} = 30\text{nm}$ ,  $\phi_{\text{Orai}} = 1.8221$ ,  $dt = 10^{-6}\text{s}$ ,  $T = 10^{-4}\text{s}$ .

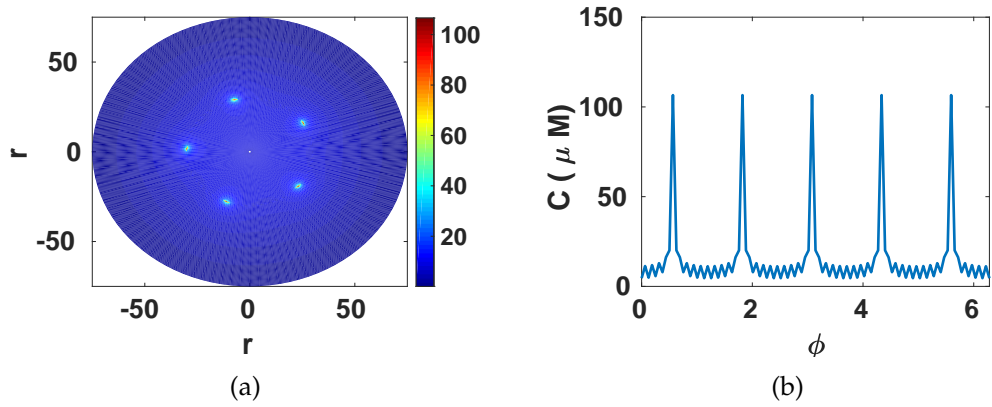


**Figure 4.2:**  $\text{Ca}^{2+}$  profiles generated in the ER-PM junction with five Orai channels present. (a)  $\text{Ca}^{2+}$  profile at the PM. (b) Slice in the azimuthal direction through the Orai channel in (a) to examine the  $\text{Ca}^{2+}$  profile in  $\phi$  direction. Parameters:  $\Delta\phi = 0.0628$  radians,  $\Delta r = 0.5\text{nm}$ ,  $\Delta z = 0.15\text{nm}$ ,  $N = 50$ ,  $J = 150$ ,  $M = 100$ ,  $r_{\text{Orai}} = 30\text{nm}$ ,  $dt = 10^{-6}\text{s}$ ,  $T = 10^{-4}\text{s}$ .

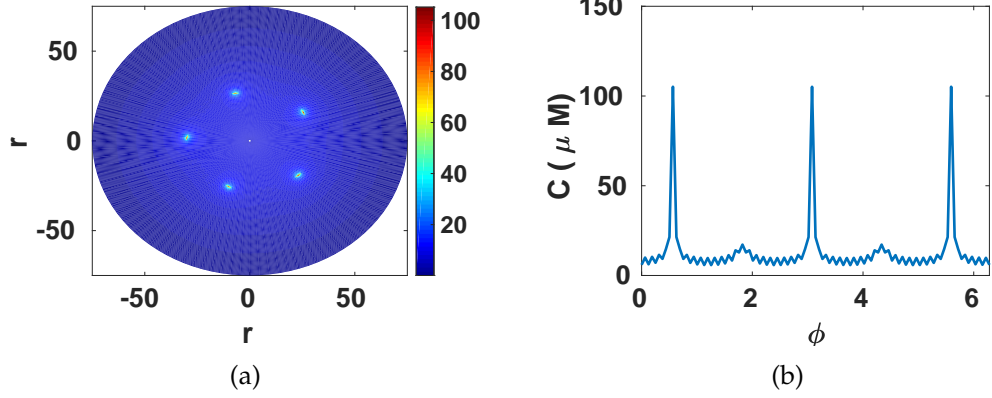


**Figure 4.3:** Ca<sup>2+</sup> profiles generated using five Orai channels in the offset Orai distribution. (a) Ca<sup>2+</sup> profile at the PM. (b) Ca<sup>2+</sup> profile in the azimuthal direction along the  $r = 30\text{nm}$  ring. Parameters:  $\Delta\phi = 0.0628$ ,  $\Delta r = 0.5\text{nm}$ ,  $\Delta z = 0.15\text{nm}$ ,  $N = 50$ ,  $J = 150$ ,  $M = 100$ ,  $dt = 10^{-6}\text{s}$ ,  $T = 10^{-4}\text{s}$ .

The Orai channels are placed equidistantly along the radius  $r = 30\text{nm}$  and in Figure 4.2(a) the Ca<sup>2+</sup> microdomains generated around each channel overlap. We also observe small oscillations along the ring  $r = 30\text{nm}$ , where the channels are placed. To directly examine these oscillations we take a slice in the azimuthal direction along  $r = 30\text{nm}$  in Figure 4.2(b). The oscillations are more pronounced when five Orai channels are included in the ER-PM junction, compared to the magnitude of the oscillations produced when the ER-PM junction contains only one Orai channel, as seen in Figure 4.1(b). Effector molecules or Ca<sup>2+</sup> pumps, such as the PMCA pump, close to the Orai channels on the PM could be activated in response to the increased or decreased Ca<sup>2+</sup> concentration caused by the oscillations. Therefore, these oscillations could introduce additional Ca<sup>2+</sup> dynamics into the system through unrealistic activation of effector molecules or Ca<sup>2+</sup> pumps.

The Ca<sup>2+</sup> oscillations became more pronounced when the Orai channels were placed along the same ring of radius  $r = 30\text{nm}$  so we now place the channels in an 'offset' arrangement, where the second and fourth channels are placed away from the ring, as shown in Figure 4.3(a). We take a slice in the azimuthal direction along the radius  $r = 30\text{nm}$  in Figure 4.3(b) and observe Ca<sup>2+</sup> oscillations. The magnitude of the oscillations are not as great as the oscillations in Figure 4.2(b) but the oscillations are still noticeable and could introduce artificial Ca<sup>2+</sup> behaviour into the system.

These oscillations are a result of the  $\theta(\phi)$  solution used in Chapter 3 to calculate the steady state solution,  $V_J$ . We prescribed the shape of the Ca<sup>2+</sup> flux in

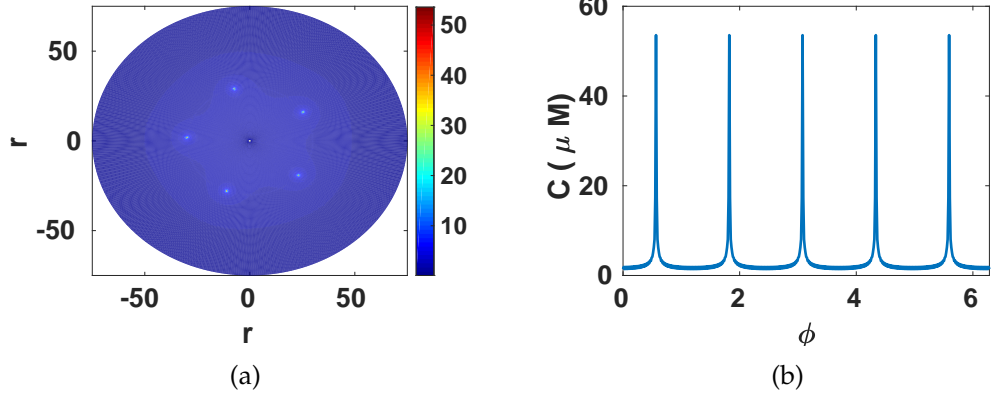


**Figure 4.4:** Ca<sup>2+</sup> profiles generated in the ER-PM junction with five Orai channels present. (a) Ca<sup>2+</sup> profile at the PM. (b) Ca<sup>2+</sup> profile in the azimuthal direction along the  $r = 30\text{nm}$  ring. Parameters:  $\Delta\phi = 0.0126$  radians,  $\Delta r = 0.5\text{nm}$ ,  $\Delta z = 0.15\text{nm}$ ,  $N = 250$ ,  $J = 150$ ,  $M = 100$ ,  $r_{\text{Orai}} = 30\text{nm}$ ,  $dt = 10^{-6}\text{s}$ ,  $T = 10^{-4}\text{s}$ .

Chapter 2 to be zero except at  $(r_{\text{Orai}}, \phi_{\text{Orai}})$ , which denotes the position of the Orai channel. The steady state solution,  $V_{J,1}$ , describes the solution with Ca<sup>2+</sup> influx via Orai channels on the PM and involves integrating over the PM surface. This surface integral, and in particular the integral over  $\phi$ , introduces the oscillations into the final Ca<sup>2+</sup> solution. It is difficult to integrate numerically over such a sharp peak, which we have used for our Ca<sup>2+</sup> influx boundary condition. The current discretisation of  $\phi$ , using  $\Delta\phi = 0.0628$ , is not sufficiently fine to ensure this integral is smooth. We refined the discretisation of  $\phi$ , using  $\Delta\phi = 0.0126$ , and simulated the Ca<sup>2+</sup> profile generated with five Orai channels placed equidistantly along a ring of radius  $r = 30\text{nm}$  in Figure 4.4.

First, we notice that the magnitude of the Ca<sup>2+</sup> peaks generated using the fine  $\phi$  discretisation is almost half the magnitude of the Ca<sup>2+</sup> peaks generated by the coarse  $\phi$  discretisation and the Ca<sup>2+</sup> microdomain is much more concentrated in Figure 4.4(a). Secondly, the Ca<sup>2+</sup> profile at the Orai channel along the azimuthal direction in Figure 4.4(b) is smooth and there are no Ca<sup>2+</sup> oscillations present when using the fine  $\phi$  discretisation. This demonstrates that the Ca<sup>2+</sup> oscillations are a result of numerically integrating over such a sharp Ca<sup>2+</sup> flux profile.

To understand why the Ca<sup>2+</sup> magnitude decreases when using the fine  $\phi$  discretisation we first consider the spatial grids generated on the PM as a result of the coarse and fine  $\phi$  discretisations, shown in Figures 4.5(a) and 4.5(b), respectively. We assume that Ca<sup>2+</sup> flux occurs through a single grid element, the Orai channel, highlighted in yellow and green in Figures 4.5(a) and 4.5(b), respec-

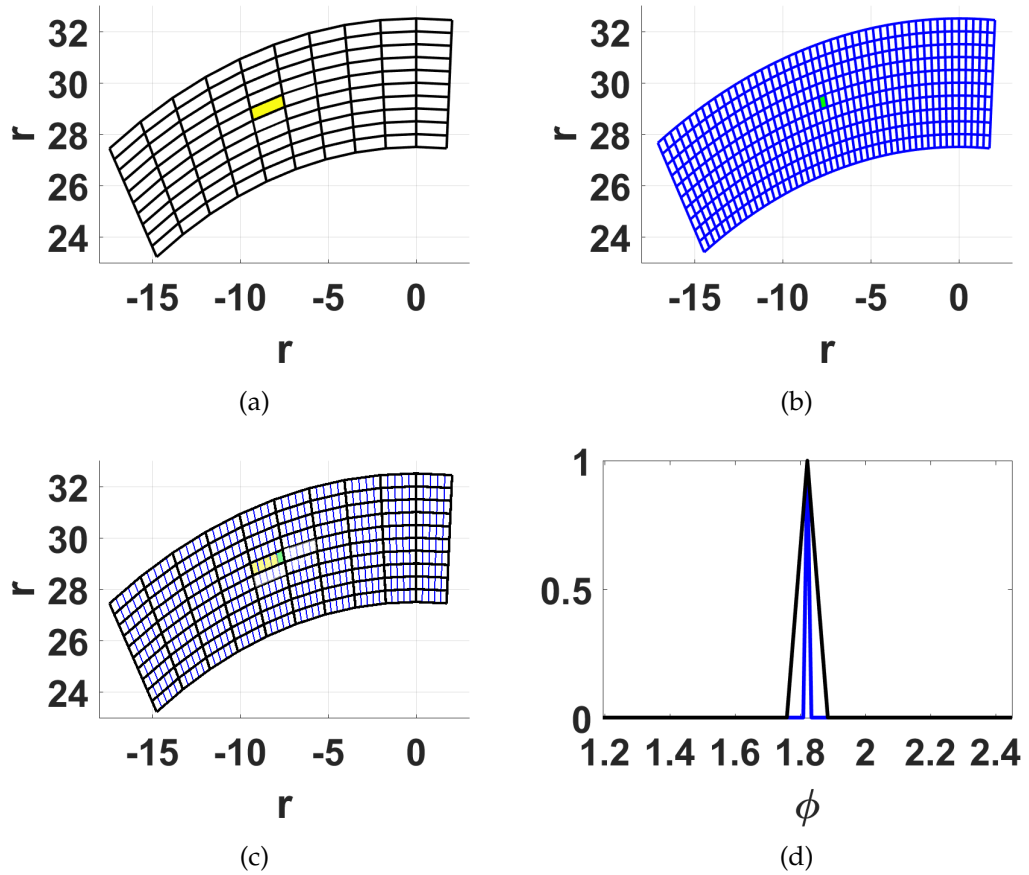


**Figure 4.5:** (a,b) Spatial grid on PM arising from coarse ( $\Delta\phi = 0.0628$ ,  $N = 50$ ) and fine ( $\Delta\phi = 0.0126$ ,  $N = 250$ )  $\phi$  discretisation with point of  $\text{Ca}^{2+}$  influx occurring through the grid element marked with yellow and green, respectively. (c) Overlap of spatial grids in (a) and (b). (d)  $\text{Ca}^{2+}$  influx profile with the coarse and fine  $\phi$  discretisation represented by the black and blue lines, respectively. Parameters:  $\Delta r = 0.5\text{nm}$ ,  $\Delta z = 0.15\text{nm}$ ,  $J = 150$ ,  $M = 100$ ,  $r_{\text{orai}} = 30\text{nm}$ ,  $\phi_{\text{Orai}} = 1.8221$ ,  $dt = 10^{-6}\text{s}$ ,  $T = 10^{-4}\text{s}$ .

tively. We prescribed the  $\text{Ca}^{2+}$  flux per unit area per Orai channel in chapter 2 but we did not take account of the effect of decreasing the  $\phi$  discretisation on the grid element area. The yellow grid element in Figure 4.5(a) is larger than the green grid element in Figure 4.5(b). If both elements are given the same  $\text{Ca}^{2+}$  flux profile then the yellow element will result in greater  $\text{Ca}^{2+}$  influx than the green element because the total flux (calculated as the  $\text{Ca}^{2+}$  flux per unit area per channel multiplied by the area of the grid element) will be greater in Figure 4.5(a) with the coarse  $\phi$  discretisation than in Figure 4.5(b) with the fine  $\phi$  discretisation. This is further demonstrated when we plot the  $\text{Ca}^{2+}$  influx profile in the azimuthal direction in Figure 4.5(d) as we see that the total flux with the coarse  $\phi$  discretisation (black line) is greater than the total flux of the fine  $\phi$  discretisation (blue line), where the total flux is proportional to the  $\phi$  integral of the  $\text{Ca}^{2+}$  flux profile. We further compare the spatial grids formed as a result of the coarse and fine  $\phi$  discretisations in Figure 4.5(c) to show the relative sizes of the grids and that the shape of the elements also change. This relationship between the total  $\text{Ca}^{2+}$  flux and area of the grid element representing the Orai channel will be something to consider to ensure that the total  $\text{Ca}^{2+}$  influx is consistent and not dependent on Orai channel placement.

So far, we have shown that  $\text{Ca}^{2+}$  oscillations arise in response to the discretisation of  $\phi$  and demonstrated that by refining the discretisation we can smooth out the  $\text{Ca}^{2+}$  profile and remove the  $\text{Ca}^{2+}$  oscillations. However, the discretisation required to ensure a smooth  $\text{Ca}^{2+}$  profile is very small,  $\Delta\phi = 0.0126$ . Unfortunately this is computationally expensive and requires large amounts of memory and results in longer simulation times. Instead, we can use a  $\phi$  discretisation of  $\Delta\phi = 0.0419$ , slightly finer than the coarse discretisation, and approximate the  $\text{Ca}^{2+}$  flux profile, shown in black in Figure 4.5(d), by the function,

$$w(r_{\text{Orai}}, \phi_{\text{Orai}}) = \exp \left( \left( (r - r_{\text{Orai}}) / \sigma_r \right)^2 + \left( (\phi - \phi_{\text{Orai}}) / \sigma_\phi \right)^2 \right), \quad (4.1)$$

where  $\sigma_r$  and  $\sigma_\phi$  control the width of the peak and the majority of  $\text{Ca}^{2+}$  influx occurs through the point,  $(r_{\text{orai}}, \phi_{\text{orai}})$ , representing the Orai channel position. Again, we look at the spatial grids created from the coarse and fine  $\phi$  distributions in Figures 4.6(a) and 4.6(b).

The coarse  $\phi$  grid has a single grid element shaded yellow representing the  $\text{Ca}^{2+}$  flux through the Orai channel whereas the fine  $\phi$  grid has one element shaded a bright green and the two neighbouring elements shaded light green

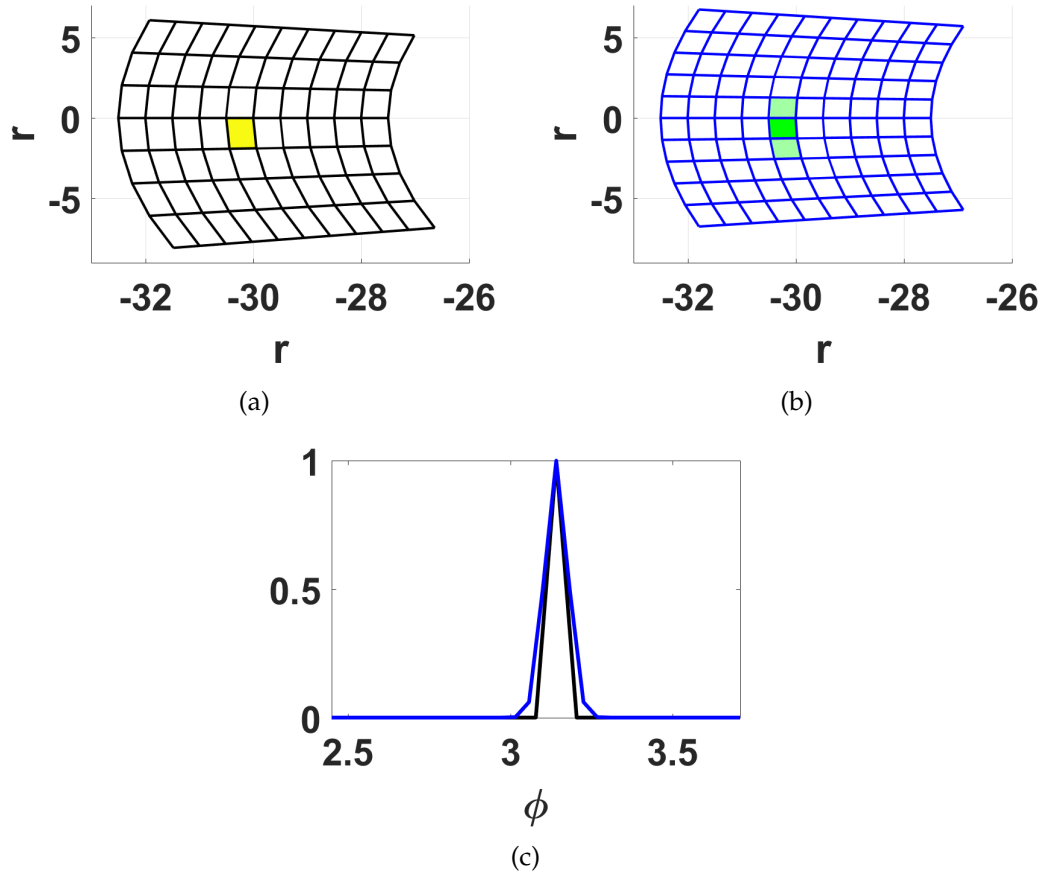


**Figure 4.6:** Spatial grid using  $\Delta r = 0.5\text{nm}$  and (a) coarse ( $\Delta\phi = 0.0628$ )  $\phi$  discretisation with  $\text{Ca}^{2+}$  influx all through the yellow grid element,  $(r_{\text{Orai}}, \phi_{\text{Orai}}) = (30, \pi)$ , (b) fine ( $\Delta\phi = 0.0419$ ,  $\sigma_\phi = 0.05$ ,  $\sigma_r = 0.1$ )  $\phi$  discretisation with majority of  $\text{Ca}^{2+}$  influx through bright green grid element,  $(r_{\text{Orai}}, \phi_{\text{Orai}}) = (30, \pi)$ , and small influx through the pale green grid elements on either side. (c)  $\text{Ca}^{2+}$  influx profile with the coarse and fine  $\phi$  discretisation represented by the black and blue lines, respectively. Parameters:  $r_{\text{Orai}} = 30\text{nm}$ ,  $\Delta r = 0.5\text{nm}$ ,  $\Delta z = 0.15\text{nm}$ ,  $J = 150$ ,  $M = 100$ ,  $dt = 10^{-6}\text{s}$ ,  $T = 10^{-4}\text{s}$ .

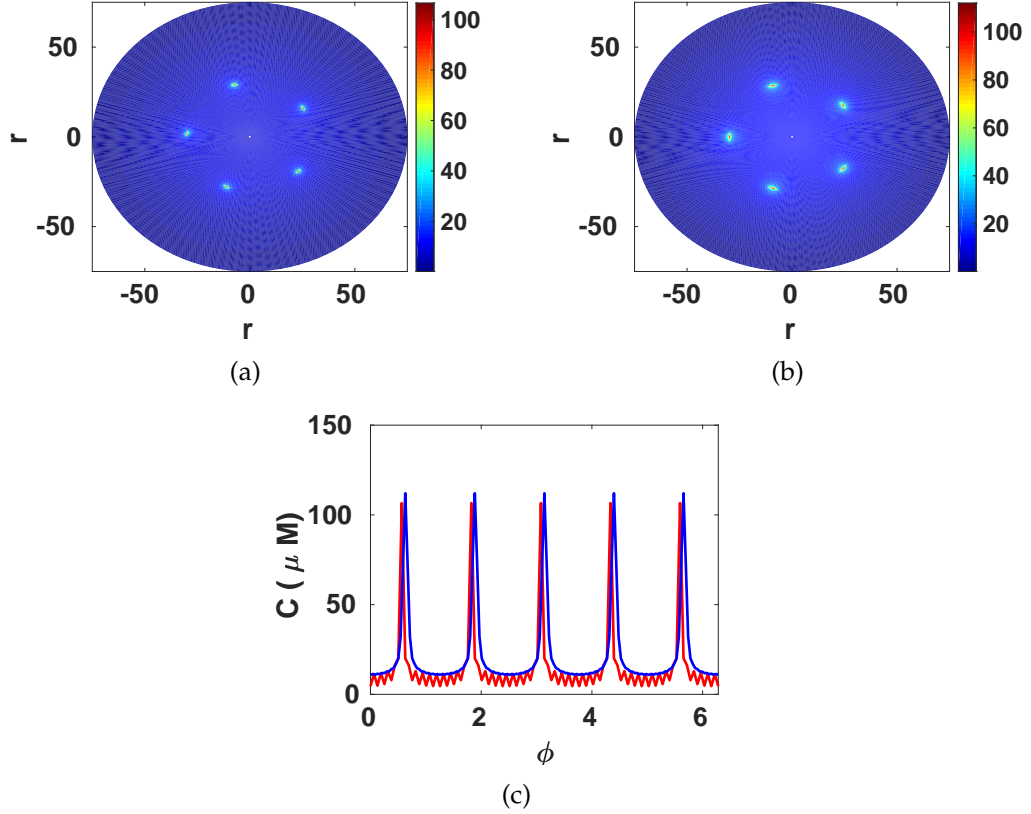


**Figure 4.7:** Ca<sup>2+</sup> profiles in the ER-PM junction with five Orai channels present using the (a) coarse ( $\Delta\phi = 0.0628$ ,  $N = 50$ )  $\phi$  discretisation and Ca<sup>2+</sup> influx profile illustrated by the black line in 4.6(c) and (b) fine ( $\Delta\phi = 0.0419$ ,  $N = 75$ ,  $\sigma_\phi = 0.05$ ,  $\sigma_r = 0.1$ )  $\phi$  discretisation and Ca<sup>2+</sup> influx profile illustrated by the blue line in 4.6(c). (c) Ca<sup>2+</sup> profile in the azimuthal direction along the ring  $r = 30\text{nm}$ , the red line represents the Ca<sup>2+</sup> profile in (a) and the blue line represents the Ca<sup>2+</sup> profile in (b). Parameters:  $r_{\text{Orai}} = 30\text{nm}$ ,  $\Delta r = 0.5\text{nm}$ ,  $\Delta z = 0.15\text{nm}$ ,  $J = 150$ ,  $M = 100$ ,  $dt = 10^{-6}\text{s}$ ,  $T = 10^{-4}\text{s}$ .

to represent that the majority of Ca<sup>2+</sup> flux occurs through the central point, the Orai channel, but a small amount of additional Ca<sup>2+</sup> flux occurs adjacent to the channel. The Ca<sup>2+</sup> flux profile is shown in figure 4.6(c) where the black line represents the coarse  $\phi$  discretisation with a single point of Ca<sup>2+</sup> influx and the blue line represents the fine  $\phi$  discretisation with the Ca<sup>2+</sup> influx occurring according to equation (4.1). The total Ca<sup>2+</sup> flux in the coarse  $\phi$  discretisation is slightly smaller than the total Ca<sup>2+</sup> flux occurring in the fine  $\phi$  discretisation, however, the change in total Ca<sup>2+</sup> flux is less noticeable in Figure 4.6(c) than in Figure 4.5(d).

The Ca<sup>2+</sup> profiles generated in response to five Orai channels placed equidistantly along a ring of radius  $r = 30\text{nm}$  with the coarse  $\phi$  discretisation and

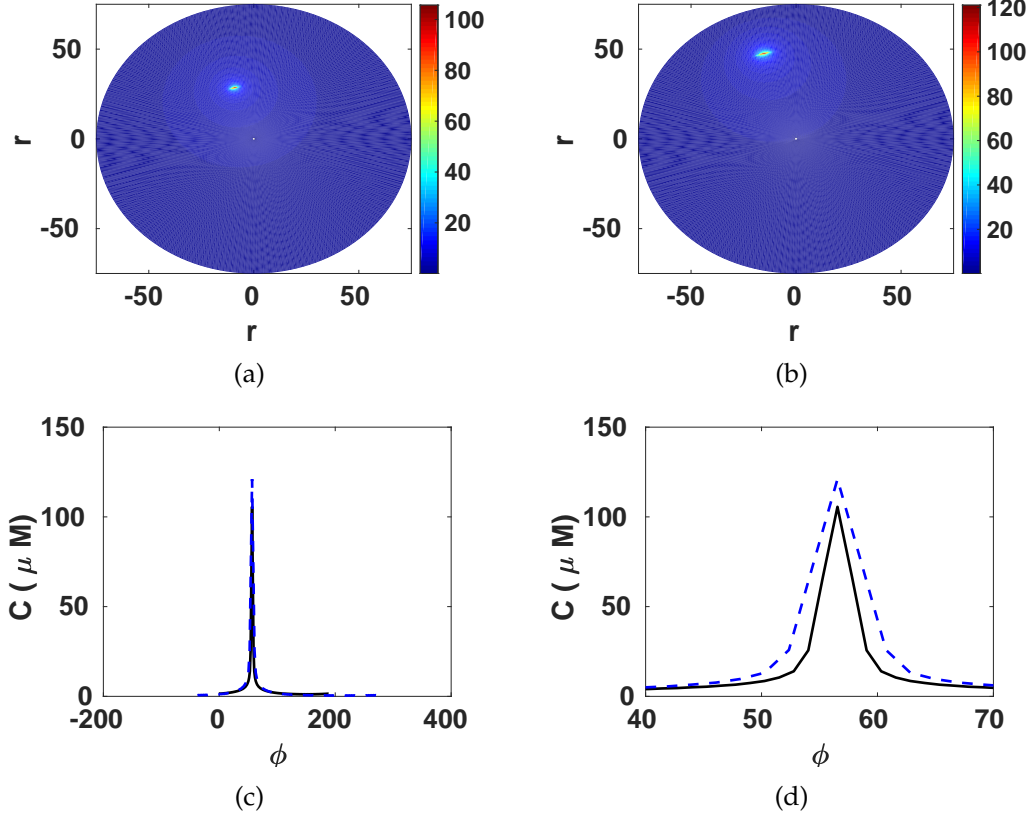


**Figure 4.8:**  $\text{Ca}^{2+}$  profile in the ER-PM junction with one Orai channel at (a)  $r = 30\text{nm}$  and (b)  $r = 50\text{nm}$ . (c)  $\text{Ca}^{2+}$  profile in the azimuthal direction along the radius  $r = 30\text{nm}$  (black line,  $s = r_{30}\phi$ ) and  $r = 50\text{nm}$  (dashed blue line,  $s = r_{50}\phi$ ). (d)  $\text{Ca}^{2+}$  profile as in (c) zoomed in on Orai channel. Parameters:  $\phi_{\text{Orai}} = 1.8221$ ,  $\Delta r = 0.5\text{nm}$ ,  $\Delta\phi = 0.0419$ ,  $\Delta z = 0.15\text{nm}$ ,  $N = 75$ ,  $J = 150$ ,  $M = 100$ ,  $\sigma_\phi = 0.05$ ,  $\sigma_r = 0.1$ ,  $dt = 10^{-6}\text{s}$ ,  $T = 10^{-4}\text{s}$ .

single  $\text{Ca}^{2+}$  influx point and the fine  $\phi$  discretisation and  $\text{Ca}^{2+}$  influx governed by equation (4.1) are shown in Figures 4.7(a) and 4.7(b), respectively. The  $\text{Ca}^{2+}$  profiles are very similar and the fine  $\phi$  discretisation does not introduce  $\text{Ca}^{2+}$  oscillations, which we see along the ring of radius  $r = 30\text{nm}$  in Figure 4.7(a), into the  $\text{Ca}^{2+}$  profile in Figure 4.7(b). However the overall shape of the  $\text{Ca}^{2+}$  microdomains are similar with both the coarse and fine  $\phi$  discretisations. We directly compare the  $\text{Ca}^{2+}$  profiles along the radius  $r = 30\text{nm}$  in Figure 4.7(c) and see that the  $\text{Ca}^{2+}$  profiles are similar. There is a slight increase in magnitude with the fine  $\phi$  discretisation (blue line) but the fine  $\phi$  discretisation is a good approximation to the coarse  $\phi$  discretisation (red line).

Therefore, we will use a  $\phi$  discretisation of  $\Delta\phi = 0.0419$  throughout the rest of the thesis with the  $\text{Ca}^{2+}$  flux profile given by equation (4.1),  $w(r_i, \phi_i)$  for  $i \in \{\text{Orai}, \text{SERCA}\}$ .

We have seen that the total  $\text{Ca}^{2+}$  flux per Orai channel depends on the area of the spatial grid element the Orai channel is centred at. We are using uniform spatial discretisations,  $\Delta r$  and  $\Delta\phi$ , so the polar plane of the cylinder will not contain a uniform spatial grid. The area of each grid element is approximately equal to  $\bar{r}\Delta r\Delta\phi$ , where  $\bar{r}$  denotes the  $r$  position of the Orai channel. Therefore, the area of the grid element increases as the Orai channel is placed closer to the mantle of the cylinder. Consequently, an Orai channel centred at  $r = 30\text{nm}$  will have a smaller grid element area than a channel centred at  $r = 50\text{nm}$ . This will result in less total  $\text{Ca}^{2+}$  flux and smaller  $\text{Ca}^{2+}$  concentration magnitudes. The  $\text{Ca}^{2+}$  profiles generated by Orai channels at  $r = 30\text{nm}$  and  $r = 50\text{nm}$  are shown in Figures 4.8(a) and 4.8(b) and we see that the region of light blue surrounding the Orai channel, corresponding to  $\text{Ca}^{2+}$  concentrations of approximately  $12\mu\text{M}$ , is larger when the channel is placed at  $r = 50\text{nm}$  than  $r = 30\text{nm}$ . This demonstrates that Orai channels placed closer to the mantle ( $r = 50\text{nm}$ ) create more highly elevated  $\text{Ca}^{2+}$  microdomains than channels placed more centrally within the cylinder ( $r = 30\text{nm}$ ). We compare the  $\text{Ca}^{2+}$  profiles through the Orai channels along the radius  $r = 30\text{nm}$ , represented by the black line, and  $r = 50\text{nm}$ , represented by the dashed blue line, directly in Figure 4.8(c). We compare the  $\text{Ca}^{2+}$  concentrations along the arc length,  $s = r\phi$  for  $r = 30\text{nm}$  and  $r = 50\text{nm}$ , to take account of the increased size of the ring when the radius is larger. We find that the  $\text{Ca}^{2+}$  profile generated with the Orai channel at  $r = 50\text{nm}$  has a greater peak magnitude than the Orai channel centred at  $r = 30\text{nm}$ . We zoom in on the  $\text{Ca}^{2+}$  concentration profile close to the Orai channels in Figure 4.8(d) and see that the  $\text{Ca}^{2+}$  profile is more highly elevated for a channel situated at  $r = 50\text{nm}$  (dashed blue line) than a channel at  $r = 30\text{nm}$  (black line).

Biologically, there is no reason for the  $\text{Ca}^{2+}$  profile and peak  $\text{Ca}^{2+}$  concentration generated by an individual Orai channel to change with channel placement, so the change in  $\text{Ca}^{2+}$  profile observed in Figure 4.8 suggests that the change in  $\text{Ca}^{2+}$  concentration is a consequence of the model, and in particular the area of the grid element the Orai channel is centred at. In Figures 4.9(a) and 4.9(b) we illustrate the spatial grid surrounding the Orai channels placed at  $r = 30\text{nm}$  and  $r = 50\text{nm}$ , respectively. The grid elements in Figure 4.9(a) are much narrower than those of Figure 4.9(b) and we see that the area of the grid element the Orai channel is centred at, the bright yellow element, is noticeably larger in Figure 4.9(b). We can reduce the size of the  $\phi$  spatial discretisation when  $r = 50\text{nm}$  to  $\Delta\phi = 0.0251$  and ensure that the grids the Orai channels

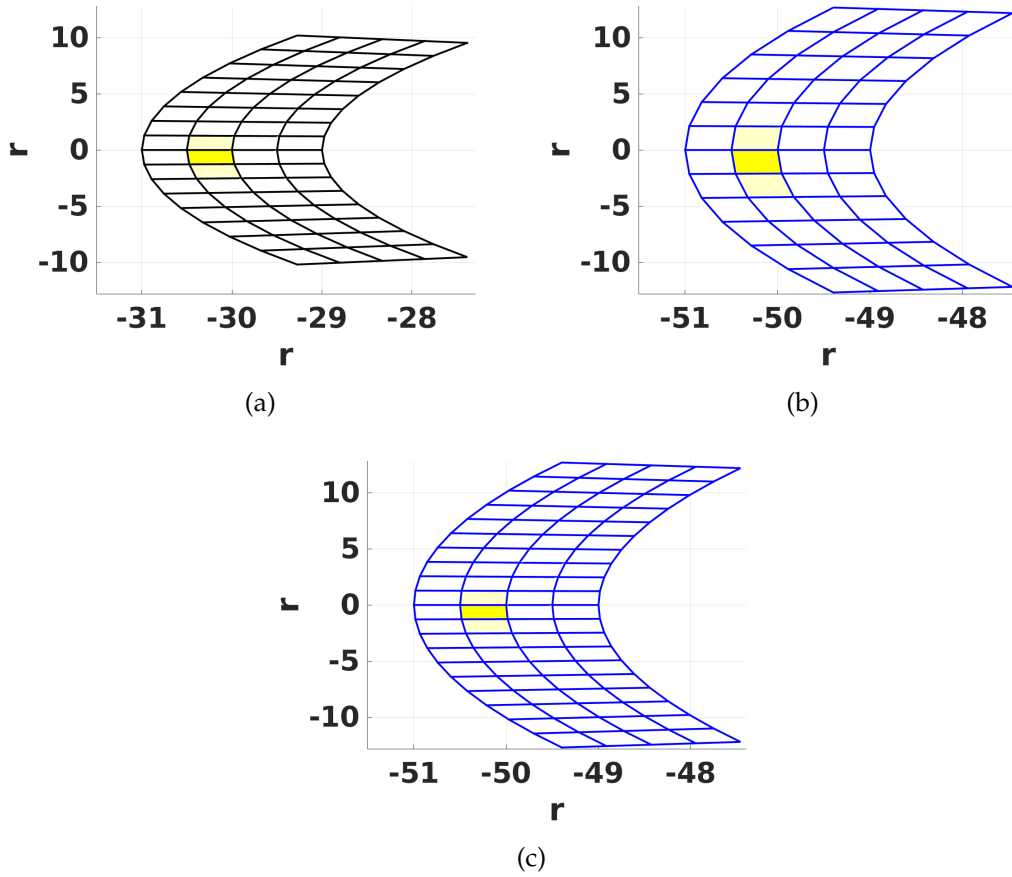


**Figure 4.9:** Spatial  $\text{Ca}^{2+}$  grid using  $\Delta r = 0.5\text{nm}$  and (a) coarse ( $\Delta\phi = 0.0419$ ,  $\sigma_\phi = 0.05$ )  $\phi$  discretisation with an Orai channel at  $r = 30\text{nm}$ , (b)  $r = 50\text{nm}$ , (c) fine ( $\Delta\phi = 0.0251$ ,  $\sigma_\phi = 0.03$ )  $\phi$  discretisation with an Orai channel at  $r = 50\text{nm}$ . Majority of  $\text{Ca}^{2+}$  influx occurs through bright yellow grid element, with some flux through neighbouring pale yellow elements. Parameters:  $\phi_{\text{Orai}} = 1.8221$ ,  $\Delta r = 0.5\text{nm}$ ,  $\Delta\phi = 0.0419$ ,  $\Delta z = 0.15\text{nm}$ ,  $N = 75$ ,  $J = 150$ ,  $M = 100$ ,  $\sigma_r = 0.1$ ,  $dt = 10^{-6}\text{s}$ ,  $T = 10^{-4}\text{s}$ .

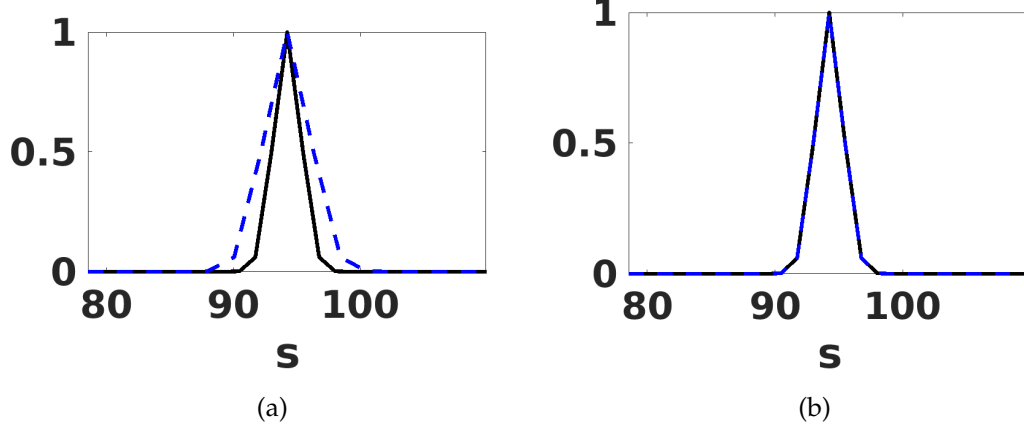


**Figure 4.10:**  $\text{Ca}^{2+}$  influx profile through Orai channel centred at  $r = 30\text{nm}$  and  $r = 50\text{nm}$ , represented by the solid black ( $s = r_{30}\phi$ ) and dashed blue lines ( $s = r_{50}\phi$ ), respectively. In (a) the  $\phi$  discretisation is coarse ( $\Delta\phi = 0.0419$ ,  $N = 75$ ,  $\sigma_\phi = 0.05$ ) for both radial distances, while in (b)  $r = 30\text{nm}$  has a coarse discretisation, as in (a), and  $r = 50\text{nm}$  has a fine  $\phi$  discretisation ( $\Delta\phi = 0.0251$ ,  $N = 125$ ,  $\sigma_\phi = 0.03$ ). Parameters:  $\Delta r = 0.5\text{nm}$ ,  $\Delta z = 0.15\text{nm}$ ,  $J = 150$ ,  $M = 100$ ,  $\phi_{\text{Orai}} = 1.8221$ ,  $\sigma_r = 0.1$ ,  $dt = 10^{-6}\text{s}$ ,  $T = 10^{-4}\text{s}$ .

are centred at have the same area. We illustrate this new spatial grid in Figure 4.9(c) and by comparing this to Figure 4.9(a) we see that the grids surrounding the Orai channels are similar in shape and size. In this way, we ensure that the total  $\text{Ca}^{2+}$  flux through each Orai channel is the same.

In Figure 4.10 we compare the  $\text{Ca}^{2+}$  flux profile of Orai channels situated at  $r = 30\text{nm}$ , represented by the black line, and  $r = 50\text{nm}$ , represented by the dashed blue lines. We find that the  $\text{Ca}^{2+}$  influx profile along the ring  $r = 30\text{nm}$  is narrower than the  $\text{Ca}^{2+}$  influx profile along the ring  $r = 50\text{nm}$  with a  $\phi$  discretisation  $\Delta\phi = 0.0419$  in Figure 4.10(a). However, the  $\text{Ca}^{2+}$  influx profile along the ring  $r = 30\text{nm}$  is well approximated by the  $\text{Ca}^{2+}$  influx profile along the ring  $r = 50\text{nm}$  when  $\Delta\phi = 0.0251$ , shown in Figure 4.10(b). It is evident from Figures 4.10(a) and 4.10(b) that the total  $\text{Ca}^{2+}$  influx is greater through the Orai channel at  $r = 50\text{nm}$  compared to the channel at  $r = 30\text{nm}$  when  $\Delta\phi = 0.0419$  but the total  $\text{Ca}^{2+}$  influx is the same through both Orai channels when  $\Delta\phi = 0.0251$ .

We simulated the  $\text{Ca}^{2+}$  profile with an Orai channel at  $r = 50\text{nm}$  with  $\Delta\phi = 0.0251$  in Figure 4.11(a) which is very similar to the  $\text{Ca}^{2+}$  profile with an Orai channel at  $r = 30\text{nm}$  in figure 4.8(a). We directly compare the  $\text{Ca}^{2+}$  profiles through the Orai channels along the rings of radius  $r = 30\text{nm}$ , represented by

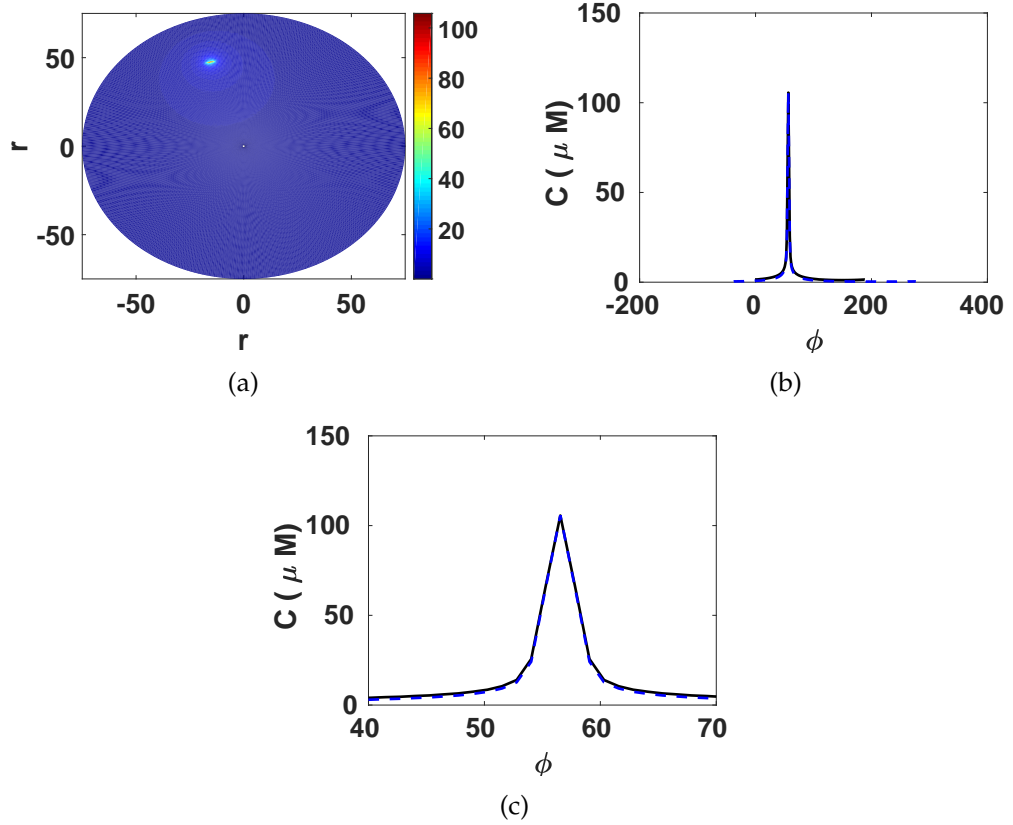


**Figure 4.11:** Ca<sup>2+</sup> profile in the ER-PM junction with one Orai channel at  $r = 50\text{nm}$ . (a) Ca<sup>2+</sup> profile at the PM. (b) Ca<sup>2+</sup> profile in the azimuthal direction along the radius  $r = 30$  (black line,  $s = r_{30}\phi$ ) with the coarse  $\phi$  discretisation ( $\Delta\phi = 0.0419$ ,  $N = 75$ ) and  $r = 50\text{nm}$  (dashed blue line,  $s = r_{50}\phi$ ) with the fine  $\phi$  discretisation ( $\Delta\phi = 0.0251$ ,  $N = 125$ ). (d) Ca<sup>2+</sup> profile as in (c) zoomed in on Orai channel. Parameters:  $\Delta r = 0.5\text{nm}$ ,  $\Delta z = 0.15\text{nm}$ ,  $J = 150$ ,  $M = 100$ ,  $\phi_{\text{Orai}} = 1.8221$ ,  $\sigma_r = 0.1$ ,  $\sigma_\phi = 0.03$ ,  $dt = 10^{-6}\text{s}$ ,  $T = 10^{-4}\text{s}$ .

the black line, and  $r = 50\text{nm}$ , represented by the dashed blue line, in Figure 4.11(b), and see that the  $\text{Ca}^{2+}$  profiles have the same peak  $\text{Ca}^{2+}$  magnitude and similar shapes. We zoom in on the  $\text{Ca}^{2+}$  concentrations surrounding the channels in Figure 4.11(c) and see that the  $\text{Ca}^{2+}$  profile generated by the Orai channel at  $r = 50\text{nm}$  is a good approximation to the Orai channel at  $r = 30\text{nm}$ . Thus demonstrating that when the grid elements the Orai channels are centred to have the same area and shape, and therefore the same total  $\text{Ca}^{2+}$  flux, then the  $\text{Ca}^{2+}$  channels emit the same  $\text{Ca}^{2+}$  concentration profile, allowing comparison of  $\text{Ca}^{2+}$  dynamics resulting from different Orai channel distributions.

Therefore, we must be careful when comparing  $\text{Ca}^{2+}$  profiles generated with Orai channels placed on rings of different radii. We will implement this approach and ensure that the grid elements the Orai channels are centred to have the same area thus allowing comparison of the  $\text{Ca}^{2+}$  profiles generated in response to the different Orai channel distributions.

## 4.2 How does the time step, $dt$ , affect the $\text{Ca}^{2+}$ dynamics?

In the previous chapter we looked at the effect of the time step,  $dt$ , on the shape of the Green's functions. If we chose a time step that is small,  $dt = 10^{-8}\text{s}$ , then very little  $\text{Ca}^{2+}$  would diffuse during one time step and we would have to run the simulations over many time steps to allow the  $\text{Ca}^{2+}$  influx through the Orai channels to diffuse sufficiently far to activate the SERCA pumps. However, if we chose a large time step,  $dt = 10^{-5}\text{s}$ , then  $\text{Ca}^{2+}$  will have diffused throughout the ER-PM junction very quickly because of the small size of the junction. We chose a time step of  $dt = 10^{-6}\text{s}$  and simulated the situation with five Orai channels at  $r = 30\text{nm}$  and ten SERCA pumps at  $r = 60\text{nm}$ . We then compare the three time steps to investigate how the time step affects the  $\text{Ca}^{2+}$  profile. We are particularly interested in the  $\text{Ca}^{2+}$  profiles generated in the sub-PM ER as the SERCA pump activity depends on the  $\text{Ca}^{2+}$  concentration near to the SERCA pumps and the different time steps will result in different activity levels of the SERCA pumps.

In Figure 4.12 we look at the  $\text{Ca}^{2+}$  profiles in the ER-PM junction and sub-PM ER after  $10^{-5}\text{s}$  to see how the different time steps are able to capture the early  $\text{Ca}^{2+}$  dynamics of the system. The solid blue line represents the smallest

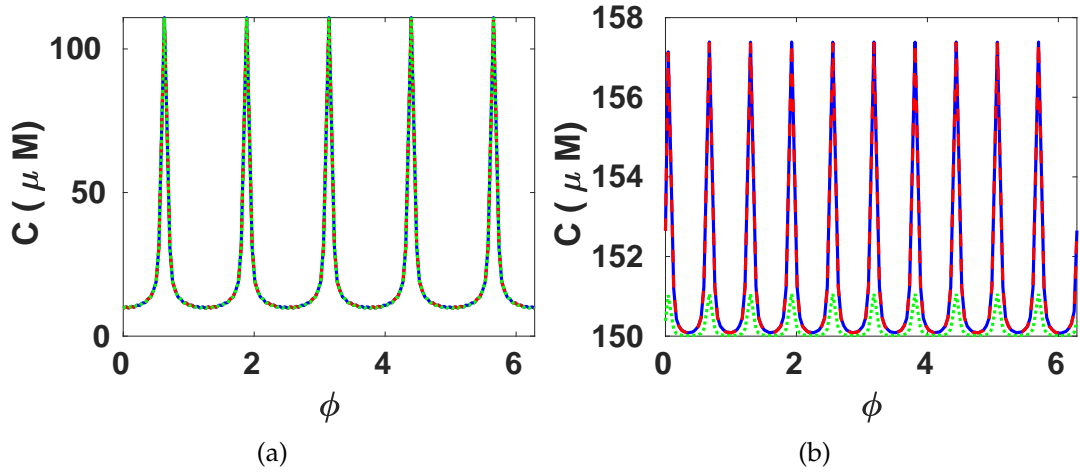


**Figure 4.12:** Comparing  $\text{Ca}^{2+}$  profiles after  $10^{-5}$ s simulated with three different time steps in the (a) ER-PM junction and (b) sub-PM ER. The blue line represents the  $\text{Ca}^{2+}$  concentration simulated with a time step  $dt = 1 \times 10^{-7}$ s, the red line represents the  $\text{Ca}^{2+}$  concentration simulated with a time step  $dt = 1 \times 10^{-6}$ s and the green line represents the  $\text{Ca}^{2+}$  concentration simulated with a time step  $dt = 1 \times 10^{-5}$ s.

time step,  $dt = 10^{-7}$  s, the dashed red line represents the intermediate time step,  $dt = 10^{-6}$  s, and the dotted green line represents the largest time step,  $dt = 10^{-5}$  s. The Orai channel has a constant  $\text{Ca}^{2+}$  influx which does not depend on the surrounding  $\text{Ca}^{2+}$  concentration and we see in Figure 4.12(a) that all three time steps are able to capture the  $\text{Ca}^{2+}$  dynamics at the Orai channel in the ER-PM junction. The SERCA pump activity depends on the surrounding  $\text{Ca}^{2+}$  concentration and the time step controls the extent of  $\text{Ca}^{2+}$  diffusion so the time step will affect SERCA activity. In Figure 4.12(b) we see that the smallest and intermediate time steps are good approximations to the  $\text{Ca}^{2+}$  dynamics but the largest time step has not captured the  $\text{Ca}^{2+}$  dynamics at this early stage. Possibly because  $\text{Ca}^{2+}$  diffuses quickly in the ER-PM junction and if the pumps are not activated to remove the elevated  $\text{Ca}^{2+}$  then it will diffuse out of the junction.

We then looked at the  $\text{Ca}^{2+}$  profiles generated by each time step after  $10^{-4}$  s to see how the time steps captured the later  $\text{Ca}^{2+}$  dynamics of the system. In both Figure 4.13(a) and Figure 4.13(b) the three time steps are able to capture the  $\text{Ca}^{2+}$  dynamics of the system as shown by the overlapping  $\text{Ca}^{2+}$  profiles in both Figures. At later times the larger time step is able to recover the  $\text{Ca}^{2+}$  profiles of the smaller time steps so the model is robust and able to cope with a variety of time steps which can be chosen depending on whether we are interested in the short term or long term behaviour of SOCE  $\text{Ca}^{2+}$  dynamics.

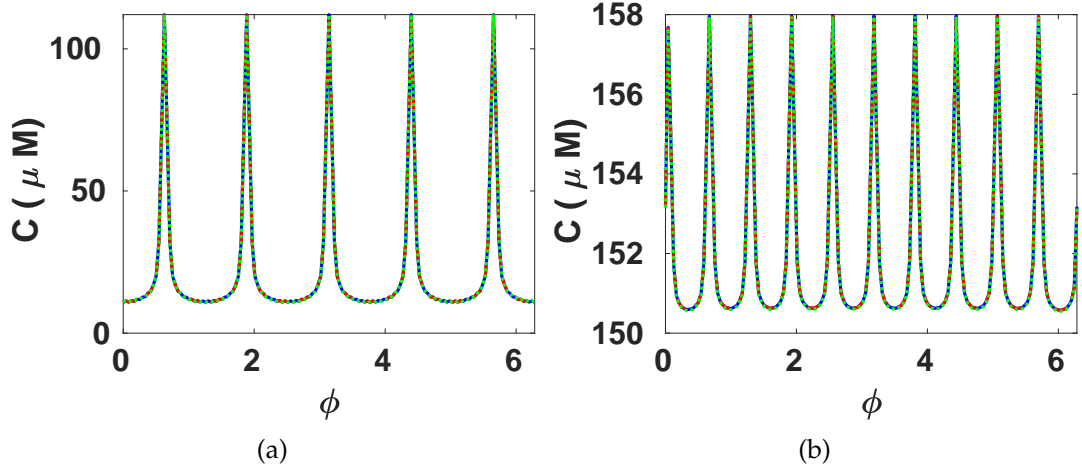


**Figure 4.13:** Comparing  $\text{Ca}^{2+}$  profiles after  $10^{-4}\text{s}$  simulated with three different time steps in the (a) ER-PM junction and (b) sub-PM ER. The blue line represents the  $\text{Ca}^{2+}$  concentration simulated with a time step  $dt = 1 \times 10^{-7}\text{s}$ , the red line represents the  $\text{Ca}^{2+}$  concentration simulated with a time step  $dt = 1 \times 10^{-6}\text{s}$  and the green line represents the  $\text{Ca}^{2+}$  concentration simulated with a time step  $dt = 1 \times 10^{-5}\text{s}$ .

### 4.3 Discussion

In this chapter we examined the effect of the spatial-temporal discretisations on the simulated  $\text{Ca}^{2+}$  profiles within the ER-PM junction and how the shape of the prescribed  $\text{Ca}^{2+}$  flux through Orai channels in the PM affected the  $\text{Ca}^{2+}$  profiles generated in the ER-PM junction. In particular, we found that coarse  $\phi$  discretisations resulted in oscillations in the  $\text{Ca}^{2+}$  concentration. We then investigated why the  $\text{Ca}^{2+}$  concentrations changed when the Orai channels were placed closer to the mantle of the cylinder and discovered that the total  $\text{Ca}^{2+}$  flux per channel was not consistent as the area of the grid elements increased. Finally, we examined the relationship between the time step and the  $\text{Ca}^{2+}$  profiles generated to understand how the time step affected the simulations.

First, we observed oscillations in the  $\text{Ca}^{2+}$  concentration which occurred because we were using a coarse  $\phi$  discretisation,  $\Delta\phi = 0.0628$ , that was not fine enough to smoothly integrate the sharp  $\text{Ca}^{2+}$  flux profile, shown by the black line in Figure 4.5(d). Such oscillations could result in PMCA pump or effector molecule activity that is not representative of the  $\text{Ca}^{2+}$  dynamics within the ER-PM junction during SOCE. For instance, if the PMCA pumps or effector molecules were subjected to an increase or decrease in  $\text{Ca}^{2+}$  concentration as a result of the oscillations instead of a true local/global increase due to SOCE this could result in unrealistic  $\text{Ca}^{2+}$  behaviour. We refined the  $\phi$  discretisation,

from  $\Delta\phi = 0.0628$  to  $\Delta\phi = 0.0126$ , to allow sufficiently smooth numerical integration over the sharp  $\text{Ca}^{2+}$  flux profile. However, this refined mesh resulted in reduced  $\text{Ca}^{2+}$  concentrations because we simultaneously reduced the total  $\text{Ca}^{2+}$  flux through the Orai channel. Furthermore, the fine  $\phi$  discretisation was not computationally feasible as it greatly increased the memory requirements and the run time of the simulations. The fine  $\phi$  discretisation loads a 39 Gb Green's function matrix into memory during the simulation whereas the coarse  $\phi$  discretisation only loads a 1.4 Gb matrix. Furthermore, the solution matrices are 1.1 Gb and 0.2 Gb, respectively, for the fine and coarse  $\phi$  discretisations. Therefore, there is a large increase in memory requirements during the simulation with the fine  $\phi$  discretisation. The run time of the simulations increased from 8 minutes to 10 hours when using the coarse and fine  $\phi$  discretisations, respectively. So, even if we adjusted the  $\text{Ca}^{2+}$  flux profile to ensure the total  $\text{Ca}^{2+}$  flux was the same using the  $\phi$  discretisation would be too computationally expensive in terms of memory requirements and simulation run time.

We then used a slightly refined  $\phi$  discretisation,  $\Delta\phi = 0.0419$ , and a  $\text{Ca}^{2+}$  flux profile given by equation (4.1) capable of approximating the sharp  $\text{Ca}^{2+}$  flux profile. The  $\text{Ca}^{2+}$  flux profiles are shown by the blue and black lines in Figure 4.6(c). The refined  $\phi$  discretisation with the  $\text{Ca}^{2+}$  flux profile given by equation (4.1) is a good approximation to the original  $\text{Ca}^{2+}$  flux profile and preserves the total  $\text{Ca}^{2+}$  influx. The  $\text{Ca}^{2+}$  concentration profile generated with  $\Delta\phi = 0.0419$  is a good approximation to the  $\text{Ca}^{2+}$  profile generated with the original  $\phi$  discretisation, shown by the blue and red lines in Figure 4.7(c). Using the slightly refined  $\phi$  discretisation with the  $\text{Ca}^{2+}$  flux profile given by equation (4.1), we successfully smoothed the  $\text{Ca}^{2+}$  profile while preserving the total  $\text{Ca}^{2+}$  flux through the Orai channel.

We notice in Figure 4.8 that the Orai channel placement affected the  $\text{Ca}^{2+}$  concentrations and channels placed towards the edge of the ER-PM junction generated greater  $\text{Ca}^{2+}$  concentrations than channels placed more centrally in the ER-PM junction. This change in the magnitude of the  $\text{Ca}^{2+}$  concentration is a consequence of the spatial discretisation as the grid elements have greater surface areas towards the edge of the ER-PM junction. The total  $\text{Ca}^{2+}$  flux through Orai channels placed at  $r = 50\text{nm}$  is greater than the total  $\text{Ca}^{2+}$  flux through Orai channels placed at  $r = 30\text{nm}$  leading to the increase in  $\text{Ca}^{2+}$  concentration seen in Figure 4.8(d). To counteract this we used a finer  $\phi$  discretisation,  $\Delta\phi = 0.0251$ , when simulating Orai channels towards the edge

of the ER-PM junction,  $r = 50\text{nm}$ , with Orai channels more centrally placed within the ER-PM junction,  $r = 30\text{nm}$ , simulated with the coarse  $\phi$  discretisation,  $\Delta\phi = 0.0416$ . We used  $\sigma_\phi = 0.05$  and  $\sigma_\phi = 0.03$  to constrain the width of the  $\text{Ca}^{2+}$  flux profile with a  $\phi$  discretisation of  $\Delta\phi = 0.0419$  and  $\Delta\phi = 0.0251$ , respectively, to ensure that the total  $\text{Ca}^{2+}$  flux through the channels is equal, as shown in Figure 4.10(b). The  $\text{Ca}^{2+}$  concentration of the Orai channel placed at  $r = 50\text{nm}$  with the fine  $\phi$  discretisation is then comparable with the  $\text{Ca}^{2+}$  concentration of the Orai channel placed at  $r = 30\text{nm}$  with the coarse  $\phi$  discretisation. Therefore, the Orai channel grid elements have the same areas and shapes to ensure the total  $\text{Ca}^{2+}$  flux is preserved and the  $\text{Ca}^{2+}$  concentration is not affected by the radial placement of the Orai channel.

Unfortunately, this limits the model to comparing  $\text{Ca}^{2+}$  concentrations generated by Orai channels arranged in a ring as we cannot include Orai channels at different radial positions within the same simulation because the total  $\text{Ca}^{2+}$  flux per channel depends on the radial position. Implementing a uniform spatial grid would remove this problem as the Orai channels will all be centred at elements of the same area and shape and therefore the total  $\text{Ca}^{2+}$  flux will be equal for each channel, this is something to consider in the future. One option would be to use a cuboid in place of the cylinder or to investigate methods which preserve the total  $\text{Ca}^{2+}$  flux through the grid elements.

Finally, we examined the effect of the time step on the  $\text{Ca}^{2+}$  profiles generated and paid particular attention to the ability of the time step to capture the SERCA pump dynamics. We were particularly interested in SERCA pump activity as the pumps depend on the  $\text{Ca}^{2+}$  concentration surrounding the channel and control the ER refilling dynamics of the model presented in Chapter 2. The ER-PM junction  $\text{Ca}^{2+}$  dynamics are dominated by the Orai channel which has a constant  $\text{Ca}^{2+}$  influx but the sub-PM ER  $\text{Ca}^{2+}$  dynamics are dominated by the SERCA pumps whose activity depends on the  $\text{Ca}^{2+}$  profile in the ER-PM junction. Since the Orai channel flux does not depend on the  $\text{Ca}^{2+}$  concentration, all three time steps can describe the ER-PM junction dynamics well, as seen in Figures 4.12(a) and 4.13(a). However, in the sub-PM ER we see that the  $\text{Ca}^{2+}$  dynamics depend on the chosen time step and if the time step is too large then the  $\text{Ca}^{2+}$  dynamics are not representative of the true behaviour of the system. We see in Figure 4.12(b) that the  $\text{Ca}^{2+}$  profile in the sub-PM ER simulated with the largest time step is smaller than the  $\text{Ca}^{2+}$  profiles simulated with the two smaller time steps. This suggests that the largest time step is not fine enough to capture transient  $\text{Ca}^{2+}$  dynamics occurring early during SOCE.

All three time steps capture the sub-PM ER  $\text{Ca}^{2+}$  dynamics later in SOCE, as seen in Figure 4.13(b). Therefore, we can choose different time steps depending on what aspect of SOCE we are interested in, e.g. early SOCE vs late SOCE, or even mix the time steps and use a small time step to capture the early transient  $\text{Ca}^{2+}$  dynamics but use a larger time step to capture the long term  $\text{Ca}^{2+}$  behaviour of the system.

In conclusion, we have shown that the spatio-temporal discretisations are important factors to consider when simulating the model from the analytical formulas. This chapter also highlights the importance of conserving the total  $\text{Ca}^{2+}$  flux when using a non-uniform mesh to ensure the magnitudes of the  $\text{Ca}^{2+}$  concentrations do not change according to the radial position of the channels. Through investigating the temporal discretisations we can now implement simulations with multiple time steps to ensure we capture the important  $\text{Ca}^{2+}$  behaviours of early, transient SOCE dynamics and long term refilling dynamics. Small time steps will capture the early  $\text{Ca}^{2+}$  dynamics occurring in response to channel opening or pump activation. Larger time steps will describe the long term  $\text{Ca}^{2+}$  dynamics well but will not provide a detailed description of the transient  $\text{Ca}^{2+}$  dynamics after channel opening or pump activation. Moreover, using a small time step to describe the long term dynamics will result in very long run times for the simulations, whereas a large time step could considerably reduce the run time. The inclusion of multiple time steps within one simulation will increase the efficiency of the simulations and decrease the run time as small time steps will not be used to look at the long term dynamics.

## Chapter 5

# The effect of Orai channel and SERCA pump placement on ER refilling

In this chapter we use the mathematical model developed in Chapters 2, 3 and 4 to investigate how the placement of the  $\text{Ca}^{2+}$  signalling machinery affects  $\text{Ca}^{2+}$  signals and ER refilling during SOCE. This chapter is an extension of the work published in Cell Calcium [50].

Since we prescribe the flux per unit area we use a spatial discretisation such that the grid elements representing the Orai channel have the same area as current estimates of the Orai channel area, approximately  $0.25\text{nm}^2$  [56]. This ensures that the total flux through the grid elements is a good approximation of the total flux through one Orai channel. The non-clustered Orai channels will be placed along a ring of radius  $r = 50\text{nm}$  in the ER-PM junction and therefore the grid elements will have larger areas than the clustered Orai channels which are placed on a ring of radius  $r = 30\text{nm}$  if the  $\phi$  discretisation is the same for the two radial placements. As discussed in Chapter 4, the non-clustered Orai channels will have a finer  $\phi$  grid to ensure that the grid element representing the Orai channel will have the same area as current estimates of the Orai channel area. This ensures that the total influx per Orai channel is the same for both the clustered and non-clustered distributions of Orai channels.

We implement the method developed in Chapters 2, 3 and 4 numerically in MATLAB; we use matrix multiplications to compute integrals, and matrix additions to include the boundary condition solutions, which are not computationally expensive. One key limitation of this approach is that the size of the

spatial discretisation needed for the Orai channels in the non-clustered configuration increases the run time of the simulations as it increases the computational intensity and memory requirements. The simulations were ran on one CPU core of a Dell R630 server with 2 x Intel(R) Xeon(R) E5-2660 v4 processors and 768Gb RAM. The clustered Orai channel simulations involved a load time (to load the precomputed variables into MATLAB) of 10 hours with a run time (the time to run the simulations) of 20 hours and used approximately 30% of the available RAM. However, the finer spatial discretisation used when the Orai channel were not clustered led to a load time of 50 hours and a run time of 60 hours and used approximately 60% of the available RAM. The code is available on GitHub at [https://github.com/emmamcivor/supplementary/tree/master/mcivor\\_three\\_2018](https://github.com/emmamcivor/supplementary/tree/master/mcivor_three_2018) and instructions for running the code are provided.

## 5.1 Clustering of Orai channels creates spatially distinct $\text{Ca}^{2+}$ profiles in the ER-PM junction

We compare the  $\text{Ca}^{2+}$  profiles generated by Orai channels in a clustered and non-clustered configuration to examine the effect of clustering on the spatial signature of the  $\text{Ca}^{2+}$  signals. Samanta *et al.* [67] estimated the inter-channel distance of an Orai channel and its nearest neighbour to be 47nm. We place the Orai channels in a ring with an inter-channel distance of 39nm when the channels are clustered, so the channels are placed closer together than the nearest neighbour estimate. When the channels are non-clustered we use an inter-channel distance of 65nm, so the channels are more widely spaced than the nearest neighbour estimate. Manjarres *et al.* [48,49] observed SERCA2b pumps co-localising to the ER-PM junction and proposed that SERCA2b pumps form a ring like structure surrounding the Orai channels in the ER-PM junction [5, 18]. We place the Orai channels and SERCA pumps in concentric rings, as depicted in Figure 5.1(a) and 5.1(b).

The  $\text{Ca}^{2+}$  profiles at the PM generated by the clustered and non-clustered Orai distributions are shown in Figures 5.1(c) and 5.1(d). The magnitude of the  $\text{Ca}^{2+}$  concentrations are similar, approximately  $60\mu\text{M}$ , but we observe different patterns for each Orai distribution. The Orai channel microdomains overlap more when the channels are clustered which results in a larger region of elevated  $\text{Ca}^{2+}$ , reaching  $\text{Ca}^{2+}$  concentrations of around  $7\mu\text{M}$  in the centre of the ER-PM

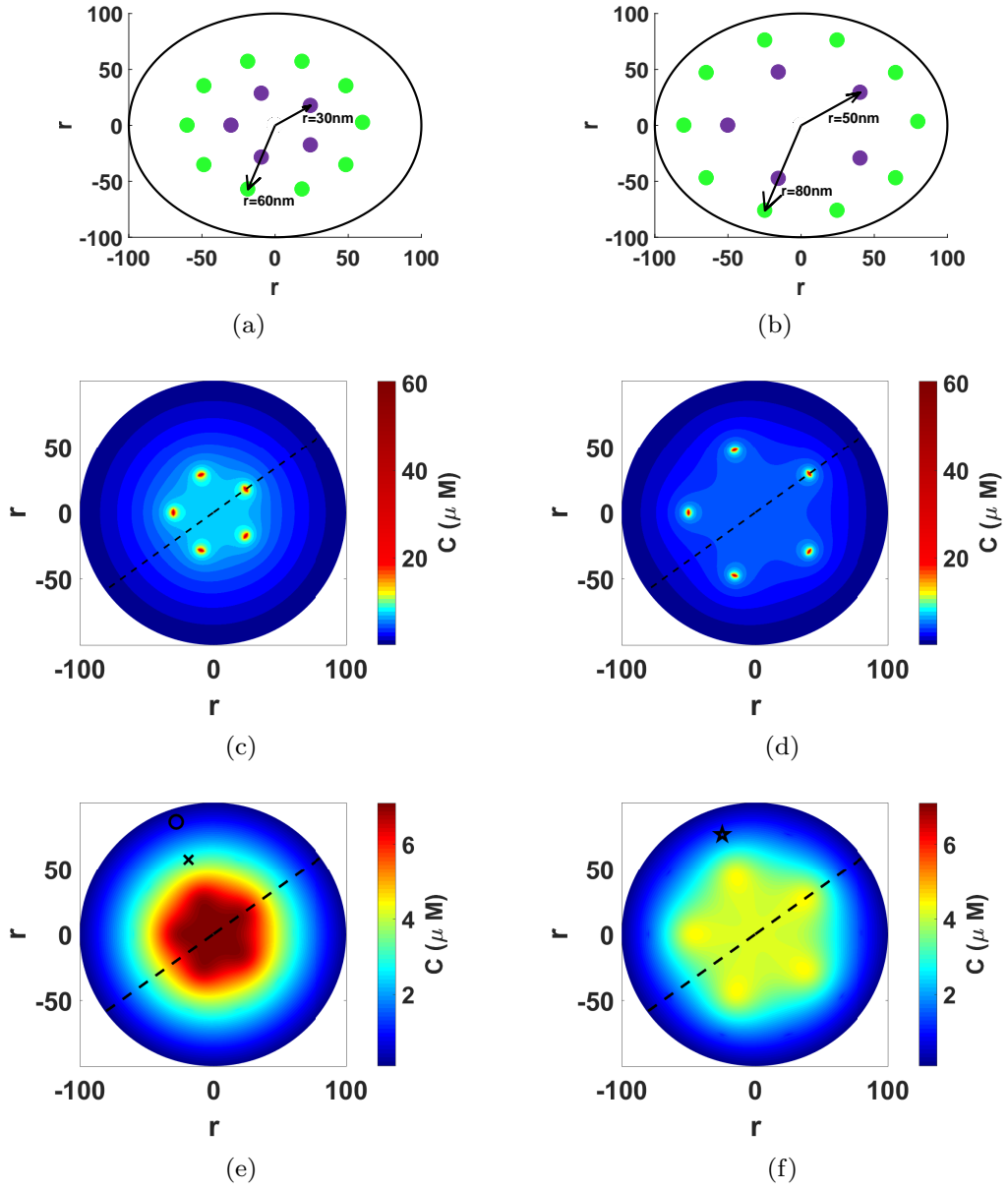


**Figure 5.1:** (a,b) Illustrations of the placement of Orai channels (purple) on the PM in a clustered and non-clustered configuration with SERCA pumps (green) placed 30nm away. (c,d)  $\text{Ca}^{2+}$  profiles at the PM when Orai channels are clustered and non-clustered. (e,f)  $\text{Ca}^{2+}$  profiles at the ER membrane when Orai channels are clustered and non-clustered. Parameters as in Tables D.1 and D.2 and non-clustered mesh has parameters  $\Delta\phi = 0.0251$  and  $\sigma_\phi = 0.03$  to ensure the size of the Orai channel is the same in both the clustered and non-clustered Orai channel configurations.

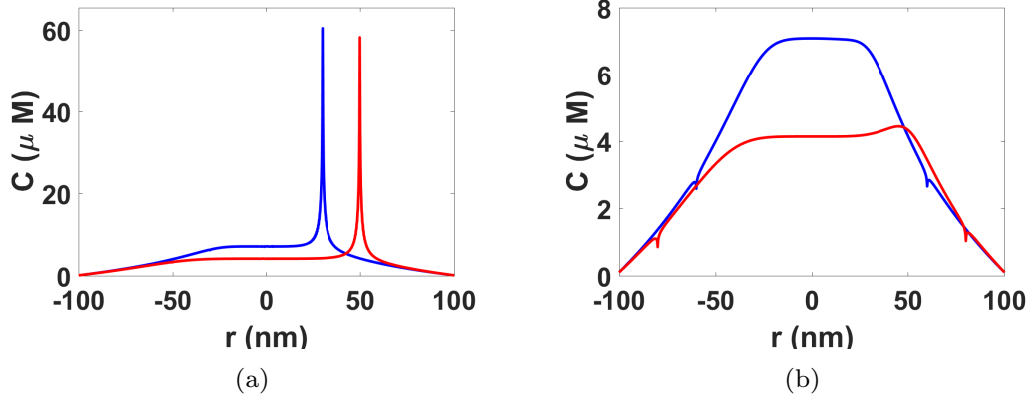


**Figure 5.2:** (a)  $\text{Ca}^{2+}$  profiles at the PM along the black dashed lines in Figure 5.1(c) and 3(d). (b)  $\text{Ca}^{2+}$  profiles at the ER membrane along the black dashed lines in Figure 5.1(e) and 3(f). The blue and red lines represent the  $\text{Ca}^{2+}$  profiles arising from the clustered and non-clustered Orai channel distributions, respectively. Parameters as in Tables D.1 and D.2.

junction. The microdomains of the non-clustered channels overlap to a lesser extent with  $\text{Ca}^{2+}$  concentrations of approximately  $4\mu\text{M}$ .

The differences in the spatial  $\text{Ca}^{2+}$  concentrations generated by clustered and non-clustered Orai channels are even more prominent at the ER membrane, as seen in Figures 5.1(e) and 5.1(f). The microdomains of the clustered Orai channels merge into one region of elevated  $\text{Ca}^{2+}$  and the individual channel microdomains are completely absorbed into this  $\text{Ca}^{2+}$  pattern. However, the microdomains of the non-clustered channels are still distinguishable as circles inside the star shaped region of elevated  $\text{Ca}^{2+}$  in Figure 5.1(f). The clustered configuration attains  $\text{Ca}^{2+}$  concentrations of around  $7\mu\text{M}$  along the ER membrane whereas the  $\text{Ca}^{2+}$  concentrations generated by the non-clustered channels peak at approximately  $4.5\mu\text{M}$ .

We directly compare the  $\text{Ca}^{2+}$  profiles generated at Orai channels on the PM in Figure 5.2(a) by plotting the  $\text{Ca}^{2+}$  profiles at a location represented by the dashed black lines in Figures 5.1(c) and 5.1(d). At the PM, we see that the clustered channel configuration (blue line) results in greater elevation of  $\text{Ca}^{2+}$  concentrations around  $r = 0$  than the non-clustered channels (red line). This increased amplitude occurs because the clustered microdomains overlap to a greater extent than the non-clustered microdomains. By comparing the  $\text{Ca}^{2+}$  profiles at the ER membrane directly beneath the Orai channels in Figure 5.2(b), we see that clustering of Orai channels (blue line) greatly increases the magnitude of the  $\text{Ca}^{2+}$  concentrations achieved in the ER-PM junction. The clus-

tered configuration reaches  $\text{Ca}^{2+}$  concentrations of  $7\mu\text{M}$  which is almost 50% greater than the  $\text{Ca}^{2+}$  concentrations of  $4.4\mu\text{M}$  generated by the non-clustered configuration. We observe small dips in the  $\text{Ca}^{2+}$  profiles at the ER membrane in Figure 5.2(b) corresponding to  $\text{Ca}^{2+}$  efflux from the ER-PM junction via SERCA pumps. The difference in the  $\text{Ca}^{2+}$  concentrations demonstrates that clustering of Orai channels controls the amplitude of the  $\text{Ca}^{2+}$  profile and creates spatially distinct  $\text{Ca}^{2+}$  profiles. Samanta *et al.* [67] observed that confinement of Orai channels within the ER-PM junctions led to increased c-fos and NFAT activation. Using a three-dimensional model of an ER-PM junction, they found that clustering of Orai channels increased the  $\text{Ca}^{2+}$  concentrations on the ER surface and proposed that the ability to control the local spatial  $\text{Ca}^{2+}$  signal via clustering would result in more effective activation of c-fos gene expression and NFAT. Our model demonstrates that the inter-channel distance is an important parameter for governing the amplitude and shape of  $\text{Ca}^{2+}$  signals generated in the ER-PM junction. Therefore, the ability of Orai channels to cluster provides a mechanism by which  $\text{Ca}^{2+}$  can specifically activate distinct downstream signalling processes, such as NFAT [72], by controlling the amplitude and shape of the  $\text{Ca}^{2+}$  signal.

## 5.2 Clustering Orai channels does not enhance ER refilling

ER refilling requires SERCA pumps to transport  $\text{Ca}^{2+}$  from the ER-PM junction to the sub-PM ER and the level of SERCA pump activity depends on the  $\text{Ca}^{2+}$  concentration surrounding the pumps. We measure the activity of the SERCA pumps in terms of the maximal activity possible, where 100% corresponds to a maximally activated SERCA pump. We have seen in Section 5.1 that clustering increases the local  $\text{Ca}^{2+}$  concentrations in the ER-PM junction, so in this section we investigate whether clustering results in more highly activated SERCA2b pumps leading to increased rates of ER refilling. We fix the distance between the Orai channels and SERCA2b pumps to ensure that any change in ER refilling is solely attributed to the Orai channel arrangement.

In our simulations we find that the  $\text{Ca}^{2+}$  profile within the ER-PM junction reaches an equilibrium concentration profile in less than 0.25ms. The resulting SERCA2b pump fluxes, and therefore activity, will remain constant once this equilibrium state has been achieved. Therefore, SERCA2b pump activity

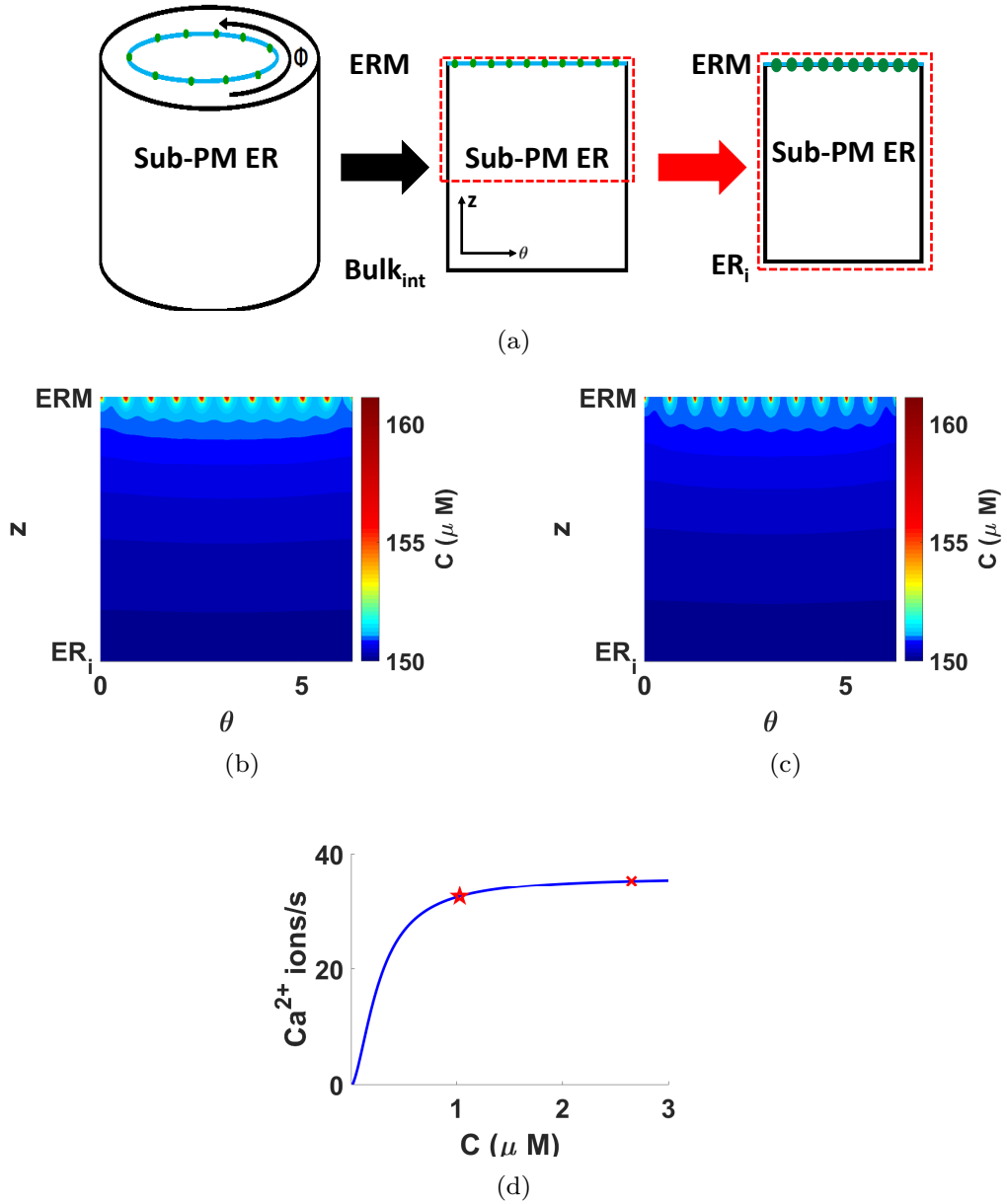


**Figure 5.3:** (a) Diagram explaining how we visualise the  $\text{Ca}^{2+}$  concentration in the sub-PM ER. The green circles represent the SERCA pumps on the ER membrane. (b,c)  $\text{Ca}^{2+}$  profiles generated in the sub-PM ER along the ring of SERCA2b pumps in response to a clustered and non-clustered Orai channel distribution. (e) Plot of the  $\text{Ca}^{2+}$  transport activity of SERCA2b. The red cross and star correspond to the transport activity in response to the clustered and non-clustered Orai channels, respectively. Parameters as in Tables D.1 and D.2 and non-clustered mesh has parameters  $\Delta\phi = 0.0251$  and  $\sigma_\phi = 0.03$ .

after 1ms will be the same as the SERCA2b pump activity after a longer time, provided the Orai channel has not switched off and disturbed the equilibrium fluxes. It is important to note that the time to achieve an equilibrium  $\text{Ca}^{2+}$  profile within the ER-PM junction depends on the  $\text{Ca}^{2+}$  channels and pumps included in the junction. Additional interactions, such as PMCA activity, could prevent or delay attainment of an equilibrium  $\text{Ca}^{2+}$  profile in which case the early ER refilling will not be representative of the long term ER refilling. In our simulations we find that the  $\text{Ca}^{2+}$  profile in the ER-PM junction reaches an equilibrium concentration within 0.25ms so the early refilling will be representative of the long term ER refilling in this study.

SERCA2b pumps are the only component in the model that transports  $\text{Ca}^{2+}$  into the sub-PM ER to refill the depleted  $\text{Ca}^{2+}$  store. Therefore, the rate of ER refilling depends on the SERCA2b pump activity and greater SERCA2b pump activity results in faster ER refilling. We can consider the SERCA2b pump activity in response to clustered and non-clustered Orai to compare the rate of ER refilling achieved in response to each Orai channel distribution. As the SERCA2b pump activity remains constant, the level of ER refilling will proceed at the same rate while the ER-PM junction is in equilibrium. This means that although the ER will have been refilled to a greater extent after a longer amount of time the rate of ER refilling with the clustered and non-clustered Orai channels will be the same at both early and late times. As we are concerned with the rate of ER refilling for the clustered and non-clustered Orai channels, and not the total magnitude of ER refilling, we will compare the  $\text{Ca}^{2+}$  profiles after 1ms.

The SERCA2b pumps denoted by the black cross and star in Figure 5.1(e) and 5.1(f) are placed a distance of 30nm from the clustered and non-clustered Orai channels, respectively. The  $\text{Ca}^{2+}$  concentration surrounding the SERCA2b pumps is higher in the clustered Orai configuration than the non-clustered configuration. The different  $\text{Ca}^{2+}$  concentrations around the SERCA2b pumps are seen in Figure 5.2(b). The SERCA2b pumps are situated at the dips in the  $\text{Ca}^{2+}$  profile at concentrations of approximately  $2.658\mu\text{M}$  and  $1.032\mu\text{M}$  in the clustered and non-clustered Orai configurations, respectively. The SERCA2b pumps are highly activated in both Orai distributions, but there is a slight decrease in SERCA2b activity from 98% with the clustered Orai channel distribution to 90% when the channels are non-clustered. Therefore, the rate of ER refilling is very similar for both the clustered and non-clustered Orai channel distributions.

We are interested in the rate of ER refilling but we can show the extent of  $\text{Ca}^{2+}$  refilling in the sub-PM ER after 1ms to allow a visual and more intuitive comparison of the ER refilling occurring in response to the clustered and non-clustered Orai channels. We take a slice along the blue line in Figure 5.3(a) on which the SERCA2b pumps sit and ‘unfurl’ this slice to visualise the  $\text{Ca}^{2+}$  concentration throughout the sub-PM ER beneath the SERCA2b pumps. We then focus on the section of the sub-PM ER from an internal point of the sub-PM ER ( $\text{ER}_i$ ) to the ER membrane, enclosed by the red dashed rectangle in Figure 5.3(a). Focusing on this section of the sub-PM ER allows us to capture the structure of the  $\text{Ca}^{2+}$  patterns produced during refilling of the ER via SERCA pumps. We can then consider the extent to which  $\text{Ca}^{2+}$  diffuses from the ER membrane to compare the relative levels of ER refilling.

We show the extent to which  $\text{Ca}^{2+}$  has diffused from the SERCA2b pumps when the Orai channels are clustered and non-clustered in Figures 5.3(b) and 5.3(c). As the SERCA2b pumps transport  $\text{Ca}^{2+}$  into the sub-PM ER regions of elevated  $\text{Ca}^{2+}$  are created around the SERCA2b pumps. These regions overlap when the Orai channels are clustered as the SERCA2b pumps are closer together, so SERCA2b pump placement also creates local  $\text{Ca}^{2+}$  patterns in the sub-PM ER. We observe that the maximum  $\text{Ca}^{2+}$  concentrations achieved after 1ms are approximately  $160\mu\text{M}$  which is an increase of  $10\mu\text{M}$ . Jousset *et al.* [37] found that the ER  $\text{Ca}^{2+}$  store is refilled within two minutes. Therefore, we would not expect to see significant levels of refilling after 1ms. However, the extent of  $\text{Ca}^{2+}$  diffusion after 1ms within the sub-PM ER is very similar for the clustered and non-clustered Orai distributions. This further demonstrates that the rate of ER refilling is roughly equal in both cases.

In Figure 5.3(d) we compare the  $\text{Ca}^{2+}$  transport rates of SERCA2b in response to clustered and non-clustered Orai channel distributions. The activity of the SERCA2b pumps are shown by the red cross and red star, respectively. As we can see, the decrease in  $\text{Ca}^{2+}$  concentration surrounding the SERCA2b pumps when Orai channels are clustered and non-clustered, predicted from the simulations, does not result in a great decrease in the SERCA2b  $\text{Ca}^{2+}$  transport rate. So, although clustering increases  $\text{Ca}^{2+}$  concentrations in the ER-PM junction, ER refilling is not enhanced by Orai channel clustering.

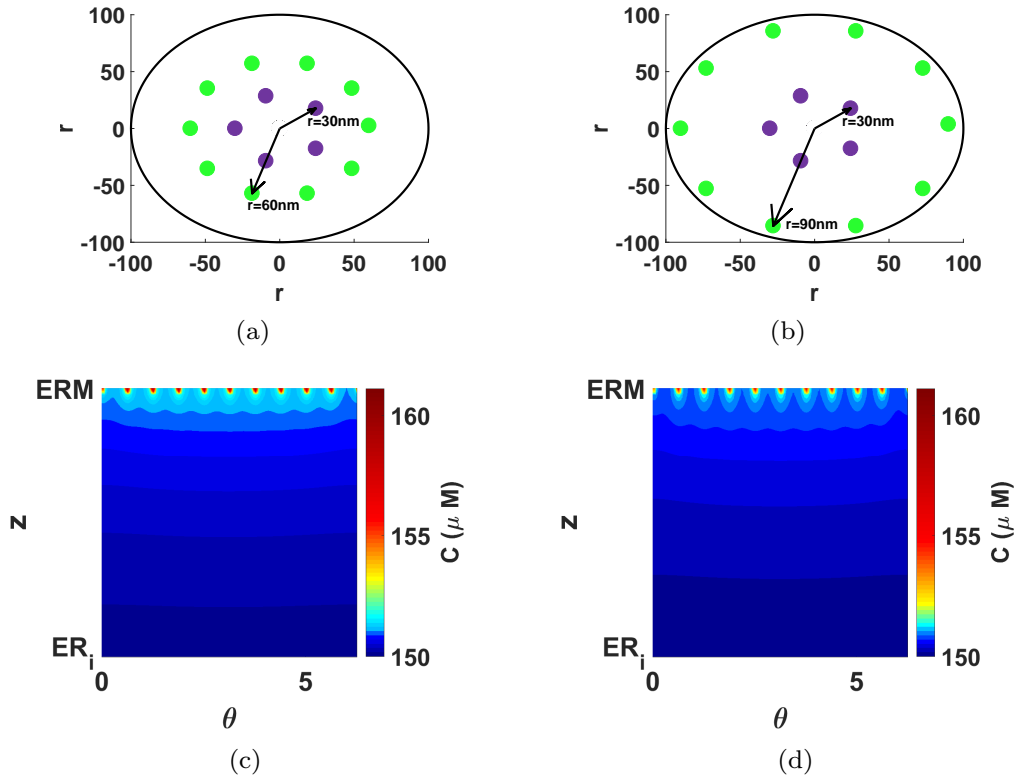


**Figure 5.4:** (a,b) Illustrations of the placement of Orai channels (purple) on the PM in a clustered configuration with SERCA pumps (green) placed 30nm or 60nm away. (c,d) Ca<sup>2+</sup> profiles generated in the sub-PM ER along the ring of SERCA2b pumps 30nm and 60nm from the Orai channels. Parameters as in Tables D.1 and D.2.

### 5.3 The distance between Orai channels and SERCA2b pumps is not a major regulator of ER refilling

In the previous section, we demonstrated that clustering does not enhance ER refilling, so we now focus on the second factor which could control SERCA pump activity and ER refilling: the distance between Orai channels and SERCA pumps.

The peripheral Ca<sup>2+</sup> concentration is roughly equal for clustered and non-clustered Orai channel distributions (see Figure 5.2). We therefore consider clustered Orai channels only, to ensure that any results are a consequence of the distance between channels and pumps. We place the SERCA2b pumps at distances of 30nm and 60nm from the Orai channels, as illustrated in Figures 5.4(a) and 5.4(b). This approach can determine how the proximity of SERCA2b pumps to Orai channels affects the rate of ER refilling. As in Section 5.2, we are concerned with the rate of ER refilling and not the total magnitude of ER

refilling. In this section we compare ER refilling after 1ms when the SERCA2b pumps are placed 30nm and 60nm from the Orai channels to investigate how the placement of the SERCA2b pumps affects the rate of ER refilling.

The black cross and circle in Figure 5.1(e) represent the SERCA2b pumps at distances of 30nm and 60nm from the Orai channels.  $\text{Ca}^{2+}$  microdomains are characterised by a steep decrease in  $\text{Ca}^{2+}$  concentration away from the Orai channels, which can be seen in Figure 5.1(e). This ensures that the SERCA2b pumps are exposed to different  $\text{Ca}^{2+}$  concentrations when placed close to and far from the Orai channels. Such decreases in the  $\text{Ca}^{2+}$  concentrations surrounding the SERCA2b pumps could reduce the activity of the SERCA2b pump and potentially reduce the rate of ER refilling.

The simulated SERCA2b pump activity 30nm and 60nm from the Orai channels is 98% and 73%, respectively. The pumps are highly activated close to the Orai channels, but continue working well above half maximal activity even in peripheral locations. This suggests that even though there is a decrease in SERCA2b activity, ER refilling will still proceed at a sufficiently high rate to ensure the ER is refilled, although it will be slightly slower.

After 1ms, we compare the  $\text{Ca}^{2+}$  concentrations in the sub-PM ER directly beneath the SERCA2b pumps in Figures 5.4(c) and 5.4(d). The  $\text{Ca}^{2+}$  concentration profiles are similar and the sub-PM ER is refilled to the same extent by SERCA2b pumps placed at both locations within the ER-PM junction.  $\text{Ca}^{2+}$  from the SERCA2b pumps has diffused similar distances away from the ER membrane with each SERCA2b pump placement.

This suggests that ER refilling does not depend greatly on the placement of SERCA2b pumps. The pumps located further from the Orai channel will refill the ER at a slower rate but the increased distance does not drastically reduce the rate of ER refilling. Therefore, the proximity of SERCA2b pumps to Orai channels is not a major regulator of ER refilling.

## 5.4 The placement of SERCA2a pumps has a greater impact on ER refilling than the placement of SERCA2b pumps

In Section 5.3 we examined how the proximity of SERCA2b pumps to Orai channels impacted ER refilling and demonstrated that the placement of SERCA2b pumps within the ER-PM junction only weakly affected ER refilling. Sampieri *et al.* [68] observed SERCA2a pumps co-localising to the ER-PM junction during SOCE. SERCA2a and SERCA2b are functionally distinct with SERCA2a having a lower affinity for  $\text{Ca}^{2+}$  and higher  $\text{Ca}^{2+}$  turnover rate [19,47]. Such different kinetic parameters could result in different ER refilling dynamics depending on the type of SERCA pump isoform. In this section we include only SERCA2a pumps to investigate how the placement of SERCA2a pumps affects the rate of ER refilling. We again find that the ER-PM junction reaches an equilibrium  $\text{Ca}^{2+}$  concentration profile within less than 0.25ms and the SERCA2a fluxes are constant after this equilibrium is reached. Therefore, we compare the rates of ER refilling after 1ms as they will be representative of the long term ER refilling rate.

As in the previous section, we consider only the clustered Orai channel arrangement and only include SERCA2a pumps to ensure that our results are a direct consequence of the distance between Orai channels and SERCA2a pumps. We illustrate the placement of the Orai channels and SERCA pumps in Figures 5.4(a) and 5.4(b), where the green circles now represent SERCA2a pumps at distances of 30nm and 60nm from the Orai channels, respectively.

The  $\text{Ca}^{2+}$  microdomains generated around the Orai channels ensure that the  $\text{Ca}^{2+}$  concentrations surrounding the SERCA2a pumps placed 30nm are larger than the concentrations surrounding the SERCA2a pumps 60nm from the Orai channel (see Figure 5.1(e)). Again, this reduction in  $\text{Ca}^{2+}$  concentration could control the level of SERCA2a activity and thus regulate ER refilling.

The simulated SERCA2a pump activity 30nm and 60nm from the Orai channels is 98% and 52%, respectively. As with the SERCA2b pumps, we see that the SERCA2a pumps located 30nm from the Orai channels are very highly activated. However, the SERCA2a pumps located peripherally within the ER-PM junction are working only slightly above half maximal activity. Therefore, the distance between SERCA2a pumps and Orai channels is an important fac-

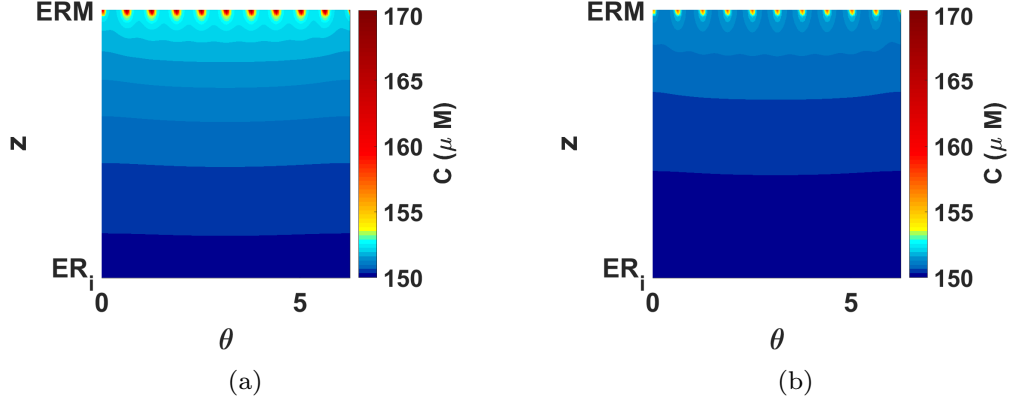


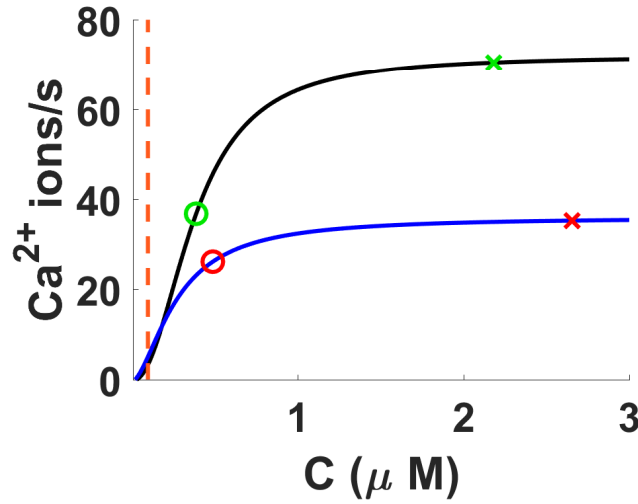
**Figure 5.5:** (a,b)  $\text{Ca}^{2+}$  profiles generated in the sub-PM ER along the ring of SERCA2a pumps 30nm and 60nm from the Orai channels. Parameters as in Tables D.1 and D.2 in section D of the Appendix.

tor controlling SERCA2a activity as increasing the distance between the Orai channel and SERCA2a pump halves SERCA2a pump activity thus drastically reducing the ER refilling rate.

We compare the  $\text{Ca}^{2+}$  concentrations in the sub-PM ER directly beneath the SERCA2a pumps in Figures 5.5(a) and (b). After 1ms,  $\text{Ca}^{2+}$  from the SERCA2a pumps placed 30nm from the Orai channels has diffused much further than  $\text{Ca}^{2+}$  from SERCA2a pumps placed 60nm from the Orai channels. Therefore, placing SERCA2a pumps 30nm from the Orai channels results in faster ER refilling than SERCA2a pumps placed 60nm from the Orai channels. In fact, the SERCA2a pumps 30nm from the Orai channels achieve  $\text{Ca}^{2+}$  concentrations of  $170\mu\text{M}$  within 1ms whereas the SERCA2a pumps 60nm from the Orai channels only attain  $\text{Ca}^{2+}$  concentrations of approximately  $160\mu\text{M}$ . Given that the depleted ER concentration is  $150\mu\text{M}$ , this shows that ER refilling is twice as fast when SERCA2a pumps are closer to the Orai channels, which is what we expect since the pumps 60nm from the channels are working at approximately 50% activity levels.

This difference in the rates of ER refilling suggests that the placement of SERCA2a pumps in the ER-PM junction and in particular their proximity to Orai channels controls the rate of ER refilling.

SERCA pumps are the only structures in our model capable of transporting  $\text{Ca}^{2+}$  from the ER-PM junction into the sub-PM ER so the SERCA pump  $\text{Ca}^{2+}$  transport activity is a measure of the ER refilling rate, with higher SERCA pump  $\text{Ca}^{2+}$  transport activity corresponding to faster ER refilling. We compare the SERCA pump  $\text{Ca}^{2+}$  transport activity for both SERCA2a and SERCA2b



(a)

**Figure 5.6:**  $\text{Ca}^{2+}$  transport rates of SERCA2a and SERCA2b pumps represented by the black and blue curves, respectively. Green circle and triangle denote clustered Orai channel arrangements with SERCA2a pumps placed 30nm and 60nm away, respectively. Red circle and triangle denote clustered Orai channel arrangements with SERCA2b pumps placed 30nm and 60nm away, respectively. The dashed orange line represents the baseline  $\text{Ca}^{2+}$  concentration of the ER-PM junction,  $[\text{Ca}^{2+}]_i = 0.1\mu\text{M}$ .

pumps in Figure 5.6. We plot the  $\text{Ca}^{2+}$  transport rate against  $\text{Ca}^{2+}$  concentration and the black and blue curves represent the SERCA2a and SERCA2b  $\text{Ca}^{2+}$  transport rates, respectively. The green (red) crosses and circles represent the activity levels of SERCA2a (SERCA2b) pumps placed 30nm and 60nm from the clustered Orai channels. The dashed orange line represents the baseline  $\text{Ca}^{2+}$  concentration of the ER-PM junction,  $[\text{Ca}^{2+}]_i = 0.1\mu\text{M}$ . In Figure 5.6 we see that both SERCA pumps have similar  $\text{Ca}^{2+}$  transport rates at  $\text{Ca}^{2+}$  concentrations just above the resting  $\text{Ca}^{2+}$  concentration and that the distance between Orai channels and SERCA pumps has a much greater impact on the  $\text{Ca}^{2+}$  transport rate of SERCA2a than SERCA2b.

Although we can plot the SERCA  $\text{Ca}^{2+}$  transport curves in Figure 5.6 we cannot predict the activity of the SERCA pumps without knowing the  $\text{Ca}^{2+}$  concentrations in the ER-PM junction. This information is not available before we simulate SOCE as we cannot measure the  $\text{Ca}^{2+}$  concentrations experimentally. Therefore, it is necessary to simulate SOCE to be able to predict the local  $\text{Ca}^{2+}$  concentrations and SERCA activities and thus compare the rates of ER refilling. The simulations of the  $\text{Ca}^{2+}$  concentrations within the sub-PM ER provide a second method of measuring and comparing the ER refilling occurring as we

visualise the  $\text{Ca}^{2+}$  profiles within the sub-PM ER.

Therefore, although the arrangement of Orai channels and placement of SERCA2b pumps have minor influences on ER refilling the key factor controlling ER refilling is the placement of SERCA2a pumps and in particular, their proximity to Orai channels.

## 5.5 Interactions between Orai channels and SERCA pumps cause highly heterogeneous $\text{Ca}^{2+}$ profiles in the ER-PM junction

In Sections 5.1 - 5.4 we showed that Orai channel placement controls the shape and amplitude of the  $\text{Ca}^{2+}$  profile and that the proximity of SERCA2a pumps to Orai channels is a key regulator of ER refilling, whereas the placement of Orai channels and SERCA pumps only weakly affect ER refilling. We now take a slice along the radius of Orai channels and SERCA pumps within the ER-PM junction, shown in Figure 5.7(a), to compare the  $\text{Ca}^{2+}$  profiles generated within the ER-PM junction. When the Orai channels are clustered the Orai channel microdomains overlap and elevate the baseline  $\text{Ca}^{2+}$  concentration to a greater extent than the non-clustered Orai channels, as seen by the light and dark blue regions in Figures 5.7(a) and (b), respectively. This leads to considerably different  $\text{Ca}^{2+}$  concentrations surrounding each set of Orai channels which could result in selective activation of nearby signalling molecules [16,17,55,58].

Orai channels dominate the  $\text{Ca}^{2+}$  profile near the channels, as seen in Figure 5.7, but as we move towards the edge of the ER-PM junction the elevation due to the Orai channel is less pronounced and SERCA pump activity begins to shape the  $\text{Ca}^{2+}$  profile, as seen in Figure 5.8 which shows the  $\text{Ca}^{2+}$  profiles 30nm from the clustered and non-clustered Orai channels and 60nm from the clustered Orai channels. Firstly, we see that the  $\text{Ca}^{2+}$  concentration is greater 30nm from the clustered Orai channels, with concentrations reaching  $3\mu\text{M}$ , than 30nm from the non-clustered Orai channels, with concentrations reaching approximately  $1.5\mu\text{M}$ , in Figures 5.8(a) and (b). Further to this, the dark red plumes extending from the PM represent the  $\text{Ca}^{2+}$  influx through Orai channels and the plumes of blue/yellow along the ER membrane (ERM) represent  $\text{Ca}^{2+}$  efflux through SERCA pumps. We see that, in both situations, the SERCA pumps introduce more heterogeneity into the  $\text{Ca}^{2+}$  profile via inter-

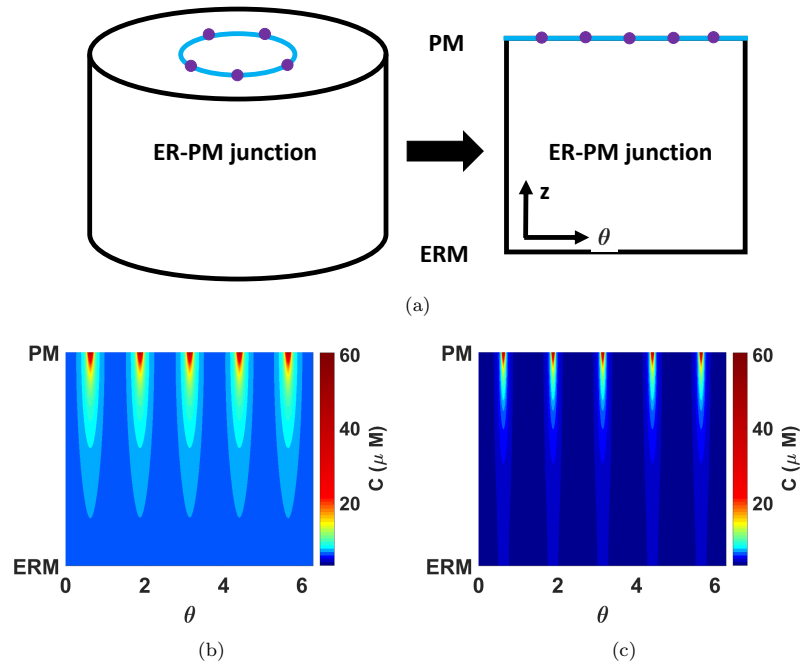


**Figure 5.7:** (a) Diagram explaining how we visualise the  $\text{Ca}^{2+}$  concentration in the ER-PM junction. The purple circles represent the Orai channels on the PM and ERM denotes the ER membrane. (b,c)  $\text{Ca}^{2+}$  profiles generated in the ER-PM junction along the ring of clustered and non-clustered Orai channels, respectively. Parameters as in Tables D.1 and D.2 in section D of the Appendix and the non-clustered mesh has parameters  $\Delta\phi = 0.0251$  and  $\sigma_\phi = 0.03$ .

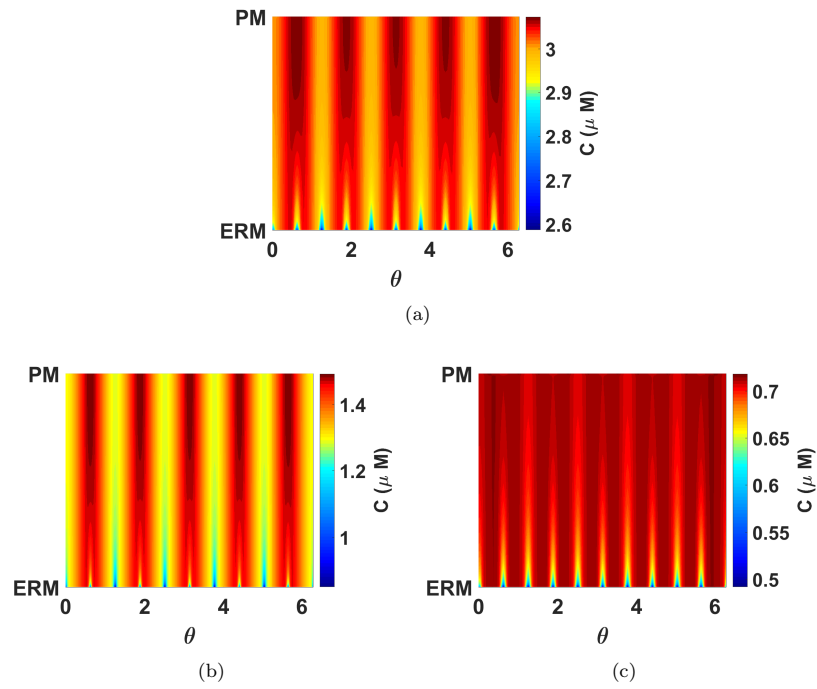


**Figure 5.8:** (a,b)  $\text{Ca}^{2+}$  profiles generated in the ER-PM junction along the ring of SERCA pumps placed 30nm from the clustered and non-clustered Orai channels, respectively. (c)  $\text{Ca}^{2+}$  profile generated in the ER-PM junction along the ring of SERCA pumps placed 60nm from the clustered Orai channels. Parameters as in Tables D.1 and D.2 in section D of the Appendix and the non-clustered mesh has parameters  $\Delta\phi = 0.0251$  and  $\sigma_\phi = 0.03$ .

actions between the Orai channel and SERCA pump plumes. In Figure 5.8(c) we visualise the  $\text{Ca}^{2+}$  concentration along the SERCA pumps 60nm from the clustered Orai channels and we find that the background  $\text{Ca}^{2+}$  concentration is significantly diminished in this region with concentrations only reaching  $0.7\mu\text{M}$  compared to Figure 5.8(a). In Figure 5.8(a) plumes of dark red along the PM represented  $\text{Ca}^{2+}$  influx via Orai channels, however, in Figure 5.8(c) these Orai channels plumes are not noticeable as we are so far from the source of  $\text{Ca}^{2+}$  influx and the only patterning occurring in this region is due to  $\text{Ca}^{2+}$  efflux via SERCA pumps.

Orai channel dynamics dominate the  $\text{Ca}^{2+}$  profile around the channels but this profile decays towards the edge of the ER-PM junction but at these distances SERCA pumps introduce additional patterning to the  $\text{Ca}^{2+}$  profile. Therefore, SERCA pumps introduce further heterogeneity into the  $\text{Ca}^{2+}$  profiles within the ER-PM junction and could be used to create more diverse and complex  $\text{Ca}^{2+}$  signals to enhance control over downstream signalling processes.

## 5.6 Discussion and Conclusion

We have constructed a three dimensional spatio-temporal model to simulate the  $\text{Ca}^{2+}$  dynamics in the ER-PM junction and sub-PM ER. Our model provides a means to visualise  $\text{Ca}^{2+}$  profiles in signalling microdomains on a nanometre scale, thus offering a highly spatially resolved view on local  $\text{Ca}^{2+}$  behaviour. Using this high spatial resolution we were able to investigate the impact of placement of signalling components, such as Orai channels and SERCA pumps, on the  $\text{Ca}^{2+}$  signals generated in response to SOCE and their effect on ER refilling.

The model shows that clustering of Orai channels causes  $\text{Ca}^{2+}$  microdomains to overlap leading to higher local  $\text{Ca}^{2+}$  concentrations in the ER-PM junction. The  $\text{Ca}^{2+}$  profiles generated by clustered and non-clustered profiles had distinct shapes and also attained different peak  $\text{Ca}^{2+}$  concentrations. The magnitude and shape of  $\text{Ca}^{2+}$  signals in the ER-PM junction could control activation of a range of downstream cellular functions [72], such as NFAT activation as hypothesised by Samanta *et al.* [67]. Therefore, clustering could act as a mechanism to create structured  $\text{Ca}^{2+}$  profiles ensuring sufficiently high  $\text{Ca}^{2+}$  concentrations are attained in regions of the signalling junction to activate specific effector molecules. The highly heterogeneous  $\text{Ca}^{2+}$  profiles also have the po-

tential to activate a diverse range of effector molecules within the junction in a controlled manner by targeting the molecules to regions of the junction according to the specific  $\text{Ca}^{2+}$  binding coefficients of each molecule [33,55,67,86].

Our model suggests a two-pronged approach to controlling spatial  $\text{Ca}^{2+}$  patterns within the ER-PM junction: Orai distribution and SERCA pump placement. The amplitude and shape of  $\text{Ca}^{2+}$  signals throughout the ER-PM junction are strongly controlled by the Orai channel distribution. This could allow Orai channels to create a structured  $\text{Ca}^{2+}$  profile so that signalling effector molecules can reside at specific locations within the ER-PM junction and allow distinct activation of multiple cellular signalling processes within restricted regions of the cell. The competition between the Orai channel and SERCA pumps could provide an additional mechanism of shaping the spatial  $\text{Ca}^{2+}$  profile and controlling  $\text{Ca}^{2+}$  signals based on Orai channel and SERCA pump location. We have only included ten SERCA pumps in our simulations as the number of SERCA pumps in the ER-PM junction has not been experimentally determined. Including more SERCA pumps would allow even greater control over the shape and magnitudes of the  $\text{Ca}^{2+}$  profiles and potentially further restrict the  $\text{Ca}^{2+}$  signalling domains within the ER-PM junction [18].

In this chapter we considered the importance of the locations of Orai channels and SERCA pumps within the ER-PM junction. We investigated the relationship between ER refilling and the inter Orai channel distance as well as the relationship between ER refilling and Orai-SERCA distance. Our results show that the rate of ER refilling is not greatly impacted by clustering of Orai channels or the placement of SERCA2b pumps. However, the rate of ER refilling does depend on the distance between SERCA2a pumps and Orai channels.

When SERCA2b pumps are placed 30nm away from the Orai channels, SERCA2b pump activity in both the clustered and non-clustered Orai channel configuration is high ( $\geq 90\%$ ). Although the  $\text{Ca}^{2+}$  concentration increases with clustered Orai channels, this does not correspond to a considerable increase in the  $\text{Ca}^{2+}$  transport rate of the SERCA2b pump, as seen in Figure 5.3(d). The reason for this is that SERCA pump activity only increases in small increments as it approaches its maximal activity level. Therefore, the rate of ER refilling is not enhanced by clustering Orai channels. Moving towards the periphery of the ER-PM junction, we observed a decrease in the  $\text{Ca}^{2+}$  concentration. Concomitantly, SERCA2b and SERCA2a pump activity was reduced from 98% to 72% and 98% to 52%, respectively, when the distance between Orai channels

and SERCA pumps was increased from 30nm to 60nm. The rate of ER refilling was similar for both distances with SERCA2b pumps but greatly reduced with SERCA2a pumps. We compared the  $\text{Ca}^{2+}$  transport rates of both SERCA2a and SERCA2b in Figure 5.6 and found SERCA2a to be much more sensitive to the observed  $\text{Ca}^{2+}$  concentration than SERCA2b, thus leading to greater control over ER refilling.

Our results suggest that co-localisation of SERCA pumps to the ER-PM junction is key to the refilling process. As a consequence, the dimensions of the ER-PM junction could play a crucial role for ER refilling [16,33]. Irrespective of the precise arrangement of Orai channels in the centre of the ER-PM junction, the  $\text{Ca}^{2+}$  concentration falls off sharply when moving towards the periphery of the junction. This suggests that larger ER-PM junctions may exhibit an extended peripheral band of low  $\text{Ca}^{2+}$  concentration. SERCA pumps that are located in this part of the junction may only be weakly activated. For small and large ER-PM junctions, containing the same number of peripherally located SERCA pumps, ER refilling would proceed more slowly for larger than for smaller junctions. However, larger ER-PM junctions could benefit from this larger peripheral band of low  $\text{Ca}^{2+}$  concentration as greater numbers of SERCA pumps may be expressed in this bigger space. While each SERCA pump only carries a small current due to the small ambient  $\text{Ca}^{2+}$  concentration, the total current of all peripheral SERCA pumps might be significant, which in turn allows for efficient and geometry mediated refilling of the ER [16]. We will pursue this in future work. The height of the ER-PM junction in our studies is taken as 15nm in accordance with current estimates in the literature. The narrow gap between the PM and ER membranes ensures that  $\text{Ca}^{2+}$  entering through Orai channels diffuses to the ER membrane very quickly, allowing fast activation of SERCA pumps within the junction. If this gap is increased, the  $\text{Ca}^{2+}$  concentrations along the ER membrane will decrease. This could result in decreased SERCA activity, and the SERCA activity and subsequent ER refilling may then depend on the Orai channel and SERCA pump placement [16]. Further simulations could test whether the gap between the PM and ER membrane regulates ER refilling and be used to investigate how altering the dimensions of the ER-PM junction affect the dynamics of Orai channels and SERCA pumps. We will address how the geometry of the ER-PM junction affects ER refilling in future work.

This initial model focuses on the fundamental properties of SOCE: ER refilling and the associated  $\text{Ca}^{2+}$  patterns. Through further development and refine-

ment of the model, we will include more components of  $\text{Ca}^{2+}$  signalling, such as PMCA pumps, and regulatory mechanisms, such as  $\text{Ca}^{2+}$  dependent inactivation of the Orai channel, to provide a more physiologically realistic description of SOCE. Currently, the model is not cell type specific, but including cell specific parameters, such as binding coefficients, and cell specific structures in the future will allow the model to be tailored for specific cell types.

In conclusion, our model reveals a novel way to simulate and visualise the highly heterogeneous  $\text{Ca}^{2+}$  concentrations generated in small sub-cellular compartments during SOCE. Using simulations of specific Orai channel and SERCA pump distributions affords a way to predict the spatial signature of the  $\text{Ca}^{2+}$  signals in the ER-PM junction and sub-PM ER. This can be used to further investigate how interactions between Orai channels and SERCA pumps generate distinct  $\text{Ca}^{2+}$  signals, which could regulate downstream cellular signals. For the first time, the model includes a spatially extended sub-PM ER domain to enable investigation into mechanisms governing ER refilling to provide further insight into the importance of specific components of SOCE. The model demonstrates that the amplitude and shape of  $\text{Ca}^{2+}$  signals throughout the ER-PM junction are strongly controlled by the Orai channel distribution. We also find that clustering of Orai channels and placement of SERCA2b pumps within the ER-PM junction have very little impact on the rate of ER refilling. However, the distance between SERCA2a pumps and Orai channels is a major factor for determining ER refilling.

Further work is required to fully address the relationship between the microscale patterning of the  $\text{Ca}^{2+}$  signal within the ER-PM junction and whole cell responses such as gene expression. Currently,  $\text{Ca}^{2+}$  imaging techniques cannot resolve the local  $\text{Ca}^{2+}$  signals, however, mathematical modelling can predict the shape of the  $\text{Ca}^{2+}$  signals generated in response to a variety of Orai channel distributions and compare the  $\text{Ca}^{2+}$  concentrations achieved. The levels of gene expression, observed in response to different Orai channel distributions, can be directly measured using experimental techniques. Mathematical modelling can provide insight to the microscale patterning of  $\text{Ca}^{2+}$  profiles created within ER-PM junctions and by combining this insight with whole cell observations we can develop a deeper understanding of how Orai channel clustering regulates whole cell behaviour such as NFAT expression.

# Chapter 6

## Conclusions

$\text{Ca}^{2+}$  signalling is important for cellular function and SOCE is the only pathway coupling ER depletion to  $\text{Ca}^{2+}$  influx across the PM. SOCE is responsible for many cellular processes, including cell proliferation and gene expression. Furthermore, disruption of SOCE has been linked to immunodeficiency diseases and impaired motor control. SOCE is a highly debated topic at the forefront of  $\text{Ca}^{2+}$  signalling research and Orai channels are one of the most highly studied SOC channels at present.

SOCE is initiated upon store depletion of ER  $\text{Ca}^{2+}$  stores which causes  $\text{Ca}^{2+}$  influx through Orai channels on the PM, generating highly spatially heterogeneous  $\text{Ca}^{2+}$  signals within the ER-PM junction. The shape of the spatial  $\text{Ca}^{2+}$  profile, also known as the signature of the  $\text{Ca}^{2+}$  signal, has been shown to be important for downstream cellular processes such as gene expression and has the potential to enhance the versatility of the signal thus allowing selective activation of signalling molecules. Therefore, the factors controlling the  $\text{Ca}^{2+}$  signature, such as Orai channel placement, are key regulators of physiological cell function.

Current experimental techniques allow direct measurement of  $\text{Ca}^{2+}$  dynamics occurring on large spatial scales, such as monitoring whole cell  $\text{Ca}^{2+}$  oscillations, and on mesoscales, such as single  $\text{IP}_3\text{R}$  clusters, but are not capable of measuring microscale  $\text{Ca}^{2+}$  dynamics such as those occurring within the ER-PM junction. Mathematical modelling can close this gap in understanding by developing spatio-temporal models to describe the local  $\text{Ca}^{2+}$  dynamics. In particular, modelling provides insight into the shape of the  $\text{Ca}^{2+}$  signals and the relationship between placement of the  $\text{Ca}^{2+}$  signalling machinery and the signals created. Therefore, mathematical modelling can act as a bridge

between microscale and macroscale dynamics by predicting local signals and their impact on global signals which can be tested against experimentally observed whole cell behaviour and hence provide additional insight into the relationship between local and global  $\text{Ca}^{2+}$  signals.

In this thesis, we created a three dimensional spatio-temporal model of SOCE which is the first to include a spatially extended sub-PM ER as well as a spatially extended ER-PM junction. The model allows investigation into the factors controlling the spatial signature of the  $\text{Ca}^{2+}$  signal and ER refilling. In particular, we focused on how the placement of  $\text{Ca}^{2+}$  signalling machinery, such as Orai channels and SERCA pumps, generates distinct  $\text{Ca}^{2+}$  profiles and their effect on ER refilling. We concentrated on the local  $\text{Ca}^{2+}$  dynamics of the ER-PM junction and local ER refilling dynamics in the sub-PM ER in this thesis but we also included global cytoplasmic and ER compartments in our model to allow exploration of the effect of the local  $\text{Ca}^{2+}$  dynamics on global  $\text{Ca}^{2+}$  dynamics. In future work we will use the global (four domain) model to investigate their impact on the global  $\text{Ca}^{2+}$  dynamics.

We implemented a semi-analytical approach using Green's functions to solve the spatio-temporal model in Chapter 3. Other approaches could also be used to solve the spatio-temporal model developed in this thesis such as finite difference and finite element methods, both of which are purely numerical methods that do not use Green's functions. After implementing our Green's function approach, we then discretised the spatial variables and numerically time stepped the solution in MATLAB to evolve the solution throughout both domains spatially and temporally. We first used Barton's method to solve the PDE, a standard solution technique for PDEs of this kind. However, we found that the non-uniform convergence of the series prevented the numerical implementation of the solution in MATLAB as this violated the prescribed boundary conditions. We then employed Felder's method which involved splitting the solution into a steady state solution, which satisfies the boundary conditions, and a complementary solution, which satisfies the initial condition with homogeneous versions of the boundary conditions. We discovered that the choice of boundary condition at the interface between the local and global compartments in the two domain model is important to ensuring a steady state solution exists. If the domain is fully insulated with  $\text{Ca}^{2+}$  flux through a channel on e.g. the PM then a steady state solution will not exist; this is another subtle feature of the solution which needs to be taken into consideration. One key feature of using the semi-analytical method to construct our solution is that we have the

closed form of the solution at each time step. This allows us to pre-compute components of the solution resulting in reduced computational intensity per time step which speeds up the simulations per time step in each domain.

In Chapter 4 we investigated the relationship between the spatio-temporal discretisation and the magnitude and shape of the  $\text{Ca}^{2+}$  profiles generated. First, we found that the oscillations present in the  $\phi$  solutions caused oscillations in the  $\text{Ca}^{2+}$  profile. These oscillations could result in PMCA pump or signalling molecule activity that is enhanced or impeded according to their placement on the oscillation. This is not representative of the true behaviour of the system. We found that approximating the sharp influx through one grid element by using a slightly finer mesh resulted in smooth  $\text{Ca}^{2+}$  profiles which would be representative of the system. The second discovery of this chapter was that the placement of the Orai channels was intrinsically linked to the magnitude of the resulting  $\text{Ca}^{2+}$  profile. We found that Orai channels placed along a radius of  $r = 50\text{nm}$  had a larger  $\text{Ca}^{2+}$  peak concentration than those placed along a radius of  $r = 30\text{nm}$ . This was unexpected as the placement of Orai channels does not affect the single channel current. We explored this further and found that the non-uniform grid was essentially allowing the size of the channel to increase as the channel was placed closer to the mantle of the cylinder. We prescribed the flux per unit area in our model and because the area of each grid element increased towards the mantle of the cylinder the resulting total flux per channel was greater for channels placed closer to the mantle of the cylinder than those placed more centrally within the cylinder. To ensure the shape of the elements were similar and thus allow better comparisons of the local dynamics around Orai channels placed at  $r = 30\text{nm}$  and  $r = 50\text{nm}$ , respectively, we refined the mesh in the  $\phi$  direction when an Orai channel was placed at  $r = 50\text{nm}$ . This ensured that the grid elements had the same area and therefore the total flux was conserved. Using this approach, the  $\text{Ca}^{2+}$  profiles have the same peak magnitude and comparable local spatial discretisations. Although this method works well for comparing rings of Orai channels, we run into the same problem if we try to place Orai channels in non-ring patterns. The grid will be fixed within the junction so placing channels at different radial positions within the same ER-PM junction will result in different peak  $\text{Ca}^{2+}$  profiles as the total  $\text{Ca}^{2+}$  flux will depend on the Orai channel placement. Additionally, we found that rescaling the flux with the grid element area, to conserve the total flux per channel, does not work with Felder's method. Therefore, we must consider moving to uniform spatial discretisation

to ensure the placement of the Orai channel does not affect the total flux per channel.

We also explored the relationship between the temporal discretisation and the  $\text{Ca}^{2+}$  profile to understand the importance of the time step to our simulations as using larger time steps will speed up the run time of the simulations, provided we do not lose vital information. We found that the ER-PM junction is well described by multiple time steps, e.g.  $10^{-5}\text{s}$ ,  $10^{-6}\text{s}$  and  $10^{-7}\text{s}$ , because the influx through the Orai channel is constant and dominates the dynamics within the junction. However, the sub-PM ER is dominated by SERCA pumps which are not necessarily constant fluxes as the amount of  $\text{Ca}^{2+}$  influx depends on the  $\text{Ca}^{2+}$  concentration surrounding the Orai channel in the ER-PM junction. We found that while the long term  $\text{Ca}^{2+}$  dynamics are well approximated by larger time steps, the early dynamics require small time steps to describe the  $\text{Ca}^{2+}$  behaviour. Therefore, we can use multiple time steps in our simulations to ensure we capture both the early  $\text{Ca}^{2+}$  dynamics and long term dynamics while reducing the run time of the simulations. This is something we will implement in future work when investigating the ER refilling occurring over long time periods.

The ER-PM junction is a very small region with a volume of approximately  $3 \times 10^{-19}\text{L}$  which corresponds to less than one  $\text{Ca}^{2+}$  ion per ER-PM junction at resting  $\text{Ca}^{2+}$  concentrations of  $\approx 0.1\mu\text{M}$ . This situation also occurs in diadic clefts of cardiac cells where it has been shown that deterministic models are good approximations to random walk simulations [30]. Dupont *et al.* [22] conclude that it can be reasonably assumed that  $\text{Ca}^{2+}$  dynamics in regions of similar size to diadic clefts, e.g. ER-PM junctions, are also well described by deterministic continuous models, such as the model developed in this thesis.

Chapter 5 is an extended version of the results section that we published in [50]. In this chapter we investigated how clustering of Orai channels affects the local  $\text{Ca}^{2+}$  profiles and the effect of Orai channel and SERCA pump placement on ER refilling. We found that clustering creates distinct  $\text{Ca}^{2+}$  profiles. However, this did not enhance ER refilling as the SERCA pumps close to the Orai channels work at almost maximal activity in response to both clustered and non-clustered Orai channel configurations. We then investigated how different placements of SERCA pumps affected ER refilling. We included two SERCA pump isoforms (SERCA2a and SERCA2b) as different kinetic parameters could have a significant impact on the SERCA pump activity induced

by the different placements. By comparing the rates of ER refilling we found that SERCA2a was more sensitive than SERCA2b. Therefore the placement of SERCA2a pumps is a key regulator of ER refilling, whereas the placement of SERCA2b pumps or Orai channels only weakly affects ER refilling. SERCA pumps are the only structures in the ER-PM junction transporting  $\text{Ca}^{2+}$  from the ER-PM junction into the sub-PM ER and SERCA activity is described by a Hill function which is non-linear. Although we can make intuitive predictions about the effect of SERCA pump placement on ER refilling these predictions are highly qualitative. Developing mathematical models to simulate the individual scenarios allows us to predict the ER refilling rates and SERCA activity thus providing more quantitative evidence about the relationship between Orai channel and SERCA pump placement on SERCA activity and ER refilling. In turn, this enhances our understanding of the impact of local factors, such as SERCA placement, on global processes, such as ER refilling.

We prescribed the flux per unit area for Orai channels and SERCA pumps. However, because the grid is non-uniform the grid element area increases as the radial placement of the channel or pump increases. Therefore, the total flux per channel or pump will increase as the channels or pumps are placed closer to the mantle of the cylinder representing the ER-PM junction. We have accounted for this change in total flux for the Orai channels by refining the  $\phi$  discretisation which increases the computational intensity of the simulations, a key limitation of the current approach. The Orai channel influx dominates the  $\text{Ca}^{2+}$  dynamics in the ER-PM junction so we fix the spatial discretisation to ensure the total Orai channel flux is conserved in both the clustered and non-clustered configurations. However, the total SERCA pump flux will increase as the SERCA pumps are placed closer to the edge of the ER-PM junction as we cannot use the same procedure to ensure the flux per SERCA pump is conserved because the grid is fixed. The SERCA pump flux is small compared to the Orai channel flux so the change in  $\text{Ca}^{2+}$  magnitude due to SERCA activity is less noticeable. This is a second limitation of the non-uniform spatial grid used. Therefore, we will consider approaches that allow us to use a uniform spatial mesh on the ER-PM junction and sub-PM ER. One approach would be to approximate the ER-PM junction and sub-PM ER by a cube, instead of a cylinder, and use uniform spatial discretisations across the face of the cube to ensure that each grid element has the same area. This approach would ensure that the Orai channel and SERCA pump placement will not affect the total flux per channel or pump. We will implement this approach in future work

as it provides greater flexibility within the model as we will remove the dependency of the total flux on the radial placement within the ER-PM junction. Thus Orai channel and SERCA pump placement will not be limited to rings of channels or pumps.

In conclusion, we have developed a novel three-dimensional spatio-temporal model of SOCE that captures the local  $\text{Ca}^{2+}$  signalling dynamics and ER refilling. The model allows investigation of how the spatial arrangement of Orai channels and SERCA pumps controls downstream cell signalling processes and ER refilling. The next stage of our research will involve validating the model using experimental data to allow further refinement of the model. We can then use the model to explore other aspects of SOCE; such as how the geometry of the ER-PM junction controls ER refilling and the relationship between local and global  $\text{Ca}^{2+}$  signals.

# Appendix A

## Green's functions

### A.1 Bulk Cytoplasm

We use the separation of variables technique applied to the original diffusion equation with homogeneous versions of the boundary conditions to calculate the Green's function in the bulk cytoplasm and let

$$C_C = \rho(r)\theta(\phi)h(z)T(t). \quad (\text{A.1})$$

We rewrite the initial condition as a combination of functions,  $\tilde{\rho}$ ,  $\tilde{\theta}$  and  $\tilde{h}$ , describing the dependence of the initial condition on  $r$ ,  $\phi$  and  $z$ ,

$$C_C(r, \phi, z, 0) = \tilde{\rho}(r)\tilde{\theta}(\phi)\tilde{h}(z)T(0). \quad (\text{A.2})$$

We can substitute equation (A.1) into the diffusion equation and separate the diffusion equation into the following equations

$$\begin{aligned} T' + D_c (\mu^2 + \eta^2) T &= 0, \\ h'' + \mu^2 h &= 0, \\ \theta'' + \gamma^2 \theta &= 0, \\ r^2 \rho'' + r \rho' + \rho (r^2 \eta^2 - \gamma^2) &= 0, \end{aligned}$$

where  $\mu = \pi m / (H - L_1)$  for  $m = 0, 1, \dots, M$ ,  $\gamma = n$  for  $n = 0, 1, \dots, N$  and  $\eta$  satisfies  $\psi_n(\eta_{n,j}b) = 0$  for  $j = 1, \dots, J$  where  $\psi$  is given by,

$$\psi_n(\eta_{n,j}r) = J_n(\eta_{n,j}r) Y_n(\eta_{n,j}b) - J_n(\eta_{n,j}b) Y_n(\eta_{n,j}r),$$

where  $J_n(x)$  and  $Y_n(x)$  represent Bessel functions of the first and second type of order  $n$ . We solve the equations subject to the homogeneous boundary conditions and achieve the following solutions

$$T(t) = T(0)e^{-D_c(\mu^2+\eta^2)t},$$

$$h(z) = \frac{1}{H-L_1} \int_{L_1}^H h(z') dz' \left[ 1 + 2 \sum_{m=1}^M \cos(\mu(z' - L_1)) \cos(\mu(z - L_1)) \right], \quad (\text{A.3})$$

$$\theta(\phi) = \frac{1}{2\pi} \int_0^{2\pi} \theta(\phi') d\phi' \left[ 1 + 2 \sum_{n=1}^N \cos(n(\phi - \phi')) \right], \quad (\text{A.4})$$

$$\rho(r) = \int_a^b r' dr' \rho(r') \sum_{j=1}^J \frac{\pi^2 \eta_{n,j}^2 (Y'_n(\eta_{n,j}a))^2 \psi_n(\eta_{n,j}r') \psi_n(\eta_{n,j}r)}{2 \left[ (Y'_n(\eta_{n,j}a))^2 - \left(1 - \left(\frac{n}{\eta_{n,j}a}\right)^2\right) Y_n^2(\eta_{n,j}b) \right]}. \quad (\text{A.5})$$

We substitute these solutions into equation (A.1) and return the initial condition to the original form, using equation (A.2), to get the solution for the PDE with homogeneous versions of the boundary conditions,

$$C_C(r, \phi, z, t) = \int_V dV' G_C(r, r', \phi, \phi', z, z', t) C_C(r', \phi', z', 0), \quad (\text{A.6})$$

where  $G_c$  is the Green's function in the bulk cytoplasm,  $V$  is the volume of the bulk cytoplasm and equation (A.6) describes the  $\text{Ca}^{2+}$  diffusion of the original  $\text{Ca}^{2+}$  profile over one time step. By setting the initial condition to a 3D polar delta function,

$$C_C(r, \phi, z, 0) = \frac{\delta(r - r')\delta(\phi - \phi')\delta(z - z')}{r'}, \quad (\text{A.7})$$

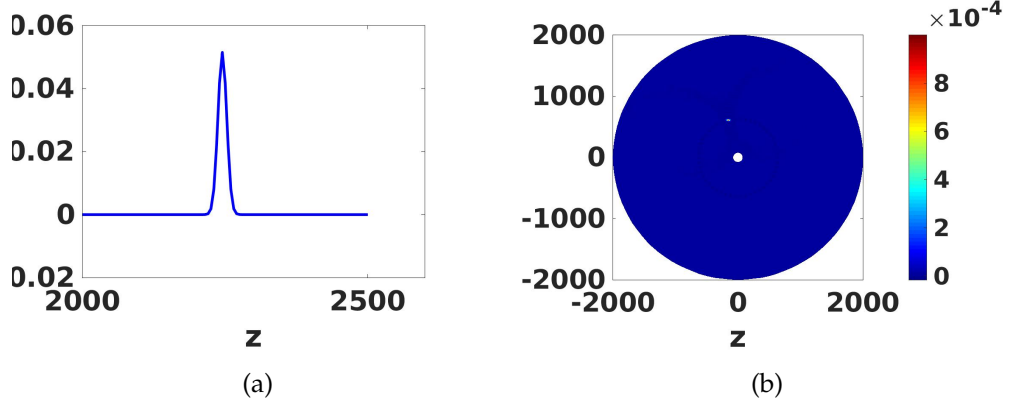


**Figure A.1:** Simulation of the Green's function in the  $z$  direction and polar direction in the bulk cytoplasm. The parameters used are  $J = 100$ ,  $M = 100$ ,  $N = 50$ .

we obtain the Green's function from equation (A.6). The Green's function in the bulk cytoplasm is given by

$$\begin{aligned}
G_C(r, r', \phi, \phi', z, z', t) = & \\
& \frac{\pi}{4(H - L_1)} \left[ 1 + 2 \sum_{m=1}^M \cos(\mu(z' - L_1)) \cos(\mu(z - L_1)) e^{-D_c \mu^2 t} \right] \\
& \times \sum_{j=1}^J \left[ \frac{\eta_{0,j}^2 (Y'_0(\eta_{0,j}a))^2 \psi_0(\eta_{0,j}r') \psi_0(\eta_{0,j}r) e^{-D_c \eta_{0,j}^2 t}}{(Y'_0(\eta_{0,j}a))^2} \right. \\
& \left. + 2 \sum_{n=1}^N \frac{\eta_{n,j}^2 (Y'_n(\eta_{n,j}a))^2 \psi_n(\eta_{n,j}r') \psi_n(\eta_{n,j}r) \cos(n(\phi - \phi')) e^{-D_c \eta_{n,j}^2 t}}{(Y'_n(\eta_{n,j}a))^2 - \left(1 - \left(\frac{n}{\eta_{n,j}a}\right)^2\right) Y_n^2(\eta_{n,j}b)} \right]. \tag{A.8}
\end{aligned}$$

The shape of the Green's function in the bulk cytoplasm is illustrated in Figure A.1. We can check that our representation given in equation (A.8) actually is a Green's function by testing the behaviour when  $dt = 0$ . We expect the Green's function to decompose into three delta functions,

$$G_C(r, r', \phi, \phi', z, z', 0) = \frac{\delta(r - r') \delta(\phi - \phi') \delta(z - z')}{r'},$$

and we can check that the decomposed Green's functions satisfy the properties of delta functions. We see in Figures A.2(a) - A.2(c) that the representations look similar to delta functions and peak only at the specified location. We still have the oscillations about zero in the  $r$  and  $\phi$  directions, however, the

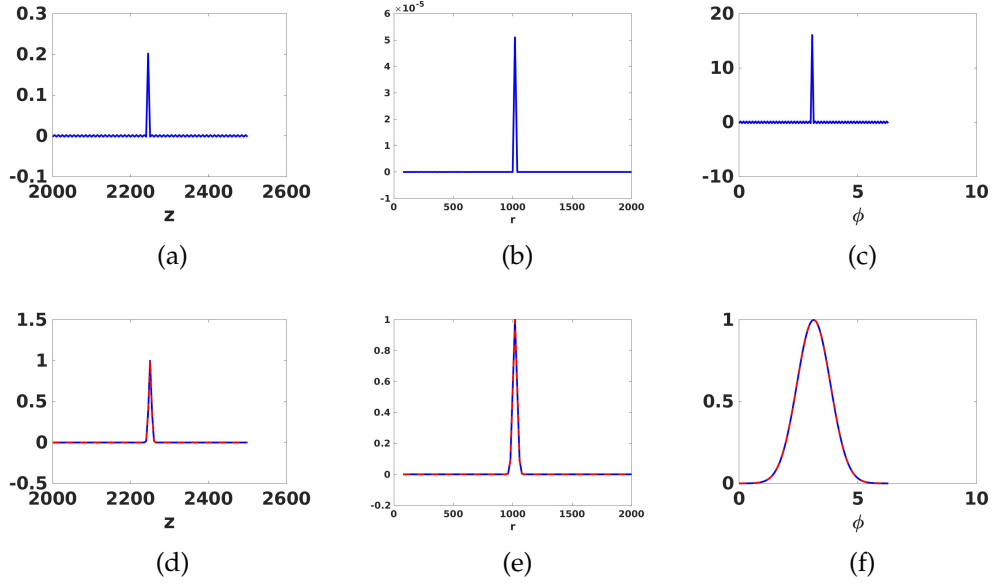


**Figure A.2:** Checks that Green's function in the bulk cytoplasm acts like a delta function when  $dt = 0$ . (a-c) show the shape of the Green's function and (d-f) show that the Green's functions convolve correctly.

oscillations are small in comparison to the peak. We can see in Figures A.2(d) - A.2(f) that the representations convolve with a Gaussian correctly, as shown by the matching of the dashed red lines with the solid blue lines.

## A.2 Bulk ER

We use the separation of variables technique applied to the original diffusion equation with homogeneous versions of the boundary conditions to calculate the Green's function in the bulk ER. We let,

$$C_E(r, \phi, z, t) = T(t)\rho(r)\theta(\phi)h(z), \quad (\text{A.9})$$

and write the initial condition in terms of functions,  $\tilde{\rho}$ ,  $\tilde{\theta}$  and  $\tilde{h}$  describing the initial condition in terms of  $r$ ,  $\phi$  and  $z$  only as,

$$C_E(r, \phi, z, 0) = T(t)\tilde{\rho}(r)\tilde{\theta}(\phi)\tilde{h}(z). \quad (\text{A.10})$$

We substitute equation (A.9) into the original diffusion equation which leads to the following separated equations

$$\begin{aligned} T' + D_S (\mu^2 + \eta^2) T &= 0, \\ h'' + \mu^2 h &= 0, \\ \theta'' + \gamma^2 \theta &= 0, \\ r^2 \rho'' + r \rho' + \rho (r^2 \eta^2 - \gamma^2) &= 0, \end{aligned}$$

where  $\mu = (2m - 1)\pi/2(L_1 - L_0)$  for  $m = 1, 2, \dots, M$ ,  $\gamma = n$  for  $n = 0, 1, \dots, N$ ,  $\eta = \alpha_{n,j}/b$  and  $\alpha_{n,j}$  satisfy  $J_n(\alpha_{n,j}) = 0$  for  $j = 1, 2, \dots, J$ . We solve the equations subject to the homogeneous boundary conditions to get the following solutions

$$\begin{aligned} T(t) &= T(0)e^{-D_e(\mu^2 + \eta^2)t}, \\ h(z) &= \frac{2}{L_1 - L_0} \int_{L_0}^{L_1} h(z') dz' \sum_{m=1}^M \cos(\mu(L_1 - z')) \cos(\mu(L_1 - z)), \end{aligned} \quad (\text{A.11})$$

$$\theta(\phi) = \frac{1}{2\pi} \int_0^{2\pi} \theta(\phi') d\phi' \left[ 1 + 2 \sum_{n=1}^N \cos(n(\phi - \phi')) \right], \quad (\text{A.12})$$

$$\rho(r) = \frac{2}{b^2} \int_0^b \rho(r') r' dr' \sum_{j=1}^J \frac{J_n(\alpha_{n,j} r'/b) J_n(\alpha_{n,j} r/b)}{J_{n+1}^2(\alpha_{n,j})}, \quad (\text{A.13})$$

We substitute the solutions into equation (A.9) and use equation (A.10) to return the initial concentration to its original form to get the solution for the PDE with homogeneous boundary conditions,

$$C_E(r, \phi, z) = \int_V dV' U_E(r', \phi', z', 0) G_E(r, r', \phi, \phi', z, z', t). \quad (\text{A.14})$$

By setting the initial condition to a 3D polar delta function,

$$C_E(r, \phi, z, 0) = \frac{\delta(r - r') \delta(\phi - \phi') \delta(z - z')}{r'}, \quad (\text{A.15})$$

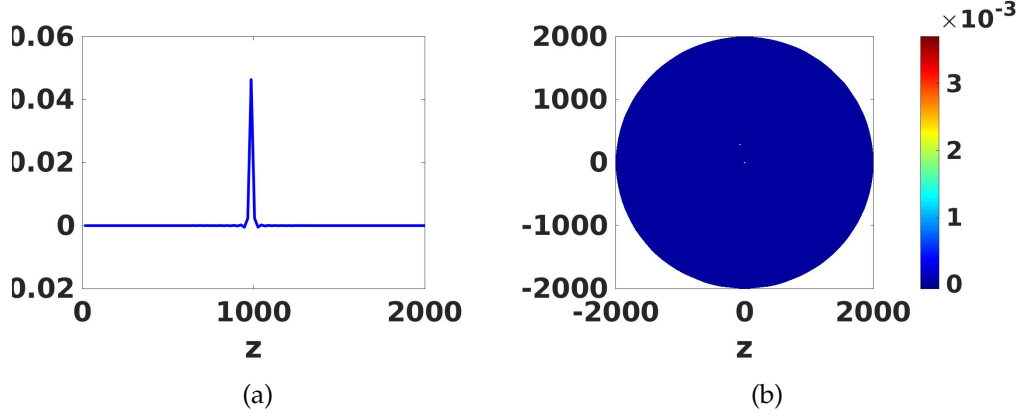


**Figure A.3:** Simulation of the Green's function in the  $z$  direction and polar direction in the bulk ER. The parameters used are  $J = 200$ ,  $M = 100$ ,  $N = 50$

we obtain the Green's function from equation (A.14). The Green's function in the bulk ER,  $G_E$ , is given by,

$$\begin{aligned}
G_E(r, r', \phi, \phi', z, z', t) = & \\
& \frac{2}{\pi b^2 (L_1 - L_0)} \sum_{m=1}^M \cos(\mu (L_1 - z')) \cos(\mu (L_1 - z)) e^{-D_e \mu^2 t} \\
& \times \sum_{j=1}^J \left[ \frac{J_0(\alpha_0, jr'/b) J_0(\alpha_0, jr/b) e^{-D_e \alpha_{0,j}^2 t/b^2}}{J_0^2(\alpha_{0,j})} \right. \\
& \left. + 2 \sum_{n=1}^N \frac{J_n(\alpha_{n,j} r'/b) J_n(\alpha_{n,j} r/b) \cos(n(\phi - \phi')) e^{-D_e \alpha_{n,j}^2 t/b^2}}{J_n^2(\alpha_{n,j}) (1 - (n/\beta_{n,j})^2)} \right]. \tag{A.16}
\end{aligned}$$

The shape of the Green's function in the bulk ER is illustrated in Figure A.3. We can check that our representation given in equation (A.16) actually is a Green's function by testing the behaviour when  $dt = 0$ . We expect the Green's function to decompose into three delta functions,

$$G_e(r, r', \phi, \phi', z, z', 0) = \frac{\delta(r - r') \delta(\phi - \phi') \delta(z - z')}{r'},$$

and we can check that the decomposed Green's functions satisfy the properties of delta functions. We see in Figures A.4(a) - A.4(c) that the representations look similar to delta functions and peak only at the specified location. We still have the oscillations about zero in the  $z$  and  $\phi$  directions, however, the oscillations are small in comparison to the peak. We can see in Figures A.4(d) - A.4(f) that the representations convolve with a Gaussian correctly, as shown

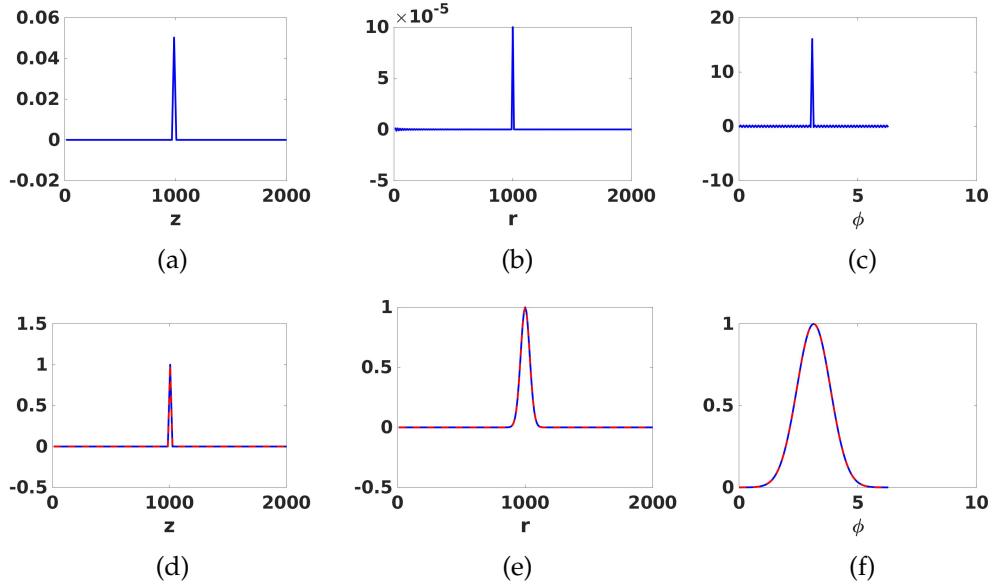


**Figure A.4:** Checks that Green's function in the bulk ER acts like a delta function when  $dt = 0$ . (a-c) show the shape of the Green's function and (d-f) show that the Green's functions convolve correctly.

by the matching of the dashed red lines with the solid blue lines.

# Appendix B

## Separation of variables in the ER-PM junction

### B.1 $V_{j,1}$

We apply the separation of variables technique by substituting equation (3.44) into the diffusion equation (3.43) to get the following separated equations

$$h'' - \eta^2 h = 0, \quad (\text{B.1})$$

$$\theta'' + \gamma^2 \theta = 0, \quad (\text{B.2})$$

$$r^2 \rho'' + r \rho' + \rho(r^2 \eta^2 - \gamma^2) = 0, \quad (\text{B.3})$$

with solutions

$$h(z) = h'(H) \frac{a}{\alpha_{n,j}} \frac{e^{-(H-z)\alpha_{n,j}/a} + e^{-(H+z-2L_2)\alpha_{n,j}/a}}{1 - e^{-2(H-L_2)\alpha_{n,j}/a}}, \quad (\text{B.4})$$

$$\theta(\phi) = \frac{1}{2\pi} \int_0^{2\pi} \bar{\theta}(\phi') d\phi' \left[ 1 + 2 \sum_{n=1}^N \cos(n(\phi - \phi')) \right], \quad (\text{B.5})$$

$$\rho(r) = \frac{2}{a^2} \int_0^a \bar{\rho}(r') r' dr' \sum_{j=1}^J \frac{J_n(\alpha_{n,j} r' / a) J_n(\alpha_{n,j} r / a)}{J_{n+1}^2(\alpha_{n,j})}, \quad (\text{B.6})$$

where  $\gamma = n$  for  $n = 0, 1, 2, \dots, N$ ,  $\eta = \alpha_{n,j}/a$  and  $\alpha_{n,k}$  satisfies  $J_n(\alpha_{n,j}) = 0$  for  $j = 1, 2, \dots, J$  where  $J_n(x)$  are Bessel's functions of order  $n$ .

## B.2 $V_{j,2}$

We apply the separation of variables technique by substituting equation (3.48) into the diffusion equation (3.43) to get the following equations

$$h'' - \eta^2 h = 0, \quad (\text{B.7})$$

$$\theta'' + \gamma^2 \theta = 0, \quad (\text{B.8})$$

$$r^2 \rho'' + r \rho' + \rho(r^2 \eta^2 - \gamma^2) = 0, \quad (\text{B.9})$$

with solutions

$$h(z) = J_{\text{SERCA}} \frac{a}{\alpha_{n,j}} \frac{e^{-(2H-z-L_2)\alpha_{n,j}/a} + e^{-(z-L_2)\alpha_{n,j}/a}}{e^{-2(H-L_2)\alpha_{n,j}/a} - 1}, \quad (\text{B.10})$$

$$\theta(\phi) = \frac{1}{2\pi} \int_0^{2\pi} \theta(\phi') d\phi' \left[ 1 + 2 \sum_{n=1}^N \cos(n(\phi - \phi')) \right], \quad (\text{B.11})$$

$$\rho(r) = \frac{2}{a^2} \int_0^a \rho(r') r' dr' \sum_{j=1}^J \frac{J_n(\alpha_{n,j} r'/a) J_n(\alpha_{n,j} r/a)}{J_{n+1}^2(\alpha_{n,j})}, \quad (\text{B.12})$$

with  $\gamma$  and  $\eta$  as defined in section B.1.

## B.3 $V_{j,3}$

We apply the separation of variables technique by substituting equation (3.50) into the diffusion equation (3.43) to get the following equations

$$h'' + \mu^2 h = 0, \quad (\text{B.13})$$

$$\theta'' + \gamma^2 \theta = 0, \quad (\text{B.14})$$

$$r^2 \rho'' + r \rho' - \rho(r^2 \mu^2 + \gamma^2) = 0. \quad (\text{B.15})$$

The solutions to  $\theta$  and  $h$ ,

$$h(z) \frac{1}{H - L_2} \int_{L_2}^H h(z') dz' \left[ 1 + 2 \sum_{m=1}^M \cos(\mu(z' - L_2)) \cos(\mu(z - L_2)) \right], \quad (\text{B.16})$$

$$\theta(\phi) = \frac{1}{2\pi} \int_0^{2\pi} \theta(\phi') d\phi' \left[ 1 + 2 \sum_{n=1}^N \cos(n(\phi - \phi')) \right], \quad (\text{B.17})$$

have the same form as the corresponding solution in the homogeneous case,  $\gamma$  is as defined in section B.1 and  $\mu_m = (2m - 1)\pi/2(L_2 - L_1)$  for  $m = 1, 2, \dots, M$ . The inhomogeneous boundary condition at  $r = a$  has altered the separable equation and now  $\rho(r)$  is an Euler differential equation when  $\mu = 0$  and a modified Bessel function when  $\mu > 0$ . We treat each case separately and find the following solutions for  $\rho(r)$ :

$$\begin{aligned}\rho_{0,0}(r) &= C_c(a, \phi, z), \\ \rho_{0,n}(r) &= C_c(a, \phi, z) \left(\frac{r}{a}\right)^n, \\ \rho_{m,n}(r) &= C_c(a, \phi, z) \frac{I_n(\mu r)}{I_n(\mu a)},\end{aligned}\tag{B.18}$$

where  $I_n(x)$  denotes a modified Bessel function of the first kind of order  $n$ .

# Appendix C

## Separation of variables in the sub-PM ER

### C.1 $V_{s,1}$

We apply the separation of variables technique by substituting equation (3.58) into the diffusion equation (3.57) to get the following equations

$$h'' - \eta_{n,j}^2 h = 0, \quad (\text{C.1})$$

$$\theta'' + \gamma^2 \theta = 0, \quad (\text{C.2})$$

$$r^2 \rho'' + r \rho' + \rho (r^2 \eta^2 - \gamma^2) = 0, \quad (\text{C.3})$$

and solutions

$$h(z) = \begin{cases} J_{SERCA}(z - L_1) & \eta_{n,j} = 0, \\ J_{SERCA} \frac{a}{\beta_{n,j}} \frac{e^{\beta_{n,j}(z-L_2)/a} - e^{-\beta_{n,j}(z+L_2-2L_1)/a}}{1 + e^{-2\beta_{n,j}(L_2-L_1)/a}} & \eta_{n,j} > 0, \end{cases} \quad (\text{C.4})$$

$$\theta(\phi) = \frac{1}{2\pi} \int_0^{2\pi} \theta(\phi') d\phi' \left[ 1 + 2 \sum_{n=1}^N \cos(n(\phi - \phi')) \right], \quad (\text{C.5})$$

$$\rho(r) = \frac{2}{a^2} \int_0^a \rho(r') r' dr' \sum_{j=1}^J \frac{J_n(\beta_{n,j} r' / a) J_n(\beta_{n,j} r / a)}{J_n^2(\beta_{n,j}) (1 - (n/\beta_{n,j})^2)}, \quad (\text{C.6})$$

where  $\gamma = n$  for  $n = 0, 1, \dots, N$ ,  $\eta = \beta_{n,j}/a$  and  $\beta_{n,j}$  satisfies  $J'_n(\beta_{n,j}) = 0$  for  $j = 1, 2, \dots, J$ . We have made a special consideration for  $\eta_{0,1} = 0$  as we have a different solution for  $h(z)$  in this case.

## C.2 $V_{s,2}$

We apply the separation of variables technique to get the following equations

$$h'' - \eta_{n,j}^2 h = 0, \quad (\text{C.7})$$

$$\theta'' + \gamma^2 \theta = 0, \quad (\text{C.8})$$

$$r^2 \rho'' + r \rho' + \rho (r^2 \eta^2 - \gamma^2) = 0, \quad (\text{C.9})$$

and solutions

$$h(z) = \begin{cases} C_e(r, \phi, L_1, t) & \eta_{0,1} = 0, \\ C_e(r, \phi, L_1, t) \frac{e^{\beta_{n,j}(z+L_1-2L_2)/a} + e^{-\beta_{n,j}(z-L_1)/a}}{1 + e^{-2\beta_{n,j}(L_2-L_1)/a}} & \eta_{n,j} > 0, \end{cases} \quad (\text{C.10})$$

$$\theta(\phi) = \frac{1}{2\pi} \int_0^{2\pi} \theta(\phi') d\phi' \left[ 1 + 2 \sum_{n=1}^N \cos(n(\phi - \phi')) \right], \quad (\text{C.11})$$

$$\rho(r) = \frac{2}{a^2} \int_0^a \rho(r') r' dr' \sum_{j=1}^J \frac{J_n(\beta_{n,j} r' / a) J_n(\beta_{n,j} r / a)}{J_n^2(\beta_{n,j}) (1 - (n/\beta_{n,j})^2)}, \quad (\text{C.12})$$

where  $\gamma$  and  $\eta$  are as defined in section C.1. We have made a special consideration for  $\eta_{0,1} = 0$  as we have a different solution for  $h(z)$  in this case.

# Appendix D

## Parameter tables

The simulations throughout the paper use the parameter values in Tables D.1 and D.2 unless otherwise specified.

Parameter	Description	Value	Unit
$D_J$	Diffusion coefficient in ER-PM junction	220 [4, 33]	$\mu\text{m}^2\text{s}^{-1}$
$D_{ER}$	Diffusion coefficient in ER-PM junction	10 [15, 75]	$\mu\text{m}^2\text{s}^{-1}$
$a$	Radius of junction	100 [55, 67]	nm
$H$	Distance to PM	2500	nm
$L_2$	Distance to ER membrane	2485	nm
$L_1$	Distance to interface between sub-PM ER and bulk ER	2000	nm
$ER_i$	Distance to internal point of sub-PM ER (see Figure 5(a))	2286.15	nm

$I_{\text{Orai}}$	Orai single channel current	2.1 [35,88]	fA
$F$	Faraday's constant	96485	C mol <sup>-1</sup>
$z$	Valency of Ca <sup>2+</sup> ions	2	
$A_{\text{O}}$	Area of Orai channel	0.25 [56]	nm <sup>2</sup>
$V_{\text{max}}$	SERCA2b pump rate	36 [47]	Ca <sup>2+</sup> ions/s
$K_F$	SERCA2b pump Ca <sup>2+</sup> affinity (forward rate)	0.27 [47]	$\mu\text{M}$
$H$	Hill coefficient for the SERCA2b pump	1.7 [47]	
$V_{\text{max}}$	SERCA2a pump rate	72 [47]	Ca <sup>2+</sup> ions/s
$K_F$	SERCA2a pump Ca <sup>2+</sup> affinity (forward rate)	0.38 [47]	$\mu\text{M}$
$H$	Hill coefficient for the SERCA2a pump	2.2 [47]	
$K_R$	SERCA pump Ca <sup>2+</sup> affinity (reverse rate)	1700 [69]	$\mu\text{M}$
$Q$	Temperature coefficient	2.6 [69]	

**Table D.1:** Table of parameter values used in model chosen according to estimates in literature. Distance to PM, ER membrane and bulk ER are defined as the distance from a point of the bulk ER.  $H$  and  $L_2$  chosen to ensure height of junction ( $H - L_2$ ) is in agreement with experimental estimates [81]. As discussed in Section ??, the height of the sub-PM ER has not been measured so we have chosen  $L_0$  so that the height of the sub-PM ER is larger than the height of the ER-PM junction.

Parameter	Description	Value	Unit
$\Delta t$	Size of time step	1	$\mu\text{s}$
$\Delta r$	Radial step size	0.2	nm
$\Delta \phi$	Angular step size for clustered Orai channel configuration	0.0419	radians
$\Delta z_J$	$z$ step size in ER-PM junction	0.15	nm
$\Delta z_S$	$z$ step size in sub-PM ER	4.85	nm
$\sigma_\phi$	Angular standard deviation of Gaussian, $w(r, \phi)$	0.05	
$\sigma_r$	Radial standard deviation of Gaussian, $w(r, \phi)$	0.05	
$T$	Simulated time	1	ms
$N_{\text{Orai}}$	Number of Orai channels	5	
$N_{\text{SERCA}}$	Number of SERCA pumps	10	

**Table D.2:** Table of parameter values used in simulations.

# References

- [1] I. F. Abdullaev, J. M. Bisailon, M. Potier, J. C. Gonzalez, R. K. Motiani, and M. Trebak. Stim1 and Orai1 mediate CRAC currents and store-operated calcium entry important for endothelial cell proliferation. *Circ. Res.*, 103(11):1289–1299, 2008.
- [2] M. Abramowitz and I. A. Stegun. *Handbook of mathematical functions with formulas, graphs, and mathematical table*, volume 2172. Dover New York, 1965.
- [3] B. Alberts, A. Johnson, J. Lewis, M. Raff, K. Roberts, and P. Walter. *Molecular Biology of the Cell*. Garland Science, fourth edition, 2002.
- [4] N. L. Allbritton, T. Meyer, and L. Stryer. Range of messenger action of calcium ion and inositol 1, 4, 5-trisphosphate. *Science*, 258:1812–1812, 1992.
- [5] M. T. Alonso, I. M. Manjarrés, and J. García-Sancho. Privileged coupling between  $\text{Ca}^{2+}$  entry through plasma membrane store-operated  $\text{Ca}^{2+}$  channels and the endoplasmic reticulum  $\text{Ca}^{2+}$  pump. *Mol. Cell. Endocrinol.*, 353(1):37–44, 2012.
- [6] H. L. Ambudkar, Indu S. and Ong and B. B. Singh. *Molecular and functional determinants of  $\text{Ca}^{2+}$  signaling microdomains*, pages 237–253. Springer, 2009.
- [7] G. B. Arfken, H. J. Weber, and F. E. Harris. *Mathematical methods for physicists: a comprehensive guide*. Academic press, 2011.
- [8] G. Barton. *Elements of Green's functions and propagation: potentials, diffusion, and waves*. Oxford University Press, 1989.
- [9] D. Bers. Regulation of Cellular Calcium in Cardiac Myocytes. *Comprehensive Physiology*, pages 335–387, 2011.

- [10] R. Casteels and G. Droogmans. Exchange characteristics of the noradrenaline-sensitive calcium store in vascular smooth muscle cells of rabbit ear artery. *The Journal of Physiology*, 317:263–279, 1981.
- [11] D. E. Clapham. Calcium signaling. *Cell*, 131(6):1047–58, 2007.
- [12] E. Covington, M. Wu, and M. Lewis. Essential role for the CRAC activation domain in store-dependent oligomerization of STIM1. *Molecular Biology of the Cell*, 21:1897–1907, 2010.
- [13] H. Croisier, X. Tan, J. F. Perez-Zoghbi, M. J. Sanderson, J. Sneyd, and B. S. Brook. Activation of store-operated calcium entry in airway smooth muscle cells: insight from a mathematical model. *PLoS One*, 8(7):e69598, 2013.
- [14] S. P. Dawson, J. Keizer, and J. E. Pearson. Fire–diffuse–fire model of dynamics of intracellular calcium waves. *Proceedings of the National Academy of Sciences*, 96(11):6060–6063, 1999.
- [15] M. J. Dayel, E. F. Hom, and A. Verkman. Diffusion of green fluorescent protein in the aqueous-phase lumen of endoplasmic reticulum. *Biophys. J.*, 76(5):2843–2851, 1999.
- [16] N. Demaurex and D. Guido. The Role of Mitochondria in the Activation/Maintenance of SOCE: Membrane Contact Sites as Signaling Hubs Sustaining Store-Operated  $\text{Ca}^{2+}$  Entry. In *Store-Operated  $\text{Ca}^{2+}$  Entry (SOCE) Pathways*, pages 277–296. Springer, 2017.
- [17] J. Di Capite, S. W. Ng, and A. B. Parekh. Decoding of cytoplasmic  $\text{Ca}^{2+}$  oscillations through the spatial signature drives gene expression. *Curr. Biol.*, 19(10):853–858, 2009.
- [18] H. Dingsdale, E. Okeke, L. Haynes, G. Lur, and A. V. Tepikin. New Aspects of the Contribution of ER to SOCE Regulation: The Role of the ER and ER-Plasma Membrane Junctions in the Regulation of SOCE. In *Store-Operated  $\text{Ca}^{2+}$  Entry (SOCE) Pathways*, pages 217–237. Springer, 2017.
- [19] L. Dode, J. P. Andersen, N. Leslie, J. Dhitavat, B. Vilsen, and A. Hovnanian. Dissection of the functional differences between sarco (endo) plasmic reticulum  $\text{Ca}^{2+}$ -ATPase (SERCA) 1 and 2 isoforms and characterization of Darier disease (SERCA2) mutants by steady-state and transient kinetic analyses. *J. Biol. Chem.*, 278(48):47877–47889, 2003.

- [20] R. E. Dolmetsch. Channels Generates  $[Ca^{2+}]_i$  Oscillations in T Lymphocytes. *The Journal of General Physiology*, 103:365–388, 1994.
- [21] G. Dupont, L. Combettes, G. S. Bird, and J. W. Putney. Calcium oscillations. *Cold Spring Harbor perspectives in biology*, 3(3):a004226, 2011.
- [22] G. Dupont, M. Falcke, V. Kirk, and J. Sneyd. *Models of Calcium Signalling*. Springer International Publishing, 1st edition, 2016.
- [23] J. L. Dynes, A. Amcheslavsky, and M. D. Cahalan. Genetically targeted single-channel optical recording reveals multiple Orai1 gating states and oscillations in calcium influx. *Proc. Nat. Acad. Sci.*, 113(2):440–445, 2016.
- [24] G. N. Felder and K. M. Felder. *Mathematical methods in engineering and physics*. John Wiley & Sons, 2015.
- [25] S. Feske. CRAC channelopathies. *Pflügers Archive: European Journal of Physiology*, 460:417–435, 2010.
- [26] S. Feske, Y. Gwack, M. Prakriya, S. Srikanth, S.-H. Puppel, B. Tanasa, P. G. Hogan, R. S. Lewis, M. Daly, and A. Rao. A mutation in Orai1 causes immune deficiency by abrogating CRAC channel function. *Nature*, 441(7090):179–185, 2006.
- [27] A. F. Fomina, C. M. Fanger, J. A. Kozak, and M. D. Cahalan. Single channel properties and regulated expression of  $Ca^{2+}$  release-activated  $Ca^{2+}$  (CRAC) channels in human T cells. *J. Cell Biol.*, 150(6):1435–1444, 2000.
- [28] D. C. Gadsby. Ion channels versus ion pumps: the principal difference, in principle. *Nature reviews Molecular cell biology*, 10(5):344–352, 2009.
- [29] T. Griffith, K. Tsaneva-Atanasova, and J. R. Mellor. Control of  $Ca^{2+}$  influx and calmodulin activation by sk-channels in dendritic spines. *PLoS computational biology*, 12(5):e1004949, 2016.
- [30] J. Hake and G. T. Lines. Stochastic binding of  $Ca^{2+}$  ions in the dyadic cleft; continuous versus random walk description of diffusion. *Biophysical journal*, 94(11):4184–4201, 2008.
- [31] J. Hartmann, E. Dragicevic, H. Adelsberger, H. Henning, M. Sumser, and J. Abramowitz. TRPC3 Channels Are Required for Synaptic Transmission and Motor Coordination. *Neuron*, 59:392–398, 2008.

- [32] J. Hartmann, R. M. Karl, R. P. Alexander, H. Adelsberger, M. S. Brill, C. Rühlmann, A. Ansel, K. Sakimura, Y. Baba, T. Kurosaki, et al. STIM1 controls neuronal  $\text{Ca}^{2+}$  signaling, mGluR1-dependent synaptic transmission, and cerebellar motor behavior. *Neuron*, 82(3):635–644, 2014.
- [33] P. G. Hogan. The STIM1–ORAI1 microdomain. *Cell calcium*, 58(4):357–367, 2015.
- [34] P. G. Hogan, R. S. Lewis, and A. Rao. Molecular basis of calcium signaling in lymphocytes: STIM and ORAI. *Annu. Rev. Immunol.*, 28:491–533, 2009.
- [35] M. Hoth and R. Penner. Depletion of intracellular calcium stores activates a calcium current in mast cells. *Nature*, 355(6358):353–356, 1992.
- [36] W. Ji, P. Xu, Z. Li, J. Lu, L. Liu, Y. Zhan, Y. Chen, B. Hille, T. Xu, and L. Chen. Functional stoichiometry of the unitary calcium-release-activated calcium channel. *Proc. Nat. Acad. Sci.*, 105(36):13668–13673, 2008.
- [37] H. Jousset, M. Frieden, and N. Demaurex. STIM1 knockdown reveals that store-operated  $\text{Ca}^{2+}$  channels located close to sarco/endoplasmic  $\text{Ca}^{2+}$  ATPases (SERCA) pumps silently refill the endoplasmic reticulum. *J. Biol. Chem.*, 282(15):11456–11464, 2007.
- [38] G. Krapivinsky, L. Krapivinsky, S. C. Stotz, Y. Manasian, and D. E. Clapham. POST, partner of stromal interaction molecule 1 (STIM1), targets STIM1 to multiple transporters. *Proceedings of the National Academy of Sciences*, 108:19234–19239, 2011.
- [39] R. Lewis. Store-operated calcium channels. In D. Armstrong and S. Rossie, editors, *Advances in Second Messenger and Phosphoprotein Research*, volume 33, chapter 12, pages 279–308. Academic Press, 1999.
- [40] R. S. Lewis. Calcium oscillations in T-cells: mechanisms and consequences for gene expression. *Biochemical Society Transactions*, 31:925–929, 2003.
- [41] R. S. Lewis. Store-operated calcium channels: new perspectives on mechanism and function. *Cold Spring Harbor Perspectives in Biology*, 3(12):a003970, 2011.
- [42] R. S. Lewis and M. D. Cahalan. Mitogen-induced oscillations of cytosolic  $\text{Ca}^{2+}$  and transmembrane  $\text{Ca}^{2+}$  current in human leukemic T cells. *Cell Regulation*, 1:99–112, 1989.

- [43] J. Liou, M. Fivaz, T. Inoue, and T. Meyer. Live-cell imaging reveals sequential oligomerization and local plasma membrane targeting of stromal interaction molecule 1 after  $\text{Ca}^{2+}$  store depletion. *Proc. Nat. Acad. Sci.*, 104(22):9301–9306, 2007.
- [44] J. Liou, M. L. Kim, W. Do Heo, J. T. Jones, J. W. Myers, J. E. Ferrell, and T. Meyer. STIM is a  $\text{Ca}^{2+}$  sensor essential for  $\text{Ca}^{2+}$ -store-depletion-triggered  $\text{Ca}^{2+}$  influx. *Curr. Biol.*, 15(13):1235–1241, 2005.
- [45] R. M. Luik, B. Wang, M. Prakriya, M. M. Wu, and R. S. Lewis. Oligomerization of STIM1 couples ER calcium depletion to CRAC channel activation. *Nature*, 454(7203):538, 2008.
- [46] R. M. Luik, M. M. Wu, J. Buchanan, and R. S. Lewis. The elementary unit of store-operated  $\text{Ca}^{2+}$  entry: local activation of CRAC channels by STIM1 at ER-plasma membrane junctions. *J. Cell. Biol.*, 174(6):815–825, 2006.
- [47] J. Lytton, M. Westlin, S. E. Burk, G. E. Shull, and D. H. MacLennan. Functional comparisons between isoforms of the sarcoplasmic or endoplasmic reticulum family of calcium pumps. *J. Biol. Chem.*, 267(20):14483–14489, 1992.
- [48] I. M. Manjarrés, M. T. Alonso, and J. García-Sancho. Calcium entry-calcium refilling (CECR) coupling between store-operated  $\text{Ca}^{2+}$  entry and sarco/endoplasmic reticulum  $\text{Ca}^{2+}$ -ATPase. *Cell Calcium*, 49(3):153–161, 2011.
- [49] I. M. Manjarrés, A. Rodríguez-García, M. T. Alonso, and J. García-Sancho. The sarco/endoplasmic reticulum  $\text{Ca}^{2+}$  ATPase (SERCA) is the third element in capacitative calcium entry. *Cell Calcium*, 47(5):412–418, 2010.
- [50] E. McIvor, S. Coombes, and R. Thul. Three-dimensional spatio-temporal modelling of store operated  $\text{Ca}^{2+}$  entry: Insights into ER refilling and the spatial signature of  $\text{Ca}^{2+}$  signals. *Cell Calcium*, 73:11 – 24, 2018.
- [51] B. a. McNally and M. Prakriya. Permeation, selectivity and gating in store-operated CRAC channels. *The Journal of Physiology*, 590:4179–4191, 2012.
- [52] S. Means, A. J. Smith, J. Shepherd, J. Shadid, J. Fowler, R. J. Wojcikiewicz, T. Mazel, G. D. Smith, and B. S. Wilson. Reaction diffusion modeling of

- calcium dynamics with realistic ER geometry. *Biophys. J.*, 91(2):537–557, 2006.
- [53] E. Neher. Usefulness and limitations of linear approximations to the understanding of  $\text{Ca}^{2+}$  signals. *Cell Calcium*, 24(5-6):345–357, 1998.
- [54] H. L. Ong, X. Liu, K. Tsaneva-Atanasova, B. B. Singh, B. C. Bandyopadhyay, W. D. Swaim, J. T. Russell, R. S. Hegde, A. Sherman, and I. S. Ambudkar. Relocalization of STIM1 for activation of store-operated  $\text{Ca}^{2+}$  entry is determined by the depletion of subplasma membrane endoplasmic reticulum  $\text{Ca}^{2+}$  store. *J. Biol. Chem.*, 282(16):12176–12185, 2007.
- [55] A. B. Parekh.  $\text{Ca}^{2+}$  microdomains near plasma membrane  $\text{Ca}^{2+}$  channels: impact on cell function. *J. Physiol.*, 586(13):3043–3054, 2008.
- [56] A. B. Parekh and J. W. Putney Jr. Store-operated calcium channels. *Physiol. Rev*, 85(2):757–810, 2005.
- [57] C. Y. Park, P. J. Hoover, F. M. Mullins, P. Bachhawat, E. D. Covington, S. Raunser, T. Walz, K. C. Garcia, R. E. Dolmetsch, and R. S. Lewis. STIM1 clusters and activates CRAC channels via direct binding of a cytosolic domain to Orai1. *Cell*, 136(5):876–890, 2009.
- [58] O. H. Petersen, R. Courjaret, and K. Machaca.  $\text{Ca}^{2+}$  tunnelling through the ER lumen as a mechanism for delivering  $\text{Ca}^{2+}$  entering via store-operated  $\text{Ca}^{2+}$  channels to specific target sites. *J. Physiol.*, 595(10):2999–3014, 2017.
- [59] M. Prakriya, S. Feske, Y. Gwack, S. Srikanth, A. Rao, and P. G. Hogan. Orai1 is an essential pore subunit of the CRAC channel. *Nature*, 443:230–233, 2006.
- [60] M. Prakriya and R. S. Lewis. Regulation of CRAC Channel Activity by Recruitment of Silent Channels to a High Open-probability Gating Mode. *The Journal of General Physiology*, 128(3):373–386, 2006.
- [61] J. W. Putney. Muscarinic, alpha-adrenergic and peptide receptors regulate the same calcium influx sites in the parotid gland. *Journal of Physiology*, 268:139–149, 1977.
- [62] J. W. Putney. A model for receptor-regulated calcium entry. *Cell Calcium*, 7:1–12, 1986.

- [63] J. W. Putney. Capacitative calcium entry: from concept to molecules. *Immunological Reviews*, pages 10–22, 2009.
- [64] J. W. Putney. The physiological function of store-operated calcium entry. *Neurochem. Res.*, 36(7):1157–1165, 2011.
- [65] J. W. Putney, J. Poggioli, and S. J. Weiss. Receptor regulation of calcium release and calcium permeability in parotid gland cells. *Phil. Trans. R. Soc. Lond.*, 296:37–45, 1981.
- [66] J. W. Putney, N. Steinckwich-Besançon, T. Numaga-Tomita, F. M. Davis, P. N. Desai, D. M. D’Agostin, S. Wu, and G. S. Bird. The functions of store-operated calcium channels. *Biochim. Biophys. Acta, Mol. Cell. Res.*, 2016.
- [67] K. Samanta, P. Kar, G. R. Mirams, and A. B. Parekh.  $\text{Ca}^{2+}$  channel re-localization to plasma-membrane microdomains strengthens activation of  $\text{Ca}^{2+}$ -dependent nuclear gene expression. *Cell Rep.*, 12(2):203–216, 2015.
- [68] A. Sampieri, A. Zepeda, A. Asanov, and L. Vaca. Visualizing the store-operated channel complex assembly in real time: identification of SERCA2 as a new member. *Cell Calcium*, 45(5):439–446, 2009.
- [69] T. R. Shannon, F. Wang, J. Puglisi, C. Weber, and D. M. Bers. A mathematical treatment of integrated  $\text{Ca}^{2+}$  dynamics within the ventricular myocyte. *Biophys. J.*, 87(5):3351–3371, 2004.
- [70] J. Sneyd, K. Tsaneva-Atanasova, D. Yule, J. Thompson, and T. Shuttleworth. Control of calcium oscillations by membrane fluxes. *Proc. Nat. Acad. Sci. U.S.A.*, 101(5):1392–1396, 2004.
- [71] J. Soboloff, B. S. Rothberg, M. Madesh, and D. L. Gill. STIM proteins: dynamic calcium signal transducers. *Nat. Rev. Mol. Cell Biol.*, 13(9):549–565, 2012.
- [72] S. Srikanth and Y. Gwack. Orai1-NFAT signalling pathway triggered by T cell receptor stimulation. *Mol. Cells*, 35(3):182–194, 2013.
- [73] P. B. Stathopoulos, G.-Y. Li, M. J. Plevin, J. B. Ames, and M. Ikura. Stored  $\text{Ca}^{2+}$  depletion-induced oligomerization of stromal interaction molecule 1 via the EF-SAM region: an initiation mechanism for capacitive  $\text{Ca}^{2+}$  entry. *Journal of Biological Chemistry*, 281:3585535862, 2006.

- [74] J. Stiber, A. Hawkins, Z.-S. Zhang, S. Wang, J. Burch, V. Graham, C. C. Ward, M. Seth, E. Finch, N. Malouf, et al. STIM1 signalling controls store-operated calcium entry required for development and contractile function in skeletal muscle. *Nat. Cell Biol.*, 10(6):688–697, 2008.
- [75] P. Swietach, K. W. Spitzer, and R. D. Vaughan-Jones.  $\text{Ca}^{2+}$ -mobility in the sarcoplasmic reticulum of ventricular myocytes is low. *Biophys. J.*, 95(3):1412–1427, 2008.
- [76] H. Takemura, A. R. Hughes, O. Thastrup, and J. W. Putney Jr. Activation of calcium entry by the tumor promoter thapsigargin in parotid acinar cells. *The Journal of Biological Chemistry*, 264(21):12266–12271, 1989.
- [77] R. Thul, K. Rietdorf, M. Bootman, and S. Coombes. Unifying principles of calcium wave propagation — insights from a three-dimensional model for atrial myocytes. *Biochimica et Biophysica Acta (BBA) - Molecular Cell Research*, 1853(9):2131 – 2143, 2015. 13th European Symposium on Calcium.
- [78] P. Várnai, L. Hunyady, and T. Balla. STIM and Orai: the long-awaited constituents of store-operated calcium entry. *Trends in Pharmacological Sciences*, 30:118–128, 2009.
- [79] P. Várnai, B. Tóth, D. J. Tóth, L. Hunyady, and T. Balla. Visualization and manipulation of plasma membrane-endoplasmic reticulum contact sites indicates the presence of additional molecular components within the STIM1-Orai1 Complex. *J. Biol. Chem.*, 282(40):29678–29690, 2007.
- [80] M. Vig, C. Peinelt, A. Beck, D. L. Koomoa, D. Rabah, M. Koblan-Huberson, S. Kraft, H. Turner, A. Fleig, R. Penner, and J.-P. Kinet. CRACM1 is a plasma membrane protein essential for store-operated  $\text{Ca}^{2+}$  entry. *Science*, 312:1220–1223, 2006.
- [81] M. M. Wu, J. Buchanan, R. M. Luik, and R. S. Lewis.  $\text{Ca}^{2+}$  store depletion causes STIM1 to accumulate in ER regions closely associated with the plasma membrane. *J. Cell. Biol.*, 174(6):803–813, 2006.
- [82] M. M. Wu, E. D. Covington, and R. S. Lewis. Single-molecule analysis of diffusion and trapping of STIM1 and Orai1 at endoplasmic reticulum-plasma membrane junctions. *Mol. Biol. Cell*, 25(22):3672–3685, 2014.

- [83] P. Xu, J. Lu, Z. Li, X. Yu, L. Chen, and T. Xu. Aggregation of STIM1 underneath the plasma membrane induces clustering of Orai1. *Biochemical and Biophysical Research Communications*, 350:969–976, 2006.
- [84] S. L. Zhang, A. V. Yeromin, X. H.-F. Zhang, Y. Yu, O. Safrina, A. Penna, J. Roos, K. A. Stauderman, and M. D. Cahalan. Genome-wide RNAi screen of  $\text{Ca}^{2+}$  influx identifies genes that regulate  $\text{Ca}^{2+}$  release-activated  $\text{Ca}^{2+}$  channel activity. *Proc. Nat. Acad. Sci.*, 103(24):9357–9362, 2006.
- [85] S. L. Zhang, Y. Yu, J. Roos, J. A. Kozak, T. J. Deerinck, M. H. Ellisman, K. A. Stauderman, and M. D. Cahalan. STIM1 is a  $\text{Ca}^{2+}$  sensor that activates CRAC channels and migrates from the  $\text{Ca}^{2+}$  store to the plasma membrane. *Nature*, 437(7060):902–905, 2005.
- [86] Y. Zhou, X. Cai, R. M. Nwokonko, N. A. Loktionova, Y. Wang, and D. L. Gill. The STIM-Orai coupling interface and gating of the Orai1 channel. *Cell Calcium*, 2017.
- [87] Y. Zhou, P. Meraner, H. T. Kwon, D. Machnes, M. Ohora, J. Zimmer, Y. Huang, A. Stura, A. Rao, and P. G. Hogan. STIM1 gates the store-operated calcium channel Orai1 in vitro. *Nature Structural and Molecular Biology*, 17:112–116, 2010.
- [88] A. Zweifach and R. S. Lewis. Mitogen-regulated  $\text{Ca}^{2+}$  current of T lymphocytes is activated by depletion of intracellular  $\text{Ca}^{2+}$  stores. *Proc. Nat. Acad. Sci.*, 90(13):6295–6299, 1993.